A Study of Shell Effects in Metal Clusters

by

Jon Ferguson Miller

A thesis presented for the degree of
Doctor of Philosophy in the
Faculty of Science at the
University of Edinburgh
1994

Declaration

This thesis is of my own composition and is based on work carried out whilst a member of the molecular beam laser spectroscopy group in the Chemistry Department at the University of Edinburgh.

Signed :

Date :

To all my family.

We should be careful to get out of an experience only the wisdom that is in it - and stop there; lest we be like the cat that sits down on a hot stove lid. She will never sit on a hot stove lid again - and that is well; but also she will never sit down on a cold one anymore.

Mark Twain.

Abstract

Clusters containing both metallic and non-metallic elements have been synthesised by pulsed laser vaporisation of a solid target, followed by entrainment and nucleation of the vaporised material in a pulsed supersonic expansion with an inert carrier gas. The resulting cluster distributions were characterised by laser photoionisation time-of-flight mass spectrometry.

Such spectra display intensity anomalies, or so-called 'magic numbers', associated with enhanced geometric and/or electronic stabilities, for particular cluster sizes. These are known as shell effects.

An overview of the shell effects used to account for cluster magic numbers is presented. Details of the types of electronic and geometric structures which can be used to rationalise the existence of particularly stable clusters are discussed. The abundance patterns and intensity anomalies found in the cluster mass spectra obtained in this work are interpreted in these terms.

Studies of clusters of the alkaline earth elements of group-IIA reveal a competition between pre-crystalline icosahedral structures and fragments of the bulk crystal form. These are the first reported laser vaporisation experiments on such systems. Barium clusters containing up to 32 atoms showed a preference for an icosahedral geometry, even on the inclusion of a small number of oxygen atoms. In comparison, strontium clusters of a similar size were found to attract more oxygen atoms, and to adopt a very different structure based on the face-centred cubic (fcc) lattice of bulk strontium oxide. These observations are related to the known structures of other group-IIA metal clusters and cluster oxides.

In order to examine shell effects in more complex systems, photoionisation mass spectra have also been recorded for iron clusters containing up to several hundred atoms. In this case, intensity anomalies in the cluster distributions could not be attributed to one particular shell effect, but involved a competition between both electronic and geometric shell structure.

Acknowledgements

This thesis was only possible with aid and inspiration from many sources.

My supervisor, Pat Langridge-Smith, deserves thanks for opening the doorway to cluster science. It has been a stimulating subject area which has constantly fascinated me. The Science and Engineering Council are duly acknowledged for providing funding during my period of research.

In a similar vein, The British Council are gratefully thanked for providing the funds which permitted a collaboration with Professor Michel Broyer's cluster group in Lyon. I thoroughly enjoyed working in France, and coming into contact with such professional scientists, and good friends, as Driss Rayane and Michel Pellarin.

Looking back to my formative years, I feel extremely privileged to have been guided by Andrew James and Jim Macdonald who both helped me to develop a sound approach to the cluster experiments. Thanks also go to Pierre-Francois Brevet for his technical expertise, and for providing a link with the Lyon group.

My colleagues in the laser group have been very helpful over the years. The nature of these experiments was such that a solo researcher could easily have become frustrated. This has been avoided (just) by the intervention of Mike Dale with his novel outlook on life, and by the friendship of Ally, Craig, Scott, Cameron, Trevor, and the others who live within the padded walls of room 6. Thanks also to Stuart Mains in the workshop, and Derek Burgess in stores for providing more than just a service.

The encouragement of my family has been appreciated over the years, and a special thanks is reserved for my mother, Susan, who has continually inspired me. In some ways the actual process of writing this thesis, combined with trying to find employment, has been as difficult as anything else I have attempted. That I have come through this period is due, in no small way, to my wife, Alli. My sincerest thanks to her, and to everyone else mentioned here.

Table of Contents

List of Figures

Chapter 1

INTRODUCTION

1.1 Background

The term "cluster" can be applied to several different types of chemical system. In an inorganic context the word evokes images of many metal atoms bonded together, and enclosed by a shell of stabilising ligands. Molecular clusters also exist where the component molecules are held together by weak van der Waals forces. The type of clusters studied in this work fall into the category of valence-bonded elemental clusters, primarily unligated metal clusters. These can consist of anywhere from two to several thousand metal atoms bonded together.

Scientific journals in the area of chemical physics have contained an increasing number of articles on the subject of cluster research over the last 15 - 20 years. One of the major driving forces behind research on these species has come from a desire to link the previously disparate areas of atomic or molecular science and solid state physics. Much is known about the properties of distinct atoms or molecules at one limit, and of bulk systems at the other limit. It is no surprise, then, that scientists were curious as to the properties of clusters lying between these two limiting states of matter.

Clearly, there must be an evolution of the electronic and physical properties of the cluster as it increases in size, eventually becoming indistinguishable from the bulk material. In terms of metal clusters, the question of where molecular chemistry and metal physics meet is an interesting one, and will depend on how metal atoms arrange themselves in a cluster, and what happens to the electronic

states of the system as the cluster grows. Thus one can see the purely scientific reasons for the study of metal aggregates.

If more incentive is required, then it can be found in the fact that metal clusters can be closely linked with various catalytic processes. If one thinks about heterogeneous catalysis by finely divided support metals, it isn't difficult to imagine that the active sites for chemisorption could be modelled by a cluster which has a similar geometric and electronic profile to the convex crystal defects thought to be responsible for catalytic activity [1,2].

Specific examples do exist. Nickel deposition has been shown to be promoted by palladium clusters containing between 4 and 20 atoms [3]. The Fischer-Tropsch catalyst [4] is composed of iron cluster microcrystals supported on an inert surface. Other metal-containing clusters such as Fe_4S_4 can be found at the active sites of some enzymes [5].

The experimental and theoretical study of transition metal clusters, in particular, is therefore of considerable relevance to the field of catalysis. Many scientists, however, embarked on a voyage into the field of cluster research mainly because it was a great uncharted area at the junction of physics and chemistry, with the potential to generate new avenues of research for years to come. The high level of research activity in the area of cluster science has spawned the development of many new techniques to create and study these species, and has led to one of the most universally exciting discoveries of modern cluster science - the detection of buckminsterfullerene [6,7].

1.2 Metal Cluster Experiments

One of the first widely used techniques for the preparation of cluster species was matrix isolation [8]. Metal atoms, usually generated by an electric discharge, or vaporised from a quartz or stainless steel cell, were co-deposited onto a cold, clean surface with an excess of matrix gas. Typical experiments involved deposition onto polished copper or platinum plates cooled to 5K, or onto a suitably cold

sapphire or NaCl window. The matrix gas was typically argon or krypton. Metal dimers were routinely made, and were studied by techniques such as absorption spectroscopy or electron spin resonance spectroscopy [9,10]. Larger clusters could also be produced by allowing a controlled temperature gradient to exist within the matrix. This encouraged metal atoms or dimers to diffuse slowly through the matrix, eventually coalescing to form larger clusters [11].

The size of clusters that could be produced in matrices was limited, however, by the need for an excess of matrix gas to keep the clusters separated. A higher proportion of metal atoms was required to make larger clusters, and this system could react to a slight disturbance by spontaneously forming macroscopic crystals.

One great difficulty with matrix studies of metal clusters was the ambiguity involved in the assignment of spectral features to a specific cluster. Matching known spectral features with gas-phase studies on metal dimers could be accomplished most of the time, but the lack of mass-selectivity allowed no definite identification of the species responsible for a new spectroscopic transition [12]. Even with a known feature, assignment could be difficult at times because of perturbations from the host matrix. Rotational structure was lost in broadened peak profiles, and the actual peaks themselves could be split and shifted by up to $1000cm^{-1}$ due to the different sites available in the solid host, and to interactions between host and cluster species [13].

The first experiments on gas-phase metal clusters used the technique of Knudsen effusion mass spectrometry [14,15]. The Knudsen cell, containing the metal of interest, was heated to the point of vaporisation, whereupon the metal vapour passed through an effusive nozzle into the ion source region of a mass spectrometer. These experiments allowed the determination of binding energies of the clusters [16], although metal aggregates larger than dimers were rarely detected due to inefficient cooling during the effusive expansion.

The use of hot ovens to produce clusters has been very successful for alkali metals. Clusters were originally produced in free jet expansions, but the oven source was subsequently coupled with seeded-beam supersonic expansion techniques to make this experimental method very powerful indeed [17,18]. In fact, some of the

larger clusters studied in recent experiments have been produced by this method. For example, the detection of sodium clusters containing up to 22000 atoms prepared in this fashion has recently been reported [19]. Access to this size range of metal aggregates is very exciting to the true cluster scientist.

The main drawback to the hot oven - seeded beam technique is that it is limited in its applicability to refractory materials, such as the transition metals. The extreme temperatures required to generate an adequate vapour pressure of a refractory metal can result in contamination from the oven walls, and even clogging of the nozzle beam orifice. The continuous nature of the molecular beam produced in these experiments also demands a large scale pumping system to cope with the constant gas throughput.

Over the years there have been a few other techniques employed for cluster generation which have met with limited levels of success. Ligand-stripping from metal-cluster-carbonyls has been studied [20], but the cluster core tends to fragment when the ligands are removed. Another approach employed an electric discharge to produce silver dimers [21]. In its infancy this method was not linked to a mass-selective detection device, and also produced internally hot clusters, giving rise to heavy spectral congestion due to the population of many rovibrational levels. It thus proved difficult to characterise the exact compositions of clusters created. A recent renaissance of this experimental method has seen it linked with supersonic expansion and mass spectrometric techniques, assuming the acronym PACIS (Pulsed Arc Cluster Ion Source) [22,23]. This source looks very promising, although its use has been mainly in experiments on positive and negative cluster ions, which are directly produced in abundance by this technique.

The barrier to the creation of large clusters of refractory materials was broken down in 1981 by Smalley's group [24]. It was already known that the supersonic expansion technique utilised for the generation of alkali metal clusters would produce a broad distribution of cluster sizes. Studies of the effects of varying the expansion conditions had been reported [25]. It had also been shown that metal targets could be vaporised easily when subjected to the radiation from pulsed, high-power lasers [26]. Smalley's idea was to combine these two techniques into a

new method for the generation of refractory metal clusters. In fact, the synergism of these two techniques proved to be astounding. The pulsed laser vaporisation allows extreme local heating of a solid metal target, but without the complications of having a complete high temperature system and the concomittant design difficulties. The pulsed, inert carrier gas facilitates very rapid cooling and clustering of the metal vapour, and supersonic expansion further cools the nascent clusters. The cluster beam then contains high concentrations of metal aggregates which have been cooled to the lowest rovibronic levels by collisional energy relaxation during the expansion process.

This laser vaporisation - supersonic expansion (LVSE) technique allowed the experimentalist to pursue either of the main topics of cluster science with far greater ease than ever before. On the one hand, spectroscopic studies of small metal clusters, dimers and trimers, would be much easier due to the spectral simplification of studying energetically cold systems. The pulsed nature of the production technique was ideal for a mass-selective detection method. Indeed, the laser vaporisation sources were commonly being coupled to time-of-flight mass spectrometers. In the space of only a few years many of the electronic states of transition metal dimers had been probed with this new technique [13]. As well as providing small, extremely cold metal dimers, trimers, etc., the laser vaporisation technique allowed the production of very large clusters, depending on the choice of source conditions. This allowed another aspect of cluster research to be followed, namely the evolution of physical and chemical properties with cluster size, through the greatly extended range of cluster sizes available. Such a laser vaporisation cluster source was employed to carry out the experiments reported in this thesis.

The increased interest in the study of metal clusters initially proved to be a boon for the theoreticians. The new experiments performed on metal dimers in particular allowed the theoretical scientists to check their predictions of molecular constants (bond lengths, vibrational constants, bond energies, etc.), and to modify the models or techniques used. It didn't take long before the amount of experimental data had exceeded the theorists postulated properties for the cluster systems. The theoreticians have revelled in this setting, being able to fine-tune

existing models, and make intuitive leaps to prepare new models which could account for the wealth of experimental data provided. As the spectroscopic studies of dimer and trimer systems became more routine, the scientists in both camps ventured into the realms of larger clusters.

Shell models were borrowed from nuclear physics, and adapted to model metal cluster systems rather than groups of nuclear particles. These were developed into theories which allowed the prediction of electronic stabilities for some metal cluster species. This area of cluster research has been far from fully explored. The continual enhancement of experimental techniques means that a larger variety of clusters can be studied, and to a greater size regime.

An excellent review of the theoretical techniques employed to study small metal clusters is presented in an article by Koutecký and Fantucci [27]. The results of calculations on many of these systems are summarised therein. The methods used for larger clusters are discussed in a later chapter of this thesis.

The actual experiments that can be performed to produce the data that is so useful to theoreticians are many. An idea of how a molecule will behave in reactions can be gained through knowledge of how likely it is to donate or accept electrons. Thus measurements of ionisation potential (IP) and electron affinity (EA) are very important, and these types of measurements are possible on metal clusters produced by laser vaporisation. Metal cluster IPs can be bracketed [28], or inferred from photoionisation spectra obtained by varying the wavelength of ionisation [29]. The electron affinities of cluster anions can be obtained simply by studying the fluence dependence of the photodetachment process at different photon energies [30,31].

An offshoot from photodetachment of electrons from metal cluster anions is the study of photofragmentation. If a specific cluster is mass-selected then its fragmentation channels can be probed by detection of the daughters produced after laser irradiation at various wavelengths [32,33,34]. Additionally, analysis of the kinetic energy of a detached electron by photoelectron spectroscopy provides a true insight into the evolution of band structure. One such study on copper clusters showed that by the time the cluster contains 410 constituent atoms, the

electronic levels have grown into electronic bands which are indistinguishable from those of bulk copper [35].

The laser vaporisation source can be modified to allow the introduction of various reagents into the cluster beam, thus permitting the study of the actual reactivities of various cluster species. The modification involves the use of a flow-tube reactor, which is simply a channel into which dilute reactants are injected as the clusters flow through. The results of the reactions may often reveal details about chemisorption processes [36,37,38].

Of course, various spectroscopic techniques can be employed to probe small metal clusters. Resonant 2-photon ionisation (R2PI) and laser-induced fluorescence (LIF) are two of the most versatile techniques used to gain information about electronically excited states of cluster species [13]. Assignment of spectral features does become very difficult for clusters containing more than three atoms, however, so the bulk of data on larger clusters consists of IP and EA measurements. Also for the larger systems, specific stabilities can be accounted for by proposing models which suggest favoured geometric or electronic structures for certain cluster species. One way in which these stabilities can manifest themselves is in the appearance of "magic numbers", anomalies in cluster abundance spectra.

Certainly, the wealth of techniques available for studying clusters is overwhelming. Another example is the observation of giant resonances within the photofragmentation cross-sections of mass-selected silver clusters [39], and similarly for sodium clusters [40]. These plasmon resonances are attributable to collective electronic excitations, and magic numbers are also exhibited in this type of experiment.

1.3 Outline of Thesis

The exact topic of study in such a diverse field is obviously very difficult to choose. The laboratory in which the present studies were carried out contains two molecular beam machines which both allow cluster generation by laser vaporisation, and, subsequent to laser photoionisation, detection by time-of-flight mass spectrometry (TOFMS). Previous workers in this particular group have concentrated on the electronic spectroscopy and IP measurements of coinage metal dimers [41,42,43]. As seen already, reviews from up to seven years ago have dealt with a vast proportion of the homonuclear metal dimers available [13]. The study of heteronuclear dimers is straightforward if the melting points of the two metals are similar (e.g. for CuAg [42]), or if the luxury of the use of two vaporisation lasers is feasible [44]. The production of a mixed metal target is more difficult for species which have vastly different melting points. The inhomogeneity of the resultant target can lead to a varying amount of the heteronuclear dimer in the cluster beam from one sampling interval to the next. Needless to say, this situation is not close enough to the stable beam composition required to perform spectroscopic experiments.

One area of the cluster field which is receiving a lot of interest now is the study of magic numbers for certain clusters. This side of the research field was considered to be an exciting alternative to the study of dimer systems, and leant more heavily towards the overall goal of cluster science, namely to help quantify the changes that occur with increasing cluster size.

It was therefore decided appropriate to carry out experiments in order to attempt to characterise some of these magic number cluster systems. This would diversify the range of experiments shown to be feasible on the cluster apparatus in this laboratory. The reasons for choosing the particular metal cluster systems that have been studied in this work are discussed in more depth in the individual chapters dealing with those experiments. The overall layout of this thesis is as follows :

In Chapter 2 the principles involved in the main components of the experimental cycle are described. Within this context the theories of the laser vaporisation and cluster growth processes are discussed, as well as the ionisation and detection techniques used for cluster identification.

In Chapter 3 details of the actual equipment used in the cluster experiments reported in the remainder of the thesis are given.

In Chapter 4 an outline of the electronic and geometric shell effects that have been used to account for cluster magic numbers is presented, together with illustrative examples from the literature of these two effects.

Chapter 5 presents mass spectra obtained in this work for a variety of cluster systems to show the versatility of the laser vaporisation technique. Magic numbers from the spectra are commented upon, some of which are rationalised within the context of the models described in Chapter 4.

In Chapter 6 the work carried out here on the Group-IIA alkaline earth metal clusters, and their cluster oxides is described. The magic numbers observed for these species are examined, and compared with other work.

Chapter 7 relates the work carried out in Lyon as part of a collaborative programme sponsored by the British Council. The experimental set-up is described, and mass spectra of iron clusters are presented. Possible explanations of the observed magic numbers for this system are detailed.

Bibliography

[1] A. Herrmann, E. Schumacher and L.Wöste, J. Chem. Phys., **68** (1978) 2327.

[2] M. Moskovits, Accounts of Chem. Research, **12** (1979) 229.

[3] J.F. Hamilton and P.C. Logel, J. Catal., **29** (1973) 253.

[4] G.A. Mills and F.W. Steffgen, Catal. Rev., **8** (1973) 159.

[5] W. Lorenberg (ed.), '*Iron-Sulphur Proteins*', Academic, New York, 1973-77, Vols. I-III.

[6] E.A. Rohlfing, D.M. Cox and A. Kaldor, J. Chem. Phys., **81** (1984) 3322.

[7] H.W. Kroto, J.R. Heath, S.C. O'Brien, R.F. Curl and R.E. Smalley, Nature, **318** (1985) 162.

[8] S. Cradock and A.J. Hinchcliffe, '*Matrix Isolation*', Cambridge University Press, 1975.

[9] D.M. Lindsay, D.R. Herschbach and A.L. Kwiram, Mol. Physics, **32** (1976) 1199.

[10] G.A. Ozin, H. Huber, D. McIntosh, S. Mitchell, J.G. Norman, Jr. and L. Noodleman, J. Am. Chem. Soc., **101** (1979) 3504.

[11] A. Herrmann, S. Leutwyler, E. Schumacher and L. Wöste, Helv. Chim. Acta, **61** (1978) 453.

[12] V.E. Bondybey and J.H. English, J. Chem. Phys., **73** (1980) 42.

[13] M.D. Morse, Chem. Rev., **86** (1986) 1049.

[14] J. Drowart, '*Condensation and Evaporation of Solids*' (ed. E. Rutner, P. Goldfinger and J.P. Hirth), Gordon and Breach Inc., New York, 1964, p.255.

[15] J. Drowart and P. Goldfinger, Angew. Chem., **6** (1967) 581.

[16] K. Hilpert, Ber. Bunsenges. Phys. Chem., **83** (1979) 161.

[17] D.R. Preuss, S.A. Pace and J.L. Gole, J. Chem. Phys., **71** (1979) 3553.

[18] S.J. Riley, E.K. Parks, C.-R. Mao, L.G. Pobo and S. Wexler, J. Phys. Chem., **86** (1982) 3911.

[19] H. Göhlich, T. Lange, T. Bergmann, U. Näher and T.P. Martin, Chem. Phys. Lett., **187** (1991) 67.

[20] W.E. Hollingsworth and V. Vaida, J. Phys. Chem., **90** (1986) 1235.

[21] C. Shin-Piaw, W. Loong-Seng and L. Yoke-Seng, Nature, **209** (1966) 1300.

[22] G. Ganteför, H.R. Siekmann, H.O. Lutz and K.H. Meiwes-Broer, Chem. Phys. Lett., **165** (1990) 293.

[23] H.R. Siekmann, C. Lüder, J. Faehrmann, H.O. Lutz and K.H. Meiwes-Broer, Z. Phys. D, **20** (1991) 417.

[24] T.G. Dietz, M.A. Duncan, D.E. Powers and R.E. Smalley, J. Chem. Phys., **74** (1981) 6511.

[25] O.F. Hagena and W. Obert, J. Chem. Phys., **56** (1972) 1793.

[26] J.F. Ready, '*Effects of High Power Laser Radiation*', Academic, New York, 1971.

[27] J. Koutecký and P. Fantucci, Chem. Rev., **86** (1986) 539.

[28] E.A. Rohlfing, D.M. Cox and A. Kaldor, J. Phys. Chem., **88** (1984) 4497.

[29] E.A. Rohlfing, D.M. Cox, A. Kaldor and K.H. Johnson, J. Chem. Phys., **81** (1984) 3846.

[30] L.-S. Zheng, P.J. Brucat, C.L. Pettiette, S. Yang and R.E. Smalley, J. Chem. Phys., **83** (1985) 4273.

[31] L.-S. Zheng, C.M. Karner, P.J. Brucat, S.H. Yang, C.L. Pettiette, M.J. Craycraft and R.E. Smalley, J. Chem. Phys., **85** (1986) 1681.

[32] L.A. Bloomfield, R.R. Freeman and W.L. Brown, Phys. Rev. Lett., **54** (1985) 2246.

[33] Y. Liu, Q.-L. Zhang, F.K. Tittel, R.F. Curl and R.E. Smalley, J. Chem. Phys., **85** (1986) 7434.

[34] W. Begemann, S. Dreihöfer, G. Ganteför, H.R. Siekmann, K.H. Meiwes-Broer and H.O. Lutz, '*Elemental and Molecular Clusters*', Springer-Verlag, 1987.

[35] K.J. Taylor, C.L. Pettiette-Hall, O. Cheshnovsky and R.E. Smalley, J. Chem. Phys., **96** (1992) 3319.

[36] M.R. Zakin, D.M. Cox and A. Kaldor, J. Phys. Chem., **91** (1987) 5224.

[37] R.J. St.Pierre, E.L. Chronister and M.A. El-Sayed, J. Phys. Chem., **91** (1987) 5228.

[38] M.R. Zakin, D.M. Cox and A. Kaldor, J. Chem. Phys., **87** (1987) 5046.

[39] J. Tiggesbäumker, L. Köller, H.O. Lutz and K.H. Meiwes-Broer, Chem. Phys. Lett., **190** (1992) 42.

[40] K. Selby, M. Vollmer, J. Masui, V. Kresin, W.A. de Heer and W.D. Knight, Phys. Rev. B, **40** (1989) 5417.

[41] A.M. Butler, *Ph.D. thesis*, Edinburgh University, 1989.

[42] A.M. James, *Ph.D. thesis*, Edinburgh University, 1990.

[43] J.W. Macdonald, *Ph.D. thesis*, Edinburgh University, 1993.

[44] S. Nonose, Y. Sone, K. Onodera, S. Sudo and K. Kaya, J. Phys. Chem., **94** (1990) 2744.

Chapter 2

EXPERIMENTAL PRINCIPLES

This chapter deals with the processes involved during the cluster experiments reported in the later chapters of this thesis. The experimental cycle can be broken down into several distinct elements from the vaporisation process to the detection of the clusters, and these are detailed here. Actual details of the equipment used to carry out the experiments are given in Chapter 3, and the slight variations for the apparatus used in Lyon are described in Chapter 7.

2.1 The Experimental Cycle

As intimated in the introduction, the technique used to generate clusters was that of pulsed laser vaporisation coupled with supersonic expansion. All of the experiments undertaken were of a pulsed nature, befitting the requirements of the laser vaporisation technique. The repetition rate of the experimental cycle was 10Hz in Edinburgh, and 7.5Hz in Lyon. The simplest way to expose the more vital components of the experiment, which will merit further discussion, is to follow the progress of a single metal atom through the molecular beam machine.

For the sake of argument, this metal atom begins life near the surface of a metal target which is housed in an evacuated vacuum chamber. Every tenth of a second a high density pulse of helium gas passes over the surface of the metal, but contained within a channel with a diameter on the order of 1mm. This gas

pulse is delivered from a molecular beam valve, and is typically a few hundred microseconds in duration. As the helium passes over the target, the focussed, Q-switched output of the Nd:YAG vaporisation laser strikes the surface of the metal. The point of interrogation is less than 1mm across. This laser pulse causes the rapid ejection of many metal atoms in the form of a hot plasma, and our atom of interest leaves its bulk surroundings to enter the gas phase. At this point it is swept along in the stream of helium carrier gas, and undergoes many collisions with atoms of both helium and metal. One metal atom may stick to another as the collision energy is removed by a third atom, and in this way clusters grow.

After many such collisions, the cluster beam expands supersonically into the high vacuum chamber from the high pressure clustering region. Our metal atom is now part of a metal cluster whose internal degrees of freedom have been cooled dramatically into mainly translational energy in the direction of the carrier gas pulse. The beam of neutral clusters is collimated by passing through a skimmer, and then enters a second high vacuum chamber.

There another pulse of laser light, normally in the ultraviolet region of the spectrum, intersects the cluster beam. The metal clusters absorb one or several photons, and the energy provided allows an electron to be ejected. The cluster is now charged, and feels an electrostatic pull in a direction perpendicular to that of its original flight. This force comes from the electric field existing between the plates of the ion source region of a time-of-flight mass spectrometer (TOFMS). The cluster ion is now accelerated to a velocity dependent on its mass. It then travels in a field-free region for a short while before it collides with a detector plate. This collision scatters many electrons which are detected, amplified and processed by a computer-controlled data acquisition system. The cluster's existence is over, but a record of it is stored in the computer, and we can judge how many atoms were incorporated in it by the length of time it took to hit the detector.

Back at the cluster source in the main vacuum chamber, the whole process is beginning again. The metal target has rotated to expose a fresh, unpitted surface to the vaporisation laser beam, and another pulse of helium carrier gas passes over the surface to promote more cluster growth.

Thus we have described the experimental cycle and the general processes involved. We can see that the important principles which should be understood include; the laser vaporisation process, the details of cluster growth and supersonic expansion, the photoionisation event, and the method of detection. These processes, which are fundamental to the workings of our cluster experiments, are now described in greater detail.

2.2 The Laser Vaporisation Process

Various processes can occur when pulsed laser radiation interacts with a metal surface [1]. The result of this interaction depends mainly on the power density, and on the duration of the laser pulse. The properties of the metal target are also important in determining how quickly heat diffuses through the material, and at what temperatures melting and vaporisation will take place.

The main interaction processes are depicted in Figure 2–1. As the laser light is absorbed by the surface (Figure 2–1a), the metal begins to heat up, and eventually reaches the melting temperature. Thermal conduction allows propagation of the solid/liquid interface into the target material (Figure 2–1b). Meanwhile, the laser pulse is continuing to heat the target surface up to the vaporisation temperature, at which point gaseous material is driven from the surface, and a hole is drilled into the metal (Figure 2–1c).

A higher power density could be obtained by using a Q-switched laser pulse [2]. The technique of Q-switching relates to rapidly changing the Quality (Q) factor of the laser. A high Q value essentially means that losses from the cavity are small. As energy is building up in the cavity, a steady state is reached when any further population inversion provided by the pump source is depleted by lasing action within the cavity. If this lasing action is halted, then the population inversion can be vastly increased. Typically, an electro-optic device is used to shield one of the cavity's end mirrors, resulting in a lowered Q value, and a build-up of energy. When the electro-optic shutter is opened, the Q factor is immediately

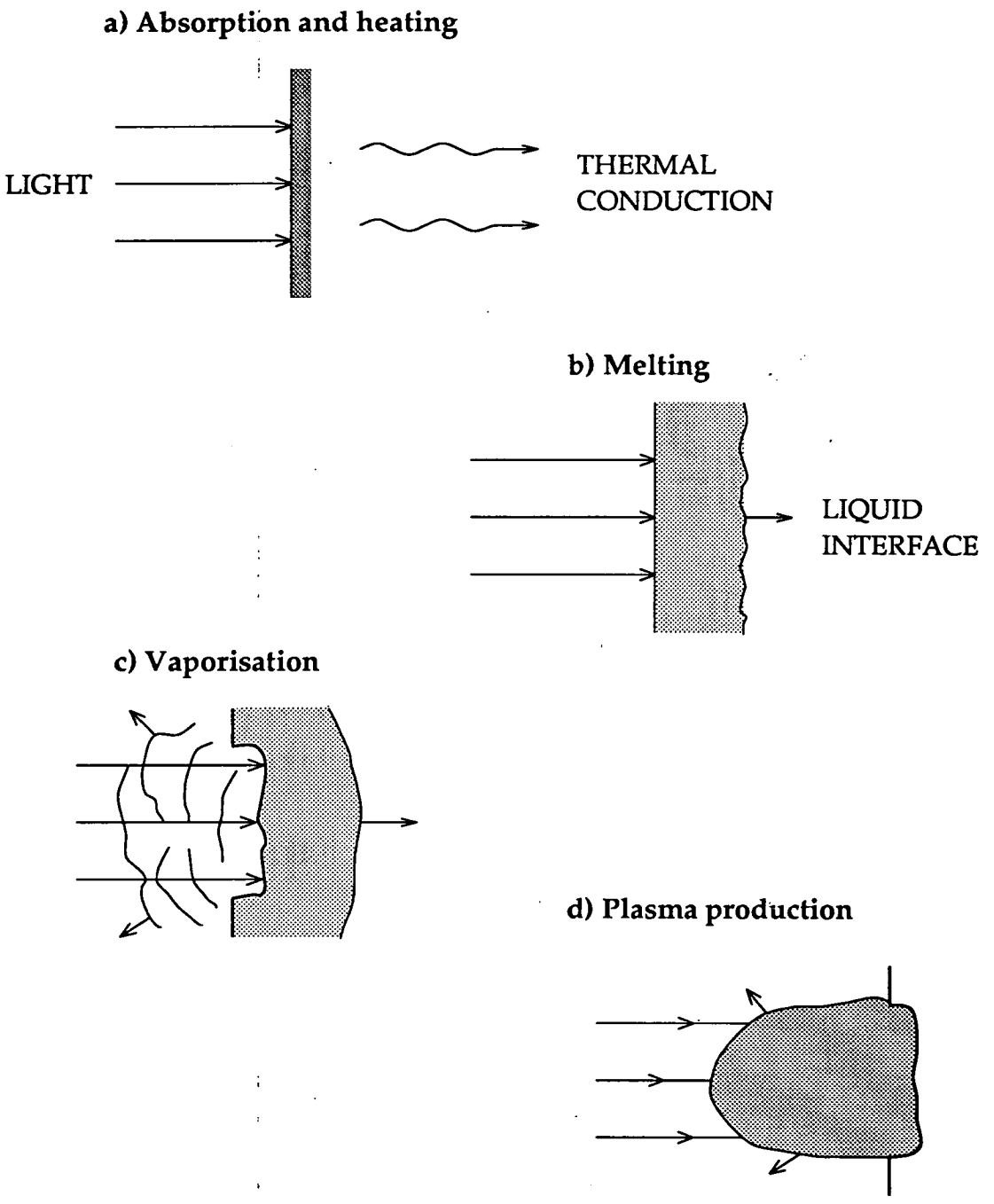

Figure 2–1: Results of laser interaction with a metal surface.

switched to a high value, and the stored energy is released as a short, intense pulse of laser radiation. This pulse is a lot shorter than that provided by an un-Q-switched laser, and power densities can easily exceed $10^8 \mathrm{Wcm}^{-2}$. Under these extreme conditions, a different interaction process with the metal target can occur. One might reasonably assume that a higher power density would remove more material from the metal surface, but in fact an unexpected phenomenon occurs. The extremely rapid heating renders the melting process insignificant, and the metal surface vaporises on the nanosecond timescale. The ejected material is in the form of a hot, opaque plasma which shields the metal surface from the rest of the laser pulse, and itself absorbs more energy to become superheated (Figure 2–1d). Thus the higher power density laser beam actually removes less material than one with a lower power density [3].

For our cluster experiments then, which process should we utilise? The less powerful laser pulses (lower than $10^8 \mathrm{Wcm}^{-2}$) of longer duration (100μs-1ms) seem to be able to remove more material. If this was our only criterion then our choice is simple. However, the state of the material after removal is of great importance, and the low power density laser pulses tend to cause the ejection of liquid droplets due to the slower heating process. These liquid droplets can act as nucleation centres and use up the supply of free metal atoms which are the base units for cluster formation.

It seems, therefore, that a compromise must be reached between the amount of material liberated from the surface, and the state it is in when released. So we return to the high power density regime depicted in Figure 2–1d, in which plasma production is favoured [4]. The only problem to be overcome is that of the excessive heating of the plasma. It turns out that entrainment in the carrier gas pulse does provide enough cooling to allow cluster growth to occur. Indeed, the scientific groups which carry out cluster experiments by this technique all tend to use a Q-switched Nd:YAG or a noble gas-halogen excimer laser to accomplish the vaporisation step.

Since we will work with a high power density and short laser pulse for our vaporisation process, let us now examine this interaction more closely. We have

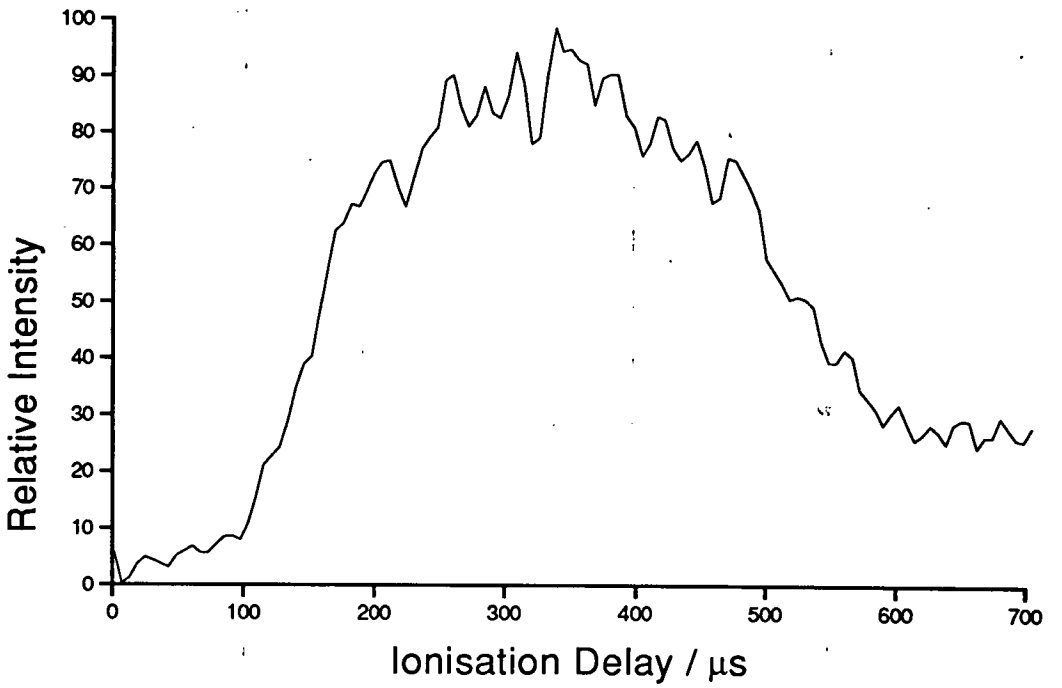

Figure 2–2: Helium pulse profile with no laser vaporisation.

seen that in this power regime an opaque plasma forms very rapidly above the metal surface, shielding the target from the rest of the laser pulse. The plasma is not static, but continues to expand due to the pressure gradient present. The plasma then decouples from the surface and propagates towards the laser as a laser-supported absorption (LSA) wave. Evidence of this LSA wave has been provided photographically [5], and its presence can also be monitored during the experiments performed here.

Since the LSA wave propagates back towards the vaporisation laser, we can reason that during these cluster experiments it must interact with the pulse of helium carrier gas which passes over the metal surface as vaporisation occurs. Comparison of the helium pulse profile when the vaporisation laser is turned off with the profile when the laser is firing should show some evidence of the LSA wave.

Figure 2–2 shows a typical helium pulse profile. This set of data is obtained

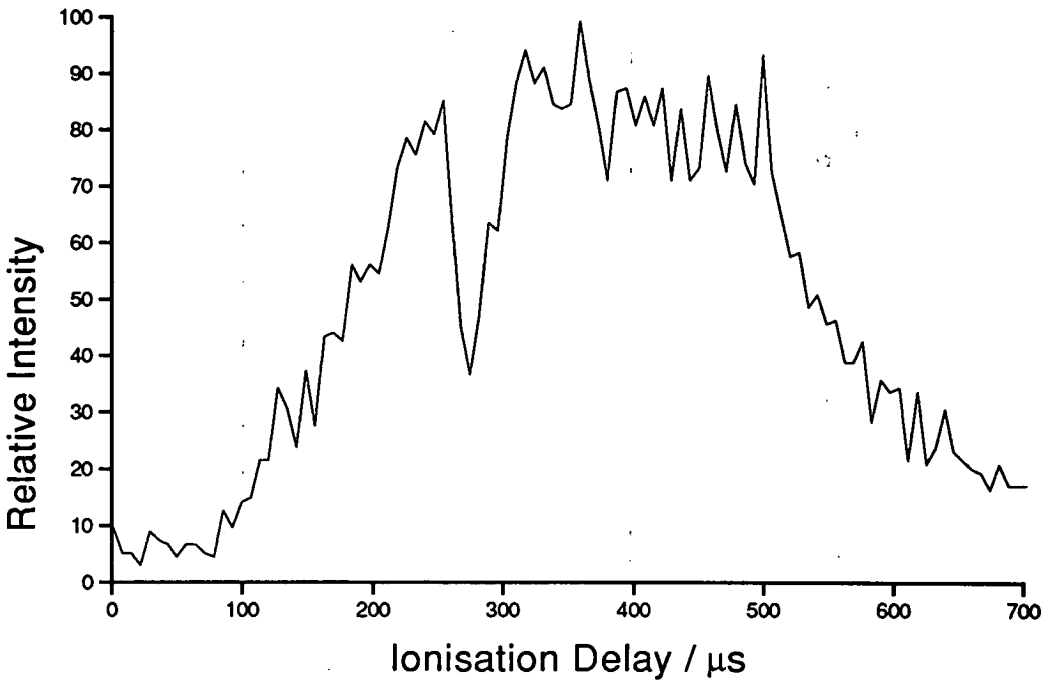

Figure 2–3: 'Hole burning' in helium profile by LSA wave resulting from the laser vaporisation process.

by ionising the helium beam after it has traversed the distance to the ion source region of the TOFMS, and detecting the signal from the resultant helium ions. The actual observation of a helium ion signal may have been unexpected due to the high ionisation potential of the helium atom. On interaction with laser light at 193 nm, four photons are required to ionise helium. The cross-section for this process is very small, but may be augmented by accidental near-resonance in one of the photon absorption steps. The overwhelming density of helium atoms in the molecular beam certainly contributes to the appreciable signal intensity which results. Varying the time at which the ionisation laser is fired provides a means of determining the helium density at different points in the gas pulse. Compare this with the pulse profile shown in Figure 2–3 in which a 'hole' is blown in the helium pulse by the LSA wave. The resulting local reduction in gas density at this point in the carrier gas pulse is preserved as the helium travels through the molecular

beam machine. Note that after the plasma has decoupled from the metal surface it does eventually dissipate to allow the vaporisation laser to interact with the surface once again.

Thus, we now have some insight into the laser vaporisation process which causes the ejection of material from the metal surface in the form of a hot, dense plasma. This material expands from the metal surface into the path of the inert carrier gas pulse, and is swept along with the helium.

2.3 Cluster Formation

The actual process by which clusters form is difficult to be absolutely certain about, but a realistic model can be constructed which accounts for the cluster distributions observed.

Firstly, the material vaporised from the metal target is assumed to be mostly in the form of single atomic units due to the extremely high temperatures at which the vaporisation process is driven [6]. This assumption is supported by the fact that the metal atom and dimer signals detected after ionisation are much more intense than any other species, even given that they generally have higher photoionisation thresholds than larger clusters. The entrainment process is accomplished by simple two-body collisions between metal species and carrier gas atoms. Once the plasma material has been swept into the carrier gas pulse with a certain amount of quenching, clustering can proceed by three-body collisions in which two metal particles collide, and excess energy is removed by collision with an inert gas atom. In this way the inert carrier gas acts as a heat bath for the dispersion of the condensation energy of clusters formed [7].

The larger clusters can be constructed either by coalescence of smaller clusters, or by an aggregation route in which single-atom addition to existing clusters is the main formation mechanism. Due to the overwhelming presence of atomic species in the beam, as mentioned previously, it is the second mechanism which is assumed to statistically dominate the cluster growth process [8,9].

Since it is the three-body collisions which promote cluster growth, then one can assume that the cluster size distribution will be related to the length of time that the beam remains in a high pressure region in which collisions are frequent. Thus larger clusters can be preferentially formed by containing the cluster beam within a constricted channel for a longer period before expansion into the high vacuum occurs, which is the next step in the experimental cycle. Various geometries have been tested for these so-called clustering channels, and the results have shown agreement with the above arguments for cluster growth [10,11,12]. The other main factor which helps determine the extent of clustering is the backing pressure of the carrier gas. A higher pressure will allow more energy transfer collisions, and should thus promote the formation of larger clusters [6]. However, there is not a linear relationship between the backing pressure of the carrier gas and the size of clusters produced. If the backing pressure is too great then cluster growth can be impeded as the metal species find it difficult to come together within this denser sea of helium atoms.

2.4 Supersonic Expansion of the Cluster Beam

After cluster formation has occurred, the cluster beam is then expanded into the high vacuum region of the apparatus. The dynamical processes involved in this expansion depend on the Knudsen number, K, which is defined as

$$K = \frac{\lambda_0}{D} \tag{2.1}$$

where

λ_0 is the mean free path of particles within the nozzle, and

D is the diameter of the nozzle orifice through which the expansion takes place.

Two distinct processes can be described. When K is large, the conditions are such that effusive flow through the nozzle occurs. In this case there are effectively no collisions taking place as material passes through the nozzle orifice. The second case is when $K \ll 1$, which is normally achieved by increasing the stagnation pressure within the nozzle to lower λ_0. These conditions lead to the beam exiting

the nozzle as a supersonic expansion [13,14]. This type of expansion was first proposed [15], and tried [16] simply in an effort to enhance the beam intensity relative to that achieved by effusive processes. However, other advantages were to result from this expansion technique.

In the regime $\lambda_0 \ll D$, many collisions take place as the particles in the beam exit the nozzle orifice. These binary collisions cool the internal degrees of freedom of the beam species, allowing the conversion of translational, rotational, and vibrational energy into directed mass flow with a corresponding increase in beam velocity [17]. As the expansion continues, this leads to very low temperatures in the beam[1], normally of the order; $T_{trans} = 0.5 - 20K, T_{rot} = 2 - 50K, T_{vib} = 10 - 100K$ [18]. Very soon after expansion the beam becomes collisionless due to the high degree of directionality, and to the small spread in the velocities of the beam species, and these energy distributions become fixed.

One effect of a seeded supersonic expansion in a carrier gas that must be noted is that of velocity slippage. The light carrier gas has a high thermal velocity, and two-body collisions will cause acceleration of the slower clusters which have been formed. It is only after this velocity averaging of all beam species takes place that the internal cooling, as mentioned above, can be promoted by lower energy collisions. For low carrier gas pressures the acceleration of seeding molecules remains incomplete, and this can give rise to velocity differences between the heavier clusters and the lighter carrier gas atoms [19]. This velocity slip effect can be overcome if a high carrier gas density is used, and the employment of a pulsed molecular beam valve leads to high enough helium pulse densities to render the velocity slippage effect negligible.

An idea of the extent of the reduction in the spread of beam velocities can be gained from Figure 2–4. The velocity spread for a beam of helium atoms at 300K is given by the typical Maxwell-Boltzmann distribution. The temperature of the

---

[1]The higher vibrational temperature reflects the smaller cross-section for collisional removal of vibrational quanta from molecules in the expansion

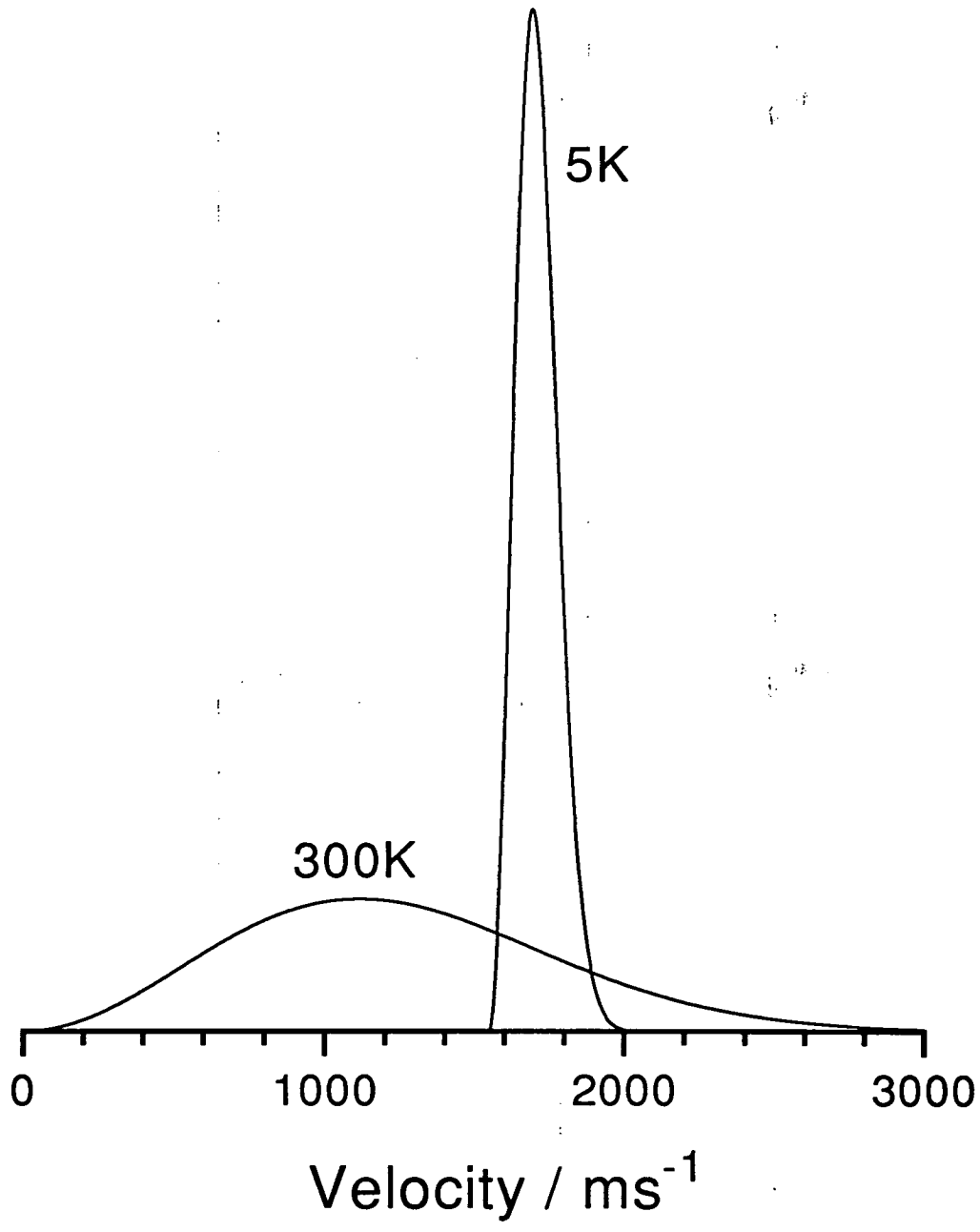

Figure 2–4: Velocity distributions in a beam of helium atoms at 300K, and at 5K.

supersonic beam produced in the experiments in this laboratory has been deduced from the comparison of experimental results with simulations [20]. A spectroscopic study of the CuAg molecule at rovibronic resolution showed rotational level populations consistent with an internal rotational temperature for the dimer of less than 20K. Since the molecules are colder translationally than rotationally, then the translational temperature was estimated to be approximately 5K. The velocity spread for such a helium beam at 5K is also shown in Figure 2–4. However, the most probable velocity is now about 1700ms^{-1}. As well as the reduced spread in velocities, we can also see that the supersonic expansion leads to a higher proportion of beam constituents having the average velocity. This property manifests itself in a reduced degradation of the beam pulse shape as it travels downstream.

The term 'supersonic expansion' refers to the fact that the beam velocity exceeds that of the local speed of sound, which is lowered by the effective temperature decrease in the beam (the speed of sound is proportional to the square root of the temperature). This supersonic expansion results in a beam which is much less diffuse than the beam emitted effusively from a nozzle. This increased directionality allows analysis of a greater proportion of the beam species, even after the expansion has proceeded a long way downstream from the nozzle orifice.

The advantages which were revealed in this new expansion process are related to the extreme cooling of the beam species which occurs during expansion. Spectroscopic work is made more straightforward. The spectral simplification and enhanced transition intensities that result from having the molecules in only a few quantum states make the assignment of spectral features much less arduous. The cooling also permits the study of very weakly bound molecules or complexes which would normally be difficult to study as they tend to dissociate even at room temperature.

The cooling process obviously depends on the carrier gas used, and studies of the degree of cooling for different carrier species have been made [21]. Normally, for the type of cluster experiment described in this work, helium is the chosen carrier gas. It leads to the creation of very cold beams, but avoids the complications which

can arise when more polarisable carrier gases, such as argon, form complexes with metal particles.

As well as the distinctive properties discussed above, the supersonic expansion also produces a shock wave which travels ahead of the expansion. This has the effect of pushing residual gas out of the path of the oncoming cluster beam [22], and thus has the bonus effect of allowing a higher background pressure in the vacuum chamber. This makes the pursuit of these types of experiments more feasible, as the pumping requirements are made less stringent.

However, one cannot simply accept this benefit which results from the shock wave without probing any disadvantageous effects which may also be present. The experiments performed in this laboratory involve skimming this supersonic cluster beam, and one study has shown that the relationship between the dimensions of the skimmer and the properties of the shock wave are very important indeed [23]. It is found that the bow shock wave tends to 'attach' itself to the tip of the skimmer cone, but it is found that when the skimmer cone angle exceeds a certain critical value, the shock wave can detach, leaving a free area between the shock front and the apex of the skimmer. This may not seem important, but if the gas passes the skimmer edges in the post-shock state, then the advantages of supersonic expansion will be lost as the beam is reheated.

One further point which must be considered is the placement of the skimmer. If it is too near a vacuum chamber wall, then backscattered gas can interfere with the cluster beam. The solution is simply to stand the skimmer off the wall upon which it is mounted.

Once all of these points have been considered, the experimental set-up produces a beam of cluster species seeded in an inert gas expansion. After passing through the skimmer for collimation purposes, the beam can be truly described as a molecular beam. Ramsey [24] describes a molecular beam as

> *a large number of molecules moving practically collision free in a highly evacuated space in straight and almost parallel trajectories.*

This molecular beam continues to travel onwards until it reaches the ion source region of the time-of-flight mass spectrometer. It is here that the clusters interact with laser light in one of various possible ionisation steps.

2.5 Laser Photoionisation Processes

The interaction of one or more photons from the laser light field with a metal cluster can have different effects depending on the energy of the photons, and on the specific configuration of eigenstates within the absorbing species. In these cluster experiments, detection requires that the metal aggregates be in the form of ions, so we must examine how this cluster-photon interaction can give rise to charged clusters.

The main processes are depicted in Figure 2–5 which show only 1- and 2-photon processes. More photons can be absorbed, but this is less likely, and in any case can be easily related to the absorption schemes shown. Figure 2–5a shows the simplest process in which the energy imparted to the cluster by absorption of a single laser photon is sufficient to cause the ejection of an electron, leaving a cluster with a single positive charge. This first case can show the versatility of the laser as an ionising tool. At low laser power densities only one photon is absorbed and an idea of the neutral cluster distribution can be obtained. If the laser power is increased, then further photon absorption above the ionisation limit can lead to fragmentation of the cluster. The important point is that it is possible to control the 'hardness' of the ionisation process with laser sources [25].

The remaining schematics in Figure 2–5 show possible 2-photon ionisation processes, which are generally much less likely to occur than 1-photon processes if no resonant enhancement takes place. We can get an idea of the relative ease of these ionisation schemes by examining the rate equation for photon absorption, which is generally given as

$$W_n = \sigma_n I^n \tag{2.2}$$

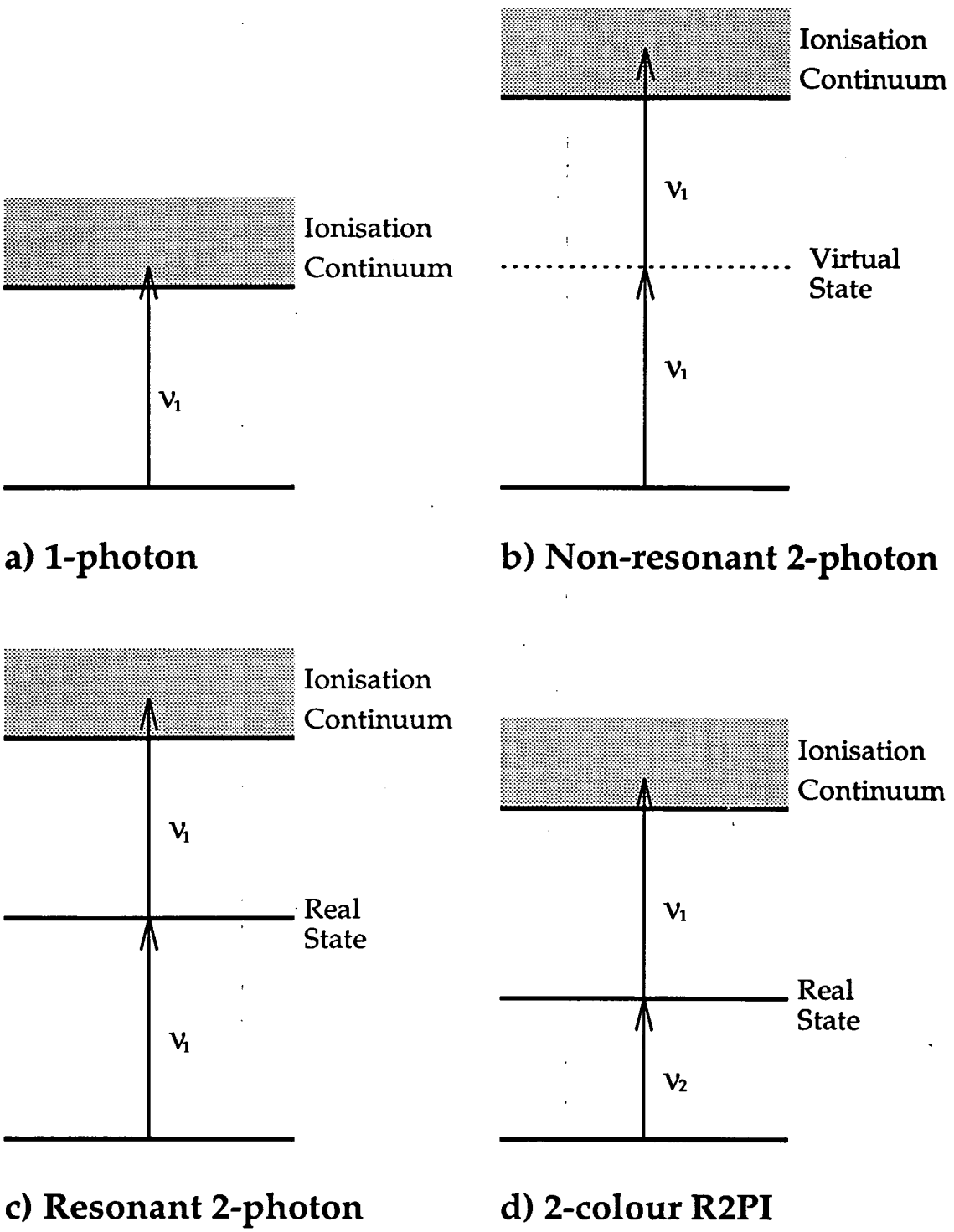

Figure 2–5: The main photoionisation schemes for laser light interactions with molecules.

where

W_n is the transition rate of an n-photon process in s^{-1},

σ_n is the absorption cross-section for an n-photon process, and

I is the radiation flux in photons cm^{-2} s^{-1}.

Typical values for the absorption cross-sections [26] are

$\sigma_1 \approx 10^{-18} cm^2$

$\sigma_2 \approx 10^{-50} cm^4 s$

It is apparent that the simultaneous absorption of two photons is much less likely. Thus a higher laser power must be used in order to provide a sufficient number of ions via a 2-photon ionisation process. This non-resonant absorption process is depicted in Figure 2–5b. The energy provided by the first photon promotes the molecule to a 'virtual' state from which the second photon can ionise the molecule [18].

If the first photon excites the cluster to real intermediate rovibronic state, as shown in Figure 2–5c, then a resonant-enhancement occurs, and the two-photon cross-section is much higher than that given above for a non-resonant transition. Similarly, if the virtual level is even close to a real eigenstate of the cluster, then some degree of enhancement of the transition probability occurs.

Finally, Figure 2–5d shows that it is possible to construct a two-colour experiment which is useful for probing electronic states less than halfway between the neutral and ionic ground states. Here, the first photon is resonant with a real level from which a more energetic second photon can ionise the molecule of interest. The R2PI schemes shown in Figures 2–5c and 2–5d were made use of in some of the spectroscopic experiments carried out. In practice this involved scanning the wavelength of a dye laser and monitoring the detected cluster ion signal intensities. A spectrum of signal intensity against laser wavelength for a particular cluster then reveals electronic level structure as enhancements in cluster ion intensity occur when a photon is resonantly absorbed.

A simple method for deducing the number of photons of a specific energy that are required to ionise a particular cluster can be found by reformulating the photon absorption rate equation given above. If logarithms are applied throughout then

the equation takes the form

$$\ln W_n = \ln \sigma_n + n \ln I \tag{2.3}$$

Thus if the logarithm of the laser power density is plotted against the logarithm of the cluster intensity, a straight line with an integral gradient should result, this gradient being equal to the number of photons, n, required to ionise the cluster [27]. In this way, the ionisation potential (IP) of the cluster can be broadly bracketed since

$$(n-1)E < IP < nE \tag{2.4}$$

where E is the energy of a single photon. By considering these power dependence plots for several different wavelengths of ionising radiation it is possible to roughly place the ionisation potentials of cluster species [28].

We can now summarise the effects of photoionisation with respect to these types of experiments. The characteristics of the laser source are very well suited to controlling whether the ionisation process is soft or hard. The properties of these photoionisation processes also mesh well with the ion source requirements for time-of-flight mass spectrometry, which is our choice of detection method. These properties include the formation of ions in a very short time, within a very definite and restricted volume if required, and resulting in a high density of nascent ions.

One final point must be made with respect to the degree of fragmentation which can be expected when ionising a particular cluster. For hydrogen-bonded, and some van der Waals clusters, fragmentation can occur even under very soft ionisation conditions. This is due to a fundamental difference between neutral and ionic ground state geometries. However, it has been calculated that for metallic clusters containing more than four atoms, the neutral and ionic ground state geometries are typically very similar. Hence for metal clusters the degree of fragmentation should only depend on the power density of the ionising laser [29].

2.6 Time-Of-Flight Mass Spectrometry

The use of time-of-flight mass spectrometry works well in the types of experiment described here, since, as previously mentioned, it provides a detection method which complements the pulsed ionisation technique very well. The main principle determining the action of this technique is very simple. It relies on the fact that the ions are all created within a uniform electric field which imparts an equivalent amount of kinetic energy to each ion formed. As the ions are accelerated out of this field, and into a field-free path leading to the detector, they each attain a velocity dependant on their mass to charge ratio. The velocities of the nascent ions are such that the flight time, t, in the field-free region is related to the cluster mass, m, assuming equal charges on all species, in the following manner:

$$t \propto \sqrt{m} \tag{2.5}$$

In this way, clusters of differing mass separate temporally during the flight period, impacting at the detector in discrete bunches. As the cluster mass increases, the time between detection of two consecutive particle bunches becomes smaller, and the resolution is eventually limited by this factor.

The advantages of using a time-of-flight detection set-up are readily apparent [30]. A particularly attractive feature is that a complete mass spectrum can be obtained from a single ionisation event, allowing very small amounts of sample to be completely characterised. Routine sampling rates can allow an entire mass spectrum to be recorded in a matter of microseconds, which compares exceedingly well with electric or magnetic sector instruments which must be slowly scanned over the course of several hours to collect a full mass spectrum. To contrast with a sector instrument again, the time-of-flight experimental set-up is far more robust, as its accuracy depends on electronic circuitry rather than on accurate mechanical alignment or stable magnetic fields. The TOFMS also caters for an effectively unlimited mass range, depending on experimental parameters.

The main disadvantage of the time-of-flight mass spectrometer when originally introduced was the very low mass resolution. On older instruments it was frequently not possible to resolve adjacent mass peaks above 100 mass units. This was a crucial drawback, and was the reason why this type of mass analyser was hardly utilised at all prior to the 1960s. Since then, there have been many advances in time-of-flight technology, resulting in enhancements in resolution of over three orders of magnitude. Nowadays, with this one major disadvantage overcome, the TOFMS instrument is one of the most versatile forms of mass spectrometer available and is extremely well regarded and widely used.

The main factors which caused the deterioration of resolution were first analysed by Wiley and McLaren [31]. Up until this analysis, conventional time-of-flight mass spectrometers consisted of a single extraction field coupled to a field-free drift region. After analysing the reasons for such low resolution, Wiley and McLaren proposed the addition of an extra extraction field, creating the double-field instrument which is the forefather of all modern time-of-flight machines.

The factors which limit the resolution can be listed and examined in order to discard the trivial points, and tackle the major problems [32]. The mass resolution depends on the time spread of a bunch of equivalent ions as it reaches the detector. This is affected detrimentally by space charge effects as the ions are created, inhomogeneous electric fields in the source, the finite frequency response of the detection system, the temporal spread of the ionising laser pulse, the initial distribution of ion velocities, and the size of the ionisation volume. Let us deal with each point in turn, presenting solutions which inhibit the contribution of specific factors to the resolution problem.

Space charge effects involve the temporal spreading of an ion packet due to coulombic repulsion. These effects are normally significant if ion densities exceed $10^7 cm^{-3}$ [33]. The densities calculated in the ion source region of our machine rarely exceed $10^6 cm^{-3}$ for a typical cluster experiment [20]. In any case, ion densities can be reduced by using lower laser powers. As such, space charge effects are anticipated to have a negligible contribution to the degradation of resolution.

Inhomogeneous electric fields must be reduced by careful design of the extrac-

tion optics. Care must be taken to decrease the effects of fringing fields and field deformations due to the presence of grids in the extraction plates. Since the ion source region is one of the most crucial areas in the experimental set-up, enough care is usually taken during fabrication to provide sufficiently homogeneous electric fields for the ion extraction. Again, this factor contributes very little towards resolution problems.

The question of the response of the detection system is irrelevant due to the sub-nanosecond rise times of microchannel plates, and the fast, high-frequency counting rates available through modern electronics.

The increase in cluster ion packet width due to the finite duration of the ionising laser pulse is another factor which has been effectively solved by modern technology. Identical ions can be created at the start or end of the laser pulse, leading to a finite time interval between the extraction of the two ions. This would have caused a great lowering of resolution were it not for the advent of very short duration pulsed lasers. The ionisation laser used here has a pulse width of about 10ns which allows us to discount this factor from influencing the resolution of the mass spectrometer to any substantial degree.

The final two points to be considered turn out to be the most influential. Since the mass spectrometer is usually mounted perpendicularly to the cluster beam source, then any off-axis velocity components in the beam species lead to problems when extracting equivalent ions which possess different initial velocities along the axis of the spectrometer. In the present work this problem is less important due to the choice of the cluster production method. The fact that a supersonic molecular beam is used means that the off-axis component of cluster velocities is several orders of magnitude smaller than can be obtained with a thermal source. This limits the effect of this factor on instrument resolution, but its contribution will be discussed anyway. In addition, the size of the ionisation volume is finite, leading to the creation of ions in different positions within the extraction field. This definitely leads to resolution problems. A closer look at these more important factors is now warranted.

Firstly, we can easily visualise the time-of-flight mass spectrometer as con-

sisting of several regions containing electric fields. Figure 2–6 shows the original single-field instrument, and the Wiley and McLaren double-field modification. In these schematics we can describe the effects on machine resolution by following the trajectories of two ions created within the first electric field, E_s, bounded by voltage plates V1 and V2. These ions have equivalent mass and charge. Three contributions to the resolution can be detailed. Time resolution is due to the creation of these two identical ions at different points in time, the maximum time difference dictated by the duration of the ionisation laser pulse. As mentioned, this factor can be neglected due to the short laser pulses in use. The contribution known as energy resolution stems from the initial velocity components along the axis of the mass spectrometer. These two identical ions formed at the same position, but with oppositely directed velocities of the same magnitude will be separated by the time taken for the electrostatic field to turn around the ion initially travelling away from the detector. The use of a molecular beam does limit the contribution of this factor.

Space resolution gives a measure of how well the spectrometer can resolve masses despite the initial space distribution of ions in the source, caused by the finite ionisation volume. Again, if we follow two identical ions, but this time separated in space, then the ion nearest the field-free region obviously enters this region first. However, the second ion attains a greater velocity while it takes longer to exit the extraction region. There is a point known as the 'space focus' where the faster ion catches up with the slower ion. If the detector is placed at this point of space focus then the optimum space resolution is achieved. However, for the single-field mass spectrometer, the space focus is given by the purely geometric condition $D = 2s_0$, where D is the distance from plate V2 to the space focus, and s_0 is the distance from the point of ion creation to plate V2. This condition requires the detector to be so close to the extraction region that the short ion flight times hinder mass discrimination for higher mass clusters. It is plain to see that longer flight times would give the opportunity to achieve a system with greater resolution. The addition of the second field by Wiley and McLaren introduced two new system parameters; the distance, d, between plates V2 and V3, and the

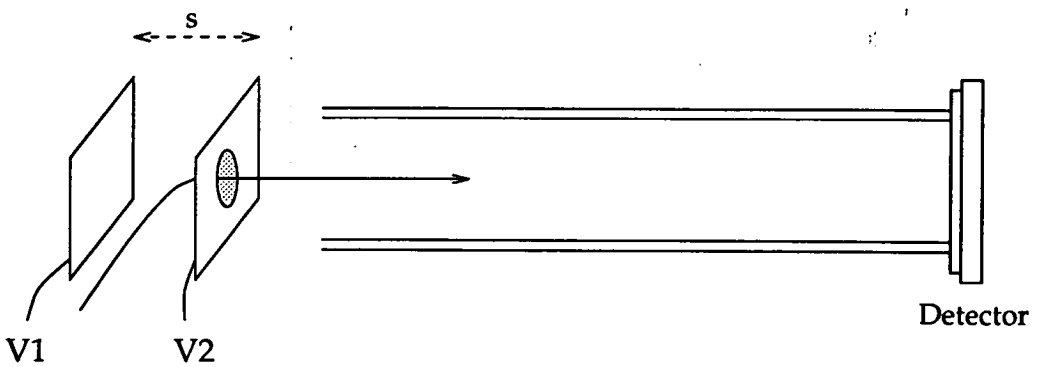

a) Single-field TOFMS

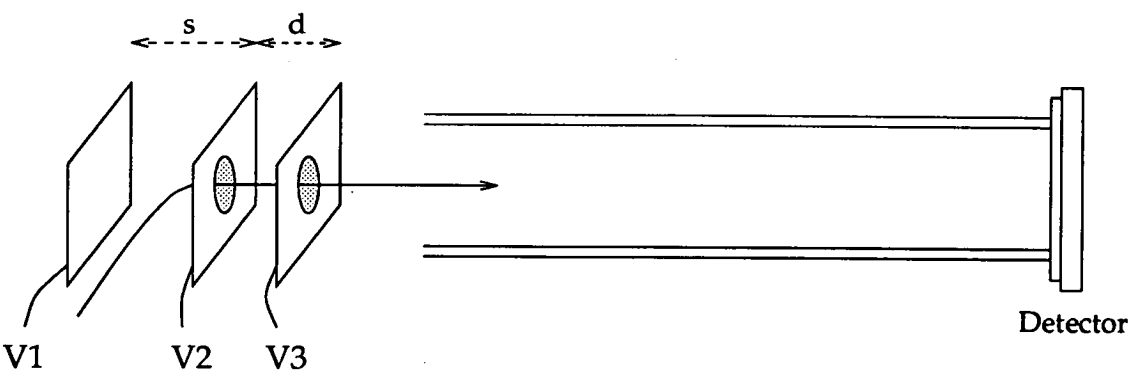

b) Double-field TOFMS

Figure 2–6: Schematics of the single- and -double-field time-of-flight mass spectrometers

ratio of the fields, E_d/E_s. Here, the space focus position is variable, depending on the field ratio parameter which is easily adjusted. It is this Wiley and McLaren set-up which is used in the experiments reported in later chapters.

Since the time of the initial improvement to the time-of-flight mass spectrometer which made the machine competitive, there have been further modifications suggested which have improved the resolution attainable with a time-of-flight detection system. For the double-field instrument mentioned above, the perpendicular arrangement of the molecular beam and mass spectrometer requires some way of compensating for the initial beam velocity after ion extraction. In our apparatus this takes the form of a set of deflection plates positioned just behind the extraction region, and this is detailed in the next chapter. Another possibility is to tilt plates in the ion source so that a component of the electric extraction field counteracts the velocity of the incoming cluster beam [34].

One of the most notable efforts to increase the resolution of the mass spectrometer was the addition of a so-called reflectron mirror described by Mamyrin and co-workers [35]. The design of the second mass spectrometer in this laboratory is based on the reflecting field time-of-flight machine (RETOFMS) of Mamyrin, and a schematic of this is presented in Figure 2–7. It is clear that a reasonably long ion flight time is required to allow clusters of different mass to charge ratios to separate sufficiently in time. In a conventional mass spectrometer, this criterion would be fulfilled at the expense of mass resolution. However, the reflecting field set-up is able to counter this problem. The lowered resolution would come about by two otherwise identical cluster ions temporally separating due to different initial kinetic energies. Although the faster ion reaches the reflecting field ahead of the slower ion, it penetrates further into the field due to its greater energy. The slower ion is reflected much more quickly, and emerges from the ion mirror ahead of the faster cluster ion. The ion mirror parameters are chosen so that the detector is positioned at the point where the fast ion catches up with the slower ion, thus resulting in an enhancement of resolution.

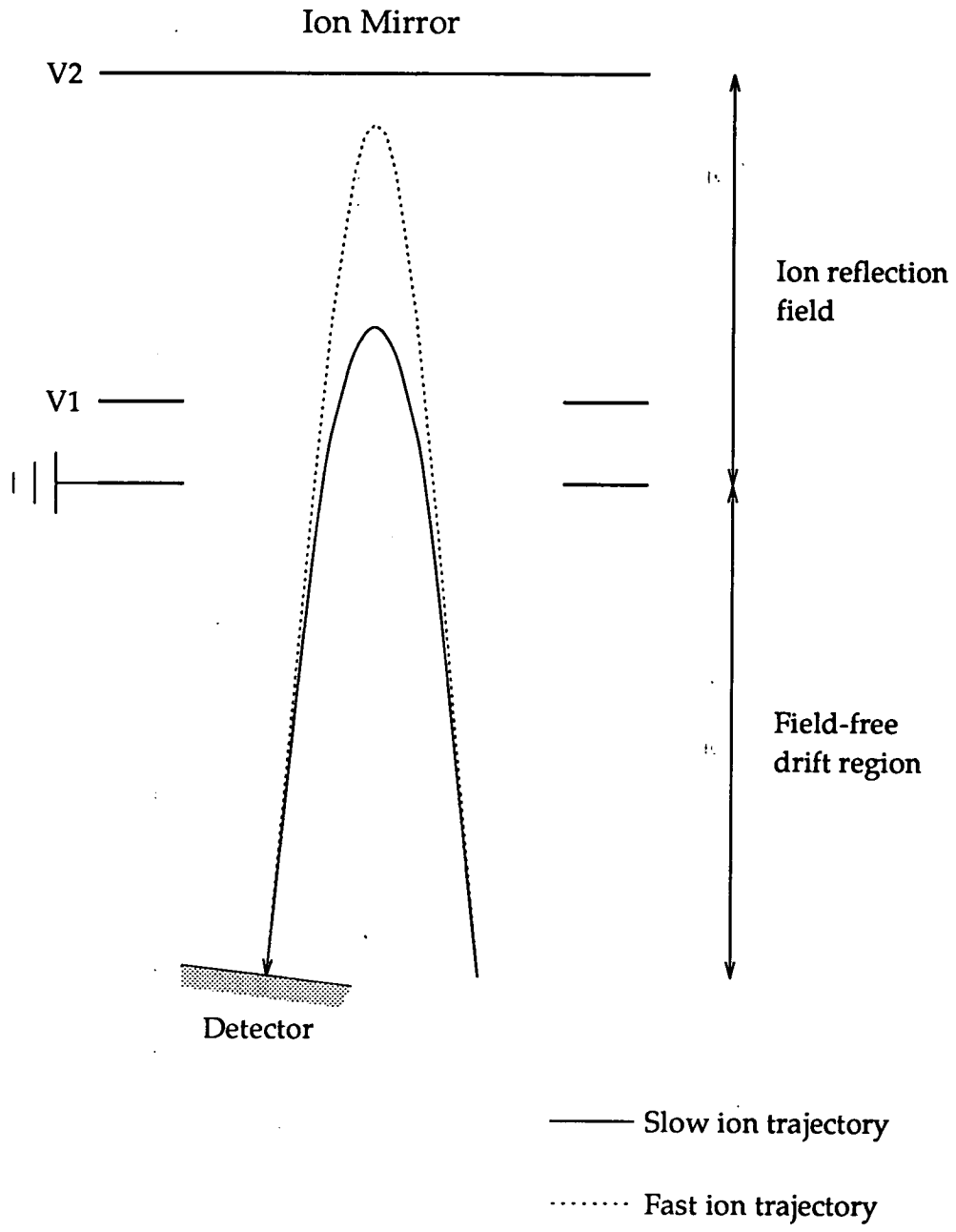

Figure 2–7: A representation of the reflecting field TOFMS, with ion trajectories shown.

Bibliography

[1] J.F. Ready, '*Industrial Applications of Lasers*', Academic Press, New York, 1978.

[2] D.A. Eastham, '*Atomic Physics of Lasers*', Tayor and Francis, London, 1989.

[3] J.F. Friichtenicht, Rev. Sci. Instrum., **45** (1974) 51.

[4] D.E. Powers, S.G. Hansen, M.E. Geusic, A.C. Puiu, J.B. Hopkins, T.G. Dietz, M.A. Duncan, P.R.R. Langridge-Smith and R.E. Smalley, J. Phys. Chem., **86** (1982) 2556.

[5] R.L. Stegman, J.T. Schriempf and L.R. Hettche, J. Appl. Phys., **44** (1973) 3675.

[6] J. Bernholc and J.C. Phillips, J. Chem. Phys., **85** (1986) 3258.

[7] K.H. Meiwes-Broer, '*Advances in Metal and Semiconductor Clusters*' (ed. M.A. Duncan), Jai Press Inc., Greenwich, Connecticut, Vol. I, 1993.

[8] M.M. Kappes, M. Schär and E. Schumacher, J. Phys. Chem., **91** (1987) 658.

[9] E.A. Rohlfing, D.M. Cox, R. Petkovic-Luton and A. Kaldor, J. Phys. Chem., **88** (1984) 6227.

[10] O.F. Hagena and W. Obert, J. Chem. Phys., **56** (1972) 1793.

[11] M.F. Cai, T.P. Dzugan and V.E. Bondybey, Chem. Phys. Lett., **155** (1989) 430.

[12] A. Maruyama, L.R. Anderson and R.E. Smalley, Rev. Sci. Instrum., **61** (1990) 3686.

[13] R.E. Smalley, L. Wharton and D.H. Levy, Acc. Chem. Res., **10** (1977) 139.

[14] A.W. Castleman Jr. and T.D. Märk, '*Gaseous Ion Chemistry and Mass Spectrometry*' (ed. J.H. Futrell), Wiley-Interscience, New York, 1986.

[15] A. Kantrowitz and J. Grey, Rev. Sci. Instrum., **22** (1951) 328.

[16] G.B. Kistiakowsky and W.P. Slichter, Rev. Sci. Instrum., **22** (1951) 333.

[17] D.R. Preuss, S.A. Pace and J.L. Gole, J. Chem. Phys., **71** (1979) 3553.

[18] W. Demtröder, '*Laser Spectroscopy: Basic Concepts and Instrumentation*', Springer Verlag, Berlin, 1982.

[19] E. Kolodney and A. Amirav, Chem. Phys., **82** (1983) 269.

[20] A.M. James, *Ph.D. thesis*, Edinburgh University, 1993.

[21] G.M. McClelland, K.L. Saenger, J.J. Valentini and D.R. Herschbach, J. Phys. Chem., **83** (1979) 947.

[22] R. Campargue, Rev. Sci. Instrum., **35** (1964) 111.

[23] J.B. Anderson, R.P. Andres and J.B. Fenn, Adv. Chem. Phys., **10** (1966) 275.

[24] N.F. Ramsey, '*Molecular Beams*', Clarendon Press, Oxford, 1956.

[25] U. Boesl, J. Phys. Chem., **95** (1991) 2949.

[26] P.M. Johnson and C.E. Otis, Ann. Rev. Phys. Chem., **32** (1981) 139.

[27] E.A. Rohlfing, D.M. Cox and A. Kaldor, Chem. Phys. Lett., **99** (1983) 161.

[28] E.A. Rohlfing, D.M. Cox and A. Kaldor, J. Chem. Phys., **81** (1984) 3322.

[29] M.M. Kappes, Chem. Rev., **88** (1988) 369.

[30] D. Price and G.J. Milnes, Int. J. Mass Spectrom. Ion Proc., **99** (1990) 1.

[31] W.C. Wiley and I.H. McLaren, Rev. Sci. Instrum., **26** (1955) 1150.

[32] R.B. Opsal, K.G. Owens and J.P. Reilly, Anal. Chem., **57** (1985) 1884.

[33] D.H. Parker, '*Ultrasensitive Laser Spectroscopy*' (ed. D.S. Kliger), Academic Press, New York, 1983.

[34] C.W.S. Conover, Y.J. Twu, Y.A. Yang and L.A. Bloomfield, Rev. Sci. Instrum., **60** (1989) 1065.

[35] B.A. Mamyrin, V.I. Karataev, D.V. Schmikk and V.A. Zagulin, Sov. Phys. -JETP, **37** (1973) 45.

Chapter 3

EXPERIMENTAL APPARATUS

This chapter presents details of the equipment used to perform the cluster experiments described later. The main experimental principles outlined in the preceding chapter rely on the use of some quite sophisticated items of scientific apparatus. The molecular beam machine and laser systems are described, as well as the main functions of the experimental control and data acquisition set-up. A schematic diagram of the cluster machine used at Edinburgh is presented in Figure 3–1, showing the main elements of the apparatus and how they are linked together. Details of the cluster apparatus in Lyon are given in Chapter 7.

3.1 The Vacuum System

The need for a high vacuum system in which to carry out molecular beam experiments is obvious. The molecular beam machine used at Edinburgh consists of three sequentially connected chambers evacuated by a system of rotary and oil diffusion pumps. All three chambers were fashioned from 16mm thick 304 stainless steel, and the pumping requirements were reduced by relying on the principle of differential pumping [1].

The main chamber is a stainless steel cuboid with outer dimensions of 635 x 370 x 370mm, producing an internal volume of 69 litres. This chamber houses the molecular beam valve, cluster source, and beam skimmer. Access to these internal

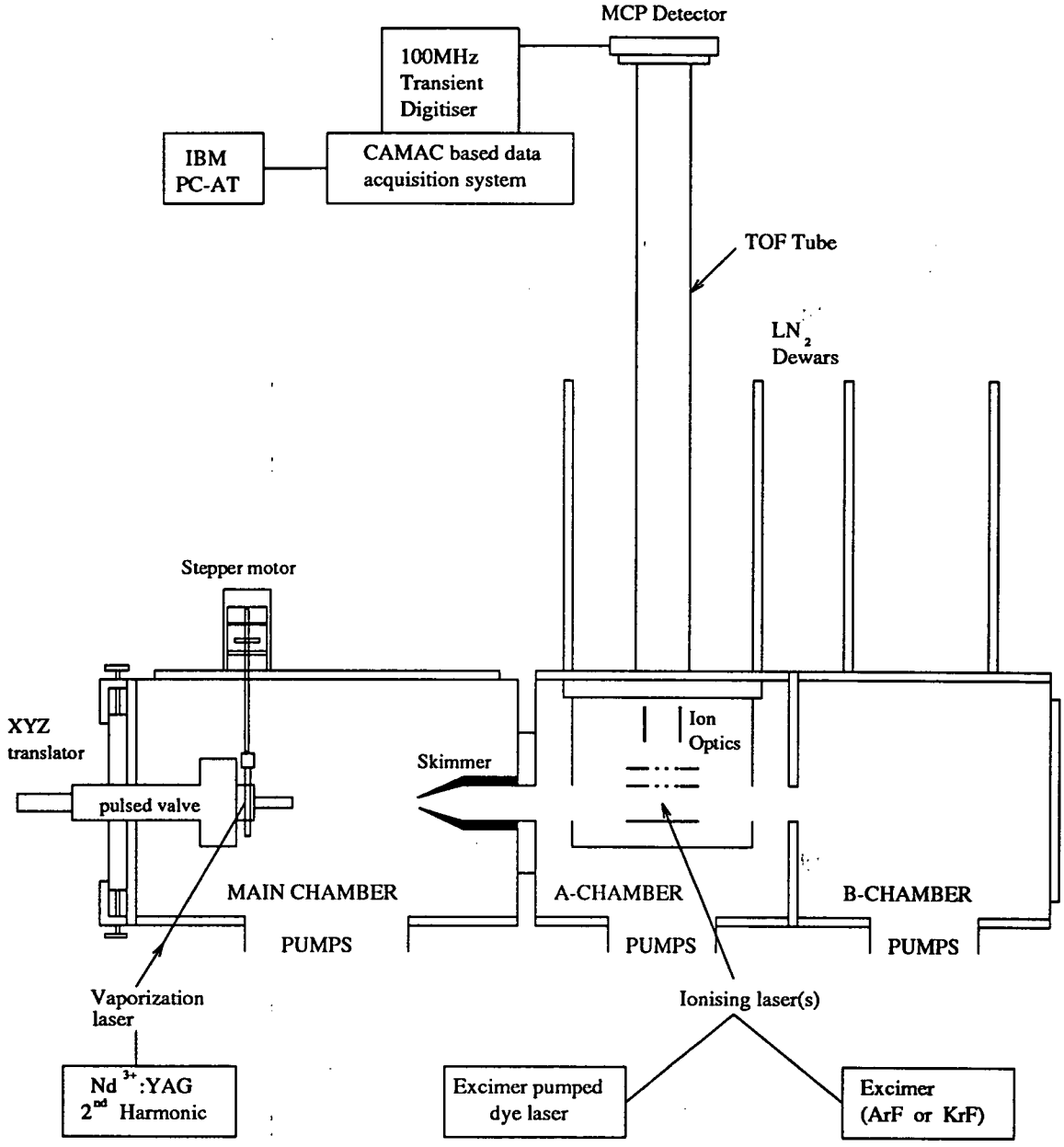

Figure 3–1: The molecular beam set-up used to create, photoionise, and detect cluster species.

components is afforded via the two aluminium side flanges which are both fitted with two 135mm diameter perspex viewing ports, and a central 50mm diameter quartz window through which the vaporisation laser is directed. The window to allow laser access is distanced from one side flange on a 300mm long stand-off tubulation which helps to minimise the deposition of vaporised material on the quartz window.

The main chamber pumping system allows base pressures of 2 x 10^{-7}mbar to be reached, usually rising by two orders of magnitude when an experiment is running. This low pressure is achieved with a CVC PBA 1000 oil diffusion pump filled with 1000ml of Convoil 20 pump fluid. This pump has a water-cooled half chevron baffle which reduces the maximum pumping speed from 5300ls^{-1} to 2690ls^{-1} for air up to 10^{-3}mbar. The diffusion pump is backed by an Edwards E2M40 two-stage rotary pump working in tandem with an Edwards EH250 roots blower which together can remove air at 8.5 mbar ls^{-1}. The chamber and pump foreline pressures are monitored by Edwards PRL 010 Pirani, and CP25-K Penning gauges.

Since this vacuum chamber houses the metal cluster target, ease of access is essential for changing or cleaning targets, or modifying the source in order to limit the down-time of the machine. Thus the chamber can be quickly isolated from the pumping system, and from the second chamber by two pneumatically operated gate valves. External adjustments to the cluster source can be made via the top and end stainless steel flanges. On the top flange is mounted the driving mechanism which continually moves the target to expose a fresh surface to the vaporisation laser, and the end flange is constructed in such a way as to allow three-axis adjustment of the cluster source position.

As mentioned, within this chamber is also a molecular beam skimmer constructed of electroformed nickel (Beam Dynamics, Inc.). The skimmer orifice has a nominal diameter of either 2.5mm or 5.0mm, and an included angle of 30°. Behind this skimmer is the gate valve which, when open, allows the cluster beam to enter the second vacuum chamber.

This chamber, known as the A-chamber, is a stainless steel cube of 285mm outside dimension with an inner volume of 16 litres. The ion extraction region

of the time-of-flight mass spectrometer is housed here, and the cluster beam is therefore photoionised within this chamber.

An Edwards E09 oil diffusion pump is suspended beneath the A-chamber, and is fitted with a water-cooled baffle, which limits the pumping speed to 2000ls^{-1}, giving an ultimate pressure of 5 x 10^{-8}mbar. This diffusion pump is backed by two Edwards E2M18 rotary pumps operating in parallel to allow easy maintenance of one of these pumps, if required. Chamber pressures are measured by a Balzers TPR 010 Pirani gauge for the range 100 - 5.6 x 10^{-4}mbar, and a Balzers IKR 020 cold cathode ionisation gauge which covers the pressure region 5 x 10^{-3} - 4 x 10^{-10}mbar. The base pressure in the A-chamber is normally 1.2 x 10^{-7}mbar, typically rising to about 1 x 10^{-6}mbar during an experiment.

The interrogation of the cluster beam entering this chamber is achieved by directing the ionising laser beam in through a 50mm diameter quartz window positioned centrally on either of the two circular, stainless steel side flanges. The nascent ions are extracted by the time-of-flight ion optics positioned here, and these are connected through four high voltage feedthroughs in one of the side flanges, via MHV connectors to the high voltage supplies which generate the required extraction and deflection fields. The stainless steel field-free drift tube of the mass spectrometer extends vertically from the top flange of the A-chamber, and is 132cm long, with an inner diameter of 4cm. This top flange also supports a double-skinned dewar which surrounds the lower 66cm of the flight tube, and extends down into the chamber by 6.4cm to support the ion optics mount. During experiments this dewar is filled with liquid nitrogen, and the resulting cryopumping effect can reduce the base pressure in the A-chamber by an order of magnitude. A copper cryoshield is affixed to the base of the dewar, and encloses the ion source region. There are four 40mm diameter holes in the copper box to allow passage of the molecular beam and the laser.

Any unionised clusters enter the third chamber (B-chamber) which acts as a dump tank to pump away the remainder of the beam. This chamber is identical in size to the A-chamber, and also has a double-skinned dewar on the top flange, but without the flight tube. The diffusion pump is an Edwards Diffstak 160, pumping

speed 1300ls^{-1}, and this is connected to the same parallel combination of two Edwards E2M18 rotary pumps which back the A-chamber diffusion pump. The chamber pressure is measured by a Balzers TPR 010 Pirani gauge, and normally registers 7 x 10^{-8}mbar, or 3 x 10^{-6}mbar whilst an experiment is running.

All of the pressure gauges in the three chambers, and on the pump forelines are connected to digital (Balzers PKG 100 and Edwards 1105) or analogue (Edwards Penning 505) controllers.

3.2 The Molecular Beam Valve

The output from the molecular beam valve is directed down the axis of the cluster machine by incorporating it within a holding mount fixed to the end flange of the main chamber. This holding mount is actually a tube which extends into the chamber from the centre of the stainless steel end flange. The degree of protrusion of the tube into the chamber can be varied by means of a screw-type Z-axis translator. The lateral and vertical position of the tube can also be varied by adjusting the positioning screws which hold the flange in place. This coarse XYZ translating device is extremely useful for adjusting the alignment of the molecular beam with respect to the skimmer and A-chamber ion source region. The molecular beam valve itself is held in place within the central tube, allowing the valve body to be exposed to exterior atmospheric pressure whilst presenting the valve orifice, through which the carrier gas is pulsed, to the high vacuum of the main chamber. The electrical and gas supplies to the valve can be passed through the hollow tube and connected easily to the rear of the valve.

The carrier gas pulse is produced by opening and closing the valve rapidly, and these events are signalled by trigger pulses from a computer-controlled pulse delay generator. The actual opening and closing mechanisms depend specifically on the type of molecular beam valve used, and two different valves were utilised during the course of these experiments. The first valve was a Newport Model BV100. Its operation has been described in the literature [2], but briefly its action relies

on the use of two coiled solenoids and a soft iron actuator. The actuator has a viton tip at one end, and this seals against the 500μm output orifice of the valve. The application of a current to the solenoid known as the 'open' coil induces a magnetic field in the coil which is sufficient to pull the actuator towards it and away from the orifice, allowing the carrier gas to escape. The current to the 'open' coil is terminated as a current is applied to the 'close' coil. This snaps the actuator back to its original position allowing the viton tip to seal the valve orifice, and cutting off the gas pulse. The use of this particular valve was limited due to its unreliability when operating at pulse lengths shorter than 900μs with high backing pressures.

A more reliable pulsed nozzle was the General Valve Corporation Series 9 pulsed valve, which was employed for the majority of the experiments reported here. The operation of this valve is essentially the same as the Newport Model BV100 but for the fact that a spring is used in place of the 'close' coil. Applying current to the 'open' coil results in the valve orifice opening as the teflon tipped actuator is retracted. When the current ceases to flow, however, the valve seals as the actuator is driven back into place by the spring.

A comparison of the performance of the two valves revealed that the Newport valve produced more intense pulses of gas with a sharper profile, but the General Valve was found to be superior in terms of reliability. Its slightly degraded pulse profile was still acceptable as is demonstrated by the profile of the helium gas pulse from this valve which was shown earlier in Figure 2–2.

For some of the experiments discussed in the later chapters the usual nylon feed line for the carrier gas from the helium cylinder to the molecular beam valve was replaced with a length of copper tubing. A section of this tubing was coiled and immersed in liquid nitrogen. This served to trap out any impurities present in the helium supply, and also cooled the helium to some extent. This alteration was used on some of the experiments on the Group-IIA metals due to the fact that these species react very readily with impurities, especially oxygen.

3.3 The Cluster Source

The entire clustering process relies on the interaction of the vaporisation laser, the metal target, and the pulse of helium carrier gas in the cluster source. The source consists of a faceplate which can be attached to the output orifice of the molecular beam valve. The specific geometric considerations of the faceplate design depend on which of two basic target types are utilised. Originally, the target was presented in the form of a cylindrical rod, but a flat disc is also commonly used as a vaporisation target.

The most often used target in this laboratory, and generally by other cluster groups is the rod source. A representation of the rod source faceplate in which clustering is promoted can be seen in Figure 3–2.

The details of the faceplate, which was made from brass, are very simple and the design originates from the earliest cluster experiments using the laser vaporisation technique [3]. Three mutually perpendicular channels are drilled through the faceplate allowing passage of the laser vaporisation beam, the helium pulse from the molecular beam valve, and accommodating the target rod. The body of the faceplate is 29 x 29 x 11mm, and the three channels have slightly differing dimensions. The access channel for the vaporisation laser pulse is 3mm in diameter, and passes laterally through the faceplate. The helium carrier gas enters and exits the faceplate via a 1mm diameter channel from the centre of the back of the plate which lies directly over the output orifice of the valve, intersecting the first channel. The third channel is 5mm in diameter, and passes vertically down through the faceplate, but slightly displaced from the central position so that when the rod is suspended through this hole the helium pulse can graze the rod's surface without having its flow characteristics perturbed too much. The faceplate has one additional feature which is necessary to minimise any off-axis gas leakage. The laser access channel is fitted with a 1mm inner diameter insert piece which still allows passage of the vaporisation beam, but limits the amount of carrier gas which may escape by this route.

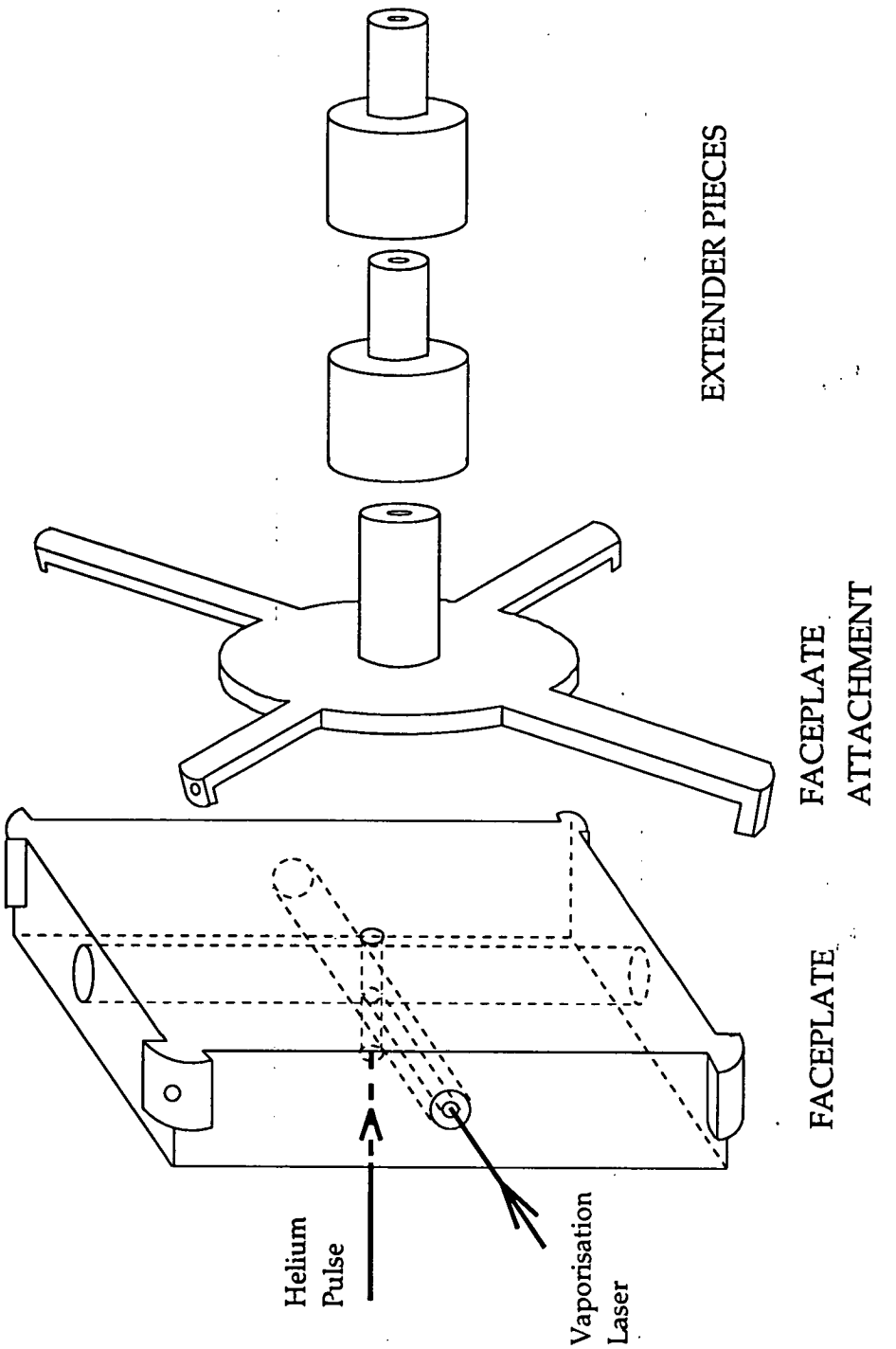

Figure 3–2: Schematic of the rod source with the available attachment pieces.

Onto the front of the faceplate is fitted an extension attachment which simply provides a longer channel in which the helium and entrained species can interact. An O-ring is positioned between the faceplate and the attachment piece, of which several were fabricated with varying channel geometries. Also shown in Figure 3–2 are extender pieces which were simply fixed over the snout of the extension attachment with a grub screw. This again allowed a quick and easy method for altering the length of the clustering region before supersonic expansion could take place.

Most of the target rods used were obtained commercially, and machined to snugly fit the appropriate channel in the faceplate. The top of the rod was coupled by universal joints to an 8-32 UNF rod which in turn was connected through a Cajon seal in the top flange of the main chamber to a stepper motor (McLennan Model 34 HS-106). This permitted rotation of the rod, along with simultaneous translation by coupling to a screw mechanism. Two microswitches were used to change the direction of travel of the rod, thus limiting the target area probed.

The range of clusters which could be generated using the rod source was limited by the bulk characteristics of the target species. If a metal is too brittle or too soft then there is a danger that the rod will break or adhere to the inner channel of the faceplate. The rod source also proved to be a hindrance when the production of mixed cluster species became a desirable goal. The formation of mixed metal rods could be accomplished in some cases such as for the studies of CuAg carried out in this laboratory [4], but the materials to be combined only mix well if they possess similar melting points and densities. One way around this problem is to vaporise two different rods mounted within the same faceplate [5]. This is not the most easily accessible solution, however, since the requirement for two vaporisation lasers is not the optimum way of utilising limited facilities in most academic laboratories.

In 1986 a modification to the cluster source region was described which allowed a circular disc of material to be used as a target in place of the usual rod [6]. Initially this was designed to allow vaporisation of circular semiconductor wafers, but it was found that discs of mixed materials could be easily made and interrogated

using this source configuration. A schematic diagram of the disc source used in this work is shown in Figure 3–3. The source consists of two eccentric cams linked by a belt drive and pivot arm. This disc source mount was fixed to the beam valve, and coupled to the stepper motor in the same way as the rod source. The motion of the stepper motor was translated into a slow rotation of the disc, and the cam shaft system also caused the axis of rotation to move slowly. In this way, the vaporisation laser cut a spiral pathway over the surface of the disc.

Target discs were produced simply by compressing metal powder within a stainless steel mould under a hydraulic press. The integrity of a mixed metal disc tended to vary according to how well matched the bulk properties of the two bulk metals were. Two separate coinage metals would combine well into a hard, strong disc, whereas a mixture of alkali and coinage metal powders resulted in the production of a brittle disc that could be used for only a moderate time before major fracturing occurred. In general, though, it should be possible to make a great variety of mixed metal targets, even using a further metal powder to help with binding, or to study cluster species containing three or more different constituent elements.

3.4 Laser Systems

The lasers used in this laboratory for cluster experiments are described below. The alignment of these laser systems with respect to the molecular beam machine is critical, so all lasers were positioned on extremely sturdy tables which were constructed of steel to allow the attachment of magnetic mounts to hold the required optical components. Adjustable feet on these tables permitted coarse movement of the laser, but the more critical manoeuvring of the output beam position was achieved by fine adjustments of the turning or focussing optics. Of the laser descriptions that follow, the Nd:YAG laser was used as the vaporisation laser, whilst the other laser systems described were used to photoionise the cluster species generated.

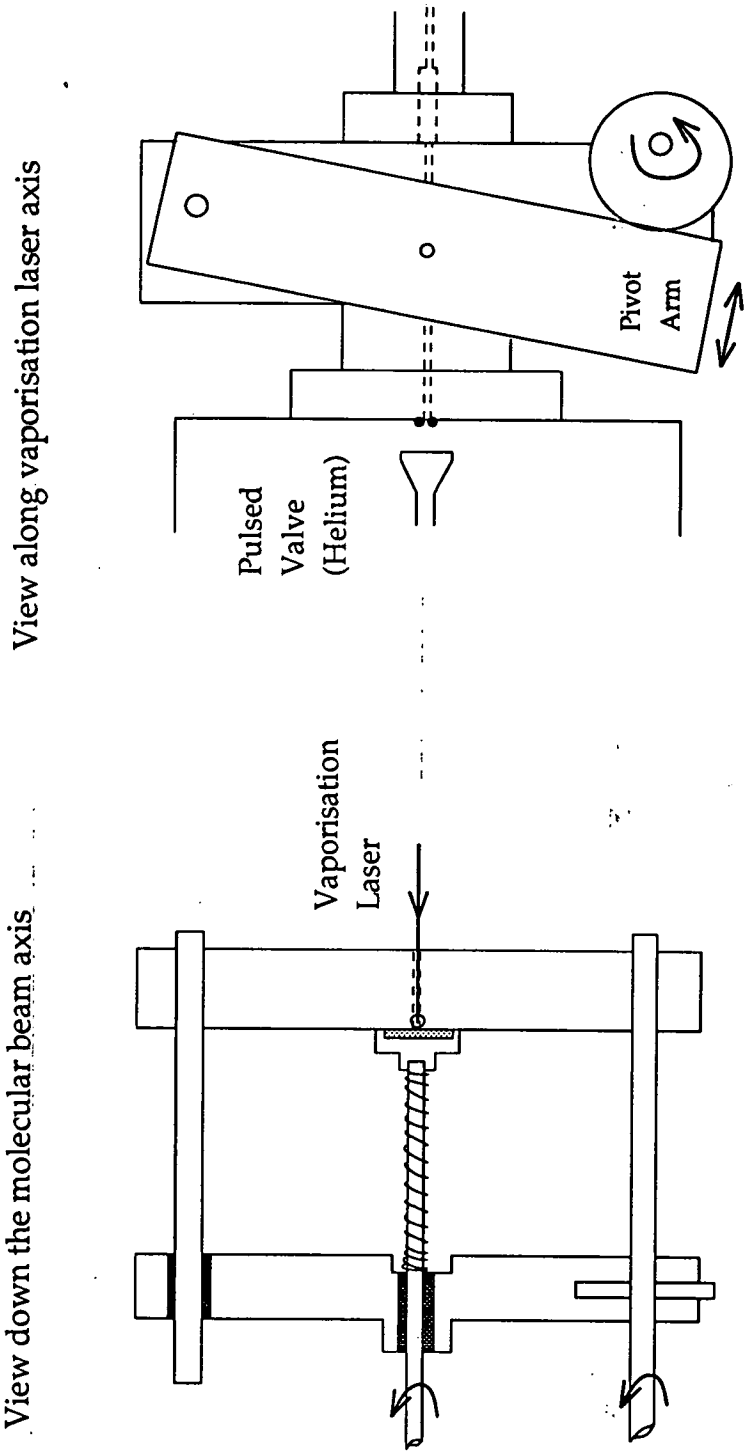

Figure 3–3: Schematic of the disc source mount shown from two angles.

3.4.1 Nd:YAG laser

The active medium in an Nd:YAG laser consists of the isotropic crystal $Y_2Al_5O_{12}$ (yttrium-aluminium garnet, YAG) in which approximately 1% of the yttrium is replaced by neodymium. Energy levels of the Nd^{3+} ion within the YAG crystal environment are positioned such that efficient lasing action can occur with the generation of predominantly 1064 nm light.

The actual model of Nd:YAG laser used in these experiments was a JK Hyper-YAG Model HY750 which was set up with a folded-geometry oscillator-amplifier configuration. The lasing material consisted of two 3″ long Nd:YAG rods, one of 4mm diameter in the oscillator assembly, and the other of 8mm diameter in the amplifier stage. Each rod was pumped by a xenon flashlamp, and both the oscillator and amplifier stages featured a x2 Galilean telescope which helped to compensate for thermal lensing effects. The oscillator cavity was bounded by a 5m radius of curvature, concave rear mirror of maximum reflectivity, and also contained a plane output coupler. Beyond the oscillator was a Pockels cell which allowed the possibility of Q-switching the laser output. The Q-switch assembly consisted of a dielectric polariser with a Brewster-angled KD*P crystal and an optical rhomb to compensate for any beam deviation. The oscillator output passed through the amplifier region, and the amplified output then impinged on a thermally stabilised oven containing CD*A and KD*P doubling crystals. The positioning of either or both of these crystals in the beam path allowed the generation of second, third, or fourth harmonics of the fundamental 1064 nm laser line. These higher harmonics were separated by passage through a pair of Brewster-angled gull wing prisms. Typical powers available from this laser at 10Hz were:

1064 nm	800 $mJpulse^{-1}$
532 nm	320 $mJpulse^{-1}$
355 nm	170 $mJpulse^{-1}$

The second harmonic 532 nm output was used to vaporise the target species for cluster generation. The operation of the laser required a trigger pulse to fire the

flashlamps, and a separate pulse to operate the Q-switch. The computer-controlled data acquisition and control system allowed precise timing of these trigger pulses, and the output power of the laser was most easily varied by changing the time delay before Q-switching. The problem of thermal lensing, which is caused by temperature gradients within the beam path leading to gradients in the refractive index [7], is minimised by running the laser at a strict, invariant repetition rate of 10Hz.

Typically the YAG output power used was anywhere up to 50 $mJpulse^{-1}$, focussed by a 1000mm Newport BK7 plano-convex lens to a spot of less than 1mm diameter on the target material. The laser power was measured outside the vacuum chamber with a Coherent Model 210 power meter.

3.4.2 Lumonics excimer laser

The class of lasers known as excimers are gas lasers in which the active molecules possess a bound excited state, but dissociative electronic ground states. Lasing action can be induced by pumping these molecules to the bound excited state from which they can emit energy as they decay to the ground state, whereupon the molecule dissociates once more. The actual molecules which fit into the category known as excimers are rare gas dimers, or rare gas halides. Since the radiative process is swift, the pumping step is the bottleneck. However, with fast transverse discharges, and high gas densities to increase the number of collisions, excimer molecules can combine very quickly, in times of the order of 10^{-8}s [8]. The wavelength emitted obviously depends on which excimer gas species is used, as the photon energy is linked to the specific energetics of the electronic levels within the excimer molecule.

The actual laser used was a Lumonics Model TE-861T-4, and this was primarily run with the excimer molecules ArF and KrF to provide photons with wavelengths at 193 nm and 248 nm respectively. A thyratron-switched electric discharge at almost 40kV was used to stimulate the lasing action, and again the timing was controlled using pulse delay generators. This excimer laser required two trigger

pulses, the first to initiate the capacitor charging cycle, the so-called 'charge on demand', and a second pulse, after a delay of approximately 12ms, to trigger the thyratron. Some degree of control over the output pulse energy could be gained by varying the charging period of the capacitors, or by limiting the peak charging voltage. The actual lasing action took place within a cavity fitted with the electrode assembly, and filled with the required excimer gases (F_2, and Ar or Kr) along with an excess of helium buffer gas to take the pressure within the gas reservoir to about 3 atmospheres. The cavity gases were continually circulated through an exhaust gas filter containing various molecular sieves. This helped to protect against loss mechanisms when excitation took place.

The cavity optics initially consisted of a fully reflecting rear mirror and a fully transmitting front optic to provide a slightly divergent beam from this stable resonator set-up. At a later stage this laser was converted to run with an unstable resonator configuration. The rear optic for this set-up possessed a slightly concave rear reflecting surface with a wedged front surface, and this was arranged confocally with the front optic. The previous front optic for the stable resonator was used here also, but was mounted with an optical baffle to prevent shock waves from the discharge from damaging the optic. The feedback was actually provided by an aluminium-coated 3mm diameter mirror mounted on a rod external to the laser vessel. The mirror position was easily adjustable to allow optimisation of the energy, beam shape, and focal position. The use of unstable resonator optics provided an output with much less divergence than with the stable resonator set-up, but the output pulse energies were reduced. Pulse energies available from the laser were of the order:

	ArF	KrF
STABLE RESONATOR OPTICS	80mJpulse^{-1}	90mJpulse^{-1}
UNSTABLE RESONATOR OPTICS	35mJpulse^{-1}	60mJpulse^{-1}

The lifetime of the excimer gas mixture was of the order of several hours, with pulse energies depreciating noticeably over this time period. This reduction in

laser power was due to the formation of non-lasing species which contribute to the loss mechanisms. To prolong the lifetime of a single gas fill, these species could be trapped out in liquid nitrogen. The gas delivery line of the laser was thus modified to carry out this function by linking a diaphragm pump (Air Dimensions Inc. Model 19313VYPR) with a gas filter to the laser cavity via lengths of copper tubing. One length of tubing was coiled and immersed in a container of liquid nitrogen. This served to trap out the contaminating species as the laser gases were pumped around this system.

This laser was used routinely to photoionise clusters. The high energy photons of the ArF line (6.4eV) meant that most cluster species could be efficiently ionised by a non-resonant two-photon absorption scheme, and many required only one photon. Thus the ArF radiation provided a good method of blanket ionisation in order to characterise the cluster species present in the molecular beam.

3.4.3 Questek excimer laser

For some of the work reported, the Lumonics excimer laser was replaced with a Questek 2740 excimer laser obtained from the loan pool operated by the SERC Laser Facility. This laser worked in the same manner as the Lumonics laser and was operated primarily on ArF. This system was configured as a stable resonator, and also featured a recirculating pump with a liquid nitrogen cryotrap to prolong the life of the laser gases. The output pulse energy for this laser tended to be higher, at around 400mJpulse^{-1} for ArF. Again, similar to the Lumonics laser, dual trigger pulses served to engage the capacitor charging cycle followed by the laser firing command. However, for the 10Hz repetition rate used during the cluster experiments, the Questek laser could be run with a single trigger pulse. In this set-up, charging occurred automatically after the laser had fired, as long as at least a 20ms delay was allowed between each laser shot.

One advanced feature of this laser was the ability to lock the output power to a user-set value. An internal high-speed detector sampled the output energy and compared a running average with the desired pulse energy which could be

easily set on the control panel. The gain of the laser would then be modified by a microprocessor to maintain the desired output energy.

3.4.4 Excimer-pumped dye laser

This tunable laser system had been previously used in this laboratory to perform spectroscopic measurements on transition metal dimers, but could also be used simply as an alternative source of ionising radiation with broadly variable wavelength. The laser system was manufactured by Lambda Physik, and consisted of an EMG 201MSC thyratron-switched excimer laser which was used to optically pump an FL3002 EC dye laser.

The excimer was run on the XeCl line at 308 nm. Typical output power from this laser was 400 mJpulse^{-1} measured at 1Hz on a Gentec Model ED200 pyroelectric joulemeter connected to a Tektronic Model 2445A 150MHz oscilloscope. Again, the exact time of firing of this laser was handled by the computer-controlled data acquisition and control system which delivered a single trigger pulse to the excimer unit at the appropriate time, repeating at the experimental frequency of 10Hz.

The excimer output beam was directed into the dye laser where three dye cuvettes were situated, the dye solutions being continually circulated around these systems. Part of the pump beam was directed transversely onto the first cuvette which acted as an oscillator within a Hänsch-type cavity [9]. The rear reflector of the laser was a Littrow grating containing 600 lines per mm. At the front end of the oscillator cavity was a dielectric reflector to couple the generated radiation to the amplifier stage. Beam expansion prisms were positioned between the grating and cuvette to reduce the chance of grating damage from high power density light. Adjustment of the grating angle provided the means to scan the output wavelength over the available gain profile of the laser dye in use.

The remainder of the 308 nm pump beam was focussed into the two amplifier cuvettes, overlapping the oscillator output already generated. The bandwidth of this laser was normally less than 0.2 cm^{-1} at 500 nm, and could be greatly reduced

with the insertion of an air-spaced intracavity etalon, which was synchronously angle-tuned with the grating if the laser was actively scanned. Single-mode operation of the laser could be accurately assured by projection of the fringes resulting from the passage of laser light through a further monitor etalon.

The typical range of dye solutions used provided output pulse energies of the order 10 - 15mJpulse^{-1} depending on the specific dye in use. This output could also be frequency doubled to produce ultraviolet radiation by means of a second harmonic generating crystal. After calibration procedures, the dye laser microprocessor could be relied upon to accurately control the position and motion of the grating and various etalons, crystals, and compensating optics to ensure a spatially stable laser beam.

The laser systems described above were those used in the experiments carried out at Edinburgh. A description of the lasers used in Lyon is given in Chapter 7.

3.5 Ion Optics

A schematic diagram of the ion optics which make up the ion source region of the Wiley-McLaren double-field time-of-flight mass spectrometer described in Chapter 2 is shown in Figure 3–4. The ion extraction fields are generated by connecting the plates shown schematically in the diagram to high voltage power supplies. The repeller plate, draw-out grid, and flight grid plates are all constructed of 0.5mm thick stainless steel, and are 72mm squares. The draw-out grid and flight grid both have 40mm diameter, centrally located holes to allow passage of the newly ionised clusters. The integrity of the electric fields in this region is disturbed somewhat by these holes, but this effect is minimised by covering the holes with 90% transmitting nickel mesh. The mesh is fixed to the plates with silver conducting paint. The plates are held in place by insulating Delrin support rods which hold the repeller 32mm from the draw-out grid, and this in turn is 6mm from the flight grid.

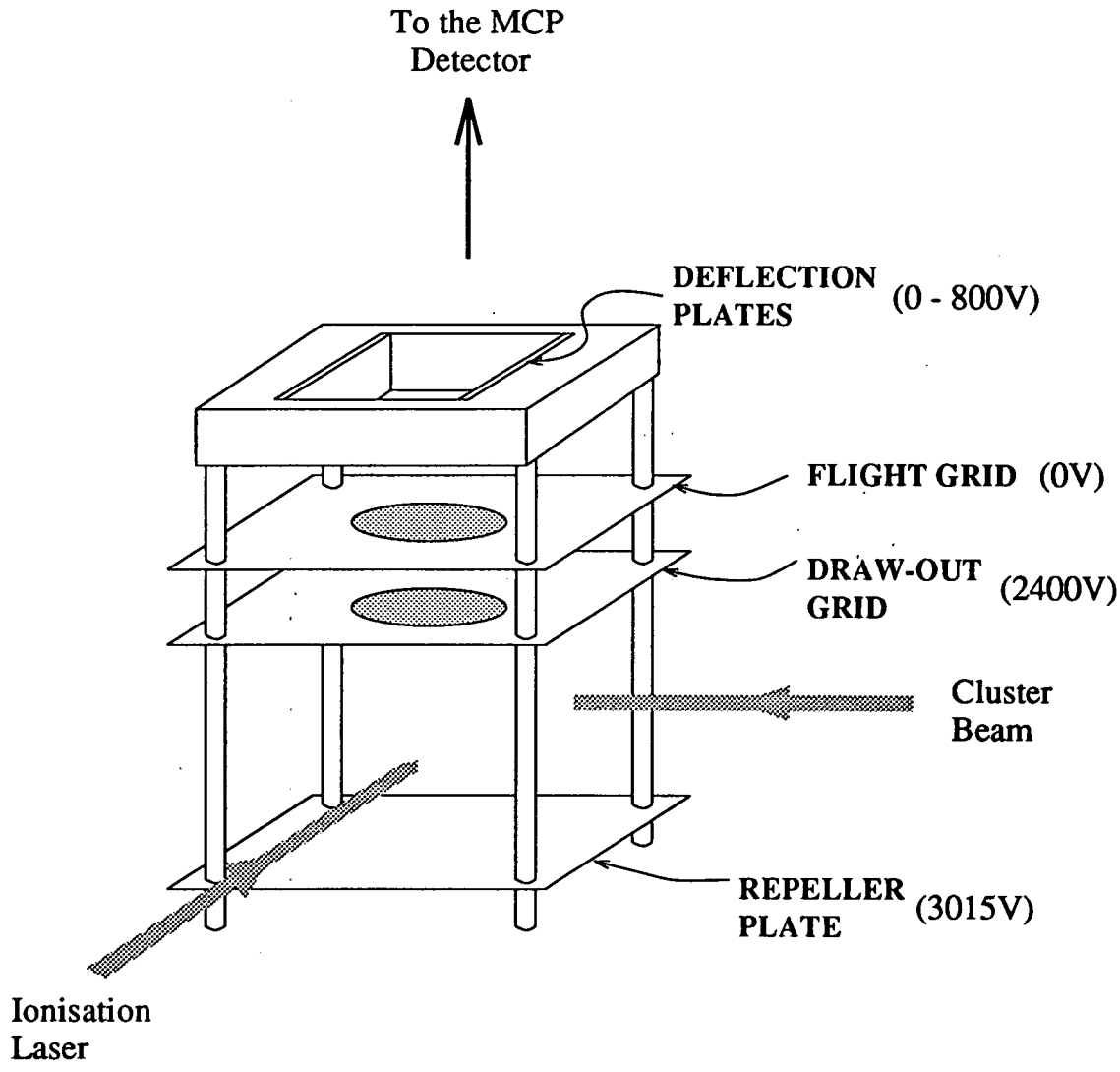

Figure 3–4: A schematic of the ion source region of the mass spectrometer.

Above the flight grid are two parallel deflection plates made of 1/4" aluminium plates. These are used to compensate for the off-axis velocity component of the clusters, as was mentioned in the previous chapter.

The entire set of ion optics are suspended from the roof of the A-chamber, enclosed within a copper box which is in thermal contact with the double-skinned liquid nitrogen dewar which sits atop this chamber. The cryopumping effect, and the isolation of the ion source area result in a reduction of the background signal which commonly arises from the presence of stray pump fluid.

The voltages applied to the plates are listed in Figure 3–4. These voltages were supplied through MHV vacuum electrical feedthroughs to which fishplated wires were connected. The grounded flight grid is also connected to the copper box, and the entire chamber is earthed to ensure the elimination of any extraneous fields. Voltages were supplied by the following high voltage power supplies:

Repeller	LeCroy Model 2415 (CAMAC-based)
Draw-out grid	Power Designs Model 1570
Deflection plates	Power Designs Model 2K20A

The extracted ions travelled along the field-free flight tube situated above the ion source region, and were detected at the end of this drift tube.

3.6 Ion Detection

The detection of cluster ions was accomplished with the use of a dual microchannel plate (MCP) obtained commercially from R.M. Jordan Co. The construction of an MCP detector makes it ideal for use in the types of experiments detailed here. The MCP used is a dual chevron type with two Galileo MCP-18B plates fabricated from a lead glass material, and with an active detection area of 2.48cm^2 per plate. Each plate is honeycombed with an array of 10μm diameter channels, the channel centres separated by 12.5μm. The lead glass material has been developed to

have optimum secondary emission characteristics from each channel, and to be sufficiently semiconducting to allow charge replenishment from an external voltage source [10]. The external voltage to the detector is supplied by a Power Designs Model 1556C high voltage power supply. The typical working voltage of 3 - 3.5kV was passed through a home-built resistor chain which divides this input voltage across the plates. The incorporation of high value capacitors into this unit helps to prevent voltage loss from successive impacts by cluster ion packets.

The high gain and fast response times of the dual MCP detector makes it the most widely used detector for pulsed laser ionisation experiments [11]. The gain expected depends on the length to diameter ratio of the channels, but is typically of the order of 10^3 at 1000V per plate [12]. The detector was used in this work in the grounded anode configuration in which the rear plate is biassed at 0V, and the front plate is negatively biassed. This field accelerates positive ions, increasing the effective gain of the detector. However, this factor is countered by the requirement for a field-free drift region, necessitating a grounded entrance grid before the detector. The grid has an 82% transmission thus lessening the detection sensitivity somewhat. The fact that the rear MCP plate is grounded makes it easy to connect the output signal to an amplifier without the need to capacitatively decouple from the anode.

During some experiments, the signal could be boosted by the use of a preamplifier. A LeCroy Model 134 linear amplifier was frequently used containing two channels, each providing a gain factor of 10, or 100 if used in series. The amplifier was situated within the CAMAC crate along with the transient digitiser to which the signal was passed.

3.7 Experimental Control

A sophisticated package of hardware and software is used in this laboratory to control the running of the experiments, and to process the data in real time. The hardware system consists of a number of units designed to allow the easy operation

of all of the equipment crucial to the experimental procedure. These modules are housed in a CAMAC crate (WES FHD-DV3) which conforms to the IEEE specifications for a Computer Automated Measurement And Control (CAMAC) system [13]. The crate provides communication lines allowing the transfer of data to and from the appropriate instrumentation. The crate itself is linked to an IBM PC-AT which runs control software written by a previous student in this laboratory [14].

The IBM PC-AT contains a 16 bit Intel 80286 microprocessor with an added 80287 maths coprocessor, and is linked to a monitor equipped with an enhanced graphics adaptor. An operating program, known as THOR, which was written in the C programming language with some assembler language routines to speed up operation when commands are issued to the crate units, was used for data acquisition and control. The interface between the IBM PC-AT and CAMAC crate was via a crate controller module (Transiac 6002) which allowed two-way communication for the functions of experimental control and data acquisition. The hardware set-up is shown in Figure 3–5, and the duties and specifications of each CAMAC module are detailed here.

3.7.1 Control hardware

The crate controller link between the crate and computer allowed data transfer between the two systems at 700Kbs^{-1}. The crate controller acted as a master unit, accepting commands from the IBM PC-AT and passing the instructions to the other control units in the crate. The timing of the specific events which take place during one experimental cycle, such as the firing of the lasers and pulsed valve, are critical. Two CAMAC modules in the crate provide the control trigger pulses, as instructed by the THOR program running on the IBM. The first module shown next to the crate controller in Figure 3–5 is a Kinetic Systems Model 3655 pulse delay generator (PDG). This provides eight separate TTL level output signals, 200ns wide, with a timing jitter of approximately 1ns. One of these outputs is used to trigger the LeCroy Model 4222 PDG which can output similar signals,

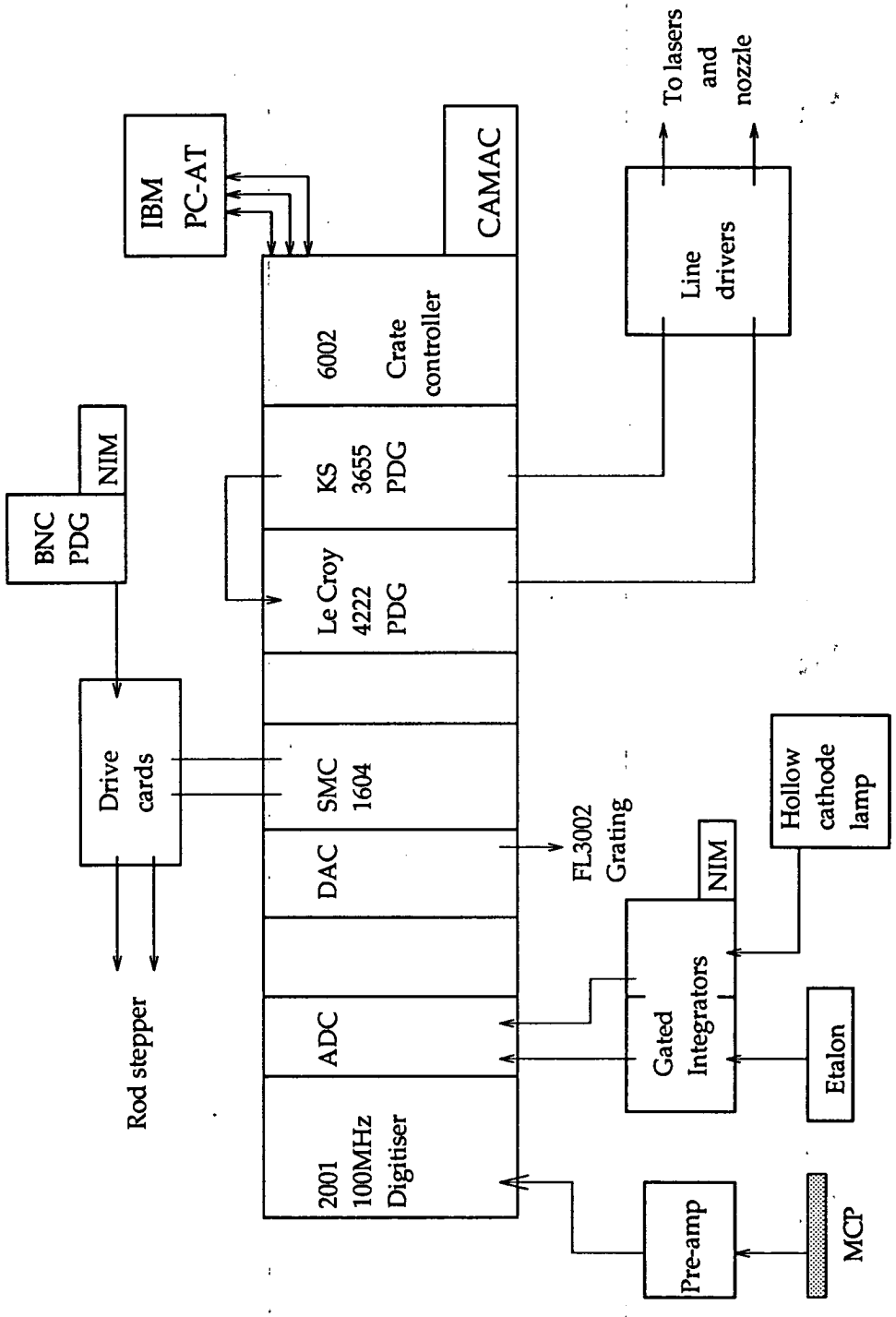

Figure 3–5: CAMAC units and connection lines used for experimental control during the course of a cluster experiment.

but with a reduced timing jitter of the order of 150ps. This second pulse delay generator was used to trigger the equipment which required more critical timing events, such as the transient digitiser. The Kinetic Systems PDG provided the trigger pulses to fire the vaporisation and ionisation lasers, and the molecular beam valve.

The output signals from these two PDG's were generally insufficient in pulse magnitude and duration to activate the required equipment. To solve this problem, the pulse delay generators were connected to home-built line driver units to ramp up the triggering pulse provided to the lasers and the pulsed valve. The two line drivers each contained eight channels with a choice of 5V, 50μs duration, or 15V, 10μs duration output signal. These two signal profiles were sufficient to trigger all of the equipment running in the laboratory between them. A typical timing sequence of trigger pulses during an actual experiment is shown in Figure 3–6.

Also housed in the CAMAC crate is a four-channel stepper motor controller (Hytec SMC 1604). This was linked to home-built drive cards which passed stepping and direction signals to the stepper motor which controlled the screw motion of the target rod during the experiment. One channel of the SMC 1604 was used to control the dye laser via a digital to analogue conversion unit (Bi Ra Model 5408) positioned in the crate. The driving pulse was timed to allow the dye laser wavelength to be scanned during the course of an experiment, with the wavelength steps taking place between laser shots.

An CAMAC-based analogue to digital converter (Bi Ra Systems Model 5303 ADC) was used to collect etalon fringes from the dye laser via a gated integrator. These systems were used in spectroscopic studies reported more fully in another thesis from this laboratory [15].

The time-of-flight mass spectra are acquired using a transient digitiser. The cluster ions strike the microchannel plate detector, with the signal being amplified as described previously, and digitised by a Transiac Model DSP 2001 transient digitiser which has a variable digitising rate and record length. It can be operated at 100MHz, and can handle 512mV signals, with a minimum detection limit of 2mV. The digitiser stores up to 2Kb of information at the 10Hz experimental

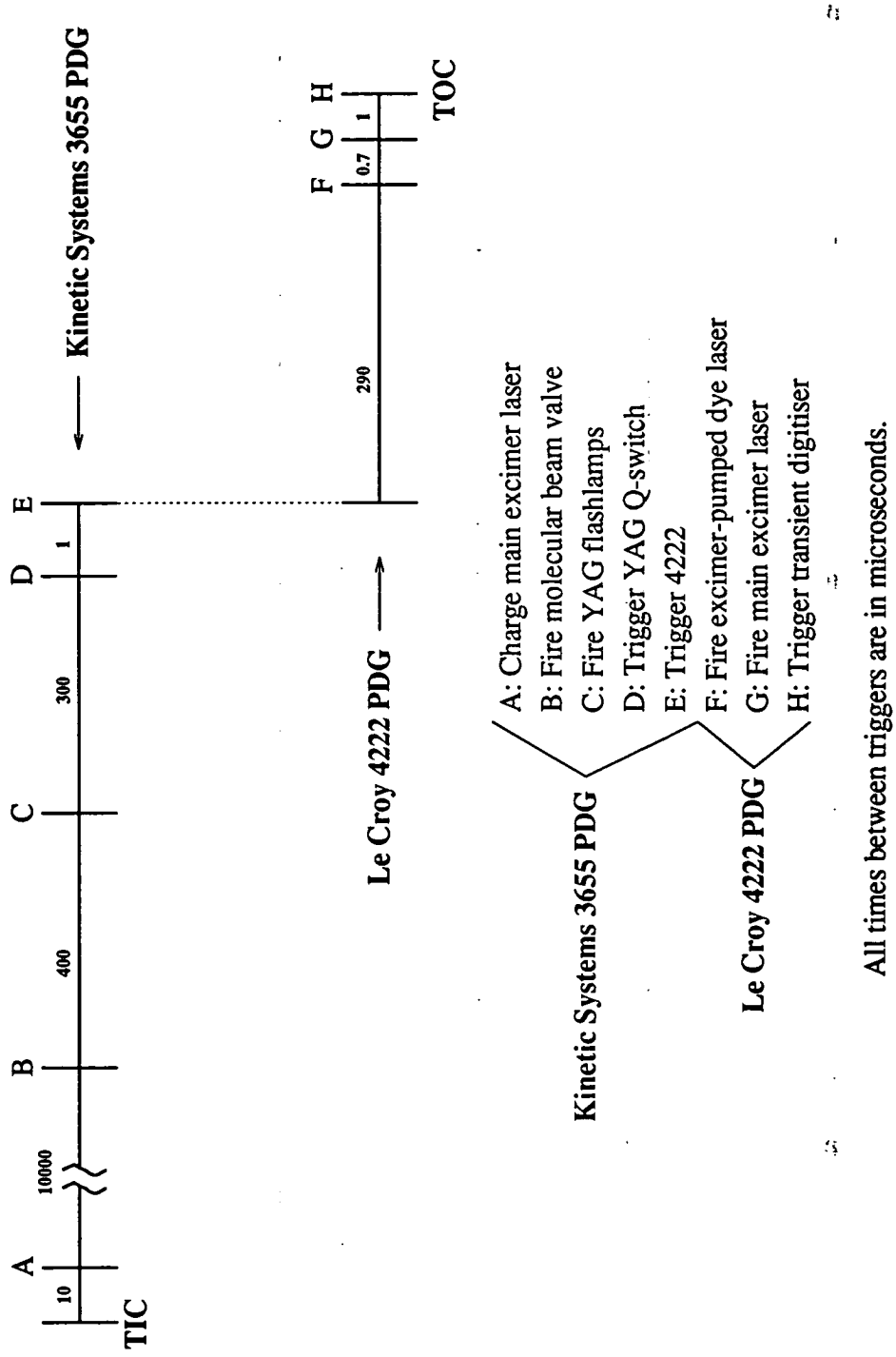

Figure 3–6: A schematic of the specific timing of the main events for one experimental shot.

repetition rate until it is commanded to download the stored data to the IBM PC-AT.

3.7.2 Software

The executive program THOR allows experimental control in real-time, and provides an immediate on-screen view of the acquired data. The program runs the experiments at a repetition rate of 10Hz. Two main commands are given by the program during the course of summing several experimental shots, and these are known as TIC and TOC. The TIC function prepares the digitiser to store data, communicates the appropriate time delays to the pulse delay generators, and kicks off the experimental cycle by triggering the first channel of the Kinetic Systems 3655 PDG. On the TOC command, the digitiser downloads stored data to the PC, and any data from the ADC is also collected.

There are three main functions which THOR allows the user to perform. The first option is the mass spectrum acquisition routine. This simply permits a user-defined number of experimental shots to be summed before displaying a spectrum showing the cluster distribution recorded. There are many manipulations which can be performed, including a calibration routine to allow the cluster flight times to be converted to a mass scale.

The second routine is the timescan function which allows the monitoring of the intensities of up to ten detected species as a function of one of the time delays shown in Figure 3–6. The normal use of this function is to optimise the time delay between the firing of the vaporisation and interrogation lasers. Examples of the result of a timescan were shown previously in Figures 2–2 and 2–3.

The final main function permitted a frequency scan to be recorded. This operates in the same manner as the timescan, but instead of altering a time delay from one shot to the next, the wavelength of the dye laser is stepped between shots (or groups of shots). This shows any enhancement in cluster intensities due to resonances in the ionisation scheme, allowing vibronic or rovibronic spectra to be recorded.

Many other routines are incorporated within THOR which make experimental control a lot more manageable than it would be otherwise. Some of these routines may be mentioned at a later stage of this thesis, and will be described as they appear.

Bibliography

[1] A. Guthrie, '*Vacuum Technology*', Wiley and Sons, Inc., New York, 1963.

[2] T.E. Adams, B.H. Rockney, R.J.S. Morrison and E.R. Grant, Rev. Sci. Instrum., **52** (1981) 1469.

[3] D.E. Powers, S.G. Hansen, M.E. Geusic, A.C. Puiu, J.B. Hopkins, T.G. Dietz, M.A. Duncan, P.R.R. Langridge-Smith and R.E. Smalley, J. Phys. Chem., **86** (1982) 2556.

[4] A.M. James, *Ph.D. thesis*, Edinburgh University, 1993.

[5] S. Nonose, Y. Sone, K. Onodera, S. Sudo and K. Kaya, J. Phys. Chem., **94** (1990) 2744.

[6] S.C. O'Brien, Y. Liu, Q. Zhang, J.R. Heath, F.K. Tittel, R.F. Curl and R.E. Smalley, J. Chem. Phys., **84** (1986) 4074.

[7] H.M. Chen and Z.A. Schelly, Chem. Phys. Lett., **145** (1988) 102.

[8] W. Demtröder, '*Laser Spectroscopy: Basic Concepts and Instrumentation*', Springer Verlag, Berlin, 1982.

[9] T.W. Hänsch, Appl. Optics, **11** (1972) 895.

[10] J.L. Wiza, Nucl. Instr. and Meth., **162** (1979) 587.

[11] E.E. Gulcicek and J.G. Boyle, Rev. Sci. Instrum., **64** (1993) 2382.

[12] M. Hellsing, L. Karlsson, H.-O. Andrén and H. Nordén, J. Phys. E: Sci. Instrum., **18** (1985) 920.

[13] L. Costrell, IEEE Trans. Nuc. Sci., **20** (1973) 557.

[14] A.M. Butler, *Ph.D. thesis*, Edinburgh University, 1989.

[15] J.W. Macdonald, *Ph.D. thesis*, Edinburgh University, 1993.

Chapter 4

CLUSTER MAGIC NUMBERS: AN OVERVIEW

4.1 Background

In this chapter the topic of magic numbers exhibited by cluster systems is examined. These types of studies lead inevitably towards an understanding of the geometries and electronic structures of cluster species. In this area, the theoretician relies heavily on experimental findings. The theoretical calculations for dimer systems are well understood, but for larger clusters the number of possible geometries available are enormous. This poses a great problem to the theoretical scientist who must have some idea of the environment in which the electrons move before being able to carry out in-depth calculations. The study of magic numbers can give the experimental scientist clues as to how the clusters are physically and electronically structured. Before any details of the occurrence of specific magic numbers, and the models used to rationalise these can be discussed, however, several questions must be addressed:

- What are magic numbers?
- How do they arise?
- How can we observe them?

In answer to the first question, magic numbers are the numbers of constituent atoms or molecules which make up exceptionally stable clusters. This stability

may manifest itself in several ways, leading to the observation of magic numbers from a host of different types of experiments. Such magic number species can be more resistant to fragmentation, have higher ionisation potentials, or have markedly different reactivities to non-magic number clusters. The specifics of these differences will be discussed later in this chapter.

It is important to understand how the magic numbers arise so as to be able to construct models to justify the effects exhibited, and to predict further magic numbers. The concepts of geometric and electronic stabilities have been extremely successful in accounting for observed magic numbers in many cluster systems already studied. It is an intuitive step to imagine that some geometries may be preferred for certain cluster systems, and the types of geometries available allow a straightforward prediction of higher magic numbers. The rationalisation for electronically stable clusters was initially developed from the theory of the nuclear shell model which has subsequently undergone much detailed advancement to apply specifically to clusters.

The experimental conditions required to observe these magic numbers depend on the exact type of experiment, but an understanding of their possible origin allows the experiment to be configured in such a way as to optimise the appearance of these effects.

The rest of this chapter is structured as follows:

In section 4.2 the various models developed to account for magic numbers due to electronic shell structure are introduced. Predictions from these models are discussed, and evidence supporting the predictions is given.

Section 4.3 deals with geometric shell structure for cluster species. Details are provided of the different types of geometries available to clusters, and the reasons why clusters can exhibit these effects are discussed.

Finally in section 4.4 examples of cluster systems that have been studied are given, and the shell effects, or other causes, responsible for the magic numbers that are observed are described. The manner in which a specific shell effect is attributed to an observed sequence of magic numbers is also discussed, as is the

possibility of competition between the two major types of shell structure for a single system.

4.2 Electronic Shells

4.2.1 The Jellium model

The development of the jellium model to account for observed magic numbers in several cluster systems was prompted by a comparison with effects seen in nuclear physics several decades before. In the late 1940s physicists had observed that certain atomic nuclei seemed to be exceptionally stable. These nuclei contained 2, 8, 20, 28, 50, 82, 126 or 184 protons or neutrons, and the challenge was to come up with a model which could be used to rationalise the observation of these magic numbers of nucleons [1].

The initial assumptions made in the nuclear shell model were that the atomic nuclei were spherically symmetric, and that the potential well in which the nucleons moved was relatively simple. The first assumption allowed the Schrödinger equation to be simplified to a radial function depending on the angular momentum quantum number, and on the radial dependence of the potential. The eigenvalues resulting from solutions of this Schrödinger equation were termed 'subshells', the filling of which led to stable numbers of nucleons. Thus the basic concept of shell effects had been formulated. However, the magic numbers predicted by filling shells in this model did not account for the observed magic numbers of nucleons. The observed shell structure could only be fitted once a strong spin-orbit interaction between the nucleons had been incorporated into the model [2,3].

The concept of shell structure was not confined to nuclei, however, as the layout of the periodic table of elements reflected a surprisingly similar type of shell structure within the atoms [4]. In this case the shell structure also results from the spherical symmetry of the system. The electrons move in a spherically

symmetric Coulomb potential generated by the positive nucleus. This symmetry again allows a grouping of the available angular momentum states into shells.

The fact that effects observed for both atoms and nuclei could be accounted for by variations of the same model was unexpected due to the vastly differing nature of the forces involved in each regime. The similarity which does exist prompts a comparison between common effects in the two systems. In both cases a group of interacting fermions are confined within an effective one-particle spherical potential. The shell structure results from a grouping of the fermion states which occurs under these conditions. It seems logical, therefore, that any physical system which fits similar constraints to those described above should exhibit a shell structure which could be adequately described by a variation of the same model.

One of the first pieces of evidence that magic numbers for metal clusters might be described by a similar model was presented in a publication by Knight and coworkers [5]. This group had generated sodium clusters in an argon expansion, and had observed high intensity mass spectral peaks for clusters containing 8, 20, 40, 58 and 92 atoms. These magic numbers corresponded well with some of the predicted numbers of fermions which would complete subshells in the nuclear model, prior to its modification for the nuclear spin-orbit effect. The specific grouping of fermion states into degenerate subshells had been calculated for several simple potentials, an example of which is shown in Figure 4–1 for electrons bound in a spherically symmetric square well potential.

The fact that observed magic numbers for sodium clusters correlated well with the shell effect predictions is not in itself a justifiable reason to apply the model generally. However, knowing that one of the goals of cluster research is to create a link between molecular and bulk properties, one can look to these areas to provide confirmation that we are heading in the right direction.

We now look at how sodium might be described in terms of solid state physics. All of the alkali metal atoms contain a single conduction electron which can be described well in a nearly-free electron approximation in the bulk. Any existing pseudopotential does not perturb the electronic motion greatly since the Fermi surface for these metals is almost spherical, and is entirely contained within the

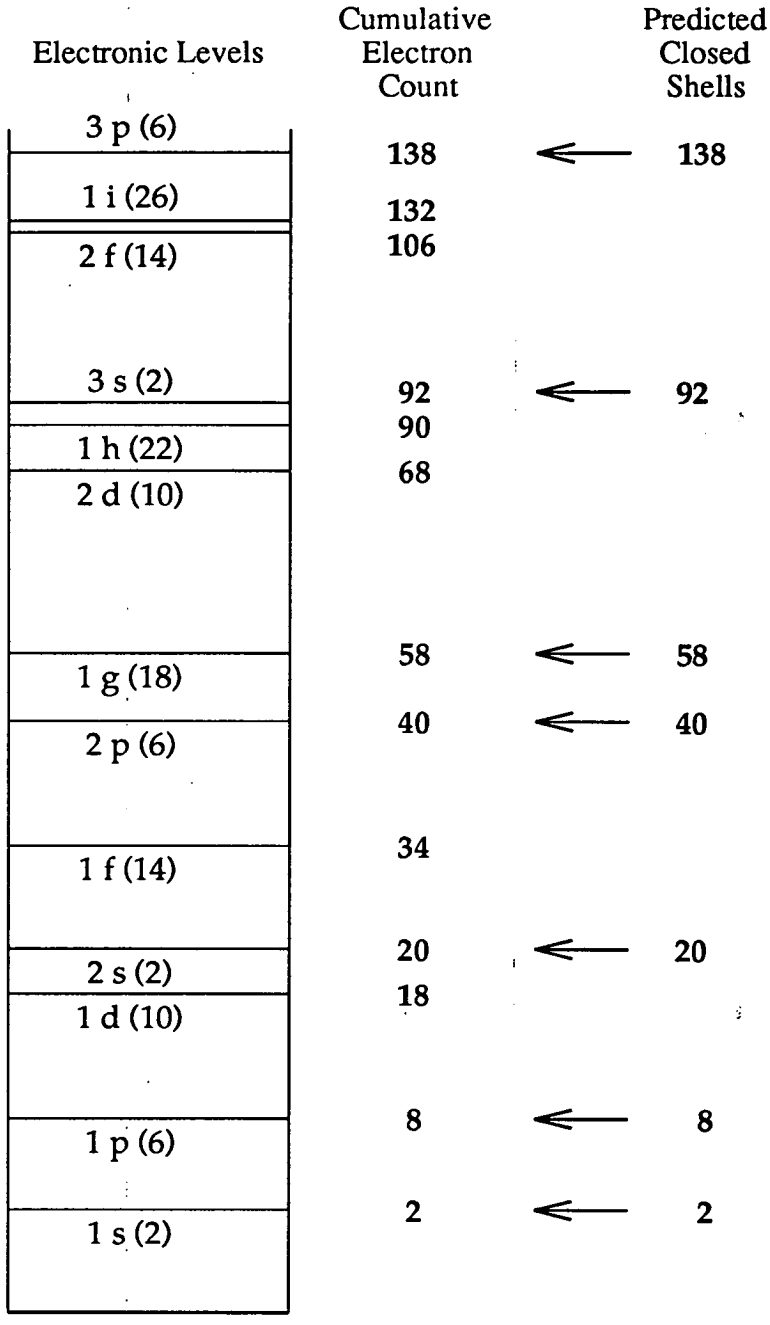

Figure 4–1: The grouping of fermion states into subshells within a square well potential.

first Brillouin zone [6]. Extrapolating these properties back to the cluster systems, we can now see the astonishing similarity with the nuclear and atomic shells. The link between these two environments was the existence of a group of interacting fermions confined to an effective one-particle spherical potential. The nearly-free electron properties of the alkali metals means that each atom in the cluster can contribute one electron (fermion) to the whole system. The potential in which these electrons move is generated by the remaining ionic cores in the cluster. At this stage we can introduce the *Jellium* model, as the positions of the ions are assumed to be unimportant, each ion merely contributing to the overall potential in which the valence electrons move. This assumption can only be made if the electrons are strongly delocalised, as is the case for metal systems which conduct well [7]. One further constraint upon the cluster system is that, like the nuclear shell model, we assume spherical symmetry for the cluster, simplifying any shell structure calculations. So, we now have a spherical jellium model, so-called because the ionic cores in the cluster are pictured as a structureless ionic jelly through which the valence electrons are free to travel.

One can see the overall similarity in the models for shell structure in nuclei, atoms, and now clusters. Each system consists of interacting fermions. In nuclei these are confined to lengths of approximately 10^{-12}cm. For atoms the confinement region is about 10^{-8}cm, and this increases to 10^{-7}cm or larger for metal clusters [8]. The jellium model, or giant atom model as it is sometimes known, should now allow the electronic shell structure to be calculated for cluster systems, although one must first decide on an appropriate potential to use as this will affect the groupings of the fermion states, leading to magic numbers which depend on the exact potential used.

Calculations have been performed to demonstrate how the electronic states in a metal cluster will group if the electrons are confined within a three-dimensional harmonic oscillator potential, or in the square well potential as demonstrated in Figure 4–1. It has been generally shown that the best type of potential to use, which will predict the correct closed shells, is close in form to the square well [9]. A fairly rigorous self-consistent calculation by Ekardt [10] provided a useful

spherical jellium background potential, but this can be well approximated by a Woods-Saxon function [11], which was originally constructed for use in nuclear physics. The form of this potential function is that of a square well with rounded edges, allowing the electrons to 'spill out' through the surface of the cluster to some extent. The general form of this potential is:

$$U(R) = \frac{V_0}{1 + \exp(\frac{R-R_0}{a_0})} \tag{4.1}$$

where

V_0 is the well depth, which can be estimated as the sum of the Fermi energy and the bulk work function,

R_0 is the effective radius of the cluster sphere, which is proportional to the cube root of the number of atoms in the cluster, and

a_0 is a surface thickness term which affects how hard the potential is at the cluster surface.

Using typical values of the above variables for sodium clusters [12], the general form of the Woods-Saxon potential is shown in Figure 4–2 for three different cluster sizes. It can be seen that the potential well becomes effectively shallower as the number of atoms within the cluster increases. The well remains the same depth, but many more electronic levels must be fitted into the well for a larger cluster. This leads to a smaller spacing between the electronic energy levels, in turn reducing the magnitude of the shell effects. Thus, as the cluster grows the available electronic states gradually evolve into the system of electronic bands which can be associated with bulk metals.

The observation of electronic shell effects depends on the type of experiment performed. For metal cluster studies in which detection follows an ionisation step, the magnitude of the observed effects depends on the specifics of the laser interaction with the metal clusters [13,14,15]. For high ionisation laser fluences, many photons are absorbed by the metal aggregates, and fragmentation occurs. Clusters with closed electronic shells are more stable, and less likely to fragment than open shell species. Thus the clusters with filled electronic shells show up as high intensity peaks in the mass spectrum.

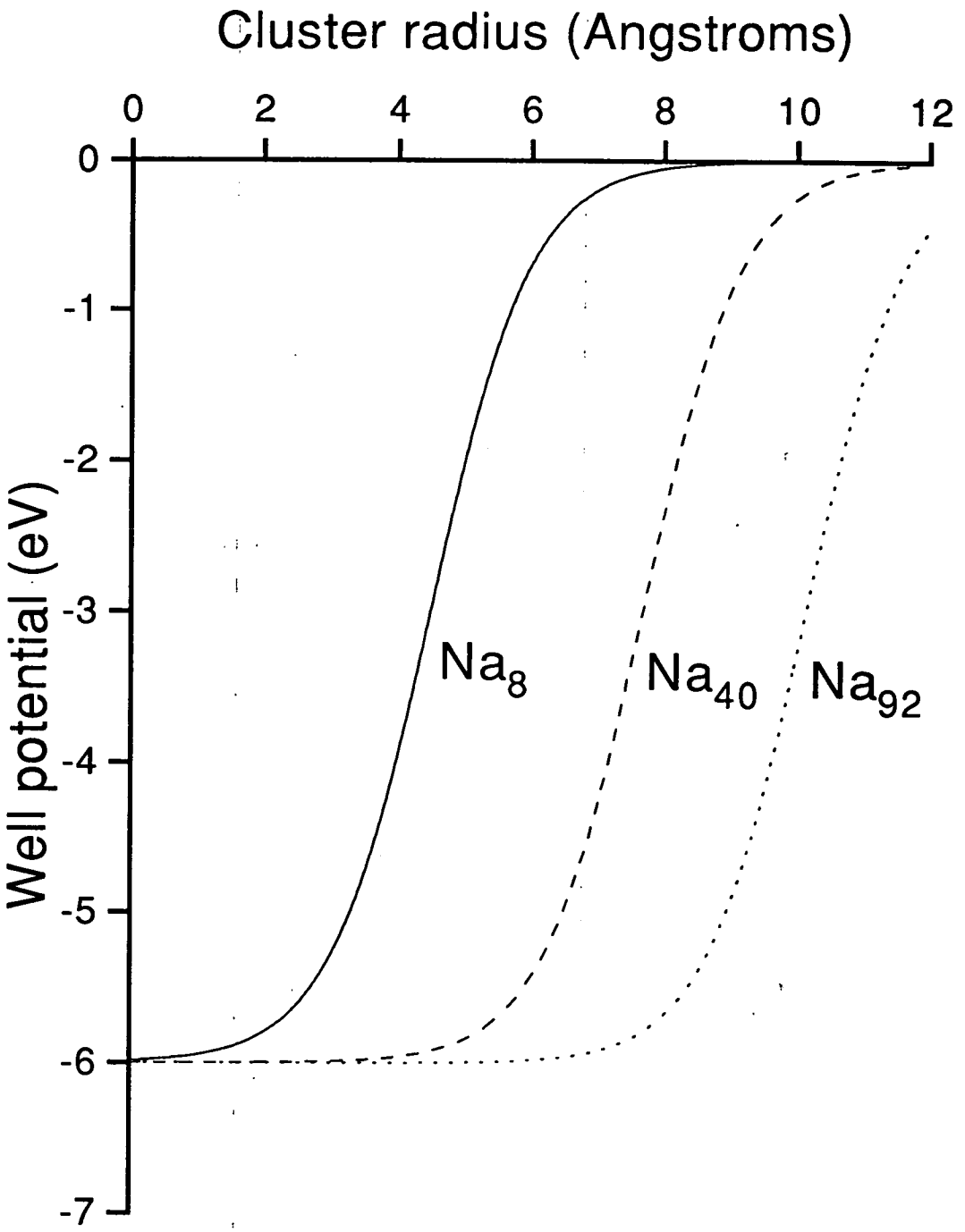

Figure 4–2: Woods-Saxon potentials for three spherical, closed-shell sodium clusters

If the ionisation conditions are such that a low laser fluence is used with laser wavelengths close to the ionisation potential for the clusters studied, then an increased signal is seen for species with newly opened shells. This arises since the closed shell clusters are very stable, and an electron in a newly-opened shell is not as tightly bound, giving rise to a lower ionisation potential for this species. Thus, the absorption of one photon of near-threshold laser radiation will produce more cluster ions of newly-opened shell species.

In general terms, then, the magic numbers attributable to electronic shell effects for cluster species can be noticed as anomalous intensity steps in cluster mass spectra. Altering the ionisation conditions allows differing degrees of fragmentation, as well as differentiating between the observation of magic numbers of the neutral or of the ionised cluster systems. Other experimental variables can help to further elucidate the origin and nature of the magic numbers. One example of this is the use of a 'warming' laser to promote some atomic evaporation from a cluster before the ionisation event [15,16]. This effect, along with others, will be discussed later for specific cluster systems.

4.2.2 Minor shell features

In mass spectra of simple metal cluster systems which conform to the spherical jellium model, there often appears to be some fine structure in addition to the main magic numbers described above. The assumption that closed shell clusters are spherical has been borne out by the fact that the model works, and also verified experimentally to a good degree in ion mobility measurements and plasmon resonance results which will be detailed later. However, for metal clusters with unfilled electronic shells, there is no reason for these systems to be constrained to a spherical shape. In fact, the Jahn-Teller effect will cause clusters with partially filled shells to distort from a spherical shape to a less symmetric configuration in which the degeneracy has been lowered [17]. The jellium model has been extended by Clemenger [18] in such a way as to account for the minor shell features observed in cluster abundance spectra. Again a parallel is drawn with the nuclear shell

model which was modified by Nilsson to allow nuclei to deform into ellipsoidal geometries [1]. Clemenger applied similar corrections to cluster systems, allowing open-shell clusters to distort. Many of these were found to assume ellipsoidal shapes as minimum energy configurations. This change from the spherical closed-shell species was accompanied by a change in the electronic level degeneracies and groupings, giving rise to new magic numbers. These new minor shells had noticeably enhanced stabilities over other open-shell clusters, but not quite of the same magnitude as the stable, spherical closed-shell species [8,19]. Typical clusters which are rendered more stable by adopting spheroidal geometries are systems containing 10, 14, 18, 26, 30, 34, 36, 38,... constituent atoms. Some understanding as to the shapes adopted by open-shell clusters can be gained with the use of a fairly simplistic picture, by looking at how the orbitals are occupied. If we direct our attention again to clusters with monovalent constituent atoms which, to a good approximation have free electrons, then we can predict cluster shapes. The dimer system (two electrons) is spherical due to the occupation solely of an s state. The tetramer assumes a prolate geometry in order to reduce the energy of the doubly-occupied p_x state. Additional occupation of the p_y state forces the five- and six-atom clusters to adopt oblate structures. The eight-atom cluster has a completely filled p shell, leading again to a geometry of spherical symmetry. This picture does give a realistic view of how the clusters are shaped, backed up by more sophisticated calculations [20].

Some evidence that this deformation does take place has been provided in the literature. The measurement of absolute photofragmentation cross-sections of small, simple metal cluster ions conforming to jellium specifications was achieved by ion-beam depletion experiments [21]. Clusters containing 8 and 20 electrons (closed electronic shells) showed a giant resonance due to a plasmon excitation, that is a collective excitation of the cluster's valence electrons. In contrast, for clusters containing 10 and 14 electrons this giant resonance was split into two peaks. This effect is explained by the fact that the electronic excitations have two possible resonance energies, corresponding to the two main axes of an ellipsoidally-shaped metal cluster. This is evidence that there does appear to be a fundamental

difference in the geometries of certain clusters, and that the spherical jellium model appears to fit cluster systems to a greater degree when the open-shell clusters are allowed to undergo an ellipsoidal deformation.

4.2.3 Supershells

Now that the jellium model, with appropriate corrections, seems to work well when applied to certain cluster systems, it would be worthwhile to see if there are any more predictions to be made with the model. Indeed, an analysis of its predecessor, the nuclear shell model, throws up one more major application. In this case the jellium model is able to go beyond the nuclear shell model because of a limitation in the size of existing nuclei.

In 1971 a paper appeared by Balian and Bloch [22] showing the results of detailed calculations related to the nuclear shell model. They showed that the oscillations in the eigenvalue density which gave rise to shell effects were themselves enveloped by a longer wavelength oscillation. This was termed supershell structure, and seemed intuitively pleasing in that it mirrored the fractal-like picture of nature. The problem with this work was that the prediction for the wavelength of the longer oscillation covered approximately one thousand fermions. Since the model's application was restricted to nuclei and atoms, there was no prospect of seeing any evidence of this supershell structure in such size-limited systems. After the development of the spherical jellium model it was realised that there now existed a system which could act as a testing ground for the hypothesis of Balian and Bloch. Metal clusters have essentially no limit to their size, allowing an analysis of aggregates containing well over one thousand fermions, enough to verify the existence of a supershell structure.

The original work of Balian and Bloch involved the calculation of the single-particle level density for fermions in a spherical cavity. This type of cavity may have seemed too simplistic to apply accurately to metal cluster systems, so the calculations were repeated using potentials known to describe cluster species well [12], such as the previously mentioned Woods-Saxon potential. In fact, these

calculations turned out to give very similar results to the original calculations by Balian and Bloch, showing that the exact form of the potential was not too critical. To gain some idea as to what principles lie behind the appearance of supershell structure, let us again look back to the electronic shell structure which is cradled within.

The range of sizes allowable for these cluster systems makes Bohr's correspondence principle assume a great deal of importance [23,24]. This states that classical mechanics will emerge from quantum mechanics as high quantum numbers are attained. In this picture there should be a correspondence between the motion of classical particles, and the properties of the energy eigenvalues of quantised particles moving in equivalent potentials.

The supershell structure itself can be pictured as a beating pattern caused by alternate constructive and destructive interference between two almost equal periodic contributions. In a quantum mechanical sense, these contributions can be attributed to two competing energy quantum numbers. However, due to the correspondence principle we are permitted to picture this system semi-classically, and this provides an easier way of visualising what is occurring. In this approach the observed shell structure can be correlated with a system of closed orbits which can be traversed by a classical particle moving within the potential of the cluster. These orbits take the form of polygons with slightly rounded corners, and Balian and Bloch showed that the triangular and square orbits, as shown in Figure 4–3, are the dominant ones. It was shown that the neighbouring shell spacing in energy is proportional to the inverse length of the shortest available orbit (triangular), and that the supershell spacing is proportional to the inverse length difference between the triangular and square orbits.

The length of a polygon contained within a sphere of unit radius is given by:

$$L(p,t) = 2p\sin(\frac{t\pi}{p}) \tag{4.2}$$

where

p is the number of sides, and

t is the number of turns required to complete the polygon (i.e. $t = 1$ for the

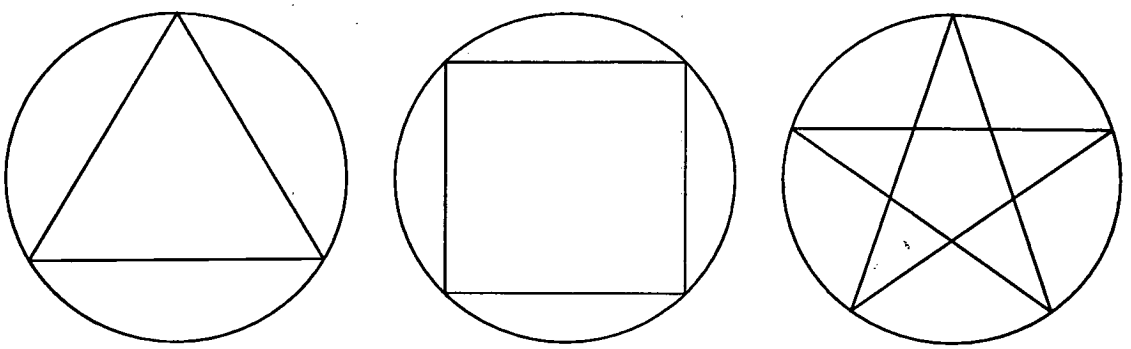

Figure 4–3: Semiclassical electron trajectories within a spherically symmetric metal cluster.

triangular and square orbits, but $t = 2$ for the star orbit shown in Figure 4–3). From the above equation it works out that approximately eleven electronic shells should group into each supershell. This phenomenon manifests itself as an oscillation in the size of the electronic shell effect over the supershell period. Thus, five or six shells after a maximum in the amplitude of the shell effect a minimum occurs. It then seems that the shell structure has disappeared, and bulk-like electronic properties have become established in the cluster. This occurs for a system containing approximately one thousand electrons. However, as the cluster size increases, the shell effects reappear again, the amplitude continuing to vary as governed by the supershell structure.

Subsequent calculations have continually upheld the existence of supershell structure [25], although difficulties were encountered during attempts to verify this experimentally. One problem was that temperature effects tended to wash out the shell structure, but this could be compensated for with appropriate scaling factors [26]. With the use of such compensation methods to magnify mass spectral intensity anomalies (magic numbers), along with the advent of experimental techniques for routinely creating metal clusters containing many thousands of constituent atoms, evidence of supershell structure was finally obtained [27]. More details of the existence of supershells will be mentioned later in this chapter.

Overall, one can see that the nuclear shell model, when modified by cluster scientists, has provided an extremely good method to account for magic numbers observed in certain cluster systems. However, the importance of electronic structure is sometimes overshadowed by another effect in some systems, so-called geometric shells, and this efect is discussed next.

4.3 Geometric Shells

The importance of discovering cluster geometries can not be stressed enough. This is the type of data which the theoretician must have in order to make any reasonable electronic calculations for cluster systems. The goal of understanding catalytic activity also hinges on this aspect of cluster research, as the active sites on catalytic surfaces are effectively small metal clusters of specific geometries. It is obviously desirable to obtain such structural information before being able to postulate on the details of the mechanisms involved in the catalytic process. Again, intuitive thought provides a guide-line as to what types of geometric structures might exist for cluster systems. These are generally highly-symmetric polyhedra, which one can imagine being very stable, and appear to be the preferential form for some clusters in the correct circumstances. There have been scientific papers showing the types of structures possible [28], with calculations of the binding energies as a function of the numbers of constituent atoms.

One interesting question is whether the bulk crystal structures of metals are responsible for the way the metal clusters are geometrically constructed. Some metal aggregate systems have indeed been shown to adopt a regular polyhedral structure of the same packing character as the bulk material. However, one type of favoured geometry which has been shown to be prevalent for many systems is not a crystalline structure at all. The ubiquitous icosahedron appears to be what might be termed a pre-crystalline phase. The general structure was proposed by Mackay [29] and is, in appearance, almost spherical with the surface atoms virtually close-packed. The first few Mackay icosahedra are depicted in Figure 4–4.

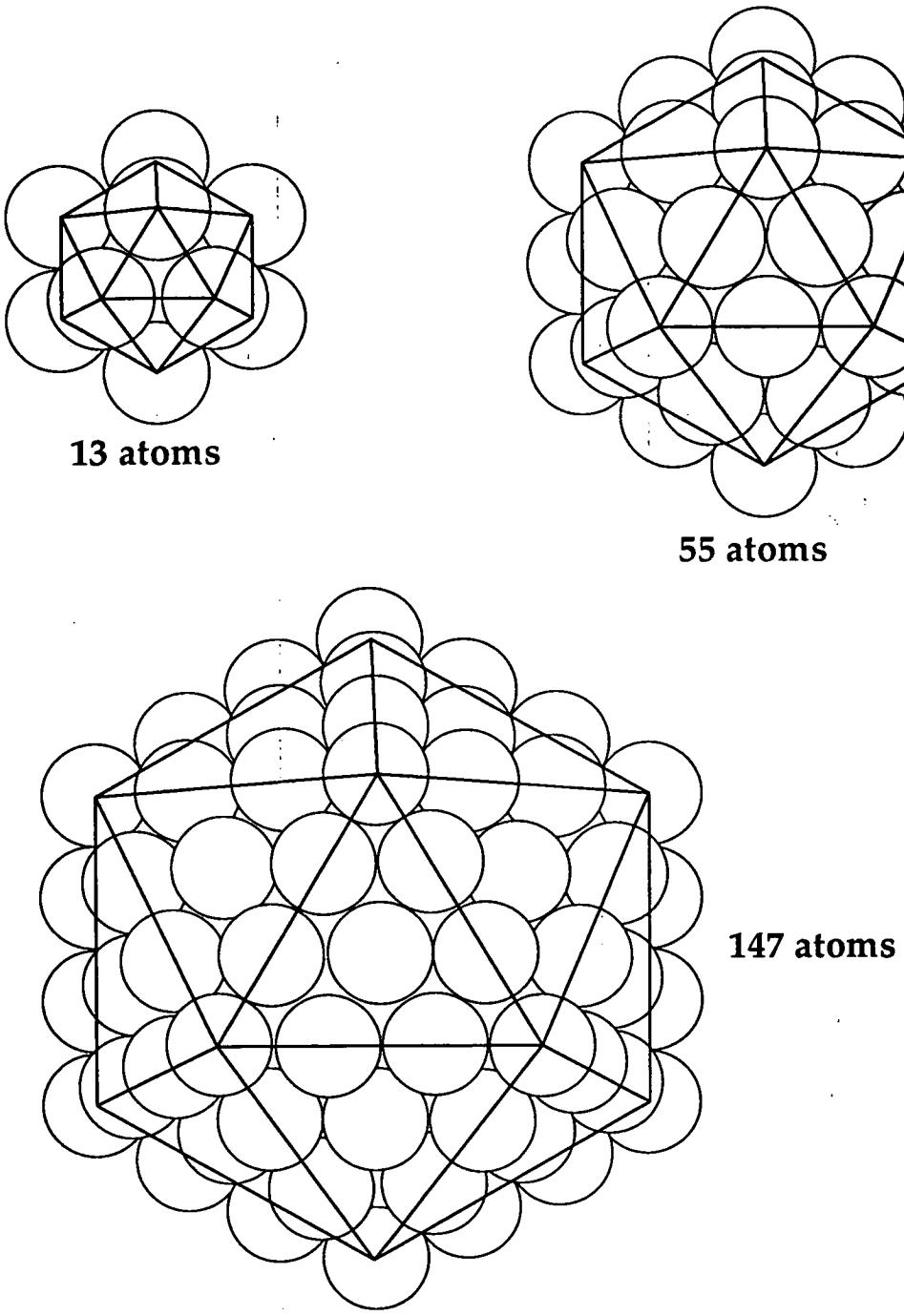

Figure 4–4: The structures of the first three Mackay icosahedral shells.

The general structure can be described as a five-fold symmetrical shape consisting of twenty close-packed, face-centred cubic tetrahedra which share a single vertex. The symmetry is preserved by a slight distortion from the tetrahedral angles, but the strain produced is virtually negligible [30].

The extension from specifically stable geometries to 'geometric shells' comes about when considering the cluster growth sequence. If one considers a growing metal aggregate when it exists in a stable geometry, a Mackay icosahedron for example, one can see that if atoms are continually added to the surface sites of the cluster, then the next largest icosahedron will eventually result. This occurs when a complete 'shell' of atoms has been added, allowing the metal particle to regain the complete symmetry of the icosahedron. So a shell of atoms is defined as one layer arranged on the surface of a cluster such that the newly formed cluster has the same overall outer symmetry as the original cluster [14]. The picture for some types of geometry is not as simple, however. If one considers an octahedron, for instance, only four of the eight faces must be covered to produce the next largest octahedron. Thus for some structures we must consider these 'irregular shells', as they are called. From a wealth of experimental evidence, however, it does seem that the icosahedron is the preferred geometry assumed by many cluster systems, and this symmetric structure does have a maximised binding energy in comparison with alternate geometries [31].

The observation of geometric structure in cluster systems again relies on the fact that complete shells should possess a greater degree of stability than aggregates whose outer surface is an incomplete shell. In the type of experiment described in this thesis, the geometric stabilities are inferred from high intensity mass spectral peaks. This has to do with the bonding sites on the surface of a cluster. A completed symmetrical structure will have no terraces, steps or kinks, and the overall binding energy of the system will be high. An incomplete shell contains atoms which are less strongly bound, which can be evaporated easily during a laser ionisation/fragmentation process. Geometrically stable species can also be identified by their distinctly different reactivities to certain molecules when compared with open shell clusters.

It is apparent that incomplete shells should also exhibit different degrees of stability depending on the structure. This leads to the concept of 'subshells', analogous to the minor shell features observed in the electronic shell regime. Thus an icosahedron will readily lose a spare surface-bound atom if this is a singular protrusion, but will be slightly more resistant to single-atom evaporation if a complete triangular face has been covered with metal atoms. With reference to the octahedron, four triangular faces must be covered to create a completed geometric shell, but minor islands of stability are attained when each single triangular surface is fully covered with atoms. The strength of these subshell stabilities is obviously dependent on the particular system, and the magic numbers will sometimes, but not always, reflect the completion of these subshells.

A generic model has been developed to show how these shell completions are spaced [32], and this incorporates these subshell effects. An extrapolation from two-dimensional examples provides an easier way of visualising what is happening in the three-dimensional case.

If one extends this picture to partially metallic heterocluster systems, and to non-metallic clusters, there is an increase in the range of stable geometries possible. These are compact structures, but not technically geometric shells. One famous example is that of buckminsterfullerene. Carbon happens to cluster preferentially with sixty atoms into a truncated icosahedral cage [33]. This is the most stable carbon cluster, although others also have a high degree of stability (such as C_{70}, C_{84}, etc.). The study of these species has now blossomed into a whole new separate area of research, and will not be discussed in detail here. With respect to heteroclusters, ionic species have been shown to be exceptionally stable when they form complete face-centred cubic structures. In a similar manner to the general geometric shells discussed above, these systems are more stable if they have no excess surface atoms, kinks or terraces.

The existence of all of the above systems, along with electronically stable clusters is totally dependent on the exact system, and some guide as to the explanations for certain magic number observations is given in the next section.

4.4 Magic Numbers of Real Cluster Systems

In this section, examples of the shell structure actually observed for specific cluster systems will be given, as well as a description of other aggregates which exhibit magic numbers not attributable to shell effects. With respect to shells, one important point to discuss is how to distinguish between the several different manifestations of the shell effects. Another question which will be dealt with concerns the cross-over between electronic and geometric shells. It is important to know if these effects are mutually exclusive, and if so the reasons why one type of effect would be favoured over the other. If both effects can exist in the same system it is useful to have some idea as to which conditions or cluster sizes promote the occurrence of each effect.

A series of magic numbers can be obtained from the mass spectra of many cluster species, simply by noting which clusters have anomalously high or low intensities (depending on the experimental conditions). Whether these magic numbers actually correspond to real shell effects is an important question. It may be possible to look at a series of magic numbers and to say that they may well be an experimental artefact, or attributable to some complex phenomenon which has not yet been suitably modelled. However, there is a general way in which anomalously stable clusters can be assigned to a specific shell effect, regardless of whether electronic or geometric stability is being manifested.

It turns out that all shell effects occur at roughly equal intervals on an $n^{\frac{1}{3}}$ scale, where n is the number of atoms in the cluster. The actual spacing is characteristic of the type of shell effect being exhibited. For geometrically stable structures the successive shells are obviously formed by completing a surface layer of atoms as described earlier. This results in the growth of the cluster by a shell with a width approximately equal to the interatomic distance. The total radius of the cluster is proportional to the cube root of the number of constituent atoms. Successive electronic shells also occur as the growing cluster radius increases by one unit of a

characteristic length, which in this case is related to the wavelength of an electron in the Fermi level.

To decide on whether a specific series of magic numbers for a cluster system belongs to an electronic or to a geometric stability is, in principle, quite straightforward. If the cluster species exhibit magic numbers which are independent of the charge state of the clusters, then geometric stability is the underlying effect. If clusters are doubly-ionised for instance, then magic numbers due to electronic shell effects would shift to different cluster sizes, so that the stable systems still contained full electronic shells.

It is reasonably straightforward to differentiate between alternate stable geometries, or between electronic and geometric stability if the preparation of clusters in differing charge states is not possible. This can be done by calculating the actual spacing of the magic numbers on an $n^{\frac{1}{3}}$ scale. If each successive shell closing (magic number) is denoted by a singularly increasing integer number known as the shell index, then this number can be plotted against the cube root of the number of atoms in the cluster. This plot results in a straight line which has a gradient indicative of the specific shell effect present for that cluster system. The gradient can be easily compared with the gradients expected for different geometric stabilities or for an electronic shell effect, and the appropriate source identified. Occasionally this gradient will not immediately match any known shell effect until subshells are accounted for. A good example of this can be gained by looking at icosahedral stability. The number of atoms, n, in a cluster made up of K icosahedral shells is given by

$$n = \frac{1}{3}\left(10K^3 - 15K^2 + 11K - 3\right) \tag{4.3}$$

which can be factored to give

$$n = \frac{10}{3}\left(K - \frac{1}{2}\right)^3 + \frac{7}{6}\left(K - \frac{1}{2}\right) \tag{4.4}$$

Since the shell index is an arbitrary integer one can remove the quadratic dependence by substituting k in place of $K - \frac{1}{2}$. This leads to a simplified relationship between the number of cluster atoms and the approximated shell index:

$$n = \frac{10}{3}k^3 + O(k) \tag{4.5}$$

This gives the gradient expected from a plot of the effective shell index against the cube root of the number of constituent atoms.

Now if subshells are included, then each shell index k actually becomes a subshell index, $\hat{k}$, which occurs more frequently. Each shell is broken down into a specific number of subshells, which depend on the cluster geometry and experimental conditions. For an icosahedron one can imagine stable subshells occurring when a triangular face is completely covered, or when a pentagonal cap of the icosahedron is filled. These two cases would give rise to twenty or to four subshells, respectively, within each complete geometric shell, so that one can replace k in the above equation by $\frac{1}{20}\hat{k}$ or by $\frac{1}{4}\hat{k}$. This would lead to a different gradient for the shell index plot, hopefully elucidating the shell effect origin for the system studied. In the case of geometric shell effects, Martin has calculated the shell index gradients expected from most of the permitted three-dimensional geometries [32].

4.4.1 Non-shell systems

Before giving an idea as to what cluster systems are likely to conform to each type of shell effect it is important to note that certain systems may exhibit magic numbers which cannot be accounted for by either model. A prime example of this is the fact that clusters of silicon containing 6, 10, 16, and 32 atoms appear as magic numbers in the mass spectrum [34,35]. The pronounced stability of these species is governed by the covalent bonding between the silicon atoms in the cluster. The structures formed are strongly determined by the directionality of the bonding in the system, which can be described as a 'network cluster'. This is in contrast with close-packing or near close-packing structures which conform to geometric shells.

Another type of system which exhibits magic numbers not linked to one of the shell effects is the fcc-type (face-centred cubic) crystalline structure. The specific layout of these frameworks again depends on bonding, though in this case ionic. The alkali halide clusters that have been studied have shown evidence of magic numbers which correlate well with fcc structures. The mass spectra of

these species have shown that, once ionised, they primarily exist with the formula $M(MX)_n^+$. These structures were predicted to be energetically favourable for alkali halide clusters [36], a result which was confirmed experimentally initially for NaCl clusters [37,38], and then for clusters of NaI, CsCl, and CsI [39]. It is not surprising that the sodium-containing clusters show a preference for an fcc framework as the bulk crystals are face-centred cubic. However, the clusters incorporating caesium atoms also proved to be particularly stable for complete fcc cubes, even though the bulk crystal structure is body-centred cubic (bcc). This fitted with Martin's earlier premise that all small crystalline clusters would adopt an fcc structure until they reached some critical size at which a phase transition could occur, if necessary, allowing a conversion to the bcc structure in appropriate cases [40].

Latterly, other mixed aggregates have been shown to exhibit a preference for structures based on the cubic lattice. These have included MgO clusters [41] and TiN clusters [42]. In all of the above cases, local stabilities are also observed for completed terraces on the surface of the exceptionally stable closed cuboid structures. These are analogous to subshells within the closed cubic shells, although this terminology does not technically belong to descriptions of these crystalline arrangements.

4.4.2 Systems with electronic shells

As described earlier, the cluster systems which best fit the electronic shell model are the alkali metals which possess strongly delocalised valence electrons. Sodium was the first metal for which the shell effects were observed in cluster abundance spectra [5]. The range of sizes of sodium clusters observed has gone from modest beginnings spanning only a handful of electronic shells [43], through to clusters containing enough electrons to show evidence of supershell structure [15,27]. These experiments have shown the existence of electronic shells in 3000-atom sodium clusters. The appearance of these effects is not restricted to cluster abundance mass spectra and ionisation potential measurements. An interesting study has shown that for sodium clusters containing between one hundred and eight hundred

atoms, those with completely filled electronic shells are noticeably less reactive towards oxygen molecules than clusters with open shells [44].

The observation of electronic shells has been extended to other metals in the first group of the periodic table, as expected due to the nearly-free electron behaviour in these species. Similar electronic shell effects have been observed for potassium [43], rubidium [45], and caesium clusters [46]. The emergence of periodic structure due to the grouping of electronic states has also been observed in lithium clusters large enough to give further credence to the existence of electronic supershells [47].

For clusters of a specific group, in this case the alkali metals, the general trend is for the electronic shell effects to become less pronounced as one goes down the group. This is due to the fact that the elements of higher atomic number have more electronic levels to be squeezed into the cluster potential. The grouping of the levels still occurs, but the spacing between the bunches of fermion states is reduced leading to less prominent shell effects.

Having seen that electronic shell structure dominates many properties of the alkali metals, an obvious question to consider is which other systems might display similar behaviour. A logical guess would be the coinage metals as they also possess one valence electron per atom. In fact, experiments have shown that copper, silver, and gold clusters all possess the same electronic shell structure as the alkali metals, exhibiting the appropriate magic numbers in abundance spectra [9,48], ionisation potentials [49,50], and electron affinities [51,52]. From the similarities between the coinage and alkali metals, it would seem that the *d*-electrons in the coinage metals do not perturb the cluster systems greatly with respect to shell structure. These electrons can be thought of as core electrons which contribute to the overall ionic potential, but leave the system in a state resembling the single free electron alkali metal aggregates.

The next logical question to consider is whether the electronic shell model can be used to describe divalent systems. Each group-II metal atom should contribute two electrons to the jellium potential so that filled electronic shells should occur for clusters containing half the number of atoms as for closed-shell alkali metal

clusters. Several of these predicted magic numbers do occur in the abundance spectra and ionisation potentials of zinc and cadmium clusters [9,53], although this is far from the complete picture. Other reproducible intensity anomalies occur in these mass spectra which do not fit with predicted electronic shell behaviour. Even more perplexing is the fact that none of the Group-IIA metal clusters show any sign of electronic shell effects at all. Does this mean that the jellium model can only be applied to univalent systems?

The answer to that question is - not necessarily. The difficulties inherent in extending this model to the divalent metals arise from the difference between the atomic and bulk electronic structures of these elements. This directs our attention towards one of the crucial areas of cluster research, that of the general evolution of electronic and metallic properties as the bulk material is approached. The problem for group-II species is that the bulk metallic properties exist due to the overlap of the s and p bands. These bands evolve from distinct electronic levels which begin to hybridize as the cluster grows. However, until hybridization is complete, these clusters are not technically metals. For mercury clusters, for instance, the hybridization occurs so slowly that only van der Waals forces hold together the smallest clusters [54]. For cadmium and zinc these effects should not be as great, but may still cause some deviation from the electronic shell structure. The magic numbers exhibited by the Group-IIA metal clusters will be discussed in detail in Chapter 6 of this thesis. It is sufficient for the moment to say that they have as yet shown no experimental evidence of electronic shell effects.

Perhaps, then, trivalent metals may prove to be successful candidates, with each atom presenting three valence electrons to the cluster? Indeed, the first experiments on aluminium clusters showed agreement with the jellium model in which each atom did contribute three quasi-free electrons to move within the bounds of the cluster. The size ranges studied were from 10 to 400 atom clusters [55,56]. However, for clusters containing less than 250 atoms there were several mass spectral features which could not be explained with reference to the proposed electronic shell effects. A possible explanation for this has been formulated based on further experiments, and is discussed towards the end of this chapter. The elec-

tronic shell behaviour of aluminium aggregates has also showed up in ion mobility experiments [57]. In these studies, the arrival time distributions for cluster ions are measured following passage through a collision gas cell under the influence of an electric field. Clusters with more compact structures travel more quickly through the collision gas cell. It was found that closed-shell aluminium clusters had enhanced mobilities, providing additional support for the predicted spherical nature of species with filled electronic shells.

Another trivalent metal that has been studied more recently is indium, which has been shown to fit the electronic shell structure well, even better than aluminium in fact [58]. Again, the reason for this is discussed later in this chapter. Some recent results on gallium have also shown evidence of electronic shell effects [59].

The cluster systems mentioned in this section appear to be the only ones which show clear evidence of electronic shell structure. Obviously, the requirement is for a metal which can provide a source of delocalised electrons. The transition metals are too complex to fit such a simple model. The d and f electrons alter the relevant electronic properties of the associated clusters, giving rise to systems totally dissimilar to the free electron systems characteristic of species which fit the electronic shell model.

An interesting point to note, however, is the appearance of regular electronic shell features in the mass spectra of alloy clusters of copper, silver and indium [60]. The closed shells still appear for clusters containing the requisite number of electrons, although each indium atom supplies three electrons to the cluster, whilst the coinage metal atoms donate one electron each.

Thus, one can see that the electronic shell model helps to explain many features which result from metal cluster experiments. The alkali metals fit best, as they possess valence electrons which can be described as almost free, moving within the potential generated by the effectively unstructured positive background of the cluster. There has been some success with the application of the jellium model to divalent and trivalent metals, although some extra features are seen to occur which

suggest a required modification to the shell model, or an alternative contribution which is affecting the stability of specific clusters.

4.4.3 Systems with geometric shells

Icosahedral packing was first observed for clusters of rare gas atoms. Intensity anomalies in the mass spectrum of xenon clusters were attributed to the stability of an icosahedral arrangement of the atoms [61]. The range of rare gas clusters fitting this picture of icosahedral shells has been extended experimentally to include argon and krypton [62,63,64,65]. Supporting evidence for the existence of 5-fold icosahedral symmetry in these systems has been provided by electron diffraction experiments [66]. The symmetric geometries assumed by rare gas clusters must be driven to a great extent by the relatively short-range atom-atom interaction potentials. An icosahedral structure allows the maximum number of atom-atom bonds, and is therefore the favoured structure for clusters smaller than some critical size at which the bulk crystalline arrangement becomes prevalent. Icosahedral structure has also been invoked to describe the stability of argon clusters containing a central aluminium atom [67].

This highly stable geometric structure is not confined in its application to rare gas species. Several papers have shown that various transition metals also form icosahedra, specifically nickel [68] and cobalt [69]. It may be expected, perhaps, that molecular clusters would form icosahedral shapes as they are bound by short-range van der Waals forces. This has been shown to be true for benzene molecules which cluster icosahedrally around a central dimer unit [70].

An excellent experiment by Martin's group has shown that icosahedral arrangements of fullerene molecules are particularly stable [71]. This study provides a good example of the variety of difficulties encountered in these types of experiment. The first problem is to try and ionise the fullerene clusters without fragmenting the individual molecules. Laser energies at the ionisation threshold are used, although the wavelength must be chosen carefully, taking into account the relative magnitude of the photon absorption cross-section when compared with

the ionisation cross-section. To actually observe the icosahedral nature of these clusters they must be allowed to thermodynamically achieve the most stable arrangements. If the cluster source is too cold the mass spectrum will remain largely unstructured. To overcome this another low power laser pulse is used to heat the clusters prior to the ionisation event, allowing molecular evaporation to proceed until the most stable clusters are reached which will then show up with enhanced intensity in the mass spectrum.

4.4.4 Shell competition

Examples of systems in which cluster magic numbers can be ascribed to either of the two shell effects have now been given. Are these cluster species so different that each effect will occur exclusively in a particular type of system? Certainly, the electronic shell effect must be limited in its application to clusters which fit the conditions required by the jellium model. As suggested earlier, the primary requirement is for clusters which can be described as having effectively delocalised electrons. With respect to geometric shells, however, there is no real reason to dismiss the possibility of the extension of this effect to cover most cluster systems in the right circumstances. In actual fact, it can be seen from the literature that some systems do exhibit both effects, either in different size regimes, or under alternate experimental conditions. The improvement in detection systems and cluster generation techniques has allowed the study of a vast size range of cluster species. On examination of sodium clusters containing up to 22000 atoms, Martin's group noticed that geometric shell effects were dominant [72]. This was in contrast to the electronic shell effects previously noticed for sodium clusters containing up to 3000 atoms. The magic numbers corresponding to geometric shell closings were representative of either icosahedral or cuboctahedral structure. These two structures happen to contain the same numbers of atoms for completed shells. They can only be distinguished by differences in subshell structure as the cluster grow, but the resolution in their experiment was not sufficient to allow the observation of geometric subshells. From previous examples, however, the icosahedral structure does seem to be the favoured geometry. The reasons for a transition from elec-

tronic to geometric shells have not been fully resolved as yet. Martin has proposed that smaller clusters are more liquid-like and mobile, so that spherical geometries can be assumed when required for a completed electronic shell. The larger clusters are thought to be more rigid, only allowing atoms to condense onto specific surface sites, and thus emphasising geometric stabilities over electronic effects [73].

The existence of the two shell effects in one cluster system is not always characterised by the appearance of each effect in a different size regime. In a study on copper clusters it was found that electronic shell effects and icosahedral structure could be observed over the same size range, but under different experimental conditions [74]. It seems reasonable that geometric effects would be more important for copper clusters than for alkali metal clusters due to the higher cohesive energies for the noble metal species. The study in question showed that copper clusters containing less than 100 atoms showed evidence of icosahedral geometries on reaction with water molecules. However, reaction of copper clusters over the same size range with oxygen molecules showed up electronic stabilities. The differences here can be attributed to the different types of reaction taking place. The O_2 reaction probably involves dissociative chemisorption which is promoted by electron transfer from the cluster. Obviously, the promoted reaction will occur more easily with a cluster having a lower ionisation potential. This is a property of the cluster as a whole, and in this case corresponds with a cluster having a newly-opened electronic shell. On the other hand, it is suggested that the H_2O reaction is more localised, and thus reflects the geometric structure of the reacting cluster. Overall, one can see that each cluster must be treated separately to determine whether geometric or electronic stability is more important. Furthermore, the root cause of a particular stability is not solely dependant on the properties of the cluster system itself, but also on the experimental interactions taking place.

An interesting case study on the assignment of mass spectral magic numbers is presented for large aluminium cluster systems. A periodic shell effect was observed for aluminium clusters containing between 200 and 1500 atoms [75,76]. The shell index plot for these magic numbers resulted in a gradient a factor of two larger than that expected from the electronic shell model. This was interpreted by suggesting

that the electrons traversed a semi-classical star orbit within the cluster. The electrons thus travel a path approximately twice as long as the one-turn triangular and square orbits normally favoured. This interpretation would also lead to the prediction that larger clusters would eventually show evidence of the triangular orbit again as the electrons spent less time at the cluster surface.

A subsequent study has shown that this shell spacing continues up to 10000-atom aluminium clusters, throwing doubt on the electronic shell description initially formulated [77]. A very good match for the shell index gradient was found when the aluminium clusters were pictured as being constructed in the form of octahedra. In a similar way to icosahedral shells, it can be shown that the number of atoms, n, in a cluster of K octahedral shells is given by the expression

$$n = \frac{1}{3}\left(2K^3 + 6K^2 + 7K + 3\right) \tag{4.6}$$

i.e.

$$n = \frac{2}{3}(K+1)^3 + \frac{1}{3}(K+1) \tag{4.7}$$

Substituting $k = K + 1$ results in the expression simplifying to

$$n = \frac{2}{3}k^3 + O(k) \tag{4.8}$$

From Figure 4–5 it can be seen that coverage of only four of the eight octahedral faces is required to arrive at the next complete shell. If subshell stability is achieved by the coverage of a single face, then the subshells occur four times as often as the shells, so k can be replaced by $\frac{1}{4}\hat{k}$. This leads to the above expression simplifying to

$$n \approx \frac{1}{96}\hat{k}^3 = 0.01042\hat{k}^3 \tag{4.9}$$

The experimentally obtained shell index plot fits the expression $n = 0.0104\hat{k}^3$, thus lending weight to the octahedral structure attributed to large aluminium clusters.

The most recent experiments on large aluminium clusters have shown that the distinction of the two shell effects is definitely temperature related. The aluminium

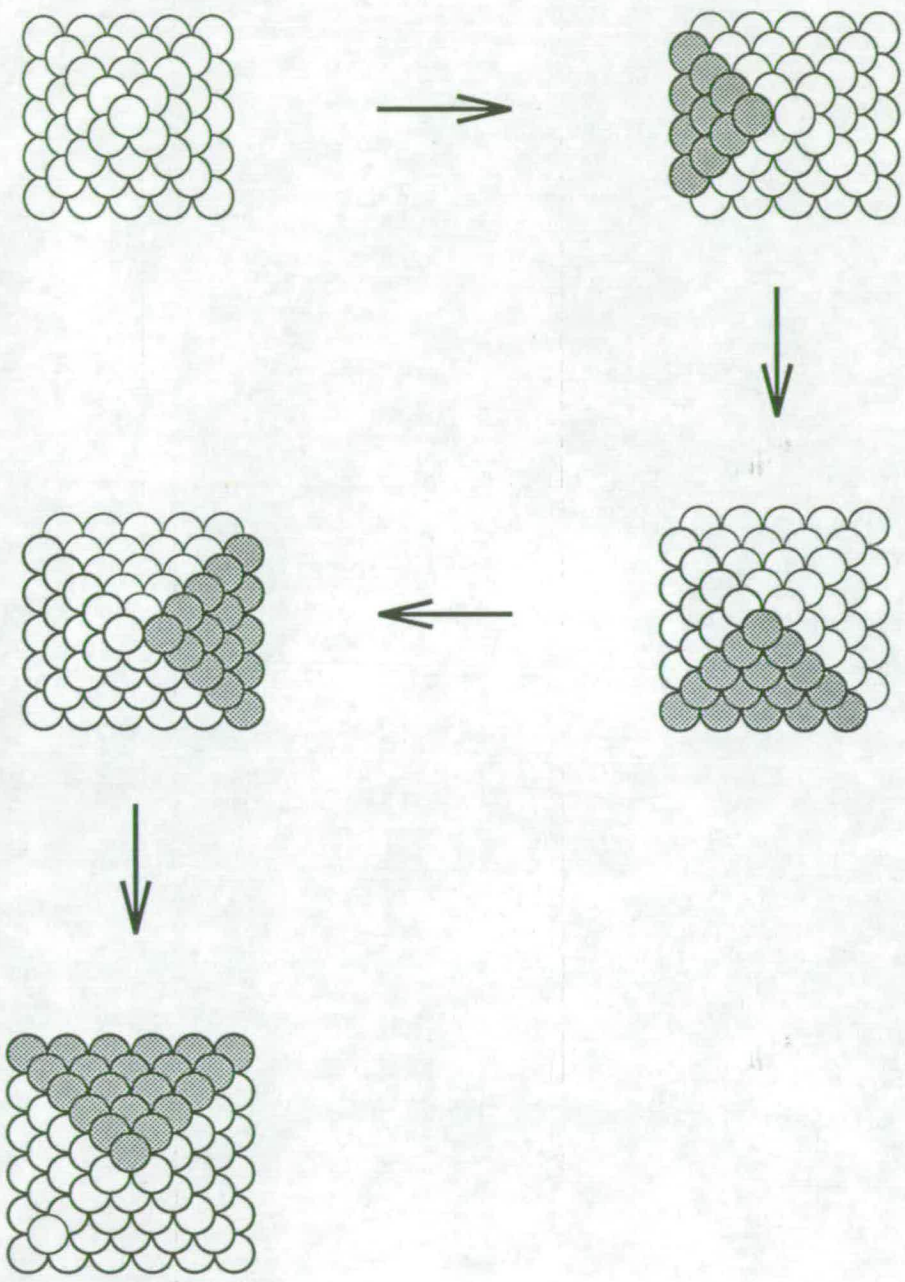

Figure 4–5: The breakdown of octahedral shells into subshells by step-wise coverage of triangular faces.

clusters produced in the experiment showing octahedral structure are expected to exist at temperatures close to the nozzle temperature, which was about 300K. The melting point of bulk aluminium is 933K, so even the clusters are expected to be solid-like. Heating the nozzle to approximately 470K resulted in the appearance of electronic shells for clusters containing between 200 and 600 aluminium atoms, with the same shell spacing as for alkali metal clusters [78]. The transition between electronic and geometric shells was seen clearly as the temperature in the source was varied. This general transition between the two shell effects had been predicted earlier [79], but the experimental manipulation of this transition is an exciting achievement in cluster research.

In summary, in this chapter an attempt has been made to discuss the diverse range of cluster systems which can be, and have been studied. The magic numbers observed have been attributed to realistic models, and these have been described generally. It would be impossible to provide an exhaustive account of all of the research which has been carried out in this area, but even a look at some general systems shows that this is an exciting avenue of research.

Bibliography

[1] M.G. Mayer and J.H.D. Jensen, '*Elementary Theory of Nuclear Shell Structure*', Wiley, New York, 1955.

[2] M.G. Mayer, Phys. Rev., **75** (1949) 1969L.

[3] O. Haxel, J.H.D. Jensen and H.E. Suess, Phys. Rev., **75** (1949) 1766L.

[4] R.M. Eisberg, '*Fundamentals of Modern Physics*'. Wiley, New York, 1967.

[5] W.D. Knight, K. Clemenger, W.A. de Heer, W.A. Saunders, M.Y. Chou and M.L. Cohen, Phys. Rev. Lett., **52** (1984) 2141.

[6] N.W. Ashcroft and N.D. Mermin, '*Solid State Physics*', Holt, Rinehart and Winston, New York, 1976.

[7] M. Brack, Rev. Mod. Phys., **65** (1993) 677.

[8] W.A. de Heer, W.D. Knight, M.Y. Chou and M.L. Cohen, Solid State Phys., **40** (1987) 93.

[9] I. Katakuse, T. Ichihara, Y. Fujita, T. Matsuo, T. Sakurai and H. Matsuda, Int. J. Mass Spectrom. Ion Proc., **69** (1986) 109.

[10] W. Ekardt, Ber. Bunsenges. Phys. Chem., **88** (1984) 289.

[11] R.D. Woods and N.D. Saxon, Phys. Rev., **95** (1954) 577.

[12] H. Nishioka, K. Hansen and B.R. Mottelson, Phys. Rev. B, **42** (1990) 9377.

[13] E.C. Honea, M.L. Homer, J.L. Persson and R.L. Whetten, Chem. Phys. Lett., **171** (1990) 147.

[14] T.P. Martin, T. Bergmann, H. Göhlich and T. Lange, J. Phys. Chem., **95** (1991) 6421.

[15] T.P. Martin, S. Bjornholm, J. Borggreen, C. Bréchignac, P. Cahuzac, K. Hansen and J. Pedersen, Chem. Phys. Lett., **186** (1991) 53.

[16] M. Pellarin, B. Baguenard, M. Broyer, J. Lermé and J.L. Vialle, J. Chem. Phys., **98** (1993) 944.

[17] H.A. Jahn and E. Teller, Proc. R. Soc. London Ser. A, **161** (1937) 220.

[18] K. Clemenger, Phys. Rev. B, **32** (1985) 1359.

[19] M.L. Cohen, M.Y. Chou, W.D. Knight and W.A. de Heer, J. Phys. Chem., **91** (1987) 3141.

[20] W.A. de Heer, Rev. Mod. Phys., **65** (1993) 611.

[21] J. Tiggesbäumker, L. Köller, H.O. Lutz and K.H. Meiwes-Broer, Chem. Phys. Lett., **190** (1992) 42.

[22] R. Balian and C. Bloch, Ann. Phys., **69** (1971) 76.

[23] S. Bjornholm, Contemporary Phys., **31** (1990) 309.

[24] S. Bjornholm, J. Borggreen, O. Echt, K. Hansen, J. Pedersen and H.D. Rasmussen, Phys. Rev. Lett., **65** (1990) 1627.

[25] O. Genzken, M. Brack, E. Chabanat and J. Meyer, Ber. Bunsenges. Phys. Chem., **96** (1992) 1217.

[26] O. Genzken and M. Brack, Phys. Rev. Lett., **67** (1991) 3286.

[27] J. Pedersen, S. Bjornholm, J. Borggreen, K. Hansen, T.P. Martin and H.D. Rasmussen, Nature, **353** (1991) 733.

[28] R. Van Hardeveld and F. Hartog, Surface Sci., **15** (1969) 189.

[29] A.L. Mackay, Acta Cryst., **15** (1962) 916.

[30] M.R. Hoare, Adv. Chem. Phys., **40** (1979) 49.

[31] B.W. van de Waal, J. Chem. Phys., **98** (1993) 4909.

[32] U. Näher, U. Zimmermann and T.P. Martin, J. Chem. Phys., **99** (1993) 2256.

[33] H. Kroto, J.R. Heath, S.C. O'Brien, R.F. Curl and R.E. Smalley, Nature, **318** (1985) 162.

[34] L.A. Bloomfield, R.R. Freeman and W.L. Brown, Phys. Rev. Lett., **54** (1985) 2246.

[35] J.C. Phillips, J. Chem. Phys., **83** (1985) 3330.

[36] T.P. Martin, Phys. Reports, **95** (1983) 167.

[37] R. Pflaum, K. Sattler and E. Recknagel, Chem. Phys. Lett., **138** (1987) 8.

[38] C.W.S. Conover, Y.A. Yang and L.A. Bloomfield, Phys. Rev. B, **38** (1988) 3517.

[39] Y.J. Twu, C.W.S. Conover, Y.A. Yang and L.A. Bloomfield, Phys. Rev. B, **42** (1990) 5306.

[40] T.P. Martin, J. Chem. Phys., **69** (1978) 2036.

[41] P.J. Ziemann and A.W. Castleman Jr., J. Chem. Phys., **94** (1991) 718.

[42] Z.Y. Chen and A.W. Castleman Jr., J. Chem. Phys., **98** (1993) 231.

[43] M.M. Kappes, M. Schär, P. Radi and E. Schumacher, J. Chem. Phys., **84** (1986) 1863.

[44] T. Lange, H. Göhlich, U. Näher and T.P. Martin, Ber. Bunsenges. Phys. Chem., **96** (1992) 1109.

[45] N.D. Bhaskar, R.P. Frueholz, C.M. Klimcak and R.A. Cook, Phys. Rev. B, **36** (1987) 4418.

[46] H. Göhlich, T. Lange, T.Bergmann and T.P. Martin, Phys. Rev. Lett., **65** (1990) 748.

[47] C. Bréchignac, P. Cahuzac, M. de Frutos, J.P. Roux and K.Bowen, '*Physics and Chemistry of Finite Systems: From Clusters to Crystals*' (ed. P. Jena *et al.*), Vol I, Kluwer Academic, Dordrecht/Boston, 1992.

[48] I. Katakuse, T. Ichihara, Y. Fujita, T. Matsuo, T. Sakurai and H. Matsuda, Int. J. Mass Spectrom. Ion Proc., **67** (1985) 229.

[49] G. Alameddin, J. Hunter, D. Cameron and M.M. Kappes, Chem. Phys. Lett., **192** (1992) 122.

[50] M.B. Knickelbein, Chem. Phys. Lett., **192** (1992) 129.

[51] C.L. Pettiette, S.H. Yang, M.J. Craycraft, J. Conceicao, R.T. Laaksonen, O, Cheshnovsky and R.E. Smalley, J. Chem. Phys., **88** (1988) 5377.

[52] K.J. Taylor, C.L. Pettiette-Hall, O. Cheshnovsky and R.E. Smalley, J. Chem. Phys., **96** (1992) 3319.

[53] M. Ruppel and K. Rademann, Chem. Phys. Lett., **197** (1992) 280.

[54] K. Rademann, B. Kaiser, U. Even and F. Hensel, Phys. Rev. Lett., **59** (1987) 2319.

[55] K.E. Schriver, J.L. Persson, E.C. Honea and R.L. Whetten, Phys. Rev. Lett., **64** (1990) 2539.

[56] J.L. Persson, R.L. Whetten, H.P. Cheng and R.S. Berry, Chem. Phys. Lett., **186** (1991) 215.

[57] M.F. Jarrold and J.E. Bower, J. Chem. Phys., **98** (1993) 2399.

[58] B. Baguenard, M. Pellarin, C. Bordas, J. Lermé, J.L. Vialle and M. Broyer, Chem. Phys. Lett., **205** (1993) 13.

[59] M. Pellarin, B. Baguenard, C. Bordas, M. Broyer, J. Lermé and J.L. Vialle, Phys. Rev. B (in press).

[60] Y. Yamada and A.W. Castleman Jr., J. Chem. Phys., **97** (1992) 4543.

[61] O. Echt, E. Sattler and E. Recknagel, Phys. Rev. Lett., **47** (1981) 1121.

[62] I.A. Harris, R.S. Kidwell and J.A. Northby, Phys. Rev. Lett., **53** (1984) 2390.

[63] W. Miehle, O. Kandler, T. Leisner and O. Echt, J. Chem. Phys., **91** (1989) 5940.

[64] P.G. Lethbridge and A.J. Stace, J. Chem. Phys., **91** (1989) 7685.

[65] S. Wei, Z. Shi and A.W. Castleman Jr., J. Chem. Phys., **94** (1991) 8604.

[66] J. Farges, M.F. de Feraudy, B. Raoult and G. Torchet, J. Chem. Phys., **84** (1986) 3491.

[67] K.E. Schriver, M.Y. Hahn, J.L. Persson, M.E. LaVilla and R.L. Whetten, J. Phys. Chem., **93** (1989) 2869.

[68] E.K. Parks, B.J. Winter, T.D. Klots and S.J. Riley, J. Chem. Phys., **94** (1991) 1882.

[69] T.D. Klots, B.J. Winter, E.K. Parks and S.J. Riley, J. Chem. Phys., **92** (1990) 2110.

[70] K.E. Schriver, A.J. Paguia, M.Y. Hahn, E.C. Honea, A.M. Camarena and R.L. Whetten, J. Phys. Chem., **91** (1987) 3131.

[71] T.P. Martin, U. Näher, H. Schaber and U. Zimmermann, Phys. Rev. Lett., **70** (1993) 3079.

[72] H. Göhlich, T. Lange, T. Bergmann, U. Näher and T.P. Martin, Chem. Phys. Lett., **187** (1991) 67.

[73] T.P. Martin, T. Bergmann, H. Göhlich and T. Lange, Z. Phys. D, **19** (1991) 25.

[74] B.J. Winter, E.K. Parks and S.J. Riley, J. Chem. Phys., **94** (1991) 8618.

[75] J. Lermé, M. Pellarin, J.L. Vialle, B. Baguenard and M. Broyer, Phys. Rev. Lett., **68** (1992) 2818.

[76] M. Pellarin, J. Lermé, B. Baguenard, M. Broyer, J.L. Vialle and A. Perez, Ber. Bunsenges. Phys. Chem., **96** (1992) 1212.

[77] T.P. Martin, U. Näher and H. Schaber, Chem. Phys. Lett., **199** (1992) 470.

[78] B. Baguenard, M. Pellarin, J. Lermé, J.L. Vialle and M. Broyer, J. Chem. Phys., **100** (1994) 754.

[79] P. Stampfli and K.H. Bennemann, Phys. Rev. Lett., **69** (1992) 3471.

Chapter 5

CLUSTER ABUNDANCE SPECTRA

5.1 Introduction

The main aim of this chapter is to demonstrate the versatility of the laser vaporisation technique, and to show how features in some of the cluster abundance spectra can be rationalised with reference to the shell effects described in the previous chapter. Cluster mass spectra which were obtained for a variety of species during the course of this work are presented here. More detailed data on the cluster abundance spectra obtained for Group-IIA metals and large iron clusters are discussed in detail separately in the following chapters. The results presented in this chapter illustrate the wide range of materials which can be studied with the experimental approach that was employed in this work. The only real limit in the generation of clusters using the laser vaporisation technique is in obtaining or creating an appropriate solid target which will sit in either of the two cluster sources that were described in Chapter 3. The principal features of the cluster mass spectra presented here are discussed, some of which provide insight into various aspects of the experimental techniques employed.

One common feature which is evident in the mass spectra presented is a 'mass windowing' effect. This is a result of the perpendicular ion extraction geometry of the cluster apparatus. The use of a static electric field between the deflection plates in the ion source region means that clusters with different mass-to-charge ratios are deflected by differing amounts. This gives rise to a mass-dependent transmission

function for ions travelling towards the detector. A specific deflection voltage will produce a maximum transmission for cluster ions of a certain mass (assuming equally-charged species). The transmission function tends to tail off smoothly for clusters which are increasingly heavier or lighter than this mass. This is due to clusters either side of this mass range missing the detector at the end of the flight tube as a result of being respectively understeered or oversteered by the deflection field. The centre of this mass window can be shifted up and down the scale range by appropriate alteration of the deflection voltage. The mass window appears in the mass spectrum as a bell-shaped envelope containing the cluster peaks. This transmission function is smooth and wide enough to allow any unusual features in the mass spectrum to be readily distinguished, and thus does not interfere with the identification of cluster magic numbers.

The spectra presented in this thesis were originally recorded experimentally as signal intensities *versus* ion-packet flight times. An existing routine in the control software, THOR, allows straightforward mass calibration of the spectra. This process simply involves measuring the time-of-arrival, t, of known species of recognised mass, m. Two or more peaks are measured and fitted to the function

$$t = a + bm^{\frac{1}{2}} \tag{5.1}$$

which emerges from the Wiley and McLaren equations [1]. A least mean squares fit enables the coefficients, a and b, to be determined which are then used to transform the x-axis from time to mass units.

Mass calibration was aided by the routine appearance of mass spectral peaks which could be easily identified, such as helium and aluminium. The presence of aluminium ions was due to this material being ablated from the cluster source block when grazed by the vaporisation laser beam. The presence of a peak due to helium in the mass spectra is perhaps not surprising as it is the carrier gas used for the cluster beam. The observation of a helium ion signal despite the relatively high ionisation potential of helium was explained when helium pulse profiles were shown in Chapter 2.

5.2 Coinage Metal Clusters

Cluster abundance spectra for the coinage metals copper and silver could be generated relatively easily using bulk targets in the rod source described in Chapter 3. Typical mass spectra obtained using photoionisation at 193 nm are shown in Figures 5–1 and 5–2. The discussion in the previous chapter has alerted our attention to the fact that coinage metal clusters tend to exhibit electronic shell effects in certain circumstances. The mass spectra shown here have noticeably pronounced intensities for the cluster species Ag_n^+ (n = 3, 9) and Cu_n^+ (n = 3, 9, 21). This fits well with the jellium model as these specific clusters have closed electronic shells containing 2, 8, and 20 electrons. Evidence for this type of shell effect in coinage metal clusters has been noted previously via ionisation potential measurements [2, 3,4] and the presence of intensity anomalies in cluster abundance spectra [5].

Superimposed on this electronic shell effect is a remarkably pronounced alternation in the intensity between clusters containing odd and even numbers of constituent atoms. Those cluster ions containing an odd number of atoms appear with greater intensities in the mass spectra. Again, similar differences in the characteristics of even and odd numbered clusters of the coinage metals have been discussed in the literature. The first observation of this effect was noted in ionisation potential measurements of small copper clusters [6]. Further evidence of these odd-even alternations has surfaced in electron affinity measurements [7, 8], and cluster abundance spectra [9]. A clue to the origin of this effect can be gained by noting that similar effects have been reported for alkali metal clusters [10]. This knowledge prompts us to look for a common factor which links the alkali metals with the coinage metals. We have already seen that a jellium model describes clusters of these two groups of elements well, and in a similar way. This is due to the free electron nature of these univalent species. A simple bonding model allows us to see that the odd-even intensity alternations can also be derived from the fact that these metals effectively possess one valence electron each. In the mass spectra presented for copper and silver clusters (Figures 5–1 and 5–2) the

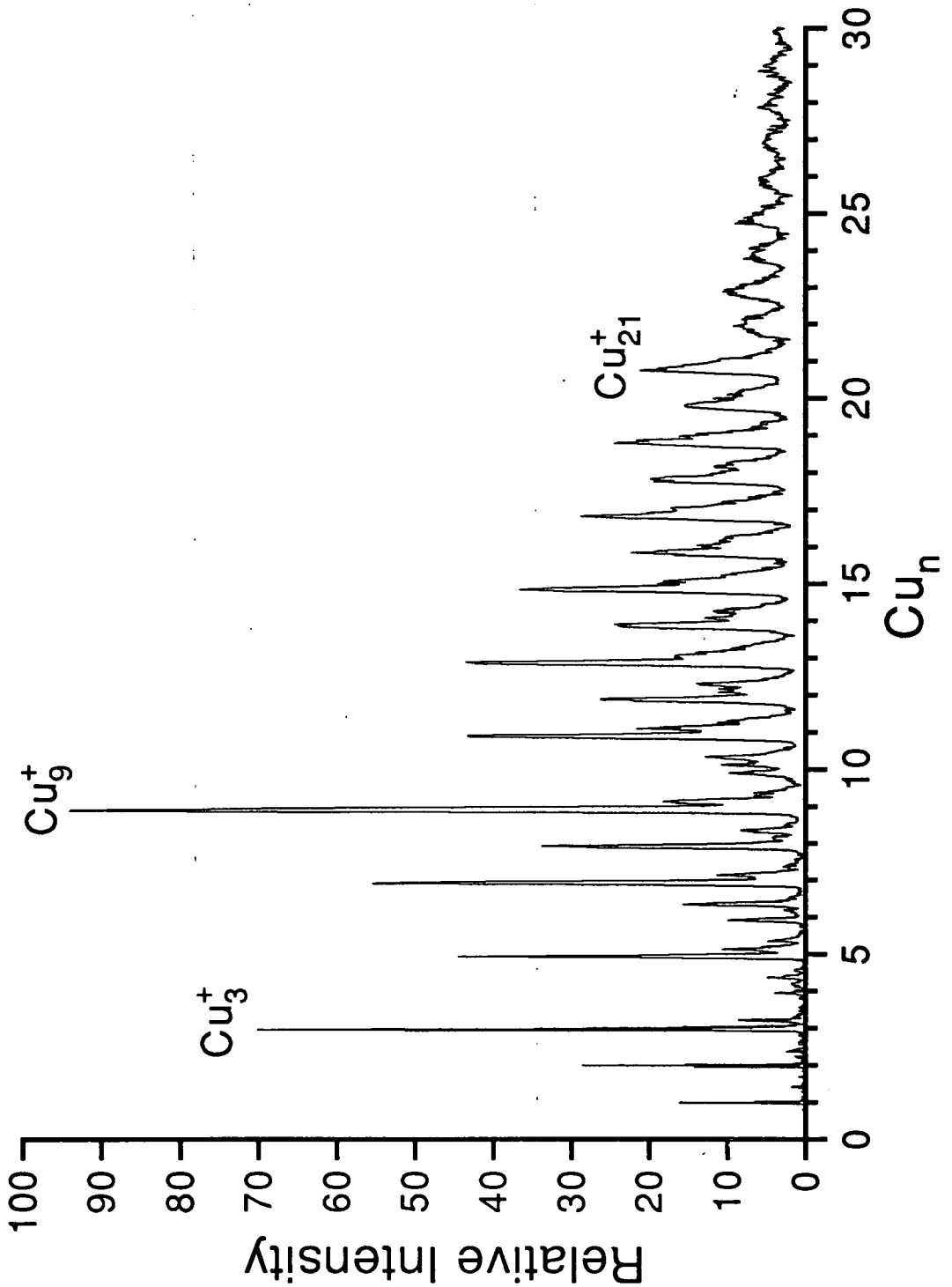

Figure 5–1: A mass spectrum of copper clusters photoionised at 193 nm.

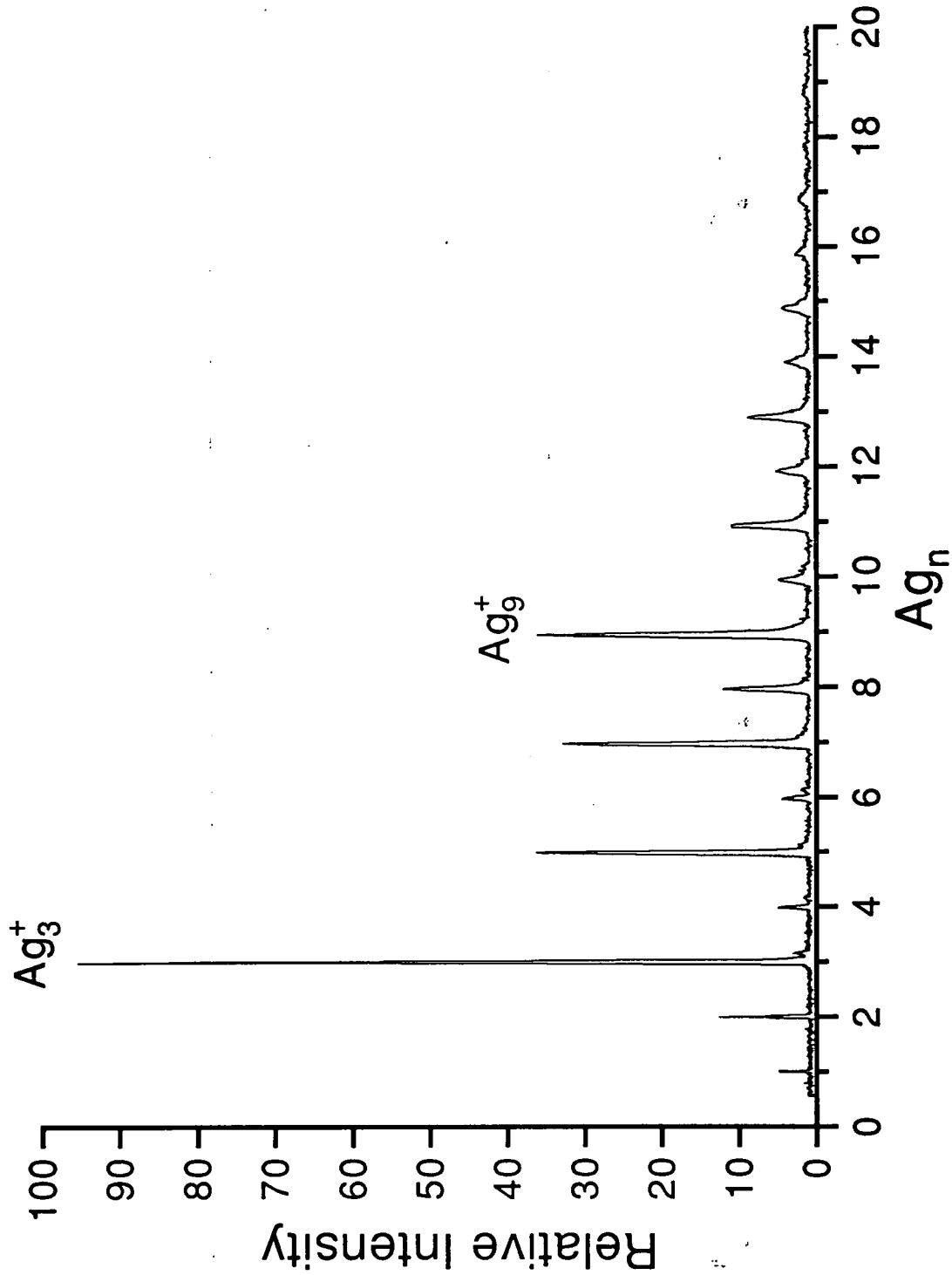

Figure 5–2: A mass spectrum of silver clusters after ionisation with an ArF excimer laser (193 nm).

more intense peaks correspond to clusters containing an even number of electrons. In a simple bonding picture for these species, a spin-pairing of the valence electrons gives rise to a singlet ground state in which the Highest Occupied Molecular Orbital (HOMO) is strongly bound and fully occupied. For clusters containing an odd number of electrons, one electron remains unpaired leading to a doublet ground state. The HOMO in this case is of non-bonding character. It is therefore easier to remove an electron from a neutral cluster originally containing an odd number of electrons. It must be stressed that the odd-even intensity alternation is not linked to the relative stabilities of the neutral clusters. Indeed, ionisation with 157 nm radiation results in a mass spectrum with no such intensity alternation. For copper clusters containing less than seven atoms, the even numbered clusters only ionise on the absorption of two 193 nm photons, whereas the odd-numbered clusters require only one photon of this wavelength to ionise. Thus the odd-even intensity alternation is linked to the photoionisation process rather than the relative abundances of the neutral clusters.

Another feature which emerges from the spectra shown is the presence of larger clusters of copper in comparison to silver. The cluster sizes observable in this type of experiment depend on two main factors, one machine-dependent and the other system-dependent. The first contribution results from the limited voltage applied to the deflection plates in the ion source region of the mass spectrometer. Since the magnitude of the deflection field determines the range of masses transmitted to the detector, then an upper limit on the size of this field naturally corresponds with a maximum observable mass in the cluster distribution. Thus, a larger range of copper clusters will fall within the observable mass region when compared with silver due simply to the fact that copper atoms are lighter than silver atoms.

The system-dependent effect is related to the clustering efficiency of a particular element. This must intuitively be related to the binding strength of the dimer unit, as this is the first species formed in the clustering process, and is the base upon which larger clusters grow [8]. Examination of the available data for dimer bond strengths shows that copper dimer is more strongly bound than the silver dimer

[11]. This is consistent with the observation of larger size clusters for copper than for silver.

A direct comparison of the clustering efficiencies of these two coinage metals could be gained if they were clustered heterogeneously. This experiment necessitated the fabrication of a mixed metal target. The melting point of copper is 1358K, and for silver is 1235K [11]. These values are close enough to make the creation of a metal alloy rod feasible. The actual process involved placing alternate 5mm-long sections of copper and silver rods in a quartz tube which could itself be safely heated to above the melting point of copper whilst retaining its solid shape. The copper and silver segments were melted with an acetylene blowtorch and encouraged to mix. Oxidation of the metal during the heating process was restricted by continuously flowing argon gas over the open end of the quartz tube. The metal in the tube was allowed to solidify, and then melted and agitated again to ensure thorough mixing. After the final solidification step the quartz tube was broken off, and the rod machined down to snugly fit the cluster source block (nominally 5mm-diameter).

Mass spectral analysis of clusters produced when vaporising this mixed metal target showed good signal stability, suggesting that the two metals were homogeneously mixed. The long term stability of the clusters produced was sufficiently good that spectroscopic experiments could be successfully carried out on the CuAg dimer by a former member of this group [12]. A typical mass spectrum of the cluster species generated using this target is presented in Figure 5–3. It is difficult to obtain information easily from this spectrum due to the different cluster combinations which are present. The general trends are more readily apparent when the mass spectral data is displayed in a more simplified format as shown in Figure 5–4. Here the intensities of cluster peaks are plotted against the number of constituent copper and silver atoms in the cluster.

The same general trends observed for the pure coinage metal clusters are also seen here in the heterogeneous clusters. The odd-even intensity alternation exists as before, the effect depending only on the number of constituent atoms, and not on their identities. Additionally, the range of cluster compositions lends weight to

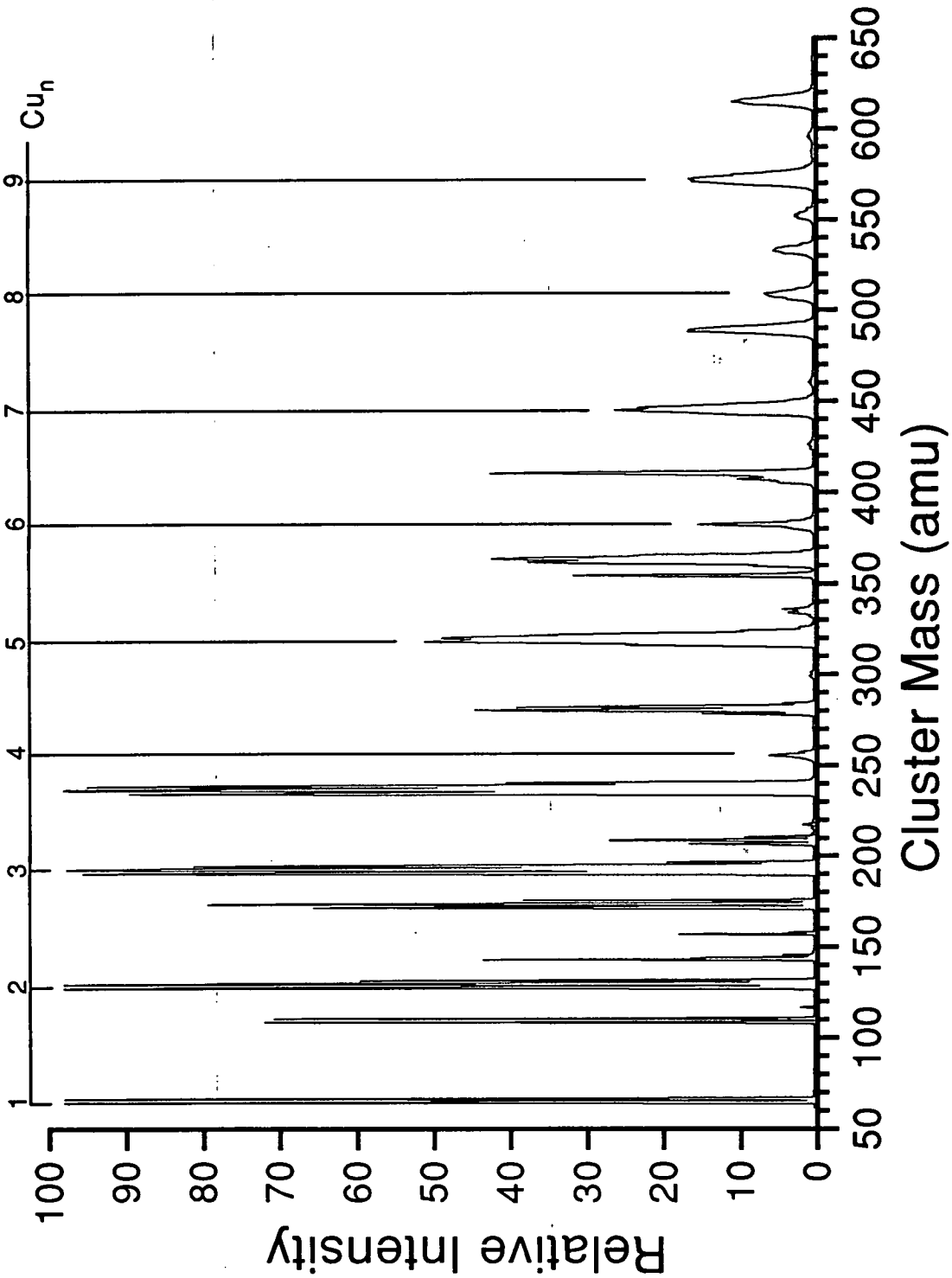

Figure 5–3: Mass spectrum showing mixed clusters produced on vaporising a copper-silver alloy target rod, and ionising with 193 nm radiation.

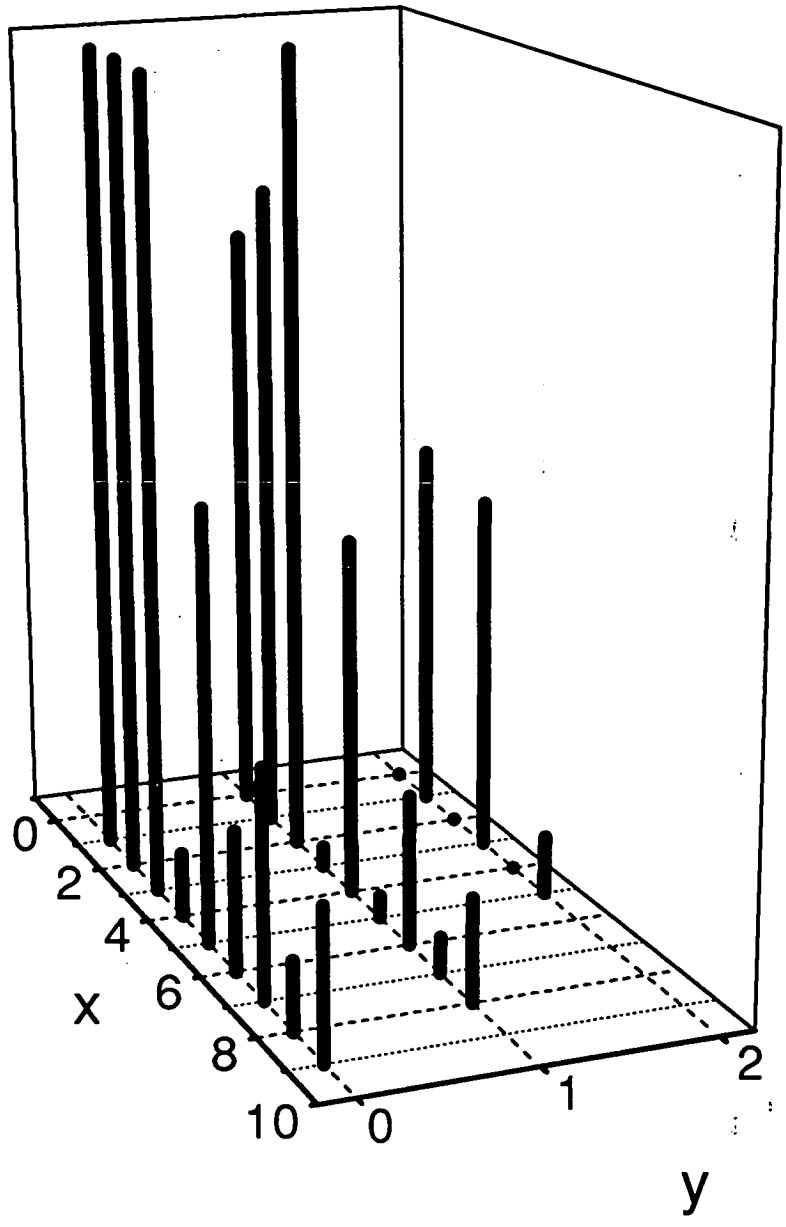

Figure 5–4: Mass spectral intensities of Cu_xAg_y cluster ions observed in the mass spectrum shown in Figure 5-3.

the premise that copper does cluster more efficiently than silver under equivalent experimental conditions.

5.3 Jellium Species

An overview of the specific species that have exhibited effects which could be described by the jellium model was presented in Chapter 4. The coinage metals have just been discussed in the previous section, and the experimental results have upheld the jellium description for these systems. The next step is to discuss whether electronic shell effects can be seen for any of the other known jellium species. Here we are limited to some extent by the nature of the laser vaporisation source. Some metals are not available in an appropriate form for use as vaporisation targets. This is especially true of the alkali metals, which have been studied extensively using oven cluster sources.

Nevertheless, an attempt was made to look at some members of the alkali metal group. None of these metals were suitable for use with the rod source due to their softness and reactivity, but it was possible to use the alternative disc source. Initially, experiments were attempted on sodium. Sodium metal sticks were obtained commercially, and a thin cross-section was cut from the end for mounting in the disc source. Obvious safety precautions were taken on handling the material. The main experimental concern was to get the metal target mounted within the source chamber, and pumped down to vacuum as quickly as possible. This was necessary in order to minimise oxidation of the metal which proceeded rapidly once removed from the paraffin-filled container in which it was stored. However, the difficulties of working with this substance did not end once it was safely housed inside the vacuum chamber. The first attempted study ended prematurely before a single mass spectrum could be collected. This was due to the sodium 'disc' adhering to the contact surface of the disc mount, resulting in the disc holder being sheared from the rotation arm at a flexible rubber connection. Following repair, another attempt was made.

The normal optimisation procedure during experiments involves ionisation of the clusters with a fairly wide laser beam initially to achieve an appreciable signal. Twin razor blades are then used as a slit to narrow the laser beam width, and thus decrease the ionisation volume. This has the effect of increasing the resolution of the observed peaks by decreasing the effective spatial distribution of nascent ions. A specific peak is then chosen, and its intensity monitored as the firing time of the ionisation laser is scanned. In this way, the optimum firing time can be found and selected. This parameter would be expected to remain almost constant for any species in the molecular beam, but it is found to alter slightly, showing a mass-dependence. This is due to an effect known as velocity slippage. This is common in seeded beams, where the velocity transferred to larger cluster species is not quite as great as to the lighter clusters [13,14]. This is because the light buffer gas atoms undergo less efficient energy transfer collisions with the heavier cluster species.

Figure 5–5 shows the mass spectrum for sodium clusters which was recorded initially. However, before any optimisation of the signal or improvement of the resolution could be undertaken the signal disappeared. It was discovered that the sodium disc had broken free from its holder and become stuck to the source block again. It was decided that no further attempts would be made to continue with this type of target. Apart from the very short run time, it was found that the soft sodium metal had also clogged up the vaporisation laser access channel, and the cleansing of this proved to be an arduous process. A number of comments can be made, however, on the spectrum that was obtained.

Pure sodium clusters can only be distinguished up to Na_5, and cluster oxides seem to be formed readily. Due to the inadequate length of time available to optimise the signal in this experiment, the resolution is too low beyond about 100 amu to allow single peak identification. The broad peaks observed are a convolution of signals attributable to several different cluster species. The lack of any observable even-odd intensity effects or electronic shell effects is not evidence against the existence of these effects as they have been documented in other work. As well as the lack of resolution here, the presence of cluster oxides would tend to

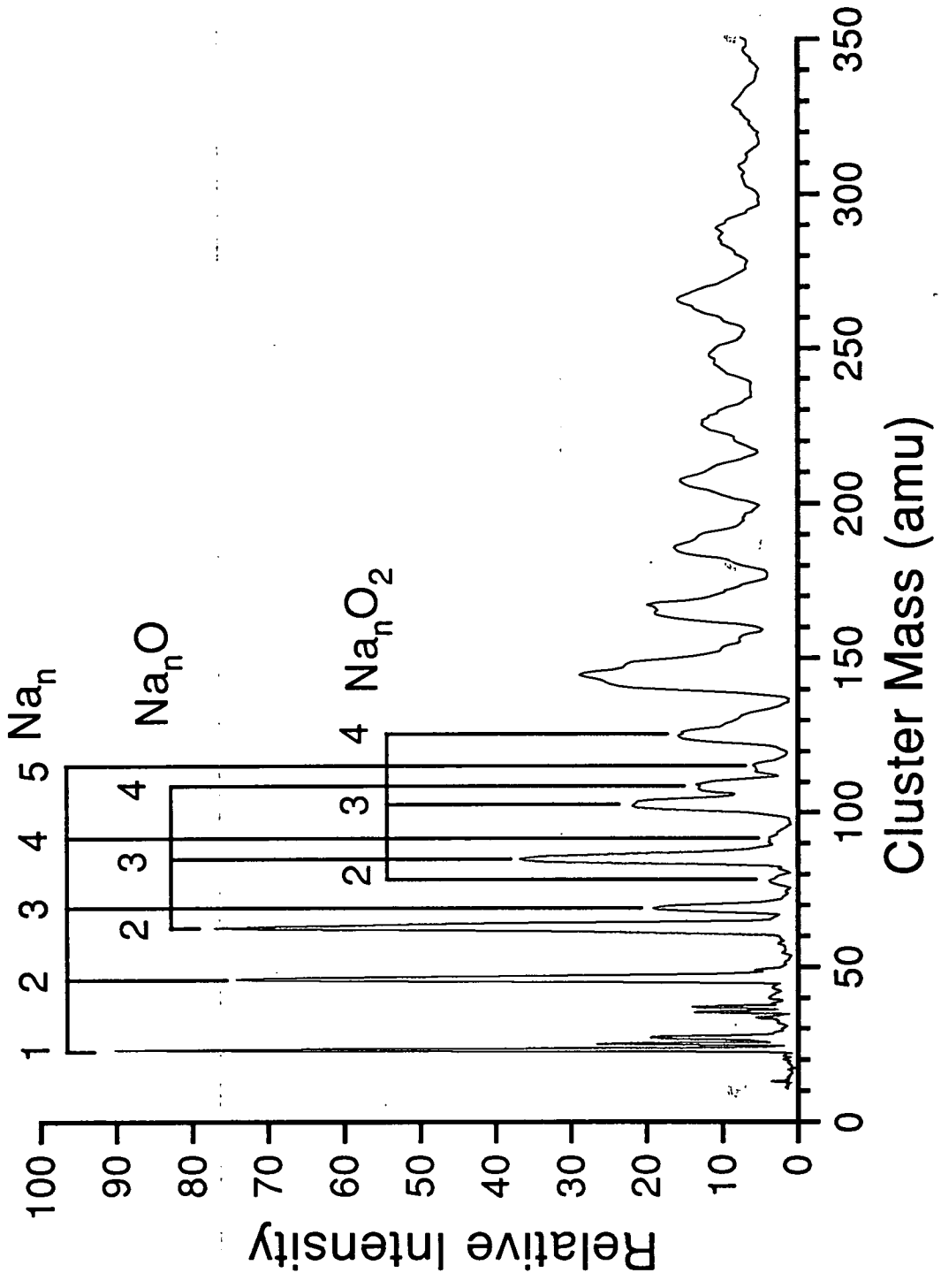

Figure 5–5: A mass spectrum showing clusters obtained from a sodium 'disc' after photoionisation at 193 nm.

obscure any intensity anomalies. These oxide adducts are seen for several systems and are usually due to impurities in the helium carrier gas, or to surface oxidation of the metal target. The amount of cluster oxide formation can normally be reduced by repeated vaporisation over the same region of the target surface. This has the effect of removing the oxide layer, and exposing the clean metal beneath. The possibility of using this technique to reduce the oxygen presence from the sodium mass spectrum was not feasible due to the short run-times available before the experiment was halted. The added difficulty for sodium clusters is that the bond strength of sodium oxide is appreciably greater than that of the sodium dimer, which is itself quite weakly bound (bond strength of Na_2 = 74kJmol^{-1}) [11]. Therefore, clustering is more likely to proceed around a base NaO unit rather than on Na_2.

Following the work on sodium, experiments were also attempted to generate clusters of lithium. In this case, a lithium disc target was prepared more conventionally by compression of lithium powder. Figure 5–6 shows the mass spectrum obtained on vaporisation of this target. Clusters up to Li_5 are observed, but once again not sufficiently large to show the expected shell effects.

In conclusion, the first laser vaporisation experiments on these alkali metals did not reveal the expected cluster abundance effects. This simply serves to show that there are some materials which are not suited for study with the laser vaporisation technique. This is not a problem, as alkali metal clusters have been studied extensively from oven sources.

More successful were experiments on the trivalent species aluminium. Figure 5–7 shows one such mass spectrum obtained for aluminium clusters following photoionisation at 193 nm. From this spectrum it is apparent that anomalously high intensities are displayed for clusters containing 7, 14, and 23 aluminium atoms in comparison with neighbouring peaks. These ionised clusters contain 20, 41, and 68 electrons respectively. The first two magic number clusters conform well to the jellium predictions for closed electronic shells. Note that a 40-electron system is not possible for singly-charged aluminium clusters due to their trivalent nature, but the 41-electron cluster has fulfilled this shell closing, and would rather not

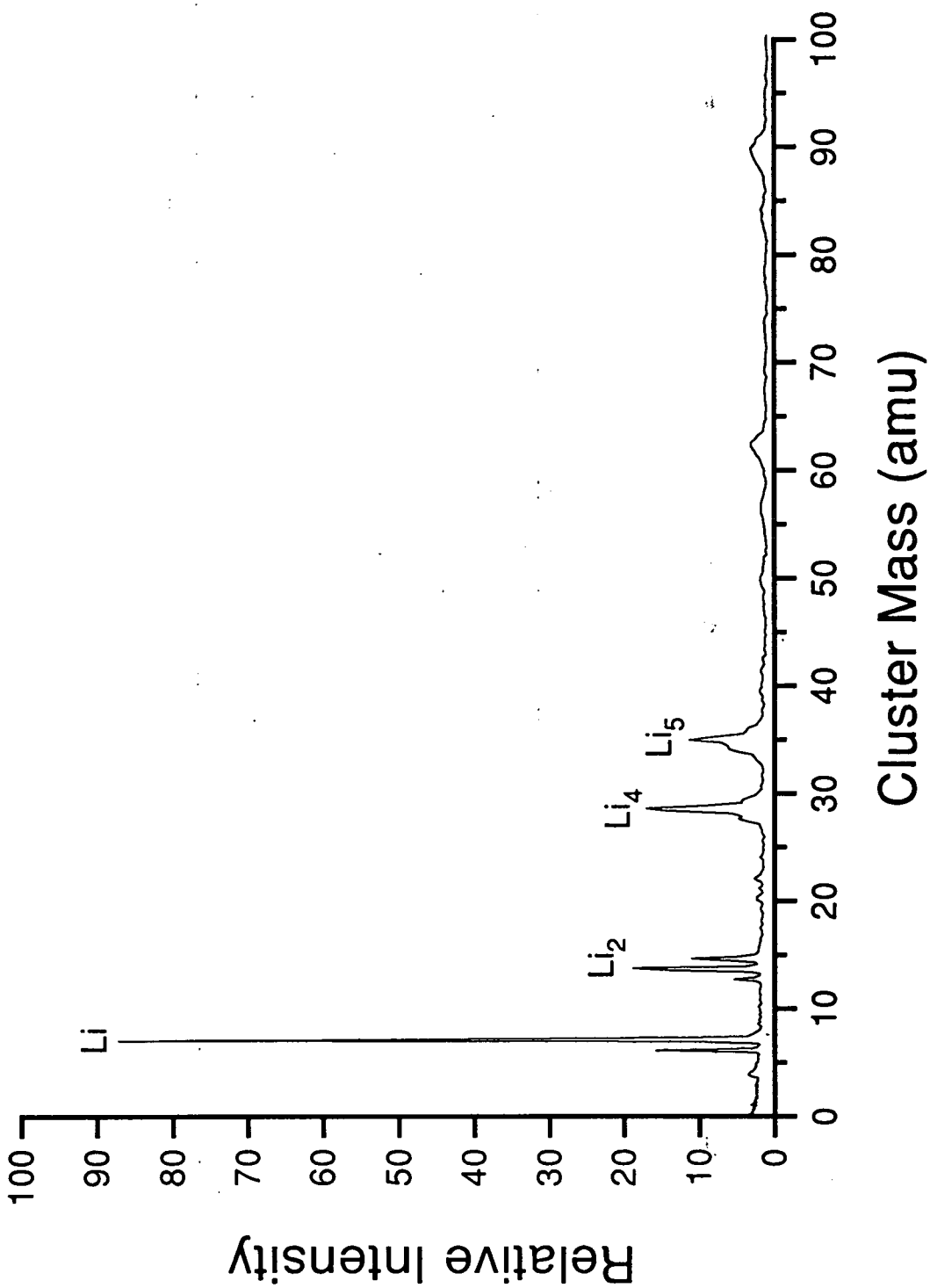

Figure 5–6: A mass spectrum of lithium clusters, photoionised at 193 nm.

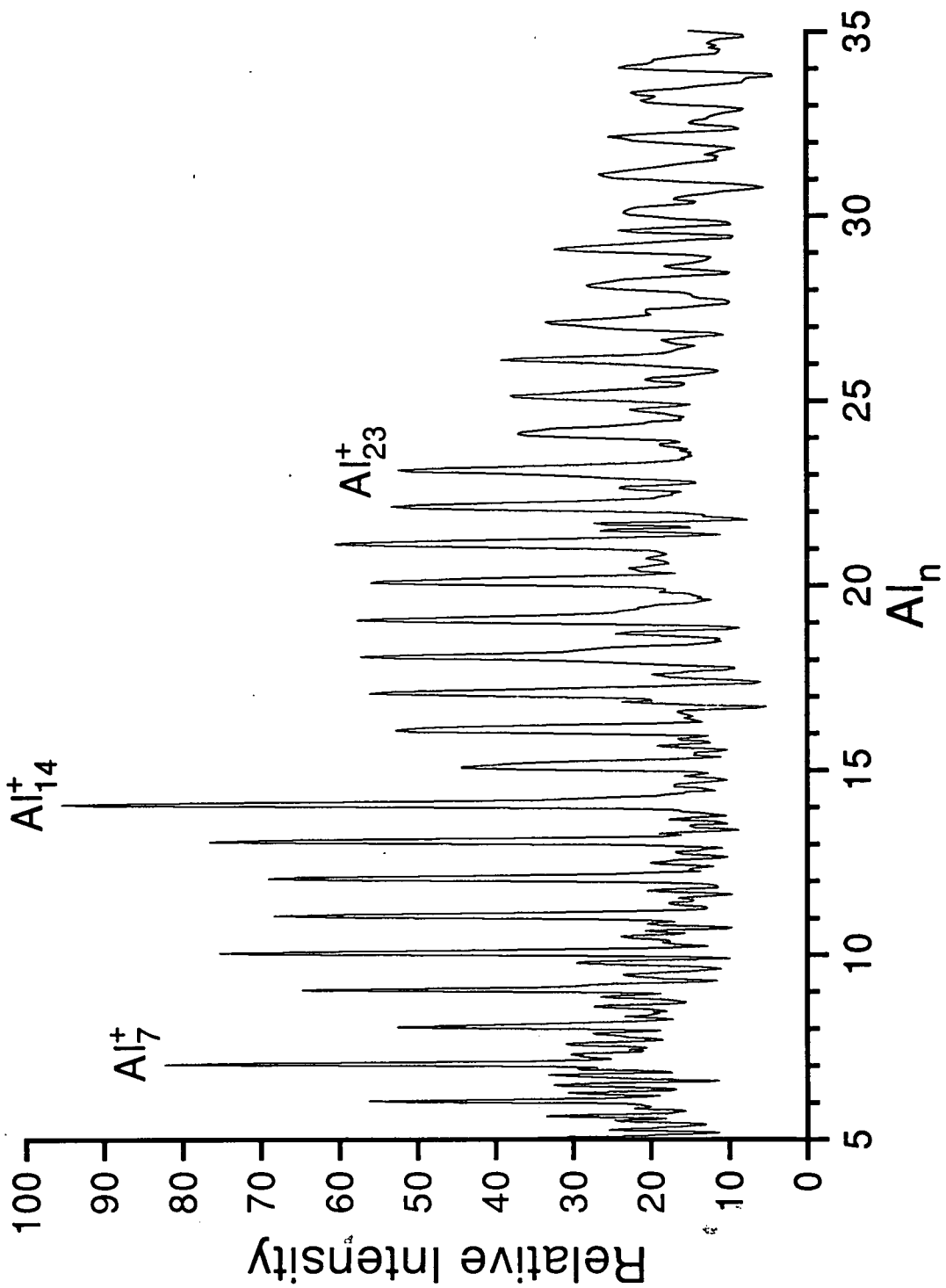

Figure 5–7: A mass spectrum of aluminium clusters after photoionisation with 193 nm radiation.

lose an aluminium atom to remove three electrons. The 68-electron system does not conform to the jellium predictions. This is a warning against the complete applicability of electronic shell effects for small clusters. The jellium model does work well for medium to large-sized cluster systems, but care must be taken when looking at smaller systems. The abundances of ionised clusters can often be affected by details of the ionisation process as well as stable cluster configurations. This is most prevalent for small clusters, as the ionisation potentials can change drastically between adjacent cluster sizes, before settling down to an asymptotic approach to the bulk work function.

It is well accepted that the jellium model describes aluminium clusters containing more than about fifty atoms well [15], but that there are differences for smaller clusters. Again the magic numbers observed are dependent on the measurement technique. Experiments to determine the electron affinities of small aluminium clusters have shown good agreement with the predicted effects from the jellium model [16]. For these effects to be evident in the mass spectrum presented here, then Al_{20}^{+} would have to possess an enhanced intensity instead of the observed anomaly for Al_{23}^{+}. The enhancement of the 23-atom cluster peak can still be explained, although outside of a jellium context. Ionisation potential measurements have been shown to dip for aluminium clusters containing 7, 14, and 23 atoms [17]. Similarly, these cluster species were found to have smaller collision-induced cross-sections than their neighbours [18], and were also present in greater abundances in a direct laser vaporisation experiment of an aluminium nitride target in which no buffer gas was used [19].

Thus for real cluster systems, the use of electronic shell effects to account for magic numbers seen in the mass spectrum of a system predicted to conform to the jellium model must be treated with caution. One must remember that the jellium model is quite simplistic in construction, and that deviations should not be unexpected when applied to real cluster systems. Some of the predicted jellium closings may well be present in the mass spectrum, but other effects may mask some of the anticipated magic numbers, and also throw up extra ones. For smaller clusters especially, the variations in ionisation potentials and photon absorption

cross-sections are very important in helping to explain enhanced abundances of ionised clusters. These competing effects are difficult to avoid, as the clusters must be ionised in order to observe them in these experiments.

5.4 Transition Metal Clusters

As has already been stated, one of the principal advantages of the laser vaporisation technique is that clusters of even the most refractory materials can be generated. It is into this category that the transition metals fall. Some data on the coinage metals has already been presented, but clusters were also successfully generated from target rods of nickel, iron, and niobium.

5.4.1 Nickel and Iron clusters

Examples of cluster abundance spectra obtained for nickel and iron clusters are shown in Figures 5–8 and 5–9, respectively. These transition metal elements have complex electronic configurations, and do not exhibit any known electronic shell effects. Any possible geometric shells will again tend to be masked by variations in photoionisation cross-sections for small clusters. For larger nickel clusters, containing more than 50 atoms, icosahedral stabilities have been reported in the literature [20].

The nickel cluster spectrum shown in Figure 5–8 does not consist entirely of pure nickel clusters, but also shows cluster oxides. As suggested in the discussion on sodium clusters, it should be possible to exclude these oxides by vaporising the same region of the target rod again to strip off any top oxide layer. However, when this procedure was performed, the oxide presence did not diminish, suggesting that these peaks are due to nickel clustering with oxygen which must be present as an impurity in the helium carrier gas.

Analysis of the iron cluster mass spectrum shown in Figure 5–9 also shows evidence of oxygen addition to the bare iron clusters. This spectrum is representative

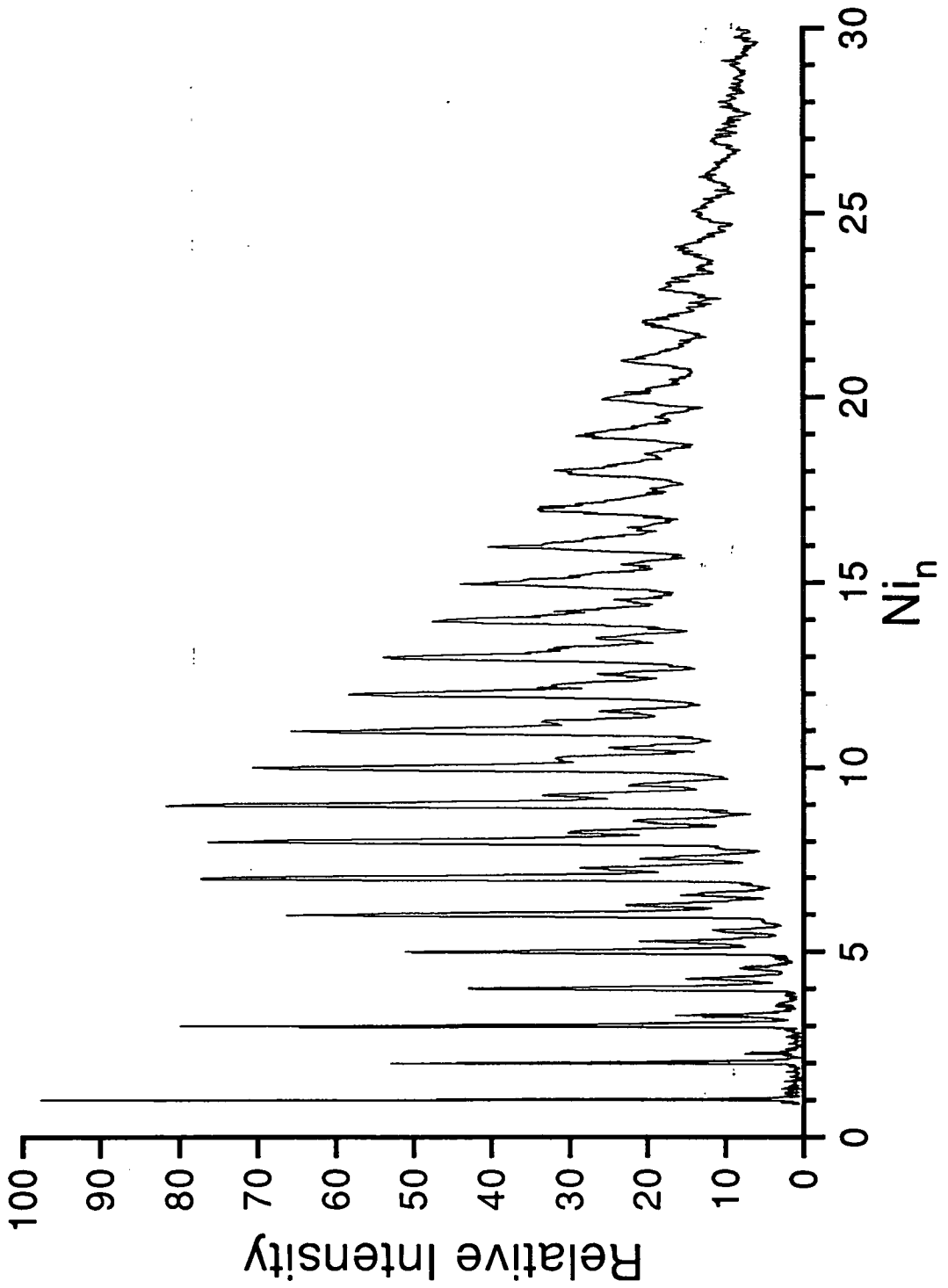

Figure 5–8: Mass spectrum of nickel clusters, photoionised at 193 nm.

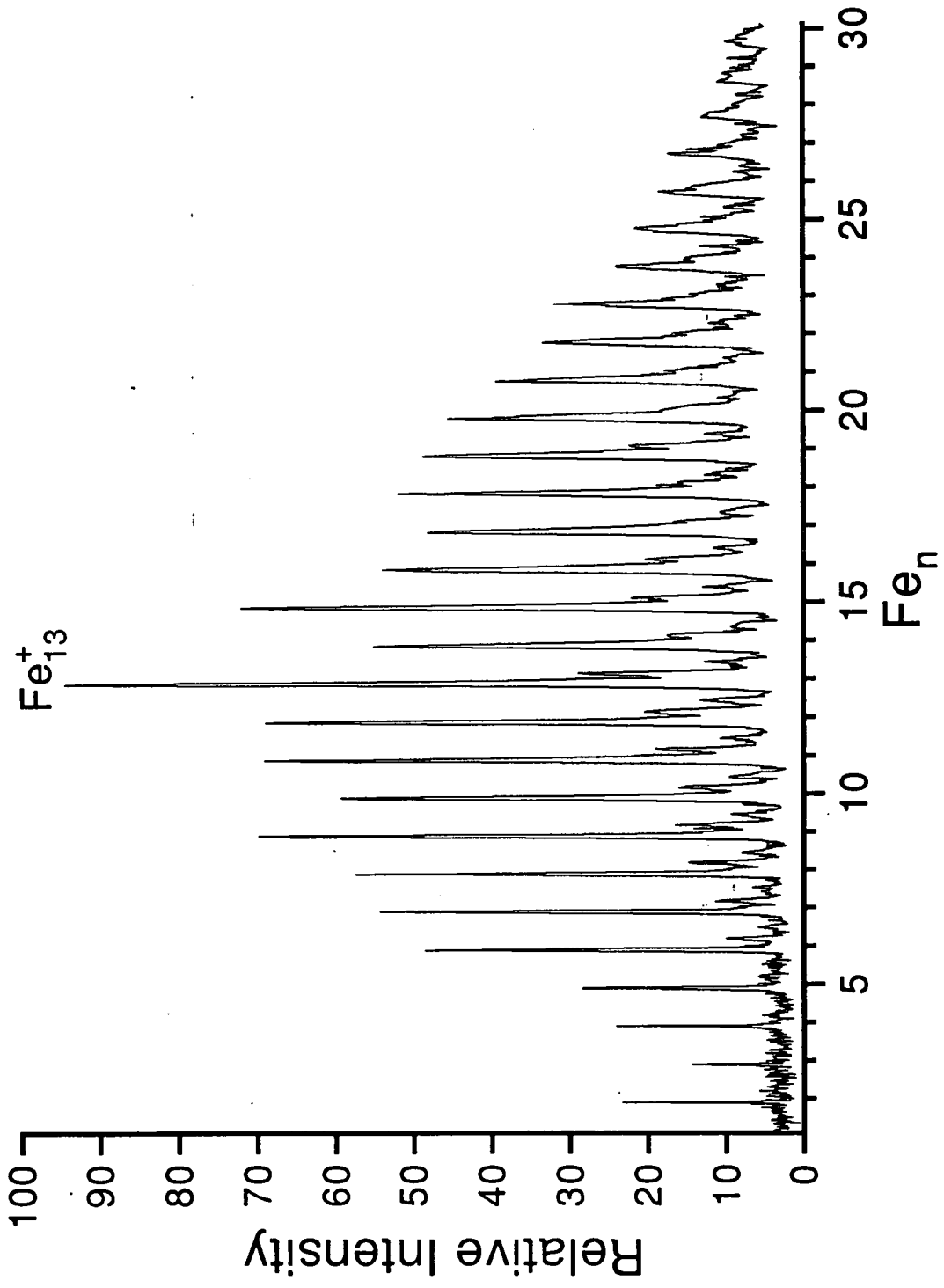

Figure 5–9: Mass spectrum of iron clusters after photoionisation with 193 nm radiation.

of all of the iron abundance spectra collected in that it shows the 13-atom cluster as having an enhanced intensity in comparison with its neighbours. This can be explained due to the stability of the 13-atom icosahedral structure. The ionisation potentials of iron clusters containing up to fifty atoms have been measured by two groups [21,22]. These do not show an especially high IP for Fe_{13}, so the high binding energy of such a symmetric structure is responsible for its increased intensity. The ionisation laser fluences used in the iron cluster experiment were high enough to promote some cluster fragmentation. The excess energy given to the cluster is such that the dominant fragmentation pathway is single-atom evaporation, although a given cluster can successively lose several atoms in this way. A cluster with a high binding energy, such as the 13-atom iron cluster, is less likely to evaporate atoms, and so shows up in the mass spectrum with a greater intensity.

5.4.2 Niobium clusters

Niobium appears to be one of the easiest transition metals to cluster. This may well be due to the fact that the bond strength of the niobium dimer is very high (511 $kJmol^{-1}$ [11]), and this promotes further cluster growth as mentioned previously. Because it was possible to generate a good distribution of niobium clusters relatively routinely, this system was used as a test-bed upon which to study the effects of different experimental conditions. An added advantage of this particular element is that it only possesses one naturally occurring isotope, making mass calibration of the spectrum much easier.

A typical mass spectrum for niobium clusters obtained in this laboratory is shown in Figure 5–10. This is the type of mass spectrum achieved on initial set-up of the cluster apparatus. One feature which is clearly evident from this spectrum is the presence of niobium cluster oxides. James [12] noticed that the relative intensities of these cluster oxides increased on photoionisation at 193 nm when compared with the use of 266 nm radiation. This fact can be related to the ionisation potentials of the cluster oxides which have been reported in the literature [23].

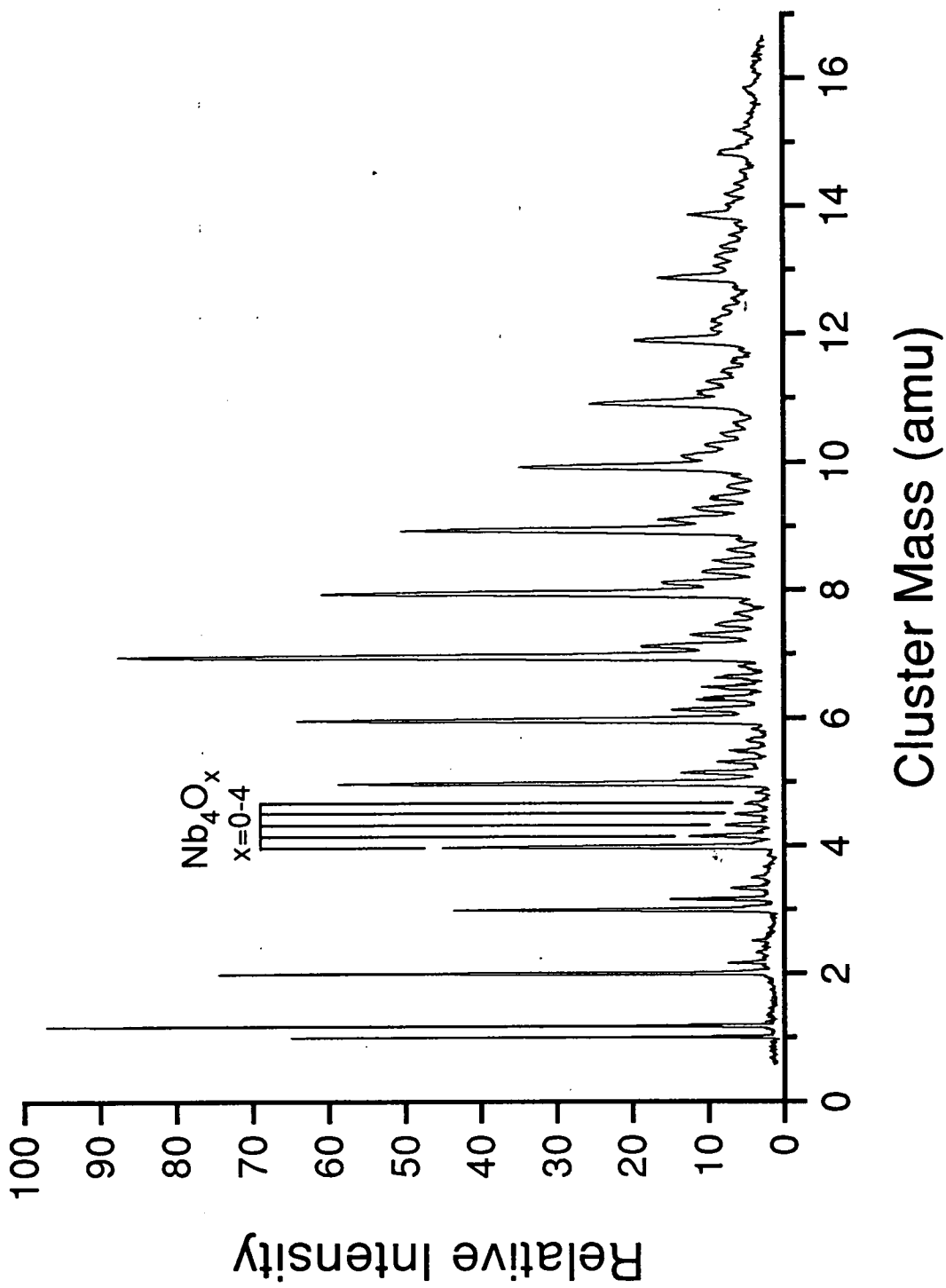

Figure 5–10: Mass spectrum of Nb clusters, ionised with 193 nm radiation.

If the experimental conditions are altered to allow the creation and detection of larger clusters, then the mass spectral abundance patterns change. The type of spectrum obtained under these conditions is shown in Figure 5–11. The main difference between the experimental conditions used to record this spectrum compared to the previous one is that the deflection plate voltage has been increases to allow the mass window to be shifted towards higher masses. The deflection voltage was set at 200V for the spectrum recorded in Figure 5–10, and this was increased to 600V to record the data displayed in Figure 5–11. As well as this adjustment, the firing time of the ionisation laser was re-optimised for ionisation of higher mass clusters. This involved a slight increase in the delay between cluster creation and photoionisation due to the greater velocity slippage which exists for heavier clusters. It can be seen from the spectrum in Figure 5–11 that local maxima in cluster intensities are seen for Nb_7, Nb_{15}, and Nb_{22}.

It must be kept in mind throughout this type of work that the physical, chemical, and electronic properties of any system are not mutually exclusive. In fact there is a strong interdependence between properties such as structure, ionisation potential, and reactivity. Niobium clusters from the dimer upwards are all 1-photon ionised at 193 nm (6.4eV). As is often the case in these experiments, the more abundant clusters in Figure 5–11 are probably more intense due to a decreased likelihood of fragmentation during the ionisation process, rather than a reflection of the neutral cluster abundances.

The good cluster distributions that could be obtained for niobium allowed comparative experiments to be performed on the effects of different source conditions upon the observed abundances. If ionisation is carried out with the excimer laser operating on the KrF line at 248 nm (4.98eV) as opposed to the ArF line at 193 nm (6.42eV), then the mass spectrum displayed in Figure 5–12 results. The new set of peaks which can be observed between the main niobium cluster ion signals for n = 7-15 correspond to the creation of doubly-charged niobium clusters containing an odd number of constituent atoms. The even-numbered doubly-ionised niobium clusters cannot be seen directly in the mass spectrum as they have the same flight times through the instrument as singly-charged niobium clusters containing half

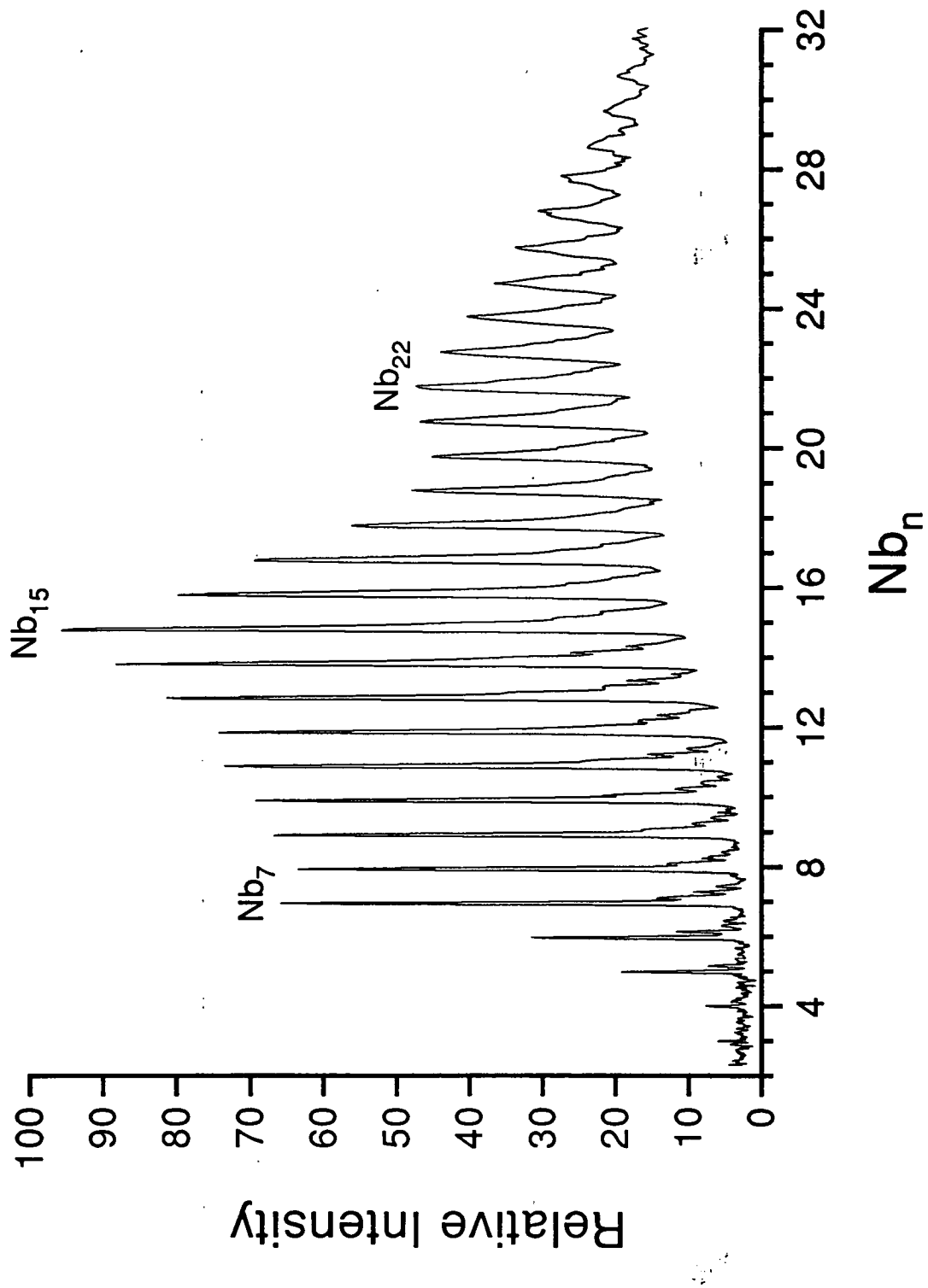

Figure 5–11: Mass spectrum of larger niobium clusters produced under the same experimental conditions as the previous figure.

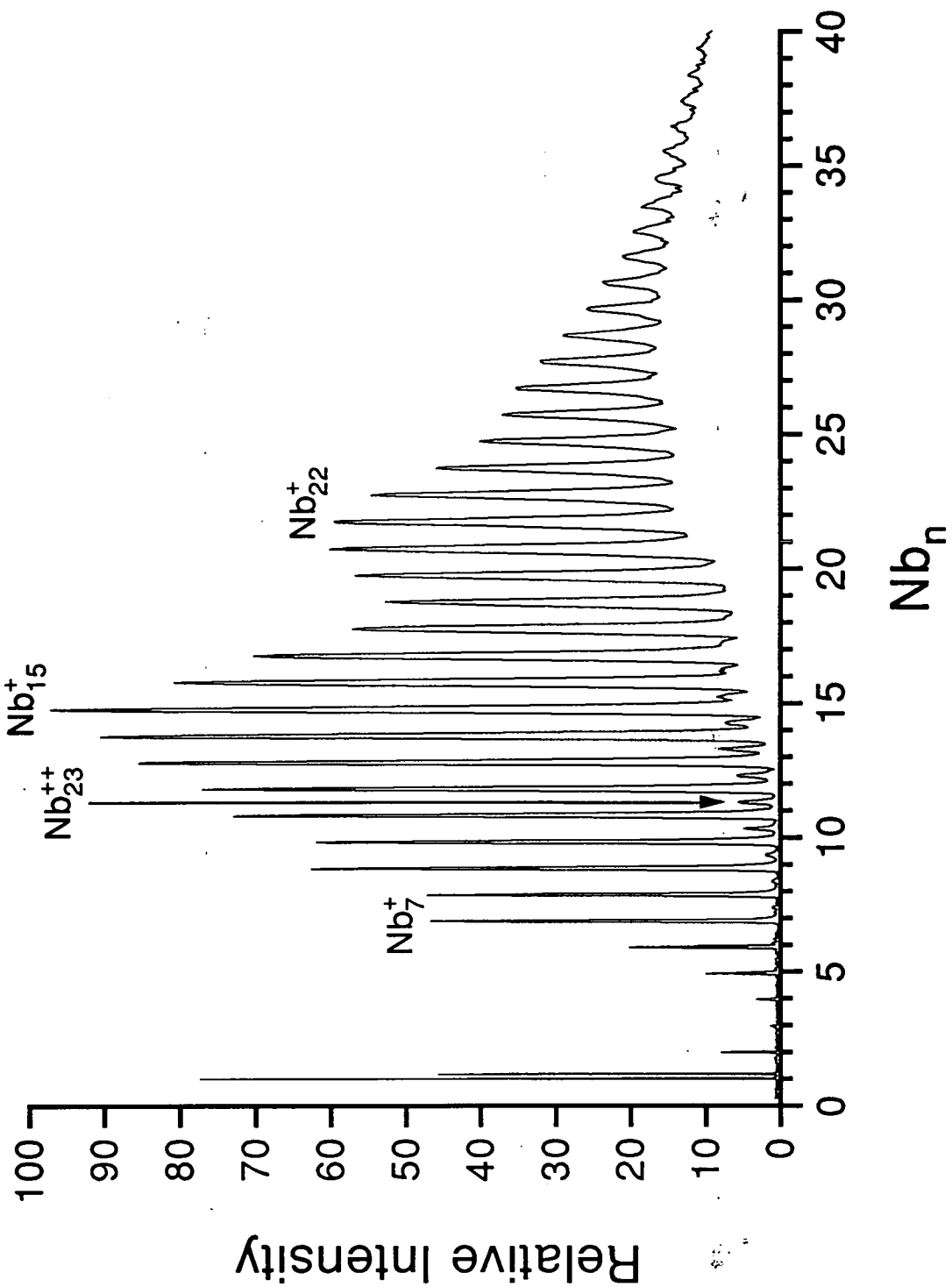

Figure 5–12: A mass spectrum of niobium clusters showing evidence of the existence of doubly-charged metal species.

that number of constituent metal atoms. Thus the intensities of the normal niobium cluster ions will contain some contribution from the doubly-charged clusters having the same mass-to-charge ratio.

These doubly-ionised niobium cluster species have been seen before, but only using much higher energy electron impact as the means of ionisation [24]. A 60eV electron beam was used for ionisation in the reported experiment, supplying over ten times as much energy to the niobium clusters in comparison with the 4.98eV excimer radiation used in these experiments.

The relative intensity of doubly-charged niobium cluster peaks can be magnified by altering the experimental conditions in favour of even larger cluster production. Firstly, the deflection voltage can be increased to a higher value to favour clusters of higher mass. Also, the effective amount of clustering produced can be altered. As has been stated before, a higher helium backing pressure will produce more effective clustering. This effect can also be achieved without changing the actual pressure at the helium source. Instead, the time of firing the vaporisation laser can be shifted to occur at a time when there is a higher density of helium passing over the target metal surface. The spectrum shown previously in Figure 5–12 was recorded with a deflection voltage of 650V, and with the vaporisation laser firing into the front edge of the helium pulse. Shifting the deflection voltage up to 680V, and vaporising at the point of maximum density of the helium pulse produced the spectrum shown in Figure 5–13. . The intensity of the doubly-charged clusters in this spectrum has clearly been enhanced. Clusters containing up to about forty-eight atoms, with a single charge can be observed, and the same size range is seen for doubly-charged clusters.

As most physical properties exhibited by atoms and molecules evolve into an analogous bulk property, then the general tendency for a metal cluster to ionise may also be linked to bulk properties. Certain niobium clusters have been shown to exhibit a delayed emission of electrons after an ionisation event [25]. This property correlates with the bulk thermionic emission characteristic. It is known that hot clusters may cool by evaporatively losing atoms in a step-wise process. However, delayed electron emission provides an alternative energy loss channel to stabilise

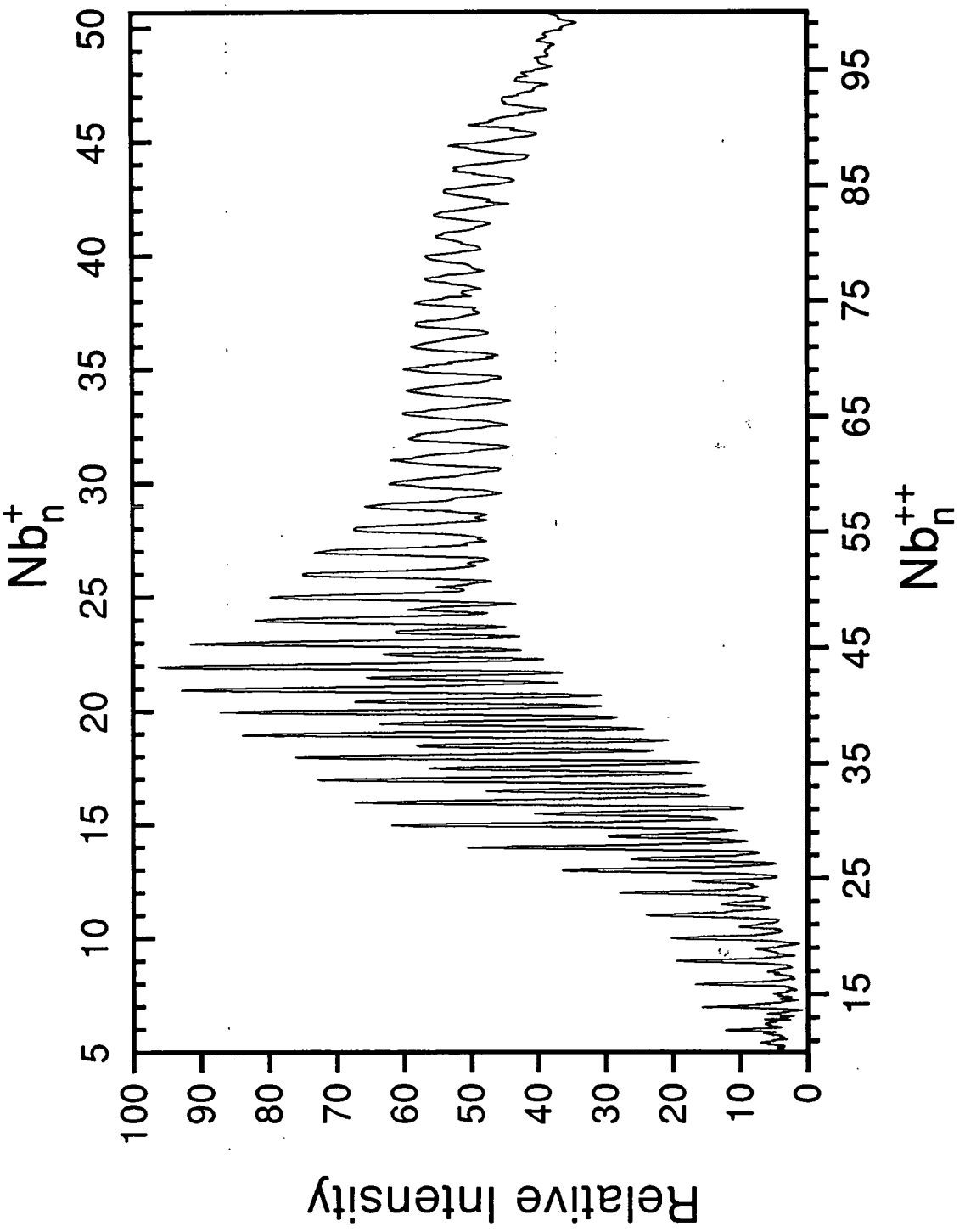

Figure 5–13: A mass spectrum of niobium clusters ionised at 248 nm, showing the production of doubly-charged clusters.

clusters which have excess internal energy [26]. The question as to whether electron or atom loss is more favourable depends on the particular system. For niobium, the bulk work function is almost half the value of the cohesive energy of the bulk metal. Thus, in general terms, it would not be energetically unfavourable for the bulk species to emit two electrons rather than lose an atom. If these properties are extrapolated back through to cluster systems, then there is justification for niobium cluster ions to become doubly-charged rather than evaporate atoms as a means of releasing excess energy.

From the known physical properties of the niobium atom, the first ionisation potential lies at an energy of 6.88eV, and the second ionisation potential is at 14.32eV [11]. The IPs of cluster species tend to asymptotically approach the bulk work function, which in this case is 4.3eV. The general approach to the bulk value can be described by a classically obtained relationship [27,28], which, to first order defines the ionisation potential of an N-atom cluster as:

$$IP(N) = W_\infty + \frac{3}{8}\frac{e^2}{R} \tag{5.2}$$

where W_∞ is the bulk work function, and R is the cluster radius, which is proportional to the cube root of the number of constituent atoms. Thus, for the range of clusters presented here, the first ionisation potentials should lie between the atomic IP value, and the bulk work function. Niobium cluster IPs have been measured by Knickelbein [29], and these are displayed in Figure 5–14. This shows that niobium clusters ($n \geq 2$) all have IPs less than that of atomic niobium. It then follows that the energy required to remove a second electron from a given cluster will most likely be less than the 14eV required to doubly ionise the niobium atom. For ionisation with KrF radiation, this only requires the absorption of three photons. This process should not be considered unlikely in a typical experiment in this laboratory. One should recall that good helium ion signals can be detected, and that this involves a four- or five-photon absorption scheme.

One interesting question is why doubly-charged niobium clusters can be observed when ionising with the KrF line (4.98eV), but not with the ArF line (6.42eV). The most likely reason is due to the increased laser output energy available on the KrF line. Pulse energies from the Lumonics excimer laser used in

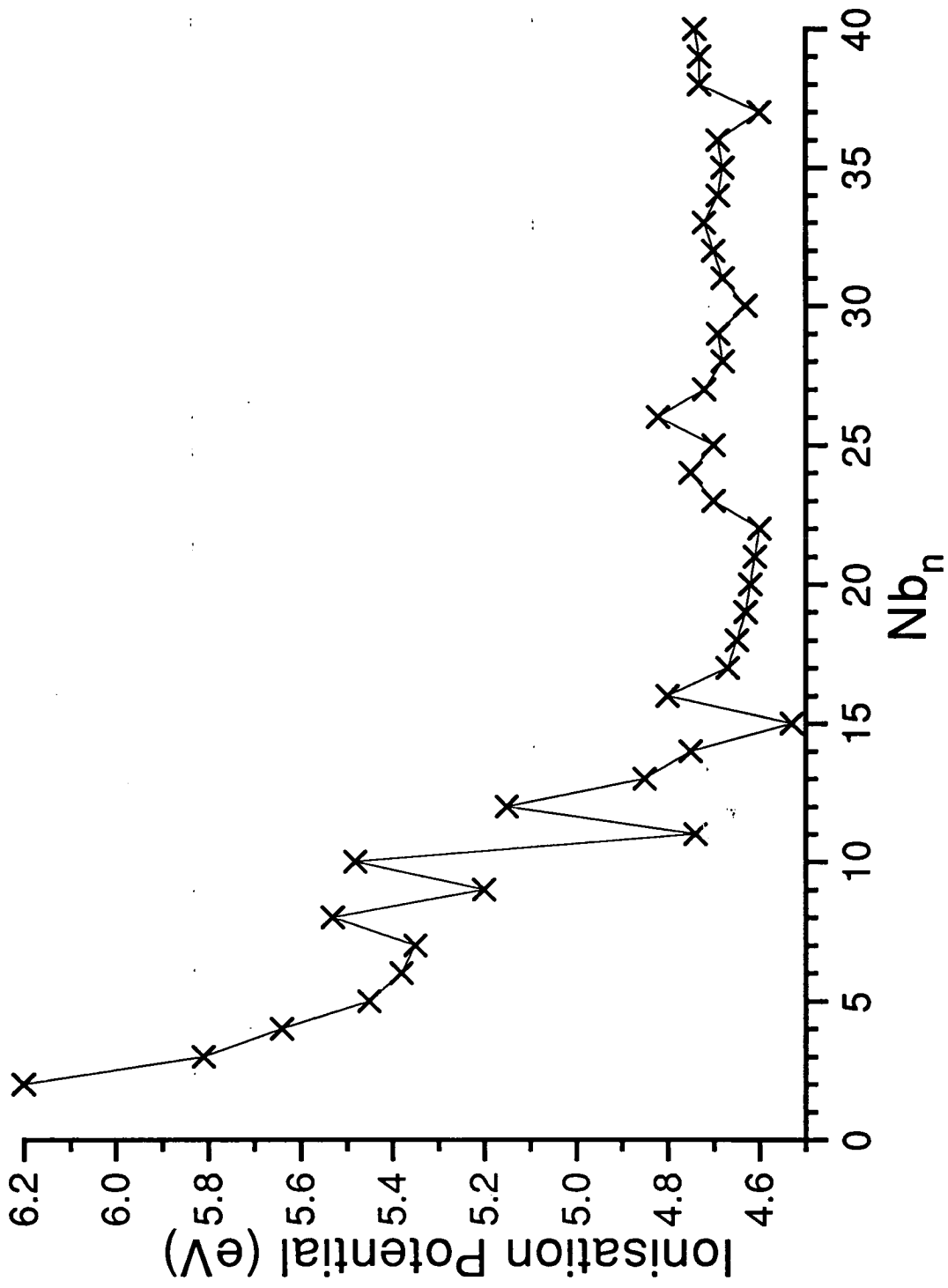

Figure 5–14: Niobium cluster ionisation potentials from reference [29].

these experiments are typically five times greater for KrF radiation than for ArF. Indeed, the optimised spectra shown in this chapter were obtained with vastly different pulse energies. The clusters in Figure 5–11 were ionised with ArF photons. The energy of this laser beam, measured before the quartz access window of the ionisation chamber, was 6 mJpulse^{-1}. The KrF laser beam used to photoionise the clusters shown in Figures 5–12 and 5–13 had a comparative energy of 40 mJpulse^{-1}. This increased photon density would favour the occurence of a double ionisation process.

A less likely factor to consider relies on the fact that the density of electronic states within a reasonably-sized cluster has grown considerably from the distinct electronic levels seen in small molecules. For the doubly-charged clusters observed in these experiments, it may well be that there is a raft of states available as a resonant step on absorption of KrF photons to make the second ionisation step more probable.

It seems remarkable that doubly-charged niobium clusters have been generated in these experiments. In fact these were the first results obtained in this laboratory to show the presence of doubly-charged clusters. As mentioned previously, doubly-charged niobium clusters have been observed by other groups, but only with more energetic means of ionisation, such as the use of electron beams. Magnesium cluster oxides have been doubly-ionised with focussed ultra-violet laser radiation [30], so this type of process is not unfeasible.

5.5 Non-metal Clusters

Although the laser vaporisation technique was originally developed to allow the study of clusters of refractory metals, particularly the transition metals, the versatility of this cluster generation method has enabled the generation of a very wide range of cluster species. The target materials extend even into the realm of non-metals. Again, the only limitation lies in being able to obtain the desired material in the form of a solid target.

One of the first non-metal materials to be clustered was carbon, and these experiments yielded some rather astounding results which have had important implications for many areas of scientific research. The range of clusters produced following vaporisation of a graphite target showed some magic numbers which did not correspond to those of any typical metal cluster systems. The most pronounced intensity anomaly in the mass spectrum correlated with a cluster containing sixty carbon atoms, and this was assigned a particularly stable truncated icosahedral cage structure, and named buckminsterfullerene [31,32]. This experiment can be easily reconstructed, and a mass spectrum of carbon clusters which was obtained during the course of this work is shown in Figure 5–15. This mass spectrum is similar to those which have been reported in the literature, with the typical bimodal structure in the carbon cluster abundances. The stability of C_{60} is evident, as is the presence of purely even-numbered carbon clusters in this mass range.

Further evidence for the particular stability of C_{60} can be illustrated by a reverse experiment, so to speak. Rather than clustering carbon atoms after vaporising a graphite rod, one can laser desorb a fullerene sample from the surface of a target rod and monitor the cluster species present after a controlled photofragmentation process. The desorption step is really just a low-powered vaporisation interaction in which the Nd:YAG laser fluence is turned down to less than 1% of typical vaporisation fluences. This means that the sample substrate, aluminium in this case, is merely heated instead of vaporised. This increased temperature is passed to the fullerene molecules that have been coated on to the surface of the rod which simply boil off the metal and into the helium stream.

The fullerene sample was obtained by the well-documented method of electrical discharge of graphite rods in a helium atmosphere contained within a simple bench top reactor [33]. The resultant fullerene mixture was purified by chromatographic methods to yield only C_{60} and C_{70}. These species were desorbed intact, but could be induced to fragment during the ionisation process. If hard ionisation conditions are used, corresponding to higher ionisation laser fluence, then the fullerene species successively lose C_2 units, as seen in the mass spectrum shown in Figure 5–16. It

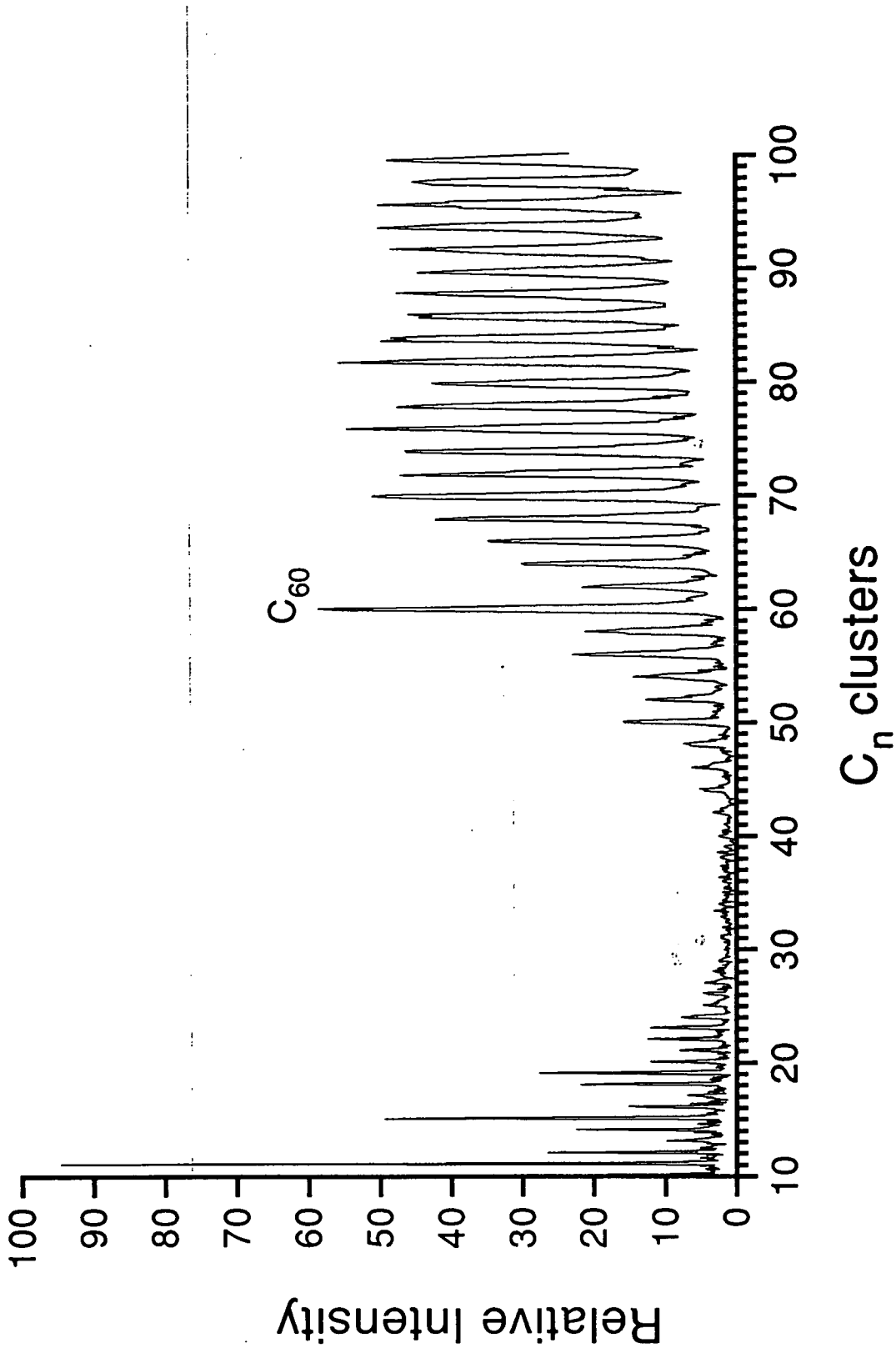

Figure 5–15: Mass spectrum resulting from vaporisation of a graphite rod and subsequent photioniisation at 193 nm.

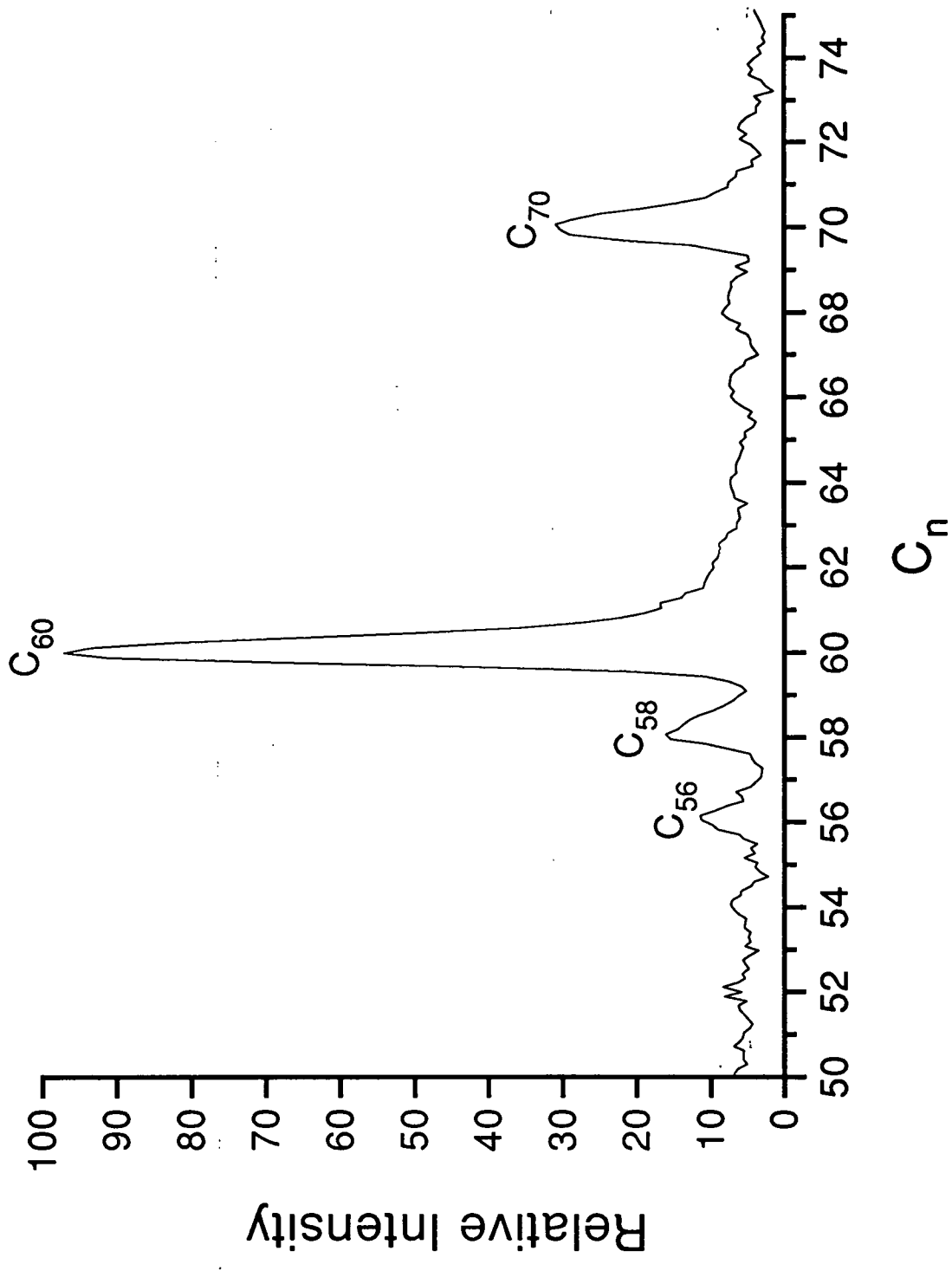

Figure 5–16: A mass spectrum of laser-desorbed fullerene sample with ionisation at 193 nm.

must be stressed that the carbon cluster species resulting from the fragmentation process were definitely not present in the original sample.

The previous discussion of the magic numbers exhibited by metal clusters has shown that the predictive power afforded by the structure of the periodic table has been very useful. Clusters of elements within the same group tend to conform to quite similar electronic or geometric stabilities. However, there is no evidence in this case to suggest that the structure of silicon clusters might resemble those of carbon clusters. This might have been expected considering that the respective bulk materials differ greatly in their properties. Studies of the stabilities of silicon clusters have shown no resemblance at all to the magic numbers exhibited by carbon clusters, and there appears to be no corresponding silicon-built fullerene molecules.

The main studies performed on silicon clusters have involved the measurement of the most dominant fragmentation channels exhibited upon cluster dissociation. The predominant fragments for smaller clusters appeared to be units containing six and ten silicon atoms [34,35,36], and the structures of Si_6 and Si_{10} have been shown to be thermodynamically stable [37]. The most probable structures of these species have been calculated, with the ten-atom cluster assuming the geometry of a crystalline fragment of an adamantane-like structure [38]. The photodissociation of larger silicon clusters has shown an evolution in the dissociation process towards a bulk description as the cluster size increases [39]. For clusters containing up to 35 atoms, the dominant fragment is Si_{10}. Clusters containing more than 35 but fewer than 60 atoms preferentially yield an Si_6 fragment. Finally, clusters made up of more than 60 atoms will simply undergo a single-atom evaporation which is what occurs for the bulk material. These changes in fragmentation products can be linked to changes in the cohesive energy of the clusters.

Heterogeneous clusters containing both silicon and carbon atoms have been reported on in the literature. The experimental set-up was the same as for the generation of bare silicon clusters, although in this case, the inert carrier gas was seeded with a quantity of gaseous hydrocarbons [40]. The hot plasma formed on vaporisation of the silicon target appears to cause the decomposition of the

hydrocarbon species, giving rise to a source of carbon atoms which can also take part in the clustering process. The main clusters formed were bare homogeneous clusters, and clusters containing only one or two atoms of the other material.

An alternative way to study these heterogeneous clusters was examined in this work. This involved laser vaporisation of a silicon carbide target which was obtained commercially. A typical mass spectrum of the cluster distribution resulting from the use of such a target is shown in Figure 5–17. The enhanced relative intensities of the Si_6 and Si_{10} clusters support the previous experimental results discussed above. Again, larger clusters containing near-stoichiometric quantities of carbon and silicon atoms do not appear to be formed in the growth process. The more favoured mixed-species clusters contain only one or two atoms of one of the materials.

5.6 Heterogeneous Cluster Systems

The study of heterogeneous clusters is a necessary step towards the understanding of real materials. Many groups of homogeneous clusters have been studied, but very few bulk systems consist of one pure element. Results from the study of heterogeneous clusters should provide insight into the interactions taking place in real alloyed systems.

Experiments using two types of heterogeneous targets have already been described in the previous sections of this chapter. The SiC target rod was commercially available, and the CuAg rod was easily fashioned due to the similar melting points of the two constituent metals. A number of other similar species were examined during the course of this work for which it would have been extremely difficult to present in the form of a suitable target for use with the conventional rod source. These studies entailed use of the disc source described in Section 3.3. Many discs of differing compositions were fabricated, mainly in an attempt to carry out spectroscopic studies on mixed-metal dimer species. Some preliminary

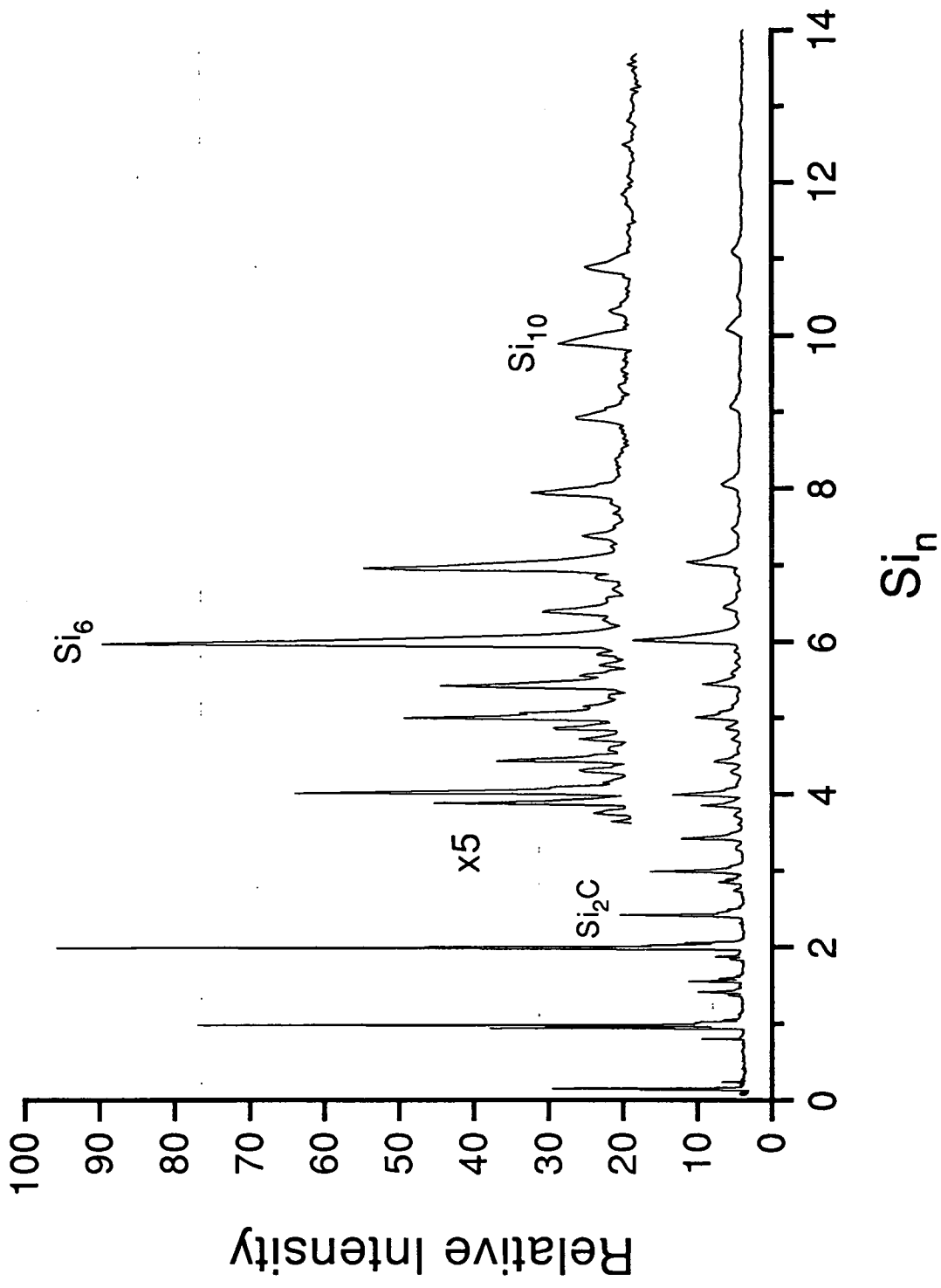

Figure 5–17: Mass spectrum of clusters obtained from a silicon carbide rod after photoionisation at 193 nm.

electronic spectra were obtained for a few of these systems by a previous member of this group [41], and these included vibronic spectra for AlNi, NiCu, and NiAg.

One group of systems of particular interest in the realm of heterogeneous clusters are the mixed alkali/coinage metal clusters. There is already a considerable amount of data available on the homogeneous alkali clusters and coinage clusters separately, but very little on the mixed systems. The alkali and coinage metal dimers, the smallest cluster units, have been extensively studied by electronic spectroscopy, and much has been learned about the nature of the bonding in these species. The obvious starting point for a study on the mixed alkali/coinage metal clusters would be the prototypical dimer LiCu. Interest would then extend to large mixed clusters where, for instance, the study of $LiCu_n$ would help ellucidate the role of a host atom as a localised defect in a bulk system. The interest in these species leads to an attempt to generate the LiCu molecule using the technique of laser vaporisation. The only previous work on this particular molecule consists of a molecular orbital calculation on the electronic ground state [42], and a measurement of its dissociation energy using a Knudsen effusion cell [43]. Thus there remains a large number of experiments to be performed on this system.

The first requirement was the preparation of a suitable mixed metal target. Since lithium melts at 453K and copper at 1356K, an alloy rod would be very difficult to fabricate in the manner described for CuAg. An easier alternative is the creation of a target disc. This was accomplished by mixing powders of the two metals and compressing these into a solid disc by the method described in Section 3.3. The process of target disc construction is not always as straightforward as it may seem. In this specific case, the resultant disc proved to be rather brittle, and several attempts were needed to press a disc, and to extricate it from the die without extensive crumbling or fracturing of the target. The inhomogeneity of the pressed mixture was also evident upon a cursory inspection of the disc, so a process of repeated grinding and recompression was carried out. The resultant target was usable, and could be mounted in the disc source.

Figure 5–18 shows the mass spectrum obtained using this target. Identification of the principal constituents in the spectrum can be confirmed from the iso-

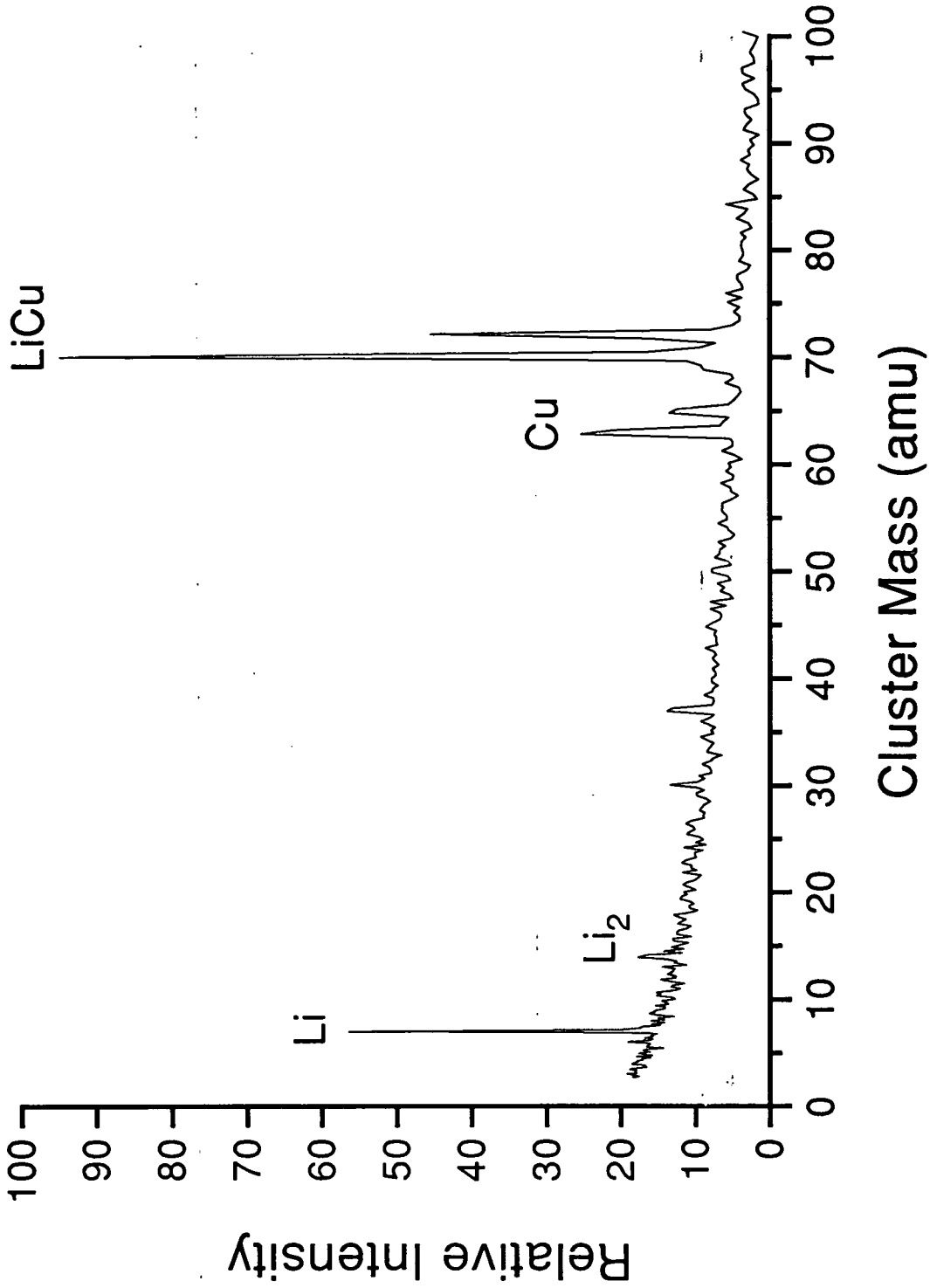

Figure 5–18: Mass spectrum of species created from a lithium/copper target disc, with ionisation at 494 nm (2.51eV).

topomers expected to be present. The main isotope of lithium is of mass 7 amu, and is 92% abundant. The only other naturally abundant isotope is of mass 6 amu. Copper has two isotopes of mass 63 and 65 amu, which have a natural abundance reflected by a 69:31 ratio. The combination of these isotopes will result in the most prominent isotopomers of LiCu at masses 70 and 72 amu, in an approximate 2:1 ratio. A possible complication to the identification of the LiCu molecule in the cluster beam would be the presence of a ten-atom lithium cluster which would also occur at mass 70. However, this could be checked by looking at the clusters produced from a pure lithium disc target under the same experimental conditions as for LiCu. This was confirmed by the fact that the lithium cluster distribution under the same conditions, which was displayed in Figure 5–6, only showed clusters containing up to five lithium atoms. The peaks at 70 and 72 amu in Figure 5–18 are therefore due solely to LiCu. The clear presence of LiCu in the beam prompted a preliminary search for the electronic spectra of this molecule using the R2PI technique discussed in Section 2.5. Unfortunately, no electronic states were found for this molecule when scanning over the range 460 nm to 500 nm. This may have been due in part to an unsteady signal still arising from the lack of uniformity in the constituents of the disc.

An important point to note is that the versatility of the disc source means that its use is not restricted to the study of the mixtures of only two materials. There is no reason why three or more different powders cannot be combined, and this has been carried out in the fabrication of a single target containing lithium, copper, and aluminium. The mass spectrum resulting from the vaporisation of this target is shown in Figure 5–19. The successful generation of clusters from this type of mixed metal target was of interest, and would be worth future study.

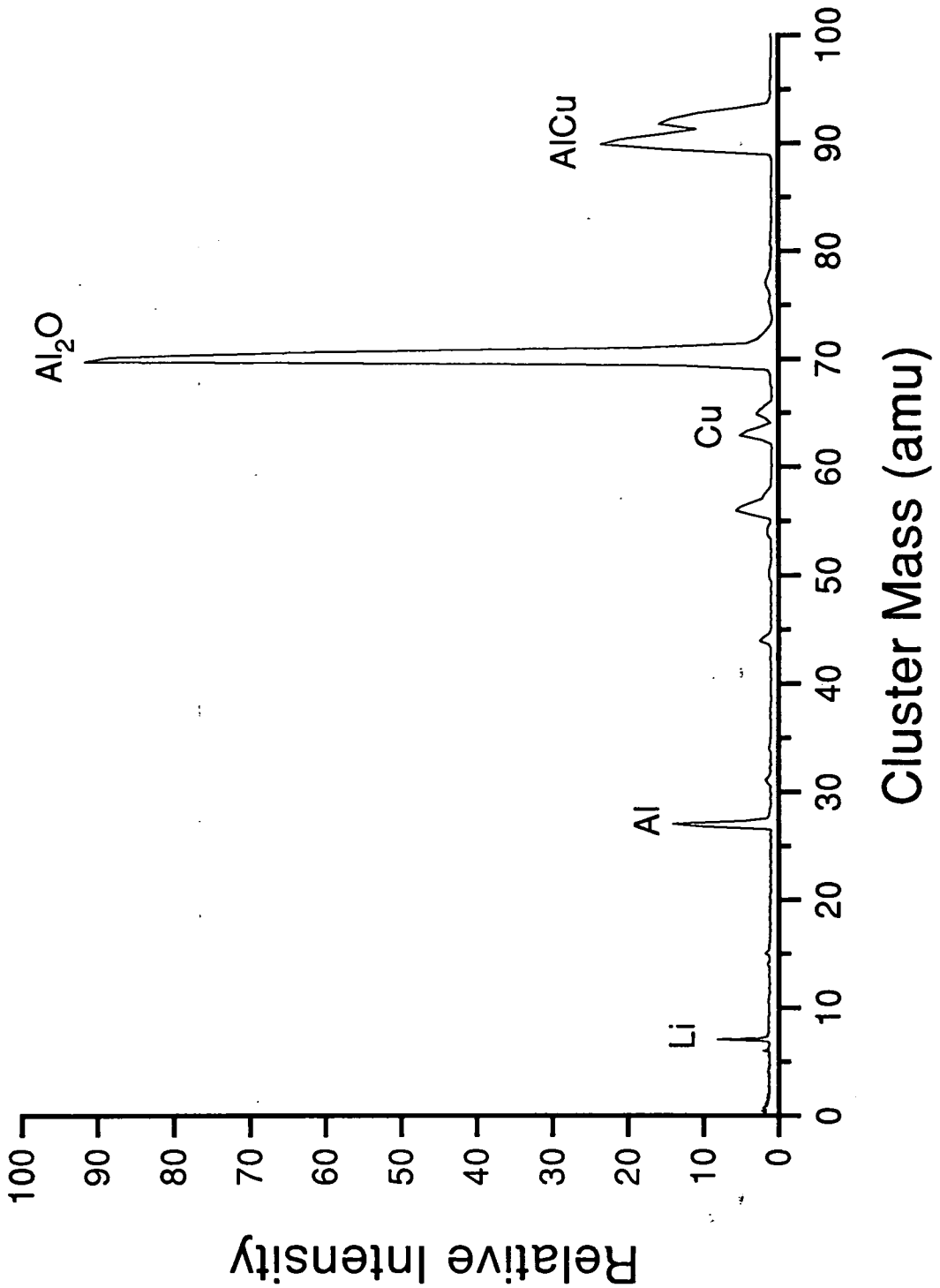

Figure 5–19: A mass spectrum obtained on vaporising a mixed metal target containing lithium, aluminium and copper. Photoionisation was carried with 193 nm radiation.

5.7 Conclusion

One of the most attractive features of the laser vaporisation technique is that it is not difficult to vary conditions in such a way that a particular range of clusters can be optimised. Some of the effects of these parameter variations have been described in this chapter, specifically for clusters of niobium atoms. Changing the deflection voltage of the ion optics allows adjustment of the centre of the so-called mass window, permitting examination of different cluster sizes. The more fundamental point of varying the actual range of clusters created obviously depends on the processes occurring in the cluster growth region of the apparatus. It has been shown that in many cluster sources increasing the length of the clustering channel promotes more aggregation, and that increasing the backing pressure of the inert carrier gas has a similar effect. These descriptions follow logically from the picture of the cluster growth mechanism which was presented in Section 2.3.

The results presented in this chapter illustrate the very wide range of materials that can be studied with the laser vaporisation technique. It must be noted that much can be inferred about the stability of certain cluster systems from their mass spectral intensities. The ideal models of geometric and electronic shells discussed in Chapter 4 have been shown to uphold descriptions of magic numbers observed in some real cluster systems, and this is an important confirmation of these models which helps to further the insight into the previously obscure region between the atomic and bulk extremes.

Bibliography

[1] W.C. Wiley and I.H. McLaren, Rev. Sci. Instrum., **26** (1955) 1150.

[2] C. Jackschath, I. Rabin and W. Schulze, Ber. Bunsenges. Phys. Chem., **96** (1992) 1200.

[3] M.B. Knickelbein, Chem. Phys. Lett., **192** (1992) 129.

[4] G. Alameddin, J. Hunter, D. Cameron and M.M. Kappes, Chem. Phys. Lett., **192** (1992) 122.

[5] B.J. Winter, E.K. Parks and S.J. Riley, J. Chem. Phys., **94** (1991) 8618.

[6] D.E. Powers, S.G. Hansen, M.E. Geusic, D.L. Michalopolous and R.E. Smalley, J. Chem. Phys., **78** (1983) 2866.

[7] L.S. Zheng, C.M. Karner, P.J. Brucat, S. Yang, C.L. Pettiette, M.J. Craycraft and R.E. Smalley, J. Chem. Phys., **85** (1986) 1681.

[8] O. Chesnovsky, P.J. Brucat, S. Yang. C.L. Pettiette, M.J. Craycraft and R.E. Smalley, '*Physics and Chemistry of Small Clusters*' (ed. P. Jena, B.K. Rao and S.N. Khanna), NATO-ASI Series No. 158, Plenum, New York, 1987.

[9] I. Katakuse, T. Ichihara, Y. Fujita, T. Matsuo, T. Sakurai and H. Matsuda, Int. J. Mass Spectrom. Ion Proc., **67** (1985) 229.

[10] E.C. Honea, M.L. Homer, J.L. Persson and R.L. Whetten, Chem. Phys. Lett., **171** (1990) 147.

[11] '*CRC Handbook of Chemistry and Physics*' (ed. D.R. Lide), 72^{nd} Edition, CRC Press, Boston, 1992.

[12] A.M. James, *Ph.D. thesis*, Edinburgh University, 1990.

[13] E. Kolodney and A. Amirav, Chem. Phys., **82** (1983) 269.

[14] M. Broyer, B. Cabaud, A. Hoareau, P. Melinon, D. Rayane and B. Tribollet, Mol. Phys., **62** (1987) 559.

[15] J.L. Persson, R.L. Whetten, H.P. Cheng and R.S. Berry, Chem. Phys. Lett., **186** (1991) 215.

[16] K.J. Taylor, C.L. Pettiette, M.J. Craycraft, O. Chesnovsky and R.E. Smalley, Chem. Phys. Lett., **152** (1988) 347.

[17] K.E. Schriver, J.L. Persson, E.C. Honea and R.L. Whetten, Phys. Rev. Lett., **64** (1990) 2539.

[18] M.F. Jarrold, J.E. Bower and J.S. Kraus, J. Chem. Phys., **86** (1987) 3876.

[19] S.B.H. Bach, S.W. McElvany, N.M. Wong and D.C. Parent, Chem. Phys. Lett., **209** (1993) 57.

[20] E.K. Parks, B.J. Winter, T.D. Klots and S.J. Riley, J. Chem. Phys., **94** (1991) 1882.

[21] E.A. Rohlfing, D.M. Cox, A. Kaldor and K.H. Johnson, J. Chem. Phys., **81** (1984) 3846.

[22] S. Yang and M.B. Knickelbein, J. Chem. Phys., **93** (1990) 1533.

[23] K. Athanassenas, D. Kreisle, B.A. Collings, D.M. Rayner and P.A. Hacket, Chem. Phys. Lett., **213** (1993) 105.

[24] P.P. Radi, G. von Helden, M.T. Hsu, P.R. Kemper and M.T. Bowers, Chem. Phys. Lett., **179** (1991) 531.

[25] A. Amrein, R. Simpson and P. Hackett, J. Chem. Phys., **95** (1991) 1781.

[26] K. Athanassenas, T. Leisner, U. Frenzel and D. Kreisle, Ber. Bunsenges. Phys. Chem., **96** (1992) 1192.

[27] D.M. Wood, Phys. Rev. Lett., **46** (1981) 749.

[28] B. Baguenard, M. Pellarin, C. Bordas, J. Lermé, J.L. Vialle and M. Broyer, Chem. Phys, Lett., **205** (1993) 13.

[29] M.B. Knickelbein and S. Yang, J. Chem. Phys., **93** (1990) 5760.

[30] P.J. Ziemann and A.W. Castleman, Jr., Phys. Rev. B, **44** (1991) 6488.

[31] E.A. Rohlfing, D.M. Cox and A. Kaldor, J. Chem. Phys., **81** (1984) 3322.

[32] H.W. Kroto, J.R. Heath, S.C. O'Brien, R.F. Curl and R.E. Smalley, Nature, **318** (1985) 162.

[33] A. Koch, K.C. Khemani and F. Wudl, J. Org. Chem., **56** (1991) 4543.

[34] L.A. Bloomfield, R.R. Freeman and W.L. Brown, Phys. Rev. Lett., **54** (1985) 2246.

[35] Q.L. Zhang, Y. Liu, R.F. Curl, F.K. Tittel and R.E. Smalley, J. Chem. Phys., **88** (1988) 1670.

[36] M.F. Jarrold and J.E. Bower, J. Phys. Chem., **92** (1988) 5702.

[37] K. Raghavachari and V. Logovinsky, Phys. Rev. Lett., **55** (1985) 2853.

[38] J.C. Phillips, J. Chem. Phys., **83** (1985) 3330.

[39] M.F. Jarrold and E.C. Honea, J. Phys. Chem., **95** (1991) 9181.

[40] A. Harano, J. Kinoshita and S. Koda, Chem. Phys. Lett., **172** (1990) 219.

[41] J.W. Macdonald, *Ph.D. thesis*, Edinburgh University, 1993.

[42] C.W. Bauschlicher Jr., S.R. Langhoff, H. Partridge and S.P. Walch, J. Chem. Phys., **86** (1987) 5603.

[43] A. Neubert and K. Zmbov, Trans. Farad. Soc., **70** (1974) 2219.

Chapter 6

GROUP-IIA METAL CLUSTERS

6.1 Introduction

The studies carried out on clusters of the alkaline earth metals during the course of this work are presented in this chapter. Clusters of some of the Group-IIA metals have been generated previously using oven sources, and results from the literature reveal a competition between an icosahedral geometric shell structure for the pure metal clusters, and a crystalline structure based on the face-centred cube for certain cluster oxides. Reported here are the first experiments in which clusters of these metals have been generated using the laser vaporisation technique. These studies were carried out in an attempt to clarify the nature of the structures assumed by these clusters. In all the experiments described here, magnesium, barium, and strontium were used as bulk targets in either the rod or disc cluster source. The results on strontium cluster oxides, in particular, are important as they have not been reported before, and they allow a more complete picture of the structures adopted by this group of clusters.

6.1.1 Background

The general reasons for interest in clusters of the Group-IIA metals can be clearly seen by looking at the characteristics of these metals. The study of a particular type of metal cluster is usually motivated by the desire to find out more about an unusual physical or chemical property specific to that system. In the case of clusters of the alkaline earth metals of Group-IIA the interest lies in probing

systems which evolve into bulk metals even though the atomic characteristics of the species show no definite tendency towards metallic behaviour. In fact the electronic structure of these divalent species is such that the exhibition of insulating properties for these materials would not, at first glance, be too surprising. This is due to the fact that the divalent atoms, in a solid state picture, each contribute two electrons to the primitive cell, resulting in a fermi sphere which possesses the same volume as the first Brillouin zone [1]. The question then is whether the pseudopotential generated by the remaining ionic cores is strong enough to shrink the pockets of electrons in the second zone back into the first zone, and remove any trace of metallicism. Since these species are bulk metals, then obviously the pseudopotential is rather weak. However, metallic bonds are typically quite strong, and yet the dimers of these elements are very weakly bound. There is therefore some interest in the development of the various properties of these cluster systems as they grow from atoms towards the bulk.

Experiments show that it is actually quite difficult to generate pure clusters of these materials. They often tend to be easily contaminated, mainly by any oxygen impurities existing in the apparatus. The two structural types which have been shown to exist for these metal clusters and their cluster oxides take the form of pre-crystalline icosahedra in the case of the pure metals, and fragments of the bulk crystal structure as more oxygen is incorporated into the cluster. Evidence for these differences has been provided for certain of the alkaline earth metal systems. Pure magnesium and calcium clusters have been shown to adopt icosahedral structures [2,3]. Clusters of magnesium oxide and calcium oxide, however, have been shown to prefer a rock salt structure [4,5,6,7] similar to that of sodium chloride [8] and other alkali halide cluster ions [9].

Previous studies of these alkaline earth metal species have used inert gas ion sputtering and gas aggregation techniques to generate the clusters. The work presented here is unique in that no other studies of these species using the laser vaporisation technique have been reported, probably due to some of the inherent difficulties involved in working with or generating clusters of these materials.

6.2 Magnesium Clusters

The first experiments carried out on the Group-IIA metals in the present work involved an attempted study of magnesium clusters. These experiments were not successful, although from comments in the literature it is prehaps not surprising that no decent magnesium cluster signals could be generated. Martin *et al.* [2] have shown that pure magnesium clusters containing up to 2869 atoms adopt icosahedral geometries. The magnesium clusters in this study were created in an inert gas condensation experiment, with subsequent laser photoionisation and detection by time-of-flight mass spectrometry. It is noted in this paper that the magnesium clusters were very difficult to observe, and an estimate was made that only one cluster was being detected for each laser shot. To achieve a reasonable degree of cluster intensities, 200,000 individual spectra were summed, and the slightly smoothed spectrum was subtracted from a more highly smoothed background envelope. Even so, the actual cluster peaks were only barely discernible from the spectral noise.

In order to have any hope of performing a similar experiment in this laboratory, then a spectrum would have taken over five and a half hours to collect at the experimental repetition rate of 10Hz. Unfortunately, it was not possible to achieve stable operation of the laser vaporisation cluster source for such an extended period of time.

Further confirmation of the difficulty in generating clusters of this element is provided by the work of Ziemann *et al.* [6] on magnesium cluster oxides. In this study no bare magnesium clusters larger than the dimer could be detected.

6.3 Barium Clusters

Following the unsuccessful experiments on magnesium, the next element on which experiments were attempted was barium. These experiments were more successful. However, before the results that were obtained are shown, the previous work that has been reported in the literature on this system is briefly discussed.

6.3.1 Previous work

Barium clusters have previously only been generated using oven sources coupled with inert gas condensation techniques. The magic numbers observed for barium clusters in these studies were consistent with an icosahedral packing arrangement of the barium atoms [10,11]. Rayane *et al.* [10] employed an electron impact ionisation source in their work, and were able to generate doubly and triply charged barium clusters. The intensity anomalies observed in these spectra occurred for the same cluster sizes irrespective of the charge state of the cluster. This result pointed to the fact that the magic numbers for barium clusters were clearly based on geometric stabilities. For an electronic shell system, a change in the charge state of the metal clusters would result in a shift in the observed series of magic numbers.

The results reported by Martin *et al.* [11] were equally interesting in that oxygen contamination of the barium clusters was observed, but this did not seem to affect the magic numbers which appeared in their spectra. Clusters were generated by quenching barium metal vapour, from a typical oven source, in helium gas. The clusters were photoionised with focussed 308 nm excimer radiation, and detected by time-of-flight mass spectrometry. Metal-rich barium oxide clusters of the formula Ba_nO_x were detected with x = 1,2,3,4. Clusters containing particular numbers, n of barium atoms were found to be especially stable irrespective of the number, x, of oxygen atoms.

6.3.2 Results

The work presented here shows the first barium cluster distribution achieved using the laser vaporisation source. A 22mm diameter barium rod was obtained from Johnson Matthey, and this was turned down to a 5mm diameter for use in the cluster rod source. The barium was initially packed under argon, but after machining was stored in mineral oil to minimise oxidation. The cluster mass spectrum obtained, following photoionisation with KrF radiation at 248 nm, is shown in Figure 6–1. Reproducibly high stabilities are observed for clusters containing 13, 19, 23, 26, 29, and 32 barium atoms, as noted in the diagram. The lower mass range of Figure 6–1 is expanded to show the distribution of oxides associated with specific barium clusters in Figure 6–2. Each grouping of cluster peaks in Figure 6–2 corresponds to a specific size of barium cluster, Ba_n, and each peak within a grouping corresponds to the barium cluster with the incorporation of x oxygen atoms. The most intense peak within each Ba_n grouping is noted on the spectrum.

It can be seen from these two figures that the individual peaks become difficult to resolve from about Ba_7O_x onwards. This is due in part to the limited resolution of the mass spectrometer, and also to the presence of a number of peaks due to the different barium isotopes. Mass spectral measurement of the peaks beyond approximately 1000 amu, along with the trends observed below this mass, leads to the conclusion that the most intense peaks within a specific Ba_nO_x group for $n \geq 7$ correspond to values of x = 1-3. The actual range of cluster oxides observed for a specific barium cluster proceeds only up to Ba_nO_{n-1}. This point will be important later on, when the results obtained on strontium cluster oxides are analysed.

The fact that homogeneous clusters of magnesium and calcium exist preferentially as icosahedra has been shown by the close match of the observed magic numbers for these systems with the known closed shell Mackay icosahedra, which were shown earlier in Figure 4–4. The fact that a 13-atom barium cluster is exceptionally stable is not enough evidence alone to infer icosahedral packing of the atoms. The size range of the barium clusters observed is such that the second

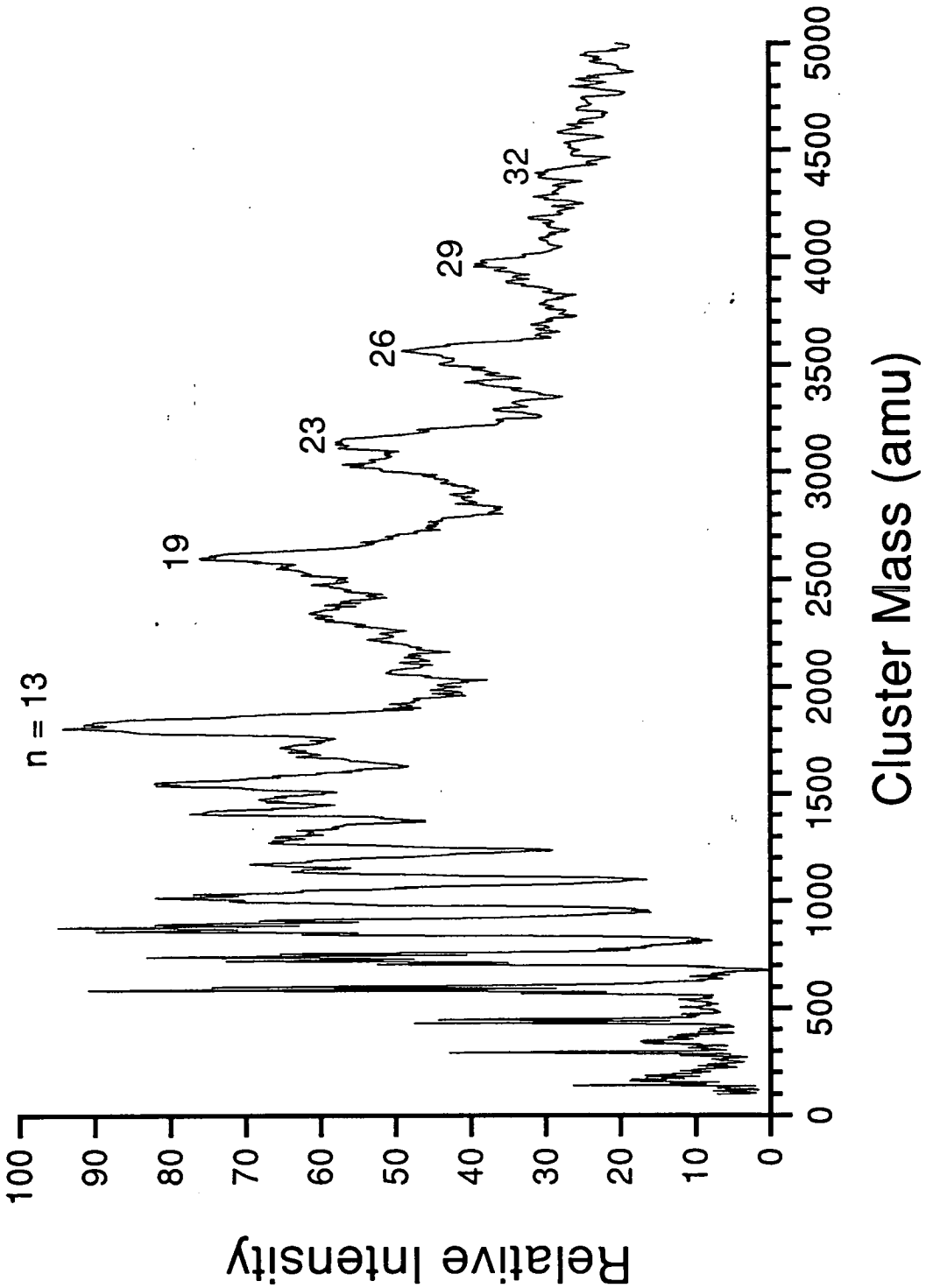

Figure 6–1: Mass spectrum of Ba_nO_x clusters. The numbers of barium atoms in the most stable clusters are indicated, and each labelled peak includes contributions from the cluster oxides containing between 1 and 3 oxygen atoms.

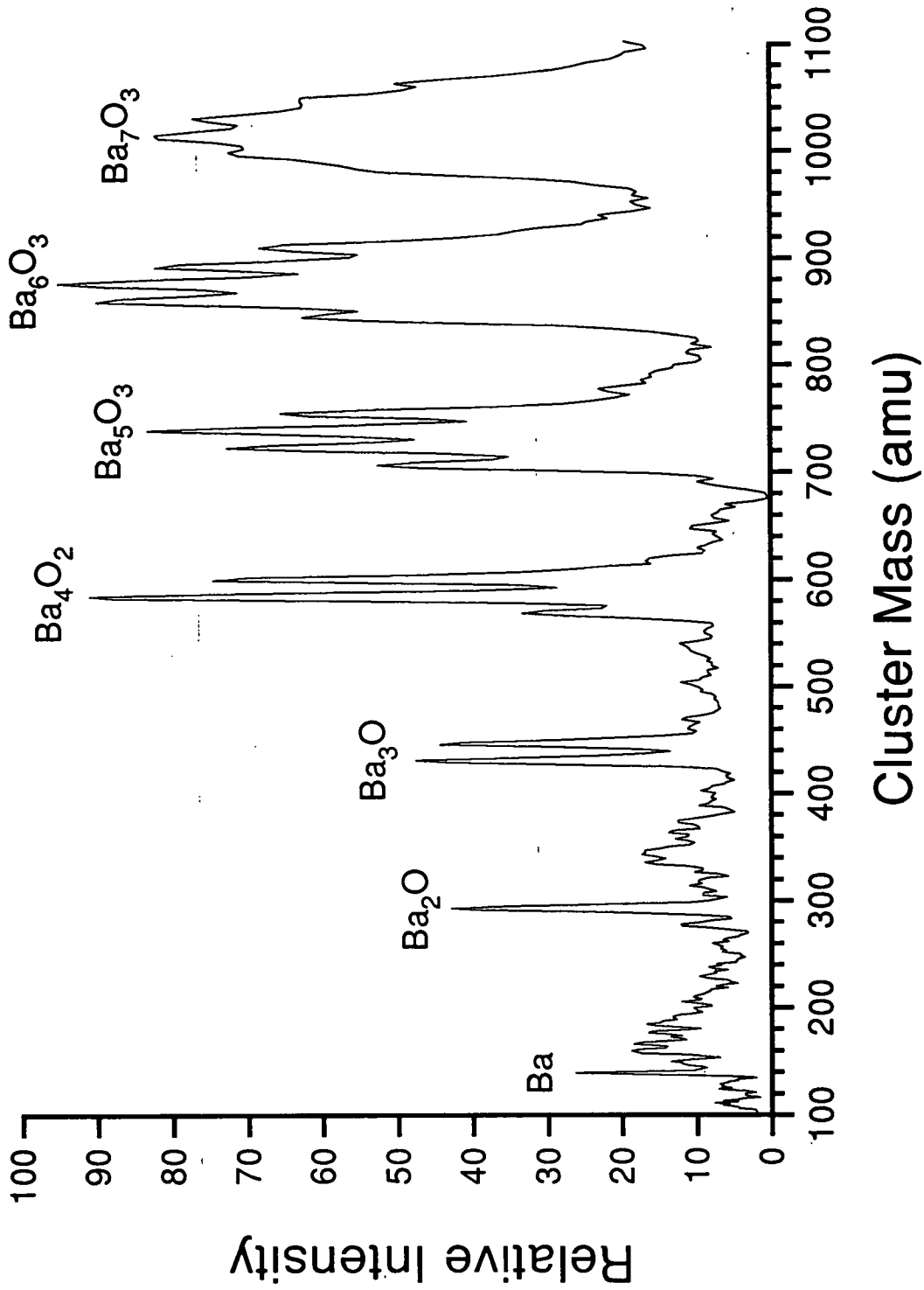

Figure 6–2: Expansion of the previous mass spectrum to show the individual cluster peaks.

closed icosahedron containing 55 atoms is not detected. Despite this, the magic numbers exhibited by barium clusters can still be said to conform to an icosahedral arrangement of the atoms if the stabilities of partially filled shells are analysed.

The concept of geometric subshells was discussed in Section 4.3, and it is this facet of the shell effect which must now be utilised. Figure 6–3 shows the most probable growth pattern of additional atoms onto a 13-atom icosahedron using the so-called 'umbrella' model. The hollow circles represent the positions in which atoms must be placed onto the 13-atom icosahedron in order to achieve coverage of this structure towards completion of the 55-atom icosahedron. Islands of stability can be reached as successive pentagonal caps are completed. Six atoms placed over one end of the icosahedron results in a very stable structure which appears as a double interpenetrating icosahedron containing 19 atoms. Completing the next adjacent pentagonal cap only requires the addition of four more atoms, as two of those required are shared with the recently filled area. Thus the next subshell occurs for a cluster containing 23 atoms. This process continues as above, and the subshells obtained fit perfectly with the magic numbers observed in the barium cluster mass spectrum presented in Figure 6–1.

The observation of icosahedral structure for pure barium clusters [10] was perhaps not unexpected. However, the persistence of this structure on the incorporation of several oxygen atoms is rather peculiar. It is difficult to say why icosahedral structures seem to be preserved on the inclusion of oxygen. If the oxygen exists in the cluster in the form of BaO molecules, then the polar nature of this species would be expected to distort the cluster. Perhaps the answer lies more simply in the relative covalent radii of the two atoms. The large Ba/O size ratio could allow a few oxygen atoms within an essentially pure barium cluster icosahedron without too great a distortion of this highly symmetric geometry. In comparison, the other alkaline earth metal clusters which have been studied (Mg and Ca) consist of atoms which are closer in size to the O atom. In these cases the inclusion of oxygen atoms within clusters of these materials destroys the overall icosahedral symmetry. This then leads to the metal oxide systems adopting stoichiometries which allow the formation of stable fcc-type structures.

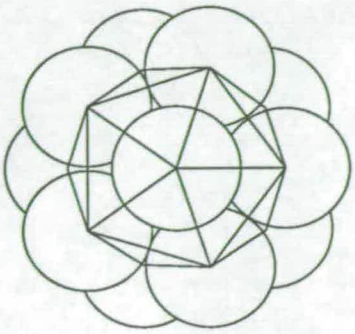

13-atom icosahedron

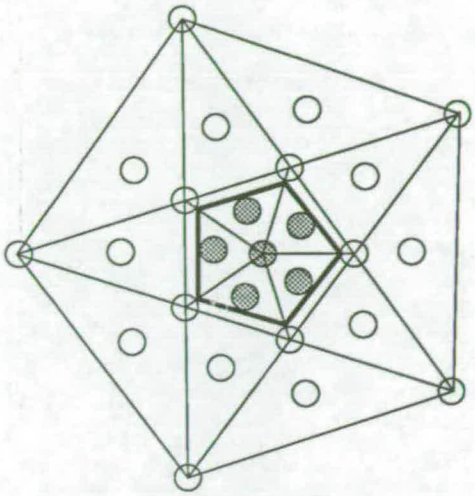

+6 = 19 atoms

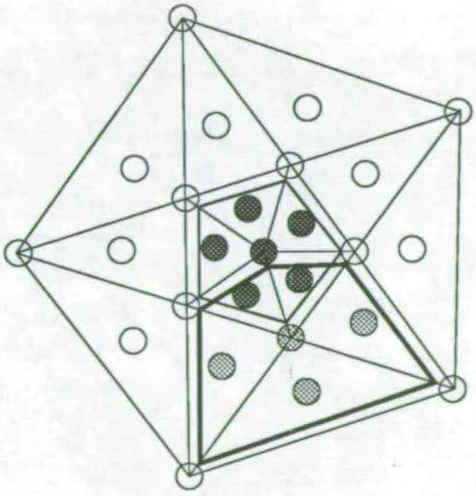

+4 = 23 atoms

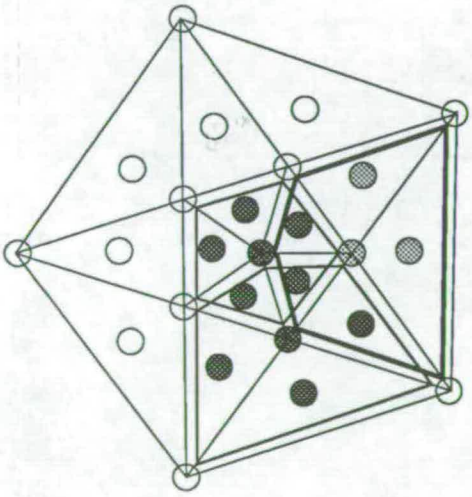

+3 = 26 atoms

Figure 6–3: The picture of icosahedral subshells used to describe the magic numbers observed in barium cluster abundances.

This observation opens up avenues of future research. Is it possible to observe Mg-O and Ca-O cluster icosahedra if only a few oxygen atoms are incorporated into the clusters? This experiment would require precise control of the amount of oxygen allowed into the clustering region. Secondly, will Ba-O clusters show bulk lattice structures if more oxygen is introduced as the aggregation proceeds? It is known that all of the bulk metal oxides from this group result in an NaCl face-centred cubic structure, but that the lattice energy decreases down the metal group. Perhaps the Ba-O lattice is not cohesive enough to show up as a stable cluster structure.

Another interesting question concerns the preferred compositions and structures of Sr-O clusters. It has been shown that Mg-O and Ca-O clusters form stoichiometric or marginally metal-rich cluster ions with magic numbers which indicate a preference to form fragments of an fcc-type lattice structure. The lack of this structure, and the preference for icosahedra has been shown for Ba-O clusters. Since strontium comes between calcium and barium in this group of the periodic table, which of the two competing structures will it conform to? As discussed below, it will be shown that in fact the Sr-O cluster abundance spectrum bears little resemblance to the barium cluster spectra shown here.

6.3.3 Barium dimer

Before leaving the barium cluster system, it is worth noting that there have been no studies of the electronic spectrum of barium dimer reported in the literature. Indeed it was only recently that the first electronic spectrum for Sr_2 was reported [12,13]. Broyer's group formed strontium clusters up to Sr_5 by coexpansion of strontium vapour with argon as a seed gas. Mass spectrometry was used to detect the photoionised clusters, and depletion spectroscopy was used to study the electronic structure of the dimer. As noted, these dimers are difficult to make as they are only weakly bound. No pure barium clusters were seen at all by Martin *et al.* [11], and they suggested that the more stable BaO molecule was the base unit around which the higher Ba_nO_x clusters grew. The laser vaporisation source,

coupled with supersonic expansion, is known to produce extremely cold clusters, with internal temperatures routinely of the order of 20K. This, therefore, should be an ideal source with which to study such a weakly bound species as Ba_2. The main problem is obviously the amount of oxygen uptake by the barium clusters as they are growing.

Several experiments were undertaken in an attempt to see if it was possible to generate a cluster beam containing a sufficiently high concentration of barium dimer for future spectroscopic studies to be carried out. In order to reduce the amount of cluster oxides present, two steps were taken. The first involved cooling the helium carrier gas in liquid nitrogen before it passed through the pulsed valve. This was carried out in an attempt to minimise the amount of impurities inherent in the helium supply. The second step involved fitting a brass block around the snout of the end extender on the clustering channel. Liquid nitrogen was then allowed to flow through a copper tube in thermal contact with the brass cooling block. Again, it was hoped that this modification would trap out any impurities in the immediate vicinity to allow a cleaner cluster growth. By using these two cooling methods, the mass spectrum shown in Figure 6–4 was obtained. The most important point about this mass spectrum is the relatively low number of experimental shots that were summed to record it. Typical cluster abundance spectra were usually recorded by summing 500 or 1000 shots to improve the signal to noise ratio. For example, the barium cluster mass spectrum presented in Figure 6–1 was recorded by summing 1000 individual spectra. The spectrum shown in Figure 6–4, however, was taken by collecting only 30 shots. This spectrum shows that the intensity of pure Ba_2 can be enhanced under the right conditions. The signal is certainly intense enough to permit spectroscopic studies of this species to be carried out. Due to time constraints and the interest in making comparative measurements on strontium clusters no spectroscopic investigation of Ba_2 was attempted at this stage.

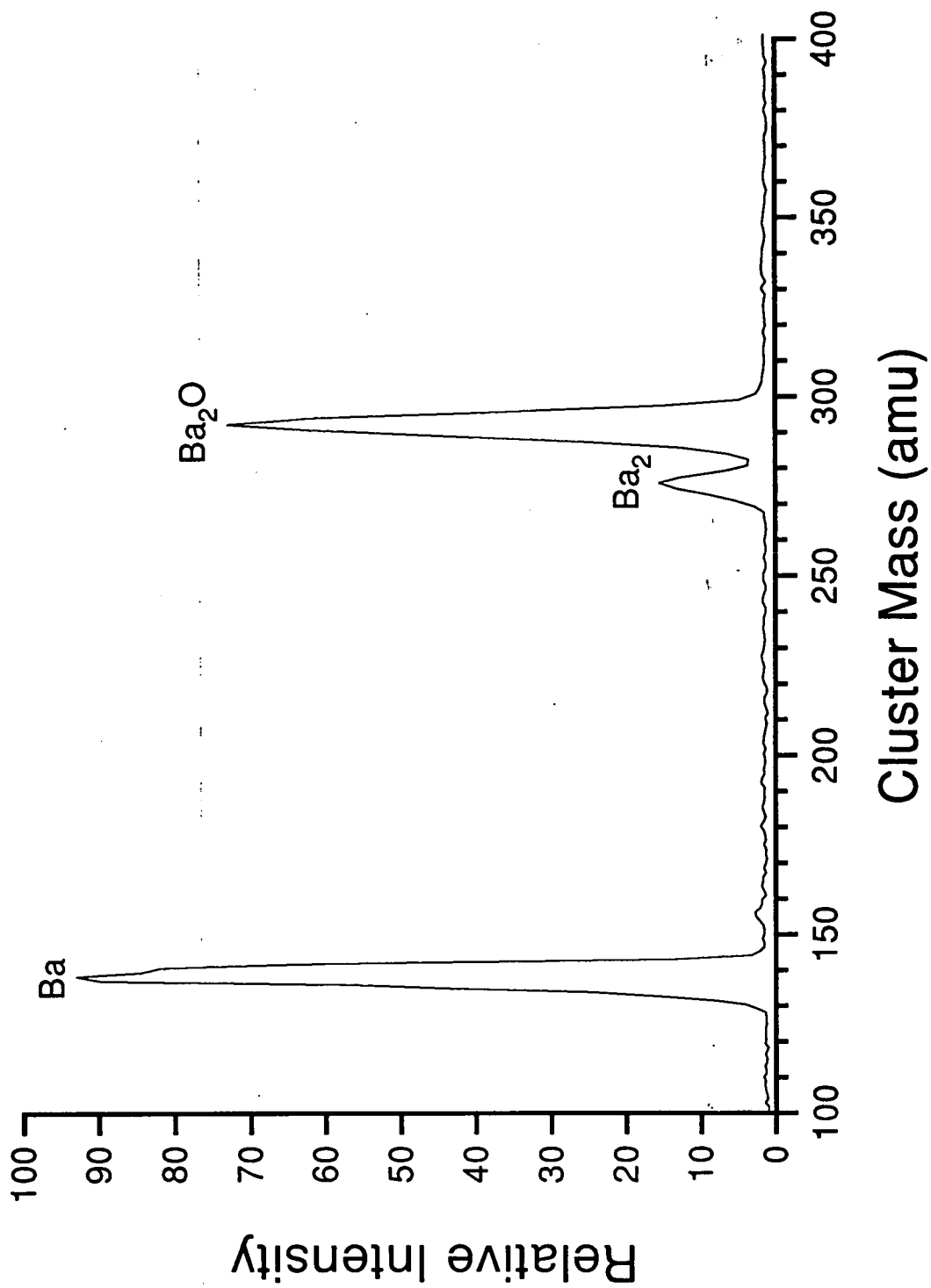

Figure 6–4: A mass spectrum showing the production of Ba_2 by cooling the helium carrier gas and the clustering channel with liquid nitrogen.

6.4 Strontium Clusters

The results presented in this section show the mass spectra obtained for strontium cluster oxides generated for the first time using the laser vaporisation technique. This system was studied to link the results obtained in this work and elsewhere for clusters of the other Group-IIA metals. Experiments on clusters of magnesium, calcium and barium have been documented, but a gap exists in the case of strontium.

A 16mm diameter strontium rod, obtained from Johnson Matthey, was turned down to 5mm diameter and used in the rod source. A mass spectrum showing the cluster species generated when using this target, following photoionisation with 248 nm radiation, is shown in Figure 6–5. Before discussing the specific magic numbers that were observed for the strontium cluster oxides, some general comments on the cluster compositions found in the mass spectra are warranted.

Immediately, the most striking feature of the spectrum shown in Figure 6–5 is that it bears little resemblance to the barium oxide cluster distributions displayed in the previous section. The next point to note from this spectrum is that the most intense peak for each specific size of strontium cluster corresponds to a cluster with the composition $Sr_nO_{n-1}^+$ after ionisation. This is sometimes presented in the form $Sr(SrO)_m^+$ (where now $m = n - 1$).

This composition has been observed in other systems as discussed below, and has frequently been indicative of structures resembling fragments of a face-centred cubic crystal. The main systems to consider for the purposes of comparison are the other group II-VI compound clusters, and the alkali halides. Both of these types of clusters have shown evidence of the fcc structure, but are there any differences which might make one system more applicable to the strontium oxides?

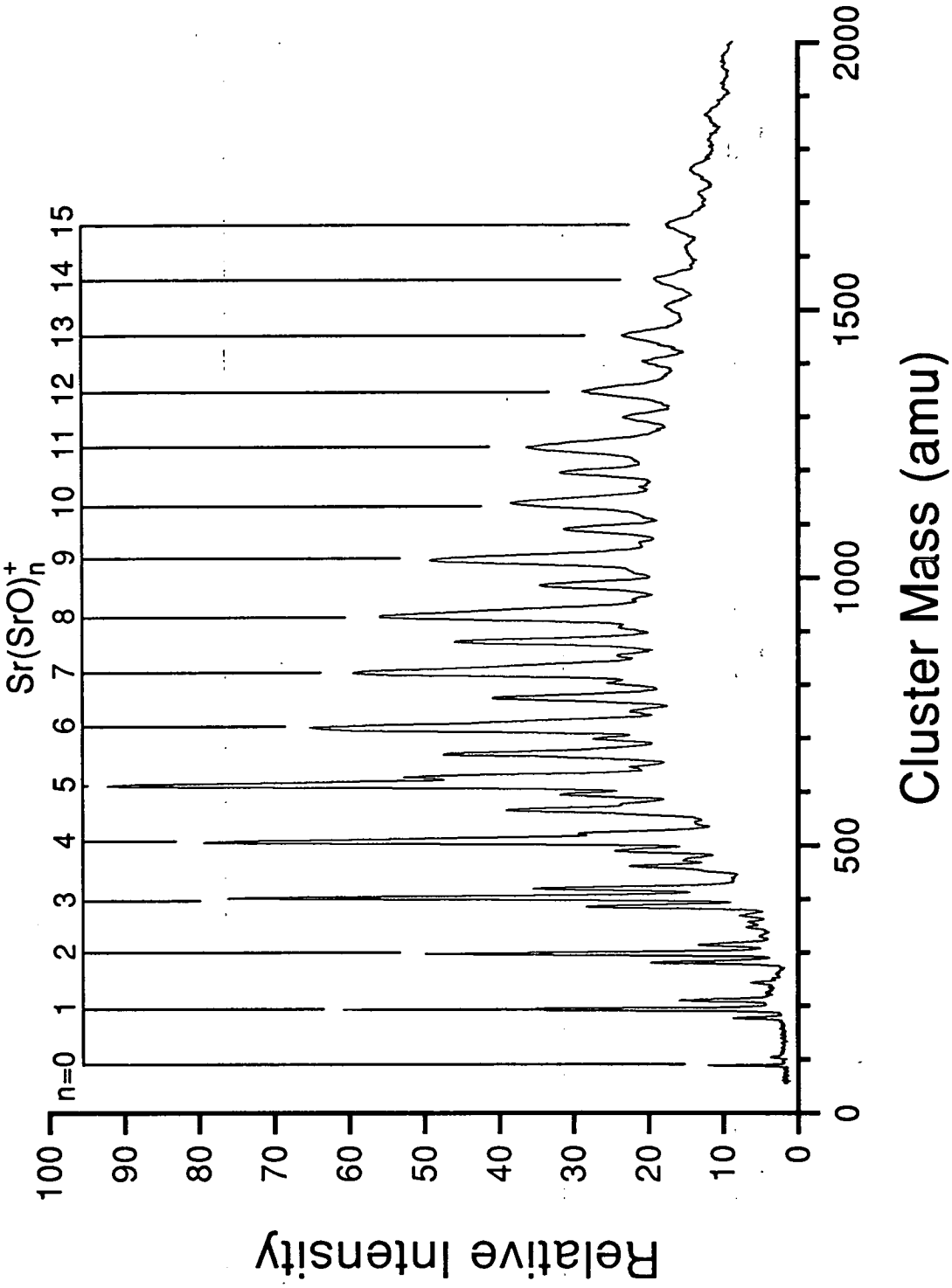

Figure 6–5: A mass spectrum showing strontium cluster oxides after photoionisation with the KrF excimer line at 248 nm.

6.4.1 Results on related systems

Alkali halide clusters

Alkali halide clusters have been shown to adopt fcc-type structures corresponding to clusters with the generic composition $M(MX)_n^+$, where M is the alkali metal, and X is the halide component of the cluster[1]. These compositions were initially demonstrated to exist for NaCl clusters [8,14,15], and then latterly for clusters of RbCl [16], NaI, CsCl, CsI [9], and NaF [17].

Within the alkali halides the prominence of the magic numbers observed is different for each system. It has been noted that an increased contrast in intensities between magic and non-magic species results for systems with a higher lattice energy [18]. Obviously, the degree to which these systems conform to the bulk fcc-type structures also depends on the degree of ionicity of the particular species. This facet manifests itself when looking at 'subshell' structure for the cubic lattices.

It has been shown that closed ion cuboids are exceptionally stable structures for the systems discussed here. It has also been suggested, and experimentally verified, that completed terraces on the surfaces of the cuboids are also stable. This is due to the fact that in an environment of ionic bonding, the atoms situated at kink sites are weakly bound, and can be easily stripped away to leave complete ion cuboids with or without terraces.

If, however, there is an appreciable degree of covalent character to the bonding within the system, then the next-nearest neighbours will contribute to the overall binding energy. This would result in an increased stability for kink site ions, perhaps to a level where ions at the corners of the cube are less strongly bound. The outcome of this scenario would be a series of magic numbers slightly displaced from those expected for fcc structures. The appearance of these clusters would

---

[1]These forms and fcc lattice structures have also been reported for doubly-charged alkali halide clusters.

also be altered to cuboid-like forms with rounded corners and, in the extreme case, rounded edges.

An important point to consider is the relationship between the neutral cluster abundances, and the observed ion intensities. For the sodium chloride system, stoichiometric clusters are the dominant neutral species but these fragment on ionisation as follows:

$$(NaCl)_{n+1} \xrightarrow{h\nu} Cl + Na(NaCl)_n^+$$

This results in the detected species being dominated by metal-excess alkali halide cluster ions.

The actual magic numbers exhibited have been shown to depend on the initial cluster temperatures. One particular study of NaCl clusters [8] reported that the magic numbers observed in the mass spectrum depended on whether the clusters generated were cold or at room temperature. The cold clusters, created by quenching sodium chloride vapour in helium at 30K, could be attributed to stable ion cuboids. The warm clusters, however, were linked to stable *neutral* cuboids. It is important to emphasise that both series of magic numbers corresponded with an fcc-structured system.

The clusters created using helium at 300K as a seed gas exhibited magic numbers for the $Na(NaCl)_n^+$ species at n = 17, 19, 23, 29, 31,.... These were due to the fact that warm clusters had enough internal energy to show a preference for stable neutral cuboids of the form $(NaCl)_{n+1}$, depicted in Figure 6–6. These species would be present in the neutral cluster beam in greater amounts, losing a chlorine atom upon ionisation to give the cluster ion magic numbers which were in fact related to the neutral cluster magic numbers.

Other Group-IIA cluster oxides

Pure clusters of magnesium and calcium have shown a preference to adopt icosahedral structures. As oxygen is allowed into the clustering region, then cluster oxides are produced with $Mg(MgO)_n^+$ and $Ca(CaO)_n^+$ as the dominant cluster ion

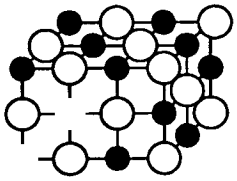

n = 17 (3x3x4)

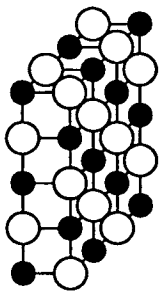

n = 19 (2x4x5)

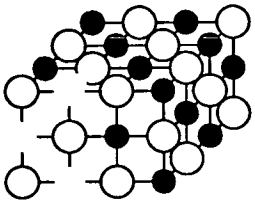

n = 23 (3x4x4)

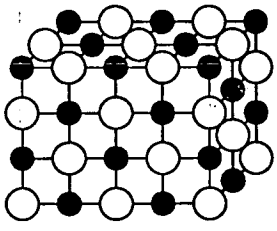

n = 29 (3x4x5)

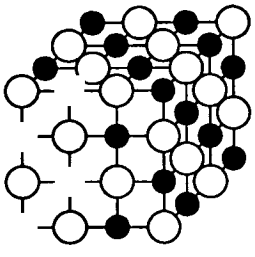

n = 31 (4x4x4)

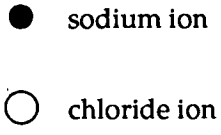

Figure 6–6: The stable $(NaCl)_{n+1}$ cuboid structures which result in appropriate magic numbers, n, for the cluster ions $Na(NaCl)_n^+$ after ionisation and dissociative loss of a chlorine atom.

compositions in the mass spectra. As well as conforming to the general $A(AB)_n^+$ composition, clusters of the Mg-O and Ca-O systems assume fcc-type geometries. The magic numbers in the mass spectra are attributable to stable ion cuboid formations. However, for the smallest clusters, there are competing structures which are very stable, and this leads to differing magic numbers for each system. For $n < 11$, $Mg(MgO)_n^+$ is stable for $n = 8$, whereas the corresponding Ca-O cluster ions are stable for $n = 5, 7, 9$. For slightly larger clusters, definite fcc structures are seen for both systems, with enhanced stabilities for $n = 11, 13, 16, 19, 22, \ldots$ [5].

Again, it is important to consider the relationship between the neutral cluster abundances for these species, and the observed cluster ion intensities. The existing evidence in the case of Ca-O clusters is that the heavy presence of $Ca(CaO)_n^+$ ions detected is due to the large population of neutral $Ca(CaO)_n$ species in the cluster beam [7]. In fact, even more metal-rich cluster ions of the form $Ca_m(CaO)_n^+$ have been detected, where m ranged from 1 - 5. The fact that the cluster ions containing a single excess metal atom were not a result of the same fragmentation step which occurs for the alkali halides was apparent from experimental observation. When the ionisation laser power was increased the cluster distributions shifted towards less excess metal atom clusters, showing that the clusters were fragmenting by losing metal atoms or ions.

A note of caution as to the exact applicability of particular structural stabilities for the smallest clusters is revealed in Ziemann's work on Mg-O clusters [5]. This study was prompted by an interest in the fact that the bonding in bulk magnesium oxide is predominantly ionic, whereas the MgO molecule has bonding character which is half ionic, and half covalent. This point can be extended so that the smaller clusters of the group II-VI compounds can be pictured as having a fair component of covalent character in the bonding of the system. It was stated above that the existence of covalent character in these systems can lead to a pattern of cluster stability which differs from an fcc system in which the bonding is purely ionic.

The fact that it has been shown in this work that the strontium cluster oxides exist with the same compositions as the Mg-O and Ca-O systems leads one to

believe that similar magic numbers will be revealed for the Sr-O system, reflecting a preferred fcc structure for these clusters.

In addition to the alkali halides, magnesium and calcium oxides already discussed, there is compelling evidence that clusters of titanium nitride [19], titanium carbide [20], and boron nitride [21,22] also exist preferentially in the general form $A_nB_{n-1}^+$ under certain conditions. Clusters with this composition have also been shown to conform to an fcc structure. The specific case of TiC clusters is rather interesting in that two distinct structural forms seem to exist, depending on the composition of a particular cluster. It was found that metal-rich clusters existed as fcc fragments with the formula $Ti_nC_{n-1}^+$. The metal deficient clusters, however, adopted a cage-like structure described by a pentagonal dodecahedron. These are known as 'Met-Cars', the archetypal cluster in this group being Ti_8C_{12}. Other Met-Car systems have been reported [23,24] and it seems that these species may well find important future applications due to their unusual structures.

6.4.2 Sr-O cluster spectra: Discussion of results

It is easier to imagine that strontium oxide clusters would be likely to resemble fellow clusters of the alkaline earth metal group, rather than the alkali halide clusters. Thus, the initial assumption would be that the $Sr(SrO)_n^+$ species observed in the spectrum shown in Figure 6–5 are due to the predominant neutral cluster species in the molecular beam being $Sr(SrO)_n$. However, this fact cannot be easily verified simply by the observation of cluster ions with this composition in the mass spectrum. For example, Figure 6–7 shows the lower mass range typical of the strontium cluster oxide spectra obtained, and the compositions of the cluster ions present require some note. As well as the intense $Sr(SrO)_n^+$ ions, there also appears to be a significant amount of $(SrO)_n^+$ species present. This indicates that the neutral counterparts of these stoichiometric species are present in the molecular beam to a considerable extent. Thus, the clusters with one excess metal atom could have been produced by ionisation of neutrals of the composition $Sr(SrO)_n$, or by fragmentation of neutrals with the composition $(SrO)_n$ following ionisation.

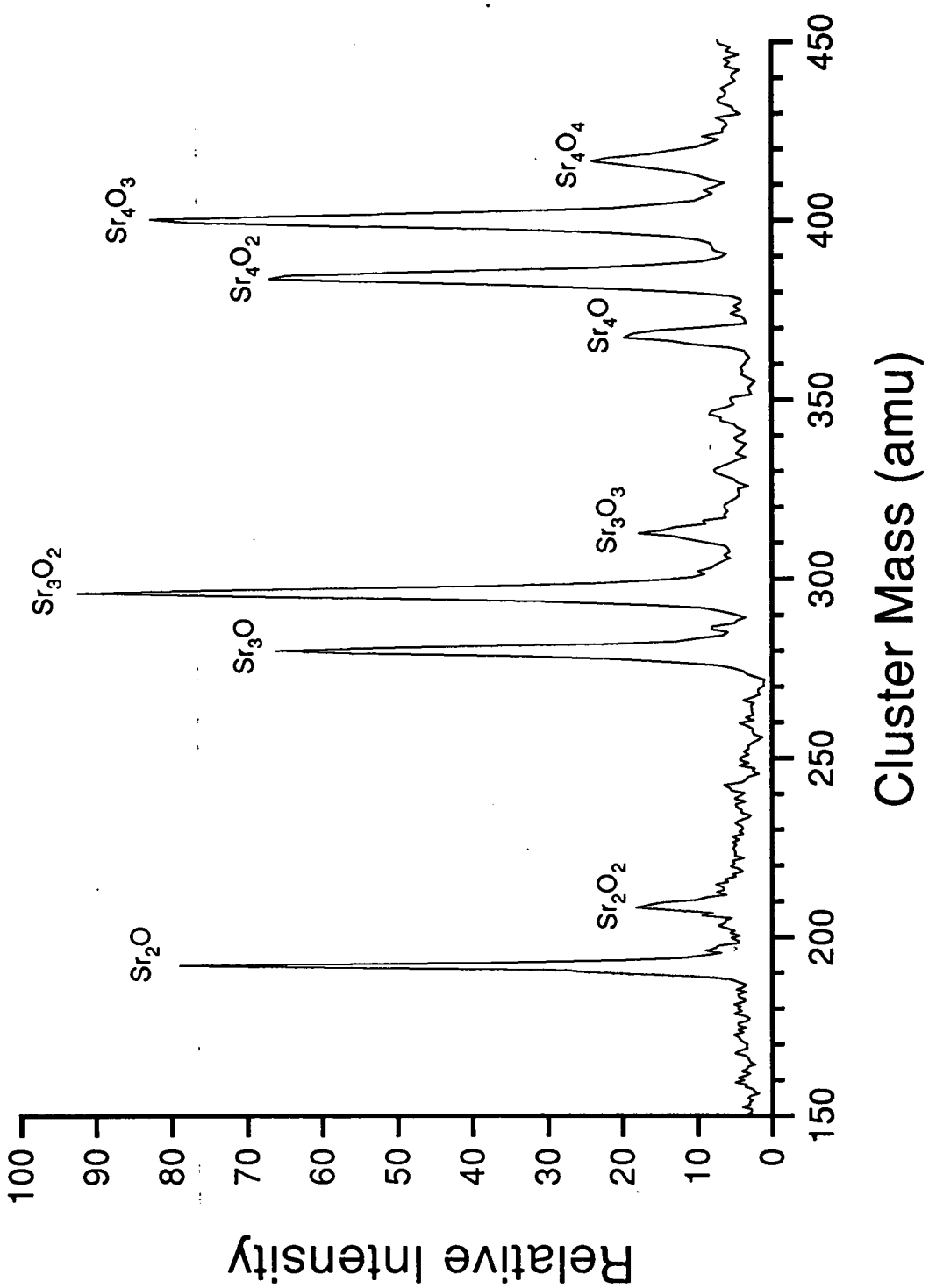

Figure 6–7: An expanded view of the lower mass range of the Sr-O cluster mass spectra, showing the range of oxides associated with each strontium cluster.

Such a fragmentation event can occur if the wavelength of the ionising laser allows access to a dissociation channel for the cluster in question. There has been a study of the fragmentation dynamics of the smallest Sr-O and Ca-O clusters [25], and this has shown that around 2eV is required to dissociate small $Sr(SrO)_n^+$ clusters, for n = 1 - 3. This value increases slightly, as does the width of the photodissociation transition as the cluster size increases. However, no data is available for the neutral $(SrO)_n$ species, so no clue as to the likelihood of cluster fragmentation can be gained from the literature for the clusters studied here. A clue as to the origin of the detected cluster ions can be gained on looking at the magic numbers of the system.

To identify the stable clusters, the mass spectra must be re-examined. The Sr-O cluster distribution obtained in the lower mass range was shown in Figure 6–5. A spectrum recorded showing the distribution to higher cluster size is presented in Figure 6–8. Again, the fact which is most immediately apparent about this spectrum is the lack of similarity with the barium oxide cluster spectra shown earlier in this chapter. At first this might seem remarkable due to the fact that strontium sits above barium in Group-IIA of the periodic table. However, we have seen that clusters of calcium oxide show different magic numbers than the barium oxide system. Since strontium lies between these two elements in this group, then it is logical that it will differ from at least one of them.

Trying to visually identify the magic numbers from a mass spectrum can sometimes be difficult, especially if there are complicating factors, such as an uneven mass transmission function over the size range studied. It is apparent from the spectra presented that n = 5 is exceptionally stable for the $Sr(SrO)_n^+$ series. However, for the rest of the cluster peaks, some spectral manipulation is necessary in order to clarify the intensity anomalies present in the mass spectra.

A very good way to enhance the emergence of magic numbers involves taking the logarithmic derivative of the cluster intensities [26]. This has the effect of eliminating the influence of the global shape of the mass spectrum. In practice, this procedure is well approximated by a logarithmic plot of the form $\ln(\frac{I_{n+1}}{I_n})$ versus n, where I is the intensity of a particular cluster. Usually, n denotes

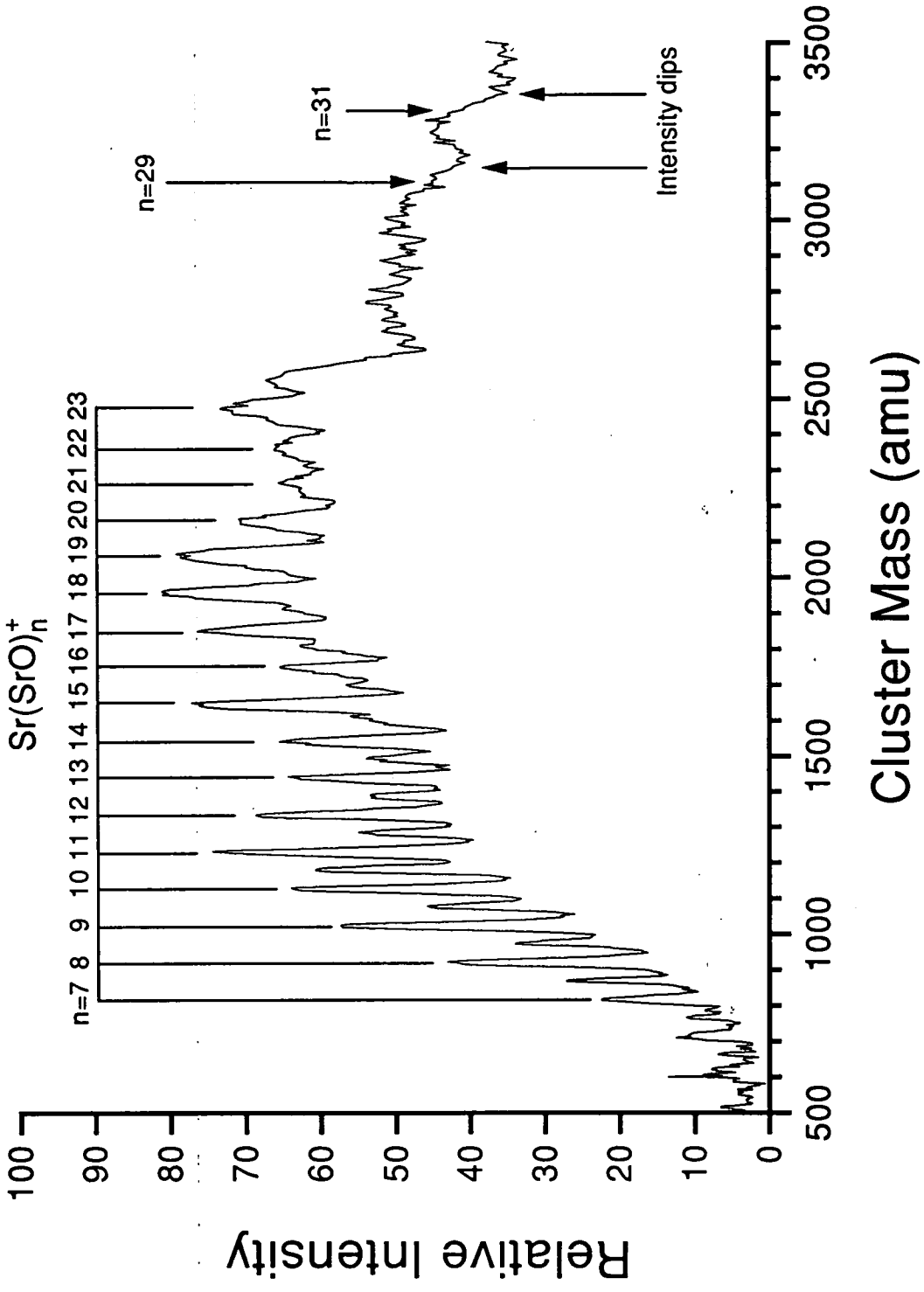

Figure 6–8: A mass spectrum of higher mass strontium oxide clusters (ionised by a KrF excimer at 248 nm).

the number of atoms in the cluster, but in this case it is equivalent to the n in the cluster formula, $Sr(SrO)_n$. In order to carry out this procedure the data in the spectrum to lower mass shown in Figure 6–5 were combined with the data in Figure 6–8 by normalising the former to the peak intensities observed for the species $Sr(SrO)_9^+$. Figure 6–9 shows the resulting plot of the logarithmic derivative of clusters intensities that was obtained. The stable clusters in this figure are signified by dips in the plot. Thus the strontium cluster oxides which show an enhanced stability on detection are those of the form $Sr(SrO)_n^+$, for n = 3, 5, 9, 11, 15, 19, and 23. Some of these magic numbers correlate with those found for various fcc-type systems, but there are a few major discrepancies.

The smallest magic numbers for the Sr-O clusters fit some of those observed for Ca-O clusters (n = 5, 9, 11), but not enough to allow a definite conclusion to be reached about the structural nature of the Sr-O system over this size range. The absence of magic numbers for n = 13 and n = 22 is the most worrying point if a match with the fcc structures of Mg-O and Ca-O clusters is desired. These values of n correspond to the most stable ion cuboids, having a 3x3x3, and a 3x3x5 structure, respectively.

However, it is not necessary to discard all thoughts of a crystalline structure for the Sr-O clusters at this stage. A clue to the differences noted with the other group II-VI compound clusters can be gained by considering the nature of the experimental techniques used. Most of the experiments on Mg-O and Ca-O clusters involved the creation of these species by inert gas condensation. The gas used was typically helium, cooled to liquid nitrogen temperatures. This would favour the exhibition of magic numbers corresponding to stable ion cuboids, whereas cluster generation in a warmer environment would allow the evaporation of atoms from the growing clusters, and thus reflect the stabilities of neutral cuboid structures as in the case of NaCl clusters shown in Figure 6–6.

If the spectrum shown in Figure 6–8 is studied more closely, then it can be seen that the observed signal intensity dips at positions just following the expected positions for the cluster oxides corresponding to n = 29 and n = 31. It is possible that these correspond to stable clusters, with the presence of an additional surface

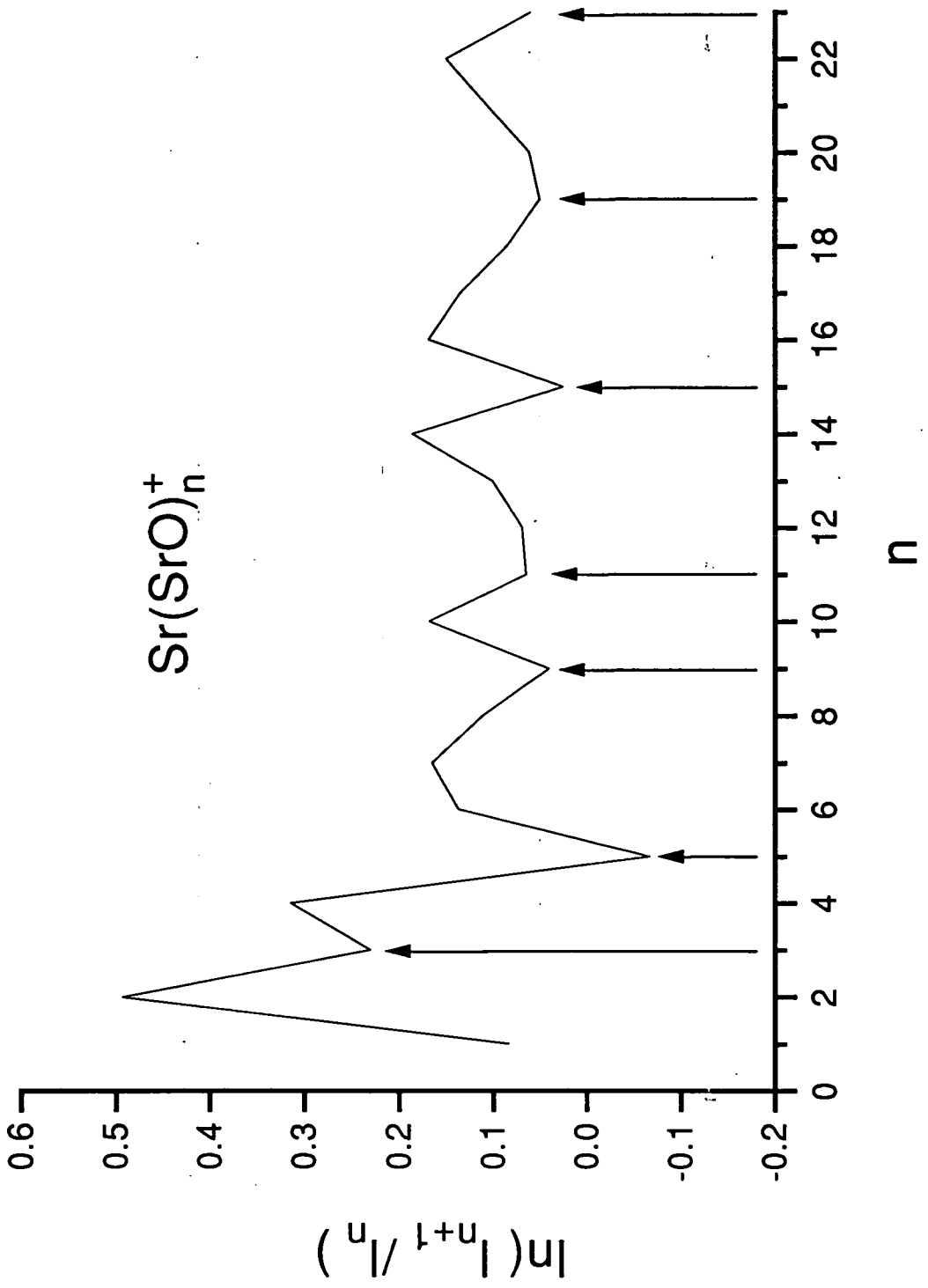

Figure 6–9: A logarithmic plot from Figures 6-7 and 6-9, showing stable $Sr(SrO)_n^+$ clusters as local minima, indicated by the arrows.

Sr atom or SrO molecule giving rise to an unstable structure which is prone to dissociative loss of the added atom or molecule. These magic numbers (n = 19, 23, 29, 31) correlate well with the stable structures shown in Figure 6–6 for NaCl clusters. This leads to the realisation that the magic numbers of strontium oxide clusters exhibited in the mass spectra shown here reflect stabilities of the neutral clusters which take the form of fcc cuboids.

6.4.3 Doubly-charged Sr-O clusters

This assignment of the structure of the Sr-O clusters as being due to an fcc-crystalline form is further backed by other cluster spectra which have been obtained during the course of this work. Since a range of metal-rich cluster ions were detected, it has been concluded that there is a fair population of these neutral species in the beam. The stability of the neutral stoichiometric clusters has been shown in this work to account for the magic numbers observed in the series of clusters ions $Sr(SrO)_n^+$. However, there is still the problem of accounting for the lack of magic numbers at $n = 13, 16, 19, 22, \ldots$ for the stable $Sr(SrO)_n^+$ clusters that would result from the neutral metal-rich clusters of the composition $Sr(SrO)_n$. It is possible that these are overshadowed by the magic numbers resulting from stable neutral stoichiometric cluster oxides. However, the mass spectrum shown in Figure 6–8 reveals very low intensities for $n = 13, 16, 22$, and this fact must be explained. This question can be addressed by examination of other cluster mass spectra which were obtained in which doubly charged cluster oxide peaks were observed. Such a spectrum is shown in Figure 6–10.

It can be seen that the magic numbers expected due to stable ion cuboids for n = 16 and 22 show up as magic numbers for doubly charged Sr-O clusters. The stability of these species is evident from the mass spectrum, the n = 16 peak exhibiting an enhanced intensity compared with the preceding doubly charged cluster peaks. Similarly, the n = 22 peak has a high intensity in comparison with the subsequent peaks due to doubly charged cluster oxides in this spectrum. Unfortunately, the limited resolution of the mass spectrometer in this size regime

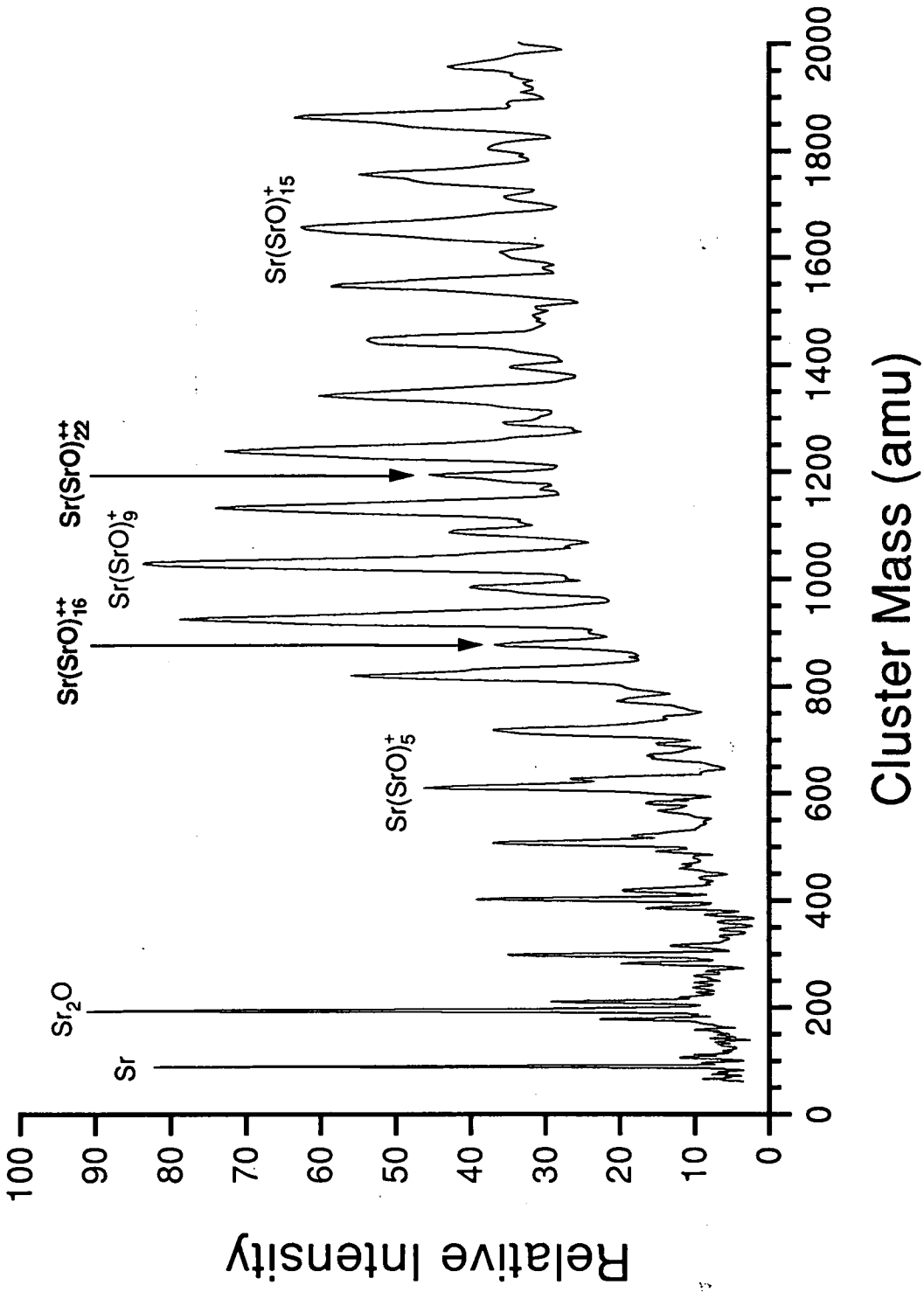

Figure 6–10: A mass spectrum of strontium cluster oxides ionised at 248 nm, showing the presence of doubly charged species.

precludes the observation of $Sr(SrO)_n^{++}$ clusters for odd values of n. For example, $Sr(SrO)_9^{++}$ has a mass-to-charge ration of 512 amu. Other cluster species in this area of the spectrum are $Sr(SrO)_4^{+}$ at 504 amu, and $(SrO)_5^{+}$ at 520 amu. Thus the doubly-charged feature in between these two peaks is swamped, or incorporated as a peak shoulder.

To sum up, the smallest strontium cluster oxides show a limited correlation with an fcc-structured system. For larger clusters, stable neutral cuboids seem to enhance the intensities of singly-charged cluster ions. The neutral cuboids lose an oxygen atom on ionisation, so that the ionised cluster has an O-atom vacancy. This is analogous to the concept of point defects in the bulk solid state. In this case the vacancy is reminiscent of a so-called colour centre [1]. Furthermore, stable ion cuboids lead to an increased intensity for their related doubly-charged cluster ions. These observation taken together support the existence of a preferred fcc form for the cluster oxides of strontium.

6.5 Summary

From the results presented in this chapter, along with the appropriate referenced works, it has been shown that it is difficult to produce pure clusters of the alkaline earth metals. The weakly bound metal dimer appears to be the main problem, with further cluster growth around the more stable metal oxide molecule being much preferred. Literature results had shown that cluster oxides of magnesium and calcium tended to exist as fragments of the bulk face-centred cubic crystal. The adoption of an icosahedral structure for barium cluster oxides was also known, and was verified here. There existed a gap in the literature as to which geometry was assumed by strontium clusters, and this system was studied here to try and reveal this information. The emergence of an fcc structural preference was observed.

At first sight an analysis of the structures of the Group-IIA metal cluster oxides as one travels down this group of the periodic table seems to show a discontinuous step on reaching the Ba-O system. However, if the cluster compositions are studied

closely, then a more gradual trend can be seen. For the fcc systems (Mg-O, Ca-O and Sr-O), the predominant cluster ion detected has the formula $M(MO)_n^+$. This can be referred to as a stoichiometric composition with one excess metal atom, M. Other cluster compositions do appear in the mass spectra, and their make-up changes gradually down the group, resulting in an increasing metal content for the species lower in the table. This trend reaches a stage at barium, when the clusters favour the incorporation of only a few oxygen atoms, and adopt the icosahedral geometry shown earlier in this chapter instead of a crystalline structure. The lattice energies of the bulk Group-IIA metal oxides do decrease down the group, and perhaps this fact contributes towards the general move away from the bulk-type structure.

The increasing metallisation is known for other systems, and has been discussed in the case of NaF clusters [27]. It was found that the excess metal atoms prefer to congregate on one face of the cuboid structure, as a degree of stability was gained as a result of the metal-metal bonding which could occur. This would eventually lead to an alkali halide system with an effectively segregated metal layer.

Clearly, in terms of future work, these systems would benefit from experiments of a confirmatory nature. For example, it would be desirable to be able to closely control the amount of oxygen uptake for each system, to see where the transitions between icosahedral and bulk lattice structures take place.

Bibliography

[1] N.W. Ashcroft and N.D. Mermin, '*Solid State Physics*', Holt, Rinehart and Winston, New York, 1976.

[2] T.P. Martin, T. Bergmann, H. Göhlich and T. Lange, Chem. Phys. Lett., **176** (1991) 343.

[3] T.P. Martin, U. Näher, T. Bergmann, H. Göhlich and T. Lange, Chem. Phys. Lett., **183** (1991) 119.

[4] W.A. Saunders, Phys. Rev. B, **37** (1988) 6583.

[5] P.J. Ziemann and A.W. Castleman, Jr., Phys. Rev. B, **44** (1991) 6488.

[6] P.J. Ziemann and A.W. Castleman, Jr., J. Chem. Phys., **94** (1991) 718.

[7] P.J. Ziemann and A.W. Castleman, Jr., J. Phys. Chem., **96** (1992) 4271.

[8] R. Pflaum, K. Sattler and E. Recknagel, Chem. Phys. Lett., **138** (1987) 8.

[9] Y.J. Twu, C.W.S. Conover, Y.A. Yang and L.A. Bloomfield, Phys. Rev. B, **42** (1990) 5306.

[10] D. Rayane, P. Melinon, B. Cabaud, A. Hoareau, B. Tribollet and M. Broyer, Phys. Rev. A, **39** (1989) 6056.

[11] T.P. Martin and T. Bergmann, J. Chem. Phys., **90** (1989) 6664.

[12] P. Dugourd, J. Chevaleyre, C. Bordas and M. Broyer, Chem. Phys. Lett., **193** (1992) 539.

[13] C. Bordas, M. Broyer, J. Chevaleyre and P. Dugourd, Chem. Phys. Lett., **197** (1992) 562.

[14] T.P. Martin, Phys. Reports, **95** (1983) 167.

[15] C.W.S. Conover, Y.A. Yang and L.A. Bloomfield, Phys. Rev. B, **38** (1988) 3517.

[16] T.P. Martin, J. Chem. Phys., **81** (1984) 4426.

[17] R.L. Whetten, M.L. Homer, X. Li, F.E. Livingston, P.M. St. John and R.D. Beck, Ber. Bunsenges. Phys. Chem., **96** (1992) 1120.

[18] T.M. Barlak, J.E. Campana, J.R. Wyatt and R.J. Cotton, J. Phys. Chem., **87** (1983) 3441.

[19] Z.Y. Chen and A.W. Castleman, Jr., J. Chem. Phys., **98** (1993) 231.

[20] B.V. Reddy and S.N. Khanna, Chem. Phys. Lett., **209** (1993) 104.

[21] S. Becker and H.J. Dietze, Int. J. Mass Spectrom. Ion Proc., **73** (1986) 157.

[22] P.A. Roland and J.J. Wynne, J. Chem. Phys., **99** (1993) 8599.

[23] B.C. Guo, S. Wei, Z. Chen, K.P. Kerns, J. Purnell, S. Buzza and A.W. Castleman, Jr., J. Chem. Phys., **97** (1992) 5243.

[24] Z.Y. Chen, B.C. Guo, B.D. May, S.F. Cartier and A.W. Castleman, Jr., Chem. Phys. Lett., **198** (1992) 118.

[25] W.A. Saunders, Z. Phys. D, **12** (1989) 601.

[26] S. Bjornholm, J. Borggreen, O. Echt, K. Hansen, J. Pedersen and H.D. Rasmussen, Phys. Rev. Lett., **65** (1990) 1627.

[27] G. Rajagopal, R.N. Barnett and U. Landman, Phys. Rev. Lett., **67** (1991) 727.

Chapter 7

STUDIES OF LARGE IRON CLUSTERS

7.1 Introduction

The experiments described in this chapter were carried out at the Université Claude Bernard in Lyon, France as part of a collaborative research project funded by the British Council Alliance Scheme. The study of a system such as iron, within the context of the types of experiment described in this thesis, is a fairly ambitious avenue of research. It has been apparent that some of the magic numbers evident in the systems already described were easy to assign to particular shell effects. Indeed, the type of shell effect found was often not unexpected given some background knowledge of the specific systems. For example, knowing the basis of the jellium model, and that potassium clusters fitted this description well, it was not difficult to predict that other monovalent metal clusters might conform to this picture.

For a system such as iron, there is no real ground upon which any such assumption can be made. As a subject for cluster research, iron is extremely exciting, and possesses many properties which make it an interesting system to look at. With respect to the goal of observing the evolution of bulk properties with increasing cluster size, then the magnetic properties of bulk iron make it a good test system for this type of study. It was hoped that these experiments on iron clusters would be useful in allowing us to see just how far the shell models (both electronic and geometric) could be pushed.

The experimental principles of these experiments on iron clusters are essentially the same as for the previous studies reported in this thesis. The apparatus basically consisted of a laser vaporisation source coupled to a supersonic nozzle, with cluster characterisation by time-of-flight mass spectrometry. There were a few differences in the equipment and procedures utilised in the work carried out at Lyon as compared with the experiments conducted in Edinburgh, and these are described below.

7.2 Experimental Details

A schematic diagram of the cluster apparatus in Lyon is shown in Figure 7–1. A general description of the basic experimental set-up has already been given in the literature [1], but a more detailed description of the areas vital to the production of the iron clusters is presented here. Note that the experiments on this apparatus were run at a repetition rate of 7.5Hz as opposed to the 10Hz repetition rate used for the experiments in Edinburgh.

7.2.1 Vacuum system

In terms of overall design, the apparatus is similar to the Edinburgh instrument. The entire apparatus was constructed of stainless steel, by the French company SDMS. The main chamber is a cylinder of 65cm radius, and 65cm height, with an internal volume of approximately 870 litres. This chamber was evacuated by a Balzers DIF630A oil diffusion pump with a pumping speed of 20,000ls^{-1}. This was backed by a combination Balzers DUO250A rotary vane pump, and a Balzers WKP1000 roots pump in series. The background pressure attained in this chamber was of the order 4 x 10^{-6}mbar. This would rise to 1 x 10^{-5}mbar during experiments. All pressures were measured on Pirani (Balzers TPR 010) and cold cathode (Balzers IKR 020) gauges, which were controlled by a Balzers TCP 310 control unit.

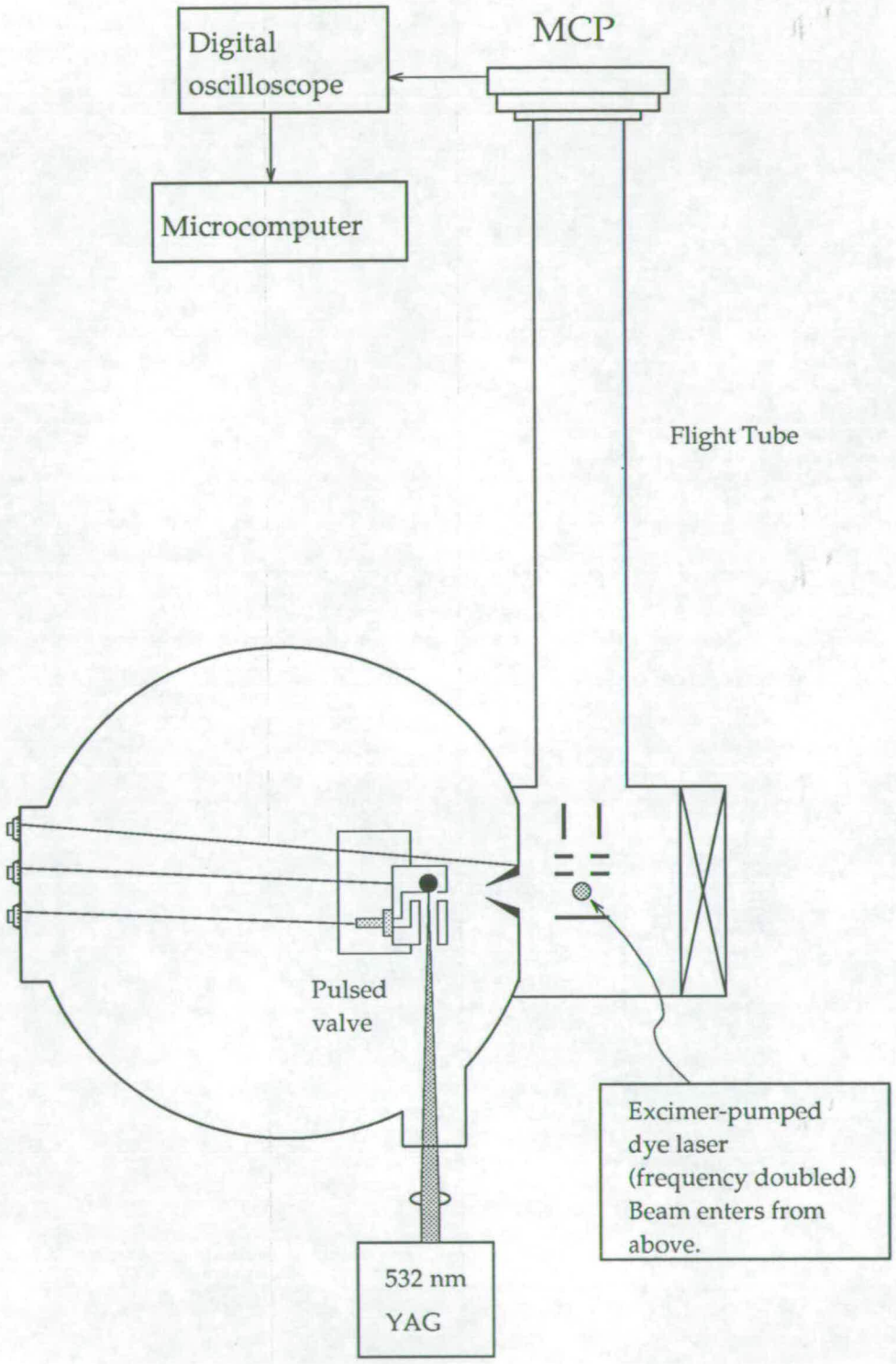

Figure 7–1: Schematic diagram of the cluster apparatus in Lyon.

The pumping system for the ionisation chamber consisted of a Balzers DIF250 oil diffusion pump with a pumping speed of $3100ls^{-1}$, backed by a Balzers UNO 30A rotary pump. The flight tube of the time-of-flight mass analyser was separately pumped by a Balzers TPH 520 turbo-molecular pump. In order to minimise mechanical vibrations, most of the pumps were housed in a separate room adjacent to the laboratory, and connected to the equipment via extended forelines.

Pumping down of the main chamber was a slow process due to its size, and access to the cluster source was gained by removal of the top flange of this chamber, which was only possible with the use of a mechanical winch.

7.2.2 The cluster source

The cluster source itself was based on the design of Milani and de Heer [2]. As in Edinburgh, the pulsed valve used was a General Valve Corporation Series 9 model. In this particular cluster source configuration, the carrier gas channel is more convoluted, but this serves to minimise gas loss.

One of the major differences between the apparatus at Lyon and the instrument used in Edinburgh was the distance between the cluster source and ionisation region. On the apparatus in Lyon, the end of the cluster growth channel was situated only 4cm from the skimmer. This made alignment of the cluster source much easier, and also allowed more material through into the ionisation region of the machine. Alignment was achieved by micrometer controlled translation arms fitted to the cluster source. It was also possible to adjust the x-y position of the skimmer itself via a similar mechanism. The overall distance from the cluster source to the ionisation region was only 15cm, compared to 40cm for the apparatus in Edinburgh. Thus the cluster density probed by the ionisation laser is much higher for the apparatus in Lyon. This was borne out by the higher mass range of clusters observed using this machine.

A further feature about the apparatus used at Lyon was that the temperature of the cluster source could be controlled, and cooled down to as low as 100 K. The pulsed valve was thermally isolated from the cluster source block by the use of

teflon spacers. Additionally, an electrical coil was used to weakly heat the valve body to keep it at room temperature when the cluster source was being cooled with liquid nitrogen. The point about creating colder clusters is that it allows intensity anomalies to be identified as being due to differences in initial cluster abundances, as the clusters are too cold to evaporate any material once created [3].

7.2.3 Laser systems

The types of lasers used in these studies were similar to those described earlier in this thesis. The vaporisation wavelength used was identical to that utilised at Edinburgh. The 532 nm output of the Nd:YAG laser is widely used for pulsed laser vaporisation experiments. The specific type used was a BMI Model 501-D-NS. This was operated at a repetition rate of 7.5Hz. Photoionisation was carried out using the frequency-doubled output of an excimer-pumped dye laser. The excimer was a Lambda Physik Model LPX-200, operating on the XeCl line and emitting at 308 nm. This output was used to pump the dye laser, a Lambda Physik Model FL-3002. The visible output from the dye laser could be converted to ultra-violet radiation using a BBO (β-BaB_2O_6) crystal for second harmonic generation.

7.2.4 Ion optics

The ion optics for the time-of-flight mass analyser were similar to those described earlier, based on the Wiley and McLaren design for the double-field time-of-flight mass spectrometer [4]. However, one major difference in practice was the use of a ramp voltage instead of a fixed voltage on the deflection plates used to direct cluster ions down the flight tube. The mass windowing effect which results from the use of a perpendicular ion extraction geometry for cluster ions has already been mentioned earlier in this thesis.

Although there have been many modifications reported for achieving higher mass resolution on time-of-flight instruments [5], there are only a few ways of ex-

tending the size of the mass transmission function. One simple way of achieving this involves tilting the entire ion extraction optics so that a component of the extraction field counteracts the initial velocity components which the clusters possess at right angles to the spectrometer drift region [6]. Obviously, the tilt angle affects the optimum transmitted mass, and in effect this arrangement bears a great deal of similarity to the deflection plate set-up.

An alternative approach which can be used to extend the mass window of clusters that can be observed in any single spectrum involves applying a linear ramp to the deflection plate voltages [7]. In the present experiments this approach was used with the deflection plate voltage being ramped linearly from 100V to 750V by a TREK Model 50/750 high voltage amplifier. It should be noted that although the width of the effective mass window is extended by this method, the resolution does suffer. However, this factor is not too crucial here due to the way in which the mass spectra are processed, as explained later.

The main parameters in the linear time-of-flight mass analyser in the Lyon apparatus were as follows:

Repeller plate	4000V
Draw-out grid	Variable 3500 - 3600V
Flight grid	0V
Drift region	130cm

Ions were detected at the end of the field-free drift region using Hamamatsu dual microchannel plates.

An additional point to note was the use of a pair of scavenging plates between the skimmer and the ion optics. These plates were biased at +500 and -500V, with the resulting electric field serving to deflect away any ions directly created in the cluster source thereby preventing them from reaching the ionisation region. For mass spectral calibration, the supply to these plates was switched off to allow these directly formed cluster ions of low mass to reach the detector. This removed

the need to alter the source parameters from a high mass cluster experiment to a low mass set-up simply to calibrate the spectra.

7.2.5 Data handling

The ion signals detected using the mass spectrometer were summed in a fast digital oscilloscope (LeCroy Model 9400A) which acts as a multichannel analyser. A typical mass spectrum required the accumulation of between 500 and 2000 shots. These averaged mass spectra were then transferred to a microcomputer for subsequent analysis.

To clearly distinguish any intensity anomalies in the cluster abundance spectra, the basic mass spectrum must be manipulated in some way. The procedure utilised is standard for this type of work, and simply makes any unusual spectral features more plainly evident. It has been noted that the mass transmission function for the Edinburgh time-of-flight analyser takes the form of a bell-shaped envelope centred around the chosen cluster mass range. On the apparatus in Lyon, this feature persists, but is of a greater width due to the voltage ramp employed on the deflection plates. A commonly used method to extract information about mass spectral intensity oscillations is the generation of a so-called difference spectrum [8,9,10]. This involves fitting a spline function to the mass spectrum to create a structureless bell-shaped curve. This is then subtracted from the slightly smoothed original mass spectrum to reveal the intensity anomalies more clearly. It is then generally somewhat easier to identify the magic numbers.

7.3 Iron Cluster Abundance Spectra

Unfortunately, there is no typical iron cluster spectrum which can be shown here as a generic example of the cluster distribution observed for this system. The general appearance of the cluster intensities recorded during these studies was seen to vary substantially as a result of changing the various experimental conditions.

The magic numbers which emerge from the mass spectra must be dealt with in two separate size regimes at this time. The abundance spectra for smaller clusters containing between 50 and 200 iron atoms can be compared with nickel and cobalt clusters under certain conditions, although variations do occur as the source parameters are modified [11]. The spectra for larger iron clusters containing more than 200 atoms clearly exhibit intensity anomalies, which also vary as above, but it is difficult to ascribe these to a particular shell effect as far as the present understanding of these systems goes.

The fact that the positions and relative intensities of the specific magic numbers vary with changing source parameters is not too surprising. This type of behaviour has been observed recently for aluminium clusters [12], where it was ascribed to variations in the temperature of the clusters. The concept of temperature is a difficult one when discussing finite quantum systems, as the normal definition of temperature is related to an averaged molecular motion in a bulk environment. In the cluster context, the temperature can still be correlated with the idea of atomic motion, but it is perfectly possible for a cluster to have distinct temperature regions.

In general, a warm cluster can be described as liquid-like, in which the constituent particles can move relatively freely. A colder cluster will have a more rigid structure, with the atomic positions being more specifically fixed. Each of these two regimes favour the appearance of one of the shell effects. Obviously, a liquid-like cluster can assume a spherical geometry, providing the correct environment for the electrons to exhibit behaviour associated with the expectations of the spherical jellium model. A more rigid cluster will show a predominant geometric shell effect, where stability is dependent on the strength with which particular atoms are bound to the rest of the cluster.

Thus, in systems which can show both electronic and geometric shell effects, there is the interesting possibility of observing a transition between the two effects depending on the cluster temperature. There is also the possibility that these two distinct types of shell effects can emerge within one experiment for different sized clusters. This can occur if the clusters all attain a similar temperature. Since

the melting points of the specific clusters vary with size [13], then at a particular temperature some clusters may be more liquid-like than others. The variation of magic numbers seen for iron clusters will be described in terms of competing shell effects, and rationalised in the same way as described above.

The data obtained for the lower size regime, (that is clusters containing between 50 and 200 atoms) will be examined first. Figure 7–2 shows a mass spectrum obtained for iron clusters in this size range following photoionisation at 252.5 nm (i.e. after frequency-doubling the dye laser fundamental output at 505 nm). This spectrum corresponds to the raw data as obtained prior to any data manipulation procedure. This photoionisation wavelength was chosen so as to ionise the metal clusters near their ionisation potential. This should result in intensity dips in the mass spectra for stable cluster species, i.e. those with high ionisation potentials. These intensity dips on the background envelope of the mass spectrum are the magic numbers for that particular cluster system. As mentioned previously, these intensity anomalies can be revealed more clearly if the spectrum is treated in such a way as to remove any global variations in the mass spectrum. Figure 7–3 shows the difference spectrum which was obtained from the raw data shown in Figure 7–2. The steps taken to process the raw experimental data involved subtraction of a highly smoothed mass spectrum from the original data. In this case the smoothed spectrum was actually the result of adjacently averaging the raw data over 100 time channels. After subtraction of this smoothed spectrum from the original data, the resultant curve was smoothed slightly to generate the difference spectrum shown in Figure 7–3. The expected positions of icosahedral shells and subshells are indicated in the figure.

The magic numbers initially evident for iron clusters in this size regime correlated well with the structures seen in experiments on nickel and cobalt clusters [11]. The intensity dip for the n = 147 closed shell icosahedron in Figure 7–3 is particularly strong, and appeared in all of the iron cluster spectra obtained. Many of the expected icosahedral subshells are also evident as local intensity minima in this difference spectrum. Thus it would seem likely that an icosahedral structure could be attributed to these iron clusters in this size range. However, as men-

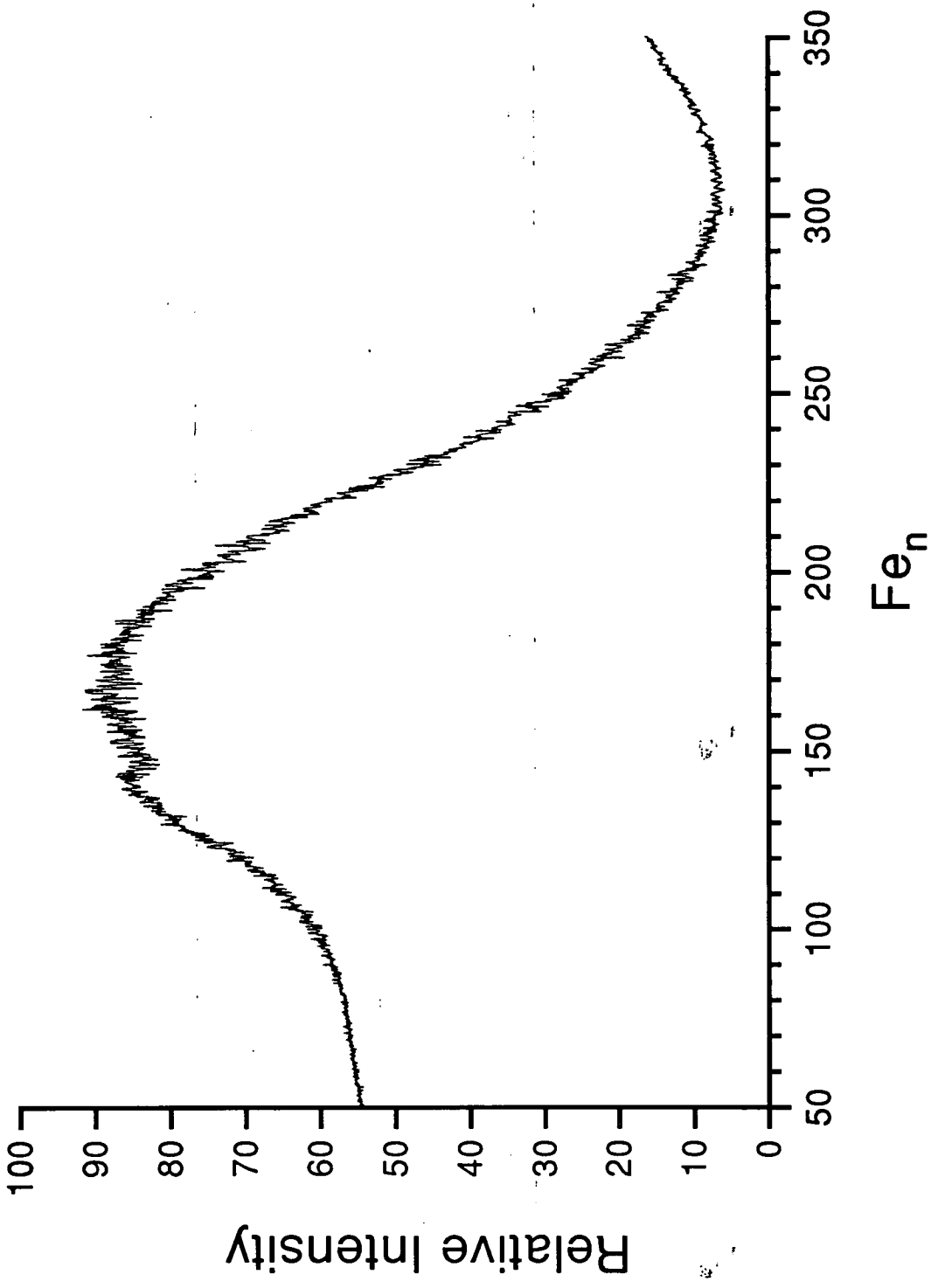

Figure 7–2: Mass spectrum of iron clusters obtained after photoionisation with 252.5 nm radiation from the frequency-doubled output of the excimer-pumped dye laser.

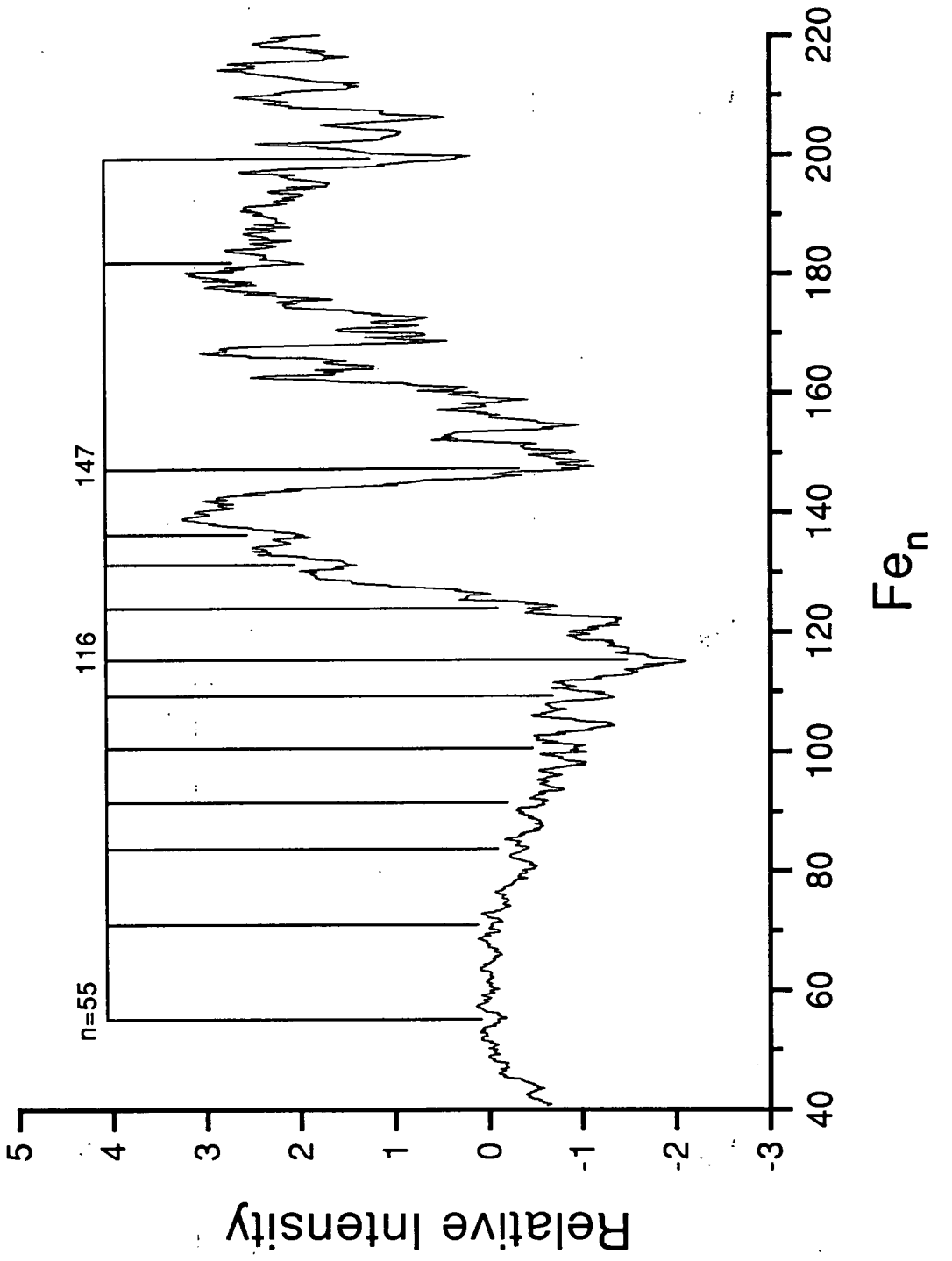

Figure 7–3: A clarification of spectral intensity anomalies after processing the data from Figure 7-2. The expected positions of icosahedral shells and subshells are indicated.

tioned earlier, the alteration of experimental parameters resulted in a change in the anomalous features in the mass spectrum. The more intense features now bore some resemblance to magic numbers predicted for a trivalent material fitting the spherical jellium model. The change in source conditions to achieve this state corresponds with warmer, more liquid-like clusters.

It must be stressed, though, that the magic numbers which emerged from the mass spectra obtained for iron clusters are difficult to explain completely within the context of one single type of shell effect. There is not an exact correspondance between the new features for higher temperature clusters, and the jellium predictions. Also, it is difficult to say for a system such as iron, with its partially filled *d* shell, how many valence electrons each atom would contribute to a jellium potential. The significant fact which points to the contribution of an electronic shell effect in this case is the way in which these new features are exhibited as the clusters become more liquid-like. This is entirely consistent with previously reported results for other systems [12].

It should be noted again that in studies of this type, the rationalisation of cluster magic numbers is rarely straightforward. Even within the realms of the geometric shell effect there are many possible geometries which can be assumed, along with various stable subshells. In the course of attempting to find a description for the stabilities observed for iron clusters, many options were considered. There seemed at one stage to be a good fit with an alternate geometry seen for aluminium clusters, but with a novel subshell filling sequence. On examination of the iron cluster magic numbers it was noticed that when considering the octahedral structure, then the addition of atoms to face centres would result in a bcc rhombic dodecahedral form. This could be considered a stable subshell between two adjacent structures in the octahedral growth sequence. Allowing the formation of the rhombic dodecahedron to occur as part of the more typical series of octahedral subshells [9] showed a good match with the stable iron clusters containing between 85 and 230 atoms. The application of this particular model did not extend well at all outwith this range, and was eventually discarded. The cluster scientist is afforded some help by the fact that the icosahedron does seem

to be a highly favoured natural geometry in many systems, and so this is a good starting place in the search for a description of cluster stabilities.

Another difficulty which can confound attempts to rationalise cluster magic numbers is the possibility that one or more structural transitions may occur within a certain size regime. A related incidence of this is the structural transition and presence of isomerism in cobalt clusters containing between 50 and 70 atoms [14]. Isomerism has also been noted for iron clusters during IP measurements [15,16], and chemical probe experiments [17]. The existence of different crystalline forms of bulk iron leads to the expectation that different isomers could feasibly exist in clusters which are the building blocks of the bulk state.

The cluster abundance spectra obtained for iron clusters containing more than 200 atoms are much more difficult to analyse. A spectrum obtained in this size range using threshold photoionisation is shown in Figure 7–4. The positions of the third and fourth closed shell icosahedra (n = 147, 309) are indicated, as well as the positions of two obvious intensity anomalies. The appropriate difference spectrum, generated in the same way as before is also shown in Figure 7–5.

Subtle changes to the source parameters result in changes in the appearance of the mass spectra. Figure 7–6 shows another mass spectrum, recorded soon after the spectrum shown in Figure 7–4. The corresponding difference spectrum is shown in Figure 7–7 The main experimental conditions such as the ionisation laser wavelength, and the cluster source temperature were kept constant, but slight changes to the helium backing pressure, and point of vaporisation produced a spectrum with a different appearance. A new anomalous intensity feature now appears for n = 268.

For these larger clusters, then, the mass spectra remain structured and are strongly dependent on the source conditions. It is not readily apparent at this stage how the magic numbers for iron clusters in this size range are affected by changes in the source conditions.

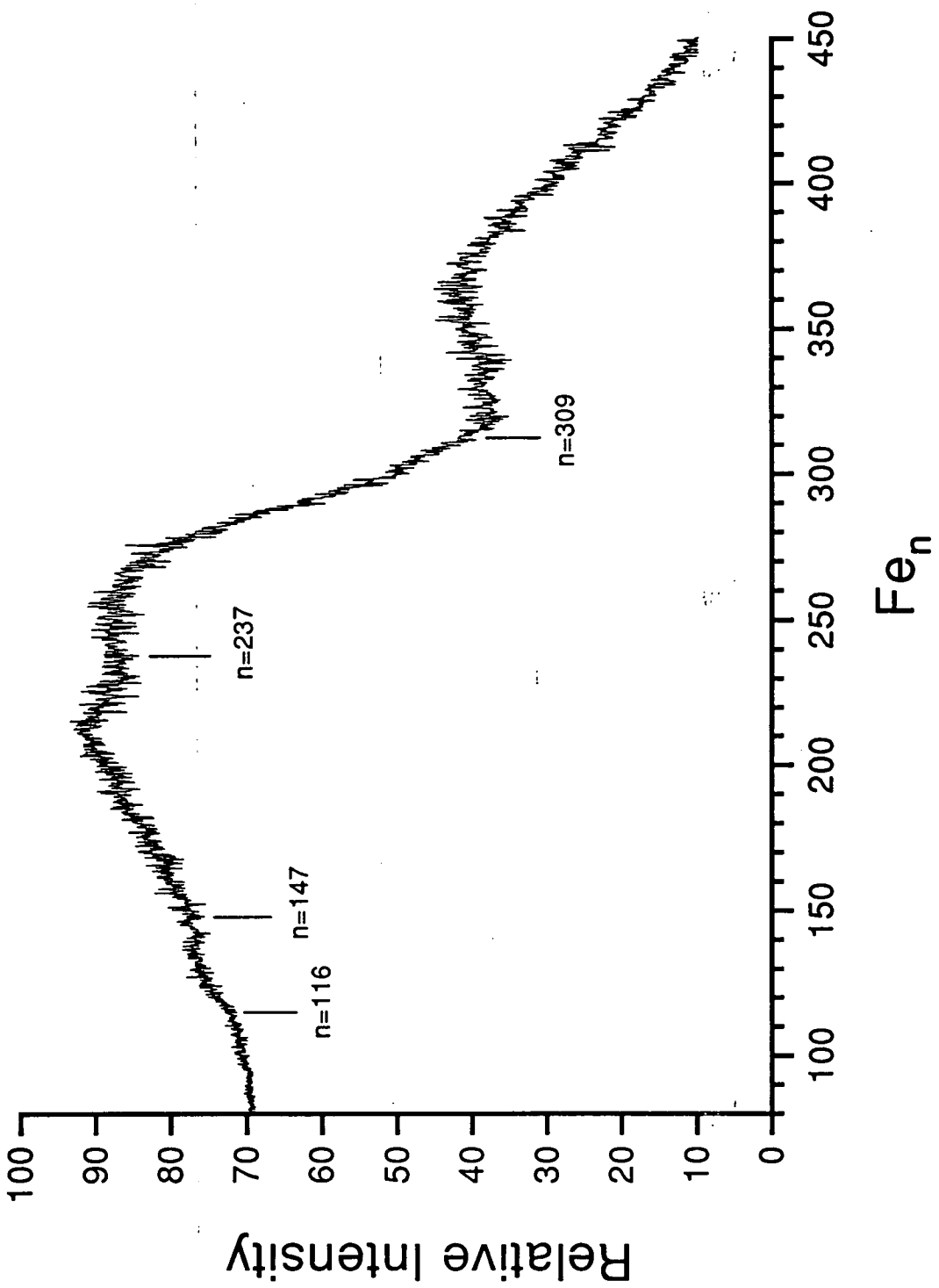

Figure 7–4: Mass spectrum of iron clusters, ionised with 252.5 nm radiation.

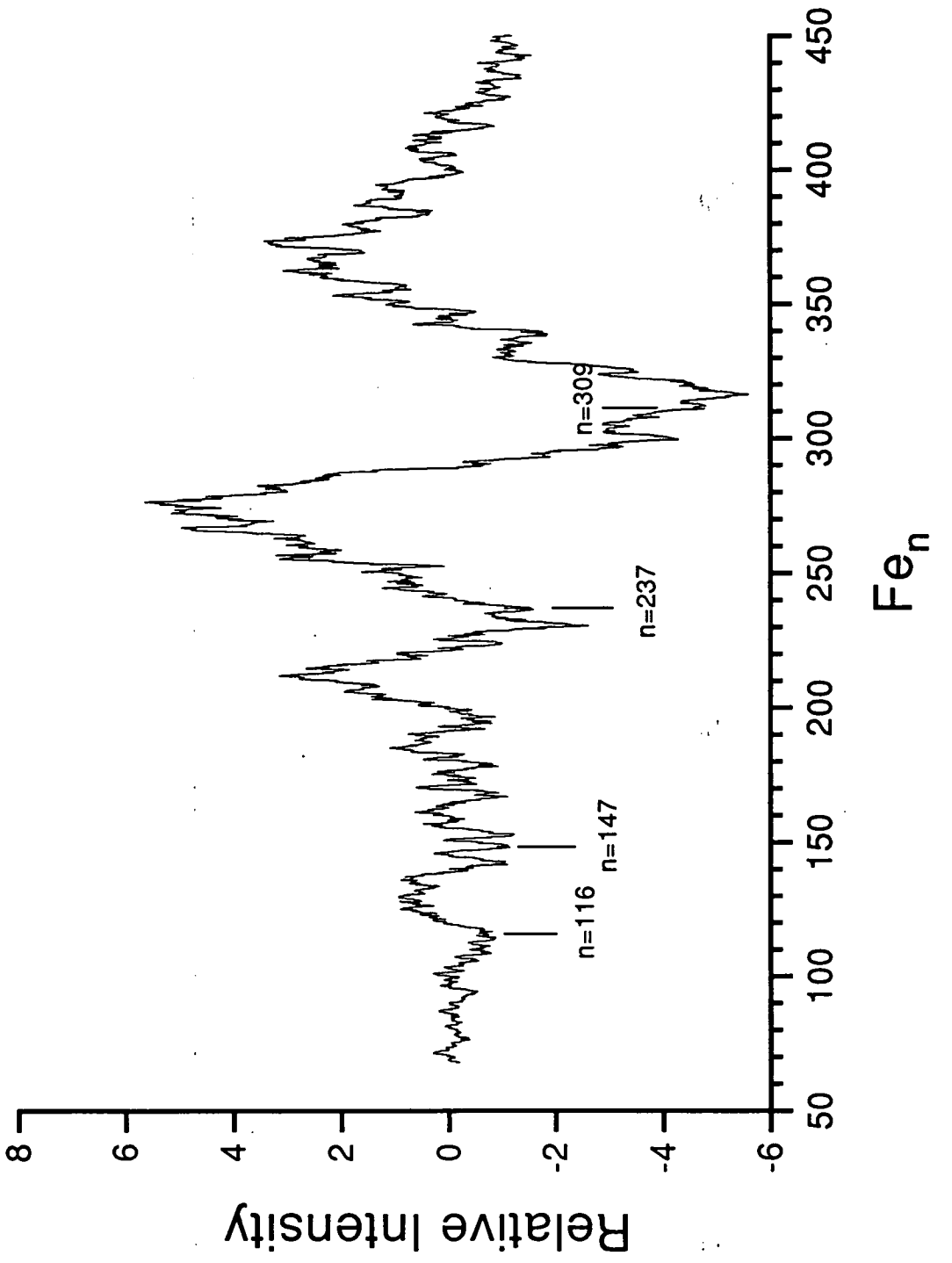

Figure 7–5: Difference spectrum resulting from manipulation of the raw data displayed in Figure 7-4.

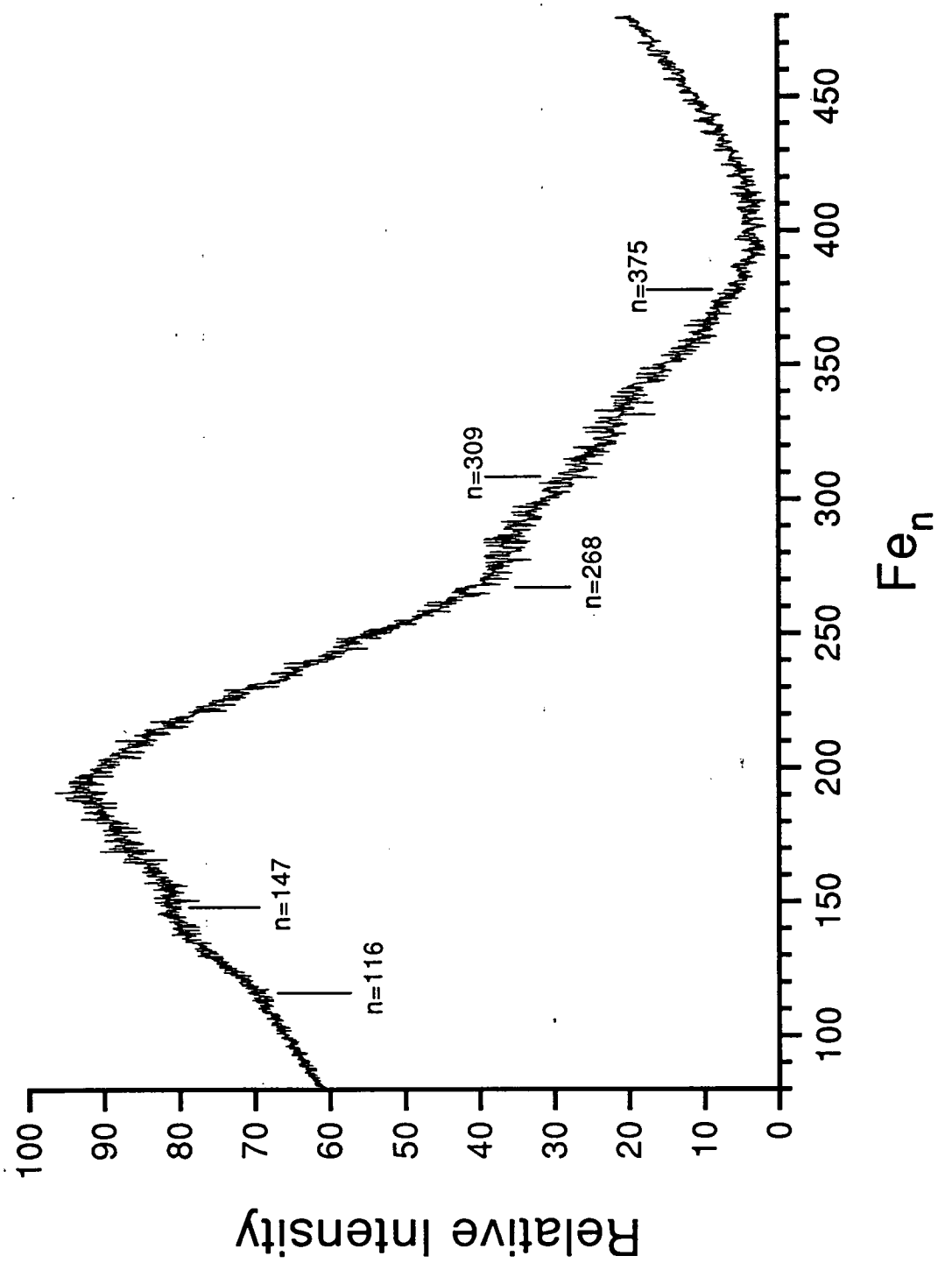

Figure 7–6: Mass spectrum of iron clusters, ionised with 252.5 nm radiation.

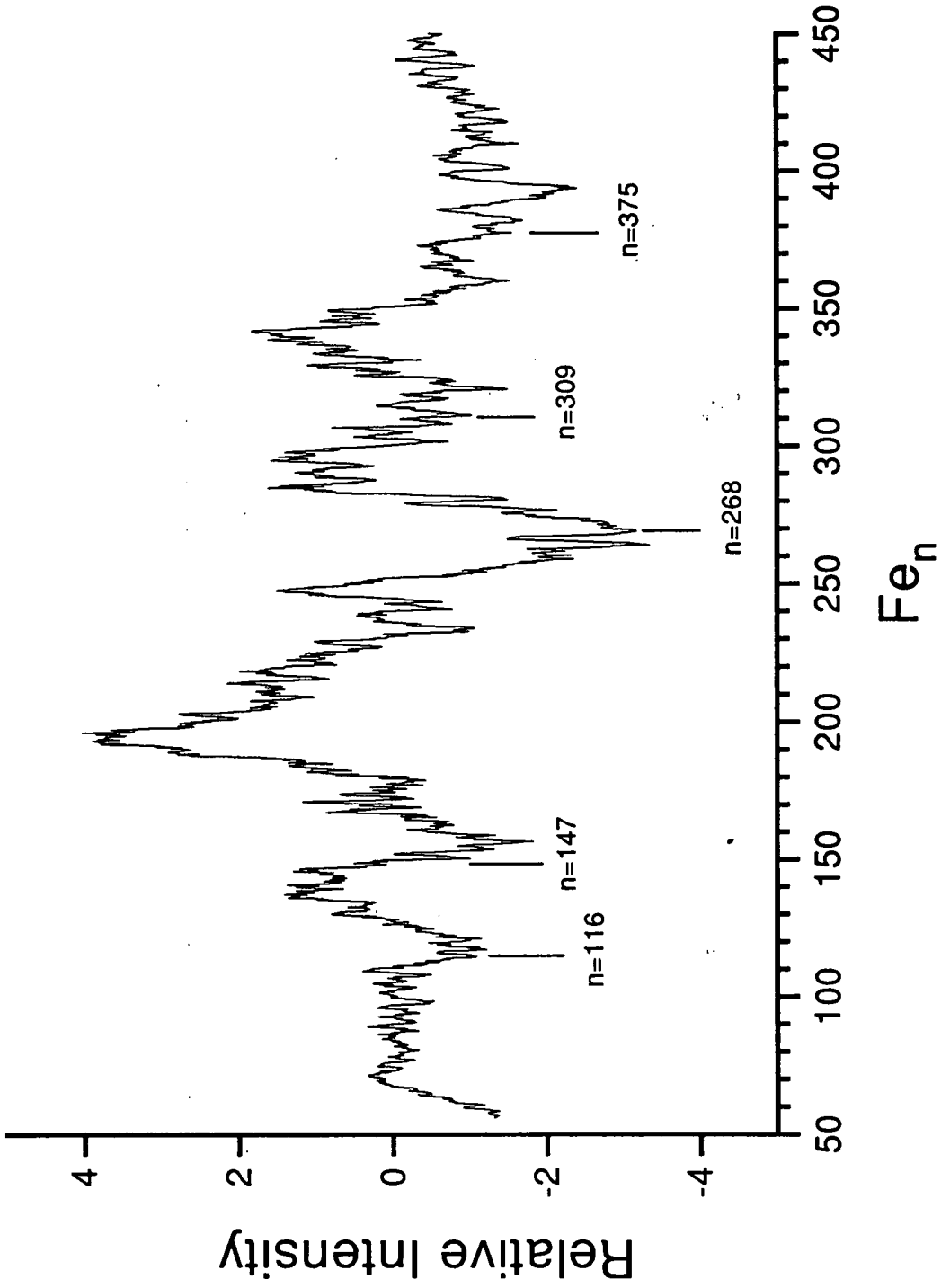

Figure 7–7: Difference spectrum resulting from manipulation of the raw data shown in Figure 7-6

7.4 Conclusion

Summing up, it can be seen that a cluster system such as iron is rather complicated to interpret in terms of shell effects. It is clear, at least, that there are competing effects evident which account for the magic numbers displayed for iron clusters. For clusters containing less than 200 atoms there seems to be a competition between an icosahedral atomic shell structure, and an electronic shell effect deriving from the spherical jellium model.

For larger clusters it is difficult to fit the observed magic numbers to any known shell effects, but it seems highly likely that the stabilities of these clusters are affected by the presence of various structural isomers.

This uncertainty will be resolved as more techniques are brought to bear on this particular system. The input of theoreticians should also shed some light over this area. The field of cluster science has been advanced rapidly by the fact that scientists from differing branches of research have pooled their knowledge effectively, and this welcome state of affairs seems likely to continue.

Bibliography

[1] M. Pellarin, B. Baguenard, M. Broyer, J. Lermé, J.L. Vialle and A. Perez, J. Chem. Phys., **98** (1993) 944.

[2] P. Milani and W.A. de Heer, Rev. Sci. Instrum., **61** (1990) 1835.

[3] J.L. Persson, R.L. Whetten, H.P. Cheng and R.S. Berry, Chem. Phys. Lett., **186** (1991) 215.

[4] W.C. Wiley and I.H. McLaren, Rev. Sci. Instrum., **26** (1955) 1150.

[5] D. Price and G.J. Milnes, Int. J. Mass Spectrom. Ion Proc., **99** (1990) 1.

[6] C.W.S. Conover, Y.J. Twu, Y.A. Yang and L.A. Bloofield, Rev. Sci. Instrum., **60** (1989) 1065.

[7] W.A. de Heer and P. Milani, Rev. Sci. Instrum., **62** (1991) 670.

[8] T.P. Martin, S. Bjornholm, J. Borggreen, C. Bréchignac, P. Cahuzac, K. Hansen and J. Pedersen, Chem. Phys. Lett., **186** (1991) 53.

[9] T.P. Martin, U. Näher and H. Schaber, Chem. Phys. Lett., **199** (1992) 470.

[10] M. Pellarin, J. Lermé, B. Baguenard, M. Broyer and J.L. Vialle, Ber. Bunsenges. Phys. Chem., **96** (1992) 1212.

[11] M. Pellarin, B. Baguenard, J.L. Vialle, J. Lermé, M. Broyer, J. Miller and A. Perez, Chem. Phys. Lett., **217** (1994) 349.

[12] B. Baguenard, M. Pellarin, J. Lermé, J.L. Vialle and M. Broyer, J. Chem. Phys., **100** (1994) 754.

[13] T.P. Martin, U. Näher, H. Schaber and U. Zimmermann, J. Chem. Phys., **100** (1994) 2322.

[14] J.P. Bucher, D.C. Douglass and L.A. Bloomfield, Phys. Rev. Lett., **66** (1991) 3052.

[15] E.K. Parks, B.H. Weiller, P.S. Bechthold, W.F. Hoffman, G.C. Neiman, L.G. Pobo and S.J. Riley, J. Chem. Phys., **88** (1988) 1622.

[16] E.K. Parks, G.C. Neiman, L.G. Pobo and S.J. Riley, J. Chem. Phys., **88** (1988) 6260.

[17] S. Yang and M.B. Knickelbein, J. Chem. Phys., **93** (1990)1533.

Appendix A

Courses and Conferences Attended

In accordance with the regulations of the Department of Chemistry, University of Edinburgh, I have attended the following courses during my period of study:

1. Laser Physics
2. Recent Developments in Physical Chemistry
3. FORTRAN 77 programming
4. 'C' programming
5. UNIX I and UNIX II
6. Vuwriter
7. Vued and Micro-emacs
8. Latex

In addition, I have attended the Laser Chemistry research group meetings, departmental seminars, joint Edinburgh - Heriot-Watt laser chemistry group meetings, and the following conferences:

1. Faraday Division High Resolution Spectroscopy Group, Heriot-Watt, 1990

2. Faraday Division High Resolution Spectroscopy Group, London, 1991

3. Northern Universities Spectroscopy and Dynamics Group, Manchester, 1991

Appendix B

Publications

1. A.M. James, J.F. Miller, J.W. Macdonald, G.W. Lemire, P.F. Brevet and P.R.R. Langridge-Smith, "Two-Colour Threshold Photoionisation Spectroscopy of Jet-Cooled Ag_2", Rutherford Appleton Laboratory, **RAL-92-020** (1992) 174.

2. M. Pellarin, B. Baguenard, J.L. Vialle, J. Lermé, M. Broyer, J. Miller and A. Perez, "Evidence for Icosahedral Atomic Shell Structure in Nickel and Cobalt Clusters. Comparison with Iron Clusters.", Chem. Phys. Lett. **217** (1994) 349.

TWO-COLOUR THRESHOLD PHOTOIONISATION SPECTROSCOPY OF JET-COOLED Ag_2

A.M.James, J.F.Miller, J.W.Macdonald, G.W.Lemire, P.F.Brevet and P.R.R.Langridge-Smith

Department of Chemistry, The University of Edinburgh

1. INTRODUCTION.

The electronic structure of small transition metal clusters is currently an area of intense research interest, both from the theoretical and experimental viewpoint. The Group IB, "coinage", dimers are in many ways the simplest of the transition metal dimers, being formed from atoms with filled *d* subshells. Consequently, they have become benchmark species for calibration of both *ab-initio* and core pseudopotential electronic structure calculations [1].

One of the most fundamental molecular properties is the first ionisation potential (IP). The magnitude of the IP provides a direct measure of the strength with which the valence electrons are bound to the molecular core, and of the stability of the molecular ion. The relatively high value of the IP's of the "coinage" metal dimers , makes direct one-photon measurements with tunable lasers somewhat difficult. Moreover, this approach often enables only the *vertical* ionisation potential to be accessed due to Franck-Condon restrictions. We report here the results of two-colour threshold photoionisation spectroscopic measurements on jet-cooled Ag_2, complementing our earlier studies on Cu_2 and CuAg [2].

In these experiments one laser is tuned into resonance to excite some specific intermediate electronic state of the molecule, whilst a second laser is scanned across the ionisation threshold, ionising molecules out of this chosen excited state. By monitoring the photoion signal as a fuction of the wavelength of the ionising laser, a photoionisation efficiency (PIE) curve can be generated. Isotopically specific, rovibronic state selective excitation can be achieved, and additionally, the use of jet-cooling removes any complicating contributions from vibrationally excited ground state molecules, thereby sharpening the threshold of the PIE curve and allowing a more accurate determination of the ionisation potential.The accuracy with which the IP may be measured is limited by the width of the threshold, which may be $<2\ cm^{-1}$ when field ionisation effects have been completely eliminated. However, the technique can provide more than simply a means of extracting accurate adiabatic ionisation potentials, since processes such as autoionisation may be probed by investigating the shape of the PIE curve in the post-threshold region yielding information on the electronic configurations involved in the ionisation process. Depending on the chosen vibrational level v' in the intermediate state, we are able to record threshold spectra (via v'=0) or high lying Rydberg state spectra (via v'=1). In both cases, we can measure IP's and access information on the molecular electronic structure, such as configuration mixing.

2. EXPERIMENTAL.

The experimental apparatus used in the present studies is shown schematically in Figure 1. A pulsed supersonic beam of silver clusters was produced by laser vaporisation of a silver rod (5mm dia.), located within the throat of a pulsed supersonic nozzle, using the second harmonic output from a Q-switched Nd:YAG laser (532 nm, 20 mj/pulse, focussed to a diameter of approximately 1 mm). The ejected atoms were entrained in a channel 2 mm in diameter and 3.5 cm in length. The resulting molecular beam was then skimmed (5 mm skimmer) prior to its entrance into the ionistion region of a high resolution reflecting geometry time-of-flight mass spectrometer (RETOFMS). There the molecular beam was crossed perpendicularly by counterpropagating, superimposed beams from two pulsed dye lasers. The first, Nd:YAG pumped dye laser (JK HY750/Quanta Ray PDL-2) was used to populate levels (v',J') in the A (O_u^+) state of Ag_2. The tunable ultraviolet radiation for the second, ionising step was generated by frequency doubling the output of an excimer pumped dye laser (Lambda Physik EMG 201MSC/FL23002EC) in a beta barium borate crystal. Since the molecular constants of the A and X states of Ag_2 had already been determined to high accuracy [3], there was no need to perform another calibration of the position of the A-X bandheads. It was sufficient to carry out a short R2PI scan before each threshold scan to ensure that the exciting laser was tuned correctly to the appropriate bandhead. Calibration of the photon energy in the second ionising step was achieved by recording monitor etalon fringes together with neon optogalvanic lines, using the fundamental visible laser output. Laser powers were monitored using photodiodes in order to enable the PIE curves to be power-normalised.

Atomic and molecular ionisation potentials are depressed in the presence of static electric fields due to the occurrence of field ionisation [4]. The static field opposes the coulombic core-electron attraction and facilitates escape of the outgoing electron at a lower ionisation energy than in the zero-field case. To circumvent this problem pulsed, rather than static extraction fields were used to enable the measurement of PIE spectra under field-free conditions. The Ag_2 molecules were ionised with the ion extraction optics of the time-of-flight mass spectrometer held at ground potential. After a short, variable delay, the newly created photoions were accelerated in to the RETOFMS by switching on the extraction voltages using a custom built fast risetime high voltage pulser.

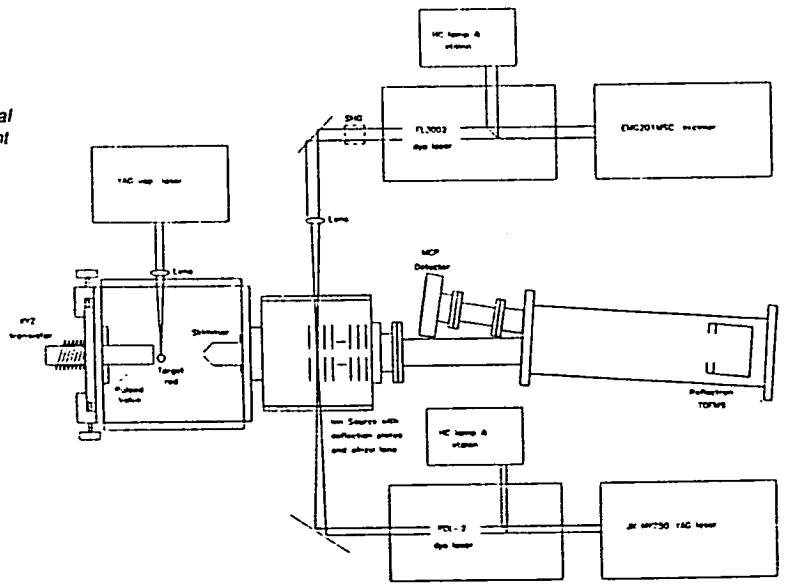

Figure 1: Schematic of the experimental apparatus used in the present studies.

3. RESULTS AND DISCUSSION

Figure 2 shows the PIE spectrum for two-colour photoionisation of $^{107}Ag_2$ under zero-field conditions. Here the exciting dye laser was tuned to the A - X (0-0) band at 22987 cm^{-1} while the ionising laser was scanned over the threshold. The time delay between the synchronised laser pulses and application of the high voltage extraction pulse was 150 ns. During this delay period, the nascent photoions drift along the molecular beam axis by only 0.3 mm, so that they are still well within the ion source when the accelerating potential is applied.

The observed field-free threshold is somewhat broader than we have observed previously for Cu_2 and CuAg. Consequently the ionisation potential for Ag_2 is somewhat more poorly determined. Summing the laser photon energies at threshold yields the value 61725 (30) cm^{-1};
(cf. Cu_2, IP= 63752(3) cm^{-1}; CuAg, IP= 62754(4) cm^{-1}) [2]. This value may be compared with the adiabatic ionisation potential recently reported by Beutel et al. [5], 61747(4) cm^{-1}, from the convergence limits of Rydberg series converging towards vibrational levels v^+ in the ground state of the cation Ag_2^+.

One slightly suprising feature of the PIE spectrum is the almost complete absence of features lying to the red of the ionisation threshold. By analogy with atomic spectroscopy, one might have expected to see sharp features due to long-lived molecular Rydberg states being field ionised by the pulsed extraction field before they decay. We apply approximately 1000 V across the repeller-draw out region in the RETOFMS, creating an extraction field of approximately 330 Vcm^{-1}. This should permit the observation, by field ionisation, of all molecular Rydberg states as far as 110 cm^{-1} below threshold, provided that they do not decay during the time delay between laser excitation and pulsed extraction. The unexpectedly short lifetimes of the Rydberg states remains a puzzle. One possible explanation is that they may be heavily predissociated by repulsive states correlating with excited neutral atomic limits. However, there is clearly scope for further work to elucidate the dynamical processes responsible.

Figure 3 shows the PIE spectrum following excitation via the (1-0) band of the A-X system, at 23181 cm^{-1}. Within experimental error, the ionisation threshold was found at the same two-laser energy as for the determination via the (0-0) band above. Qualitatively, however, the PIE spectrum in the post-threshold region is very different to that obtained when the vibrationless level of the A state was excited. The initial rise in ion signal as the first threshold is crossed is somewhat diminished compared to that observed for excitation via the origin band. More noticeably, there is considerably more post-threshold structure which we assign to vibrationally excited states that autoionise into the first ionisation limit. A detailed analysis of this post-threshold structure is currently in progress.

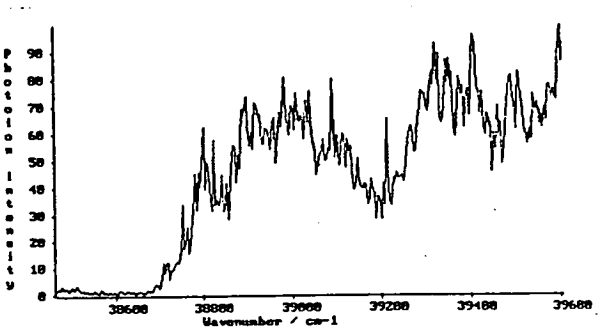

Figure 2: PIE curve for $^{107}Ag_2$. Excitation via the A - X (0-0) band.

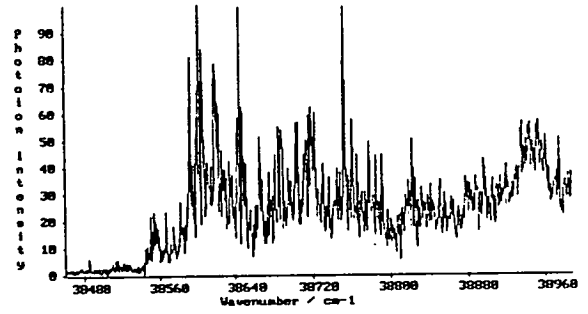

Figure 3: PIE curve for $^{107}Ag_2$. Excitation via the A - X (1-0) band.

4. REFERENCES

1. C.W.Bauschlicher, Jr., S.R.Langhoff, H.Partridge and S.P.Walch, J.Chem.Phys., **86**, 5603, 5603 (1987); E.Miyoshi, H.Tatewaki andT.Nakamura,J.Chem.Phys.,78,815(1983);H.Stoll, P.Fuentealba, M.Dolg, J.Flad, L.V.Szentpaly and H.Preuss, J .Chem.Phys., **79**, 5532 (1983).
2. A.M.James, *Ph.D. Thesis*, The University of Edinburgh (1990); A.M.James, J.F.Miller, G.W.Lemire and P.R.R.Langridge-Smith (unpublished work).
3. B.Simard, P.A.Hackett, A.M.James and P.R.R.Langridge-Smith, Chem.Phys.Lett., **186**, 415 (1991).
4. M.Broyer, J.Chevaleyre, G.Delacetaz, S.Martin and L.Woste, Chem.Phys.Lett., **99**, 266 (1983).
5. V.Beutel, G.L.Bhale, M.Kuhn and W.Demtroder, Chem.Phys.Lett., **185**, 313 (1991).

Evidence for icosahedral atomic shell structure in nickel and cobalt clusters. Comparison with iron clusters

M. Pellarin [a], B. Baguenard [a], J.L. Vialle [a], J. Lermé [a], M. Broyer [a], J. Miller [b] and A. Perez [c]

[a] *Laboratoire de Spectrométrie Ionique et Moléculaire (URA No. 171), CNRS et Université Lyon I, Bâtiment 205, 43 Boulevard du 11 Novembre 1918, 69622 Villeurbanne Cedex, France*

[b] *Department of Chemistry, University of Edinburgh, West Mains Road, Edinburgh EH9 3JJ, Scotland, UK*

[c] *Département de Physique des Matériaux (URA No. 172), CNRS et Université Lyon I, Bâtiment 203, 43 Boulevard du 11 Novembre 1918, 69622 Villeurbanne Cedex, France*

Received 25 March 1993

For the first time, the mass distribution of nickel, cobalt and iron clusters is analyzed in a large mass range with near threshold photoionization experiments and standard time-of-flight mass spectrometry. In the case of nickel and cobalt, oscillations observed in mass spectra correspond to icosahedral atomic shell structure in the studied mass range (50–800 atoms). For iron clusters, the situation is less clear. The exact location of structures in mass spectra depends on source operating conditions. We have observed the competition between different cluster geometries.

1. Introduction

Since the beginning of the eighties there has been a rapidly increasing activity in studying small free metallic clusters. One of the main goals of these studies is to find the general rules which govern the physical and chemical properties of these clusters and how they are linked either to the electronic structure of the corresponding free atom or to the solid state properties in the bulk [1]. With this motivation in mind, a lot of experimental work has been performed to look to what extent the concepts and the theoretical models, which succeeded in describing the cluster properties of some particular elements, may be applied to other species.

As an example, it is now well established that the properties of the alkali clusters, as for instance their ionization potential or their stability, are mainly explained by their electronic shell structure, at least for the not too large sizes ($N \lesssim 2000$) [2]. This structure and the associated "magic" number sequence is well predicted by the spherical jellium background model [3]. However, for larger clusters, it has been observed that the geometry of the ionic arrangement becomes the dominant effect, illustrated by a quite different magic number sequence related to the completion of successive geometrical shells of atoms [4]. Among the trivalent elements, indium and, even better, gallium clusters follow the predictions of the jellium model [5,6], while the structure of the aluminum clusters appears mainly dominated by geometric effects beyond $N \approx 250$ [7,8]. It is tempting to draw a parallel between this difference and the strongly different melting points of these elements in the bulk. As recently pointed out and qualitatively discussed by Stampfli and Benneman [9], the cluster temperature referred to the melting point temperature seems to be an essential parameter to settle what is dominant between electronic or geometric shell effects. Following this idea, one may expect that photoionization mass spectra of transition metal clusters will exhibit shell effects essentially reflecting properties rather than pure electronic (jellium-like) ones. Moreover the electronic configuration of these elements, with outer d electrons, makes the agreement with the jellium model unlikely. Testing this assumption is one of the goals of the near-threshold photoionization experiment we have performed on nickel, cobalt and iron clusters.

Studying the transition metal clusters is very in-

SSDI 00009-2614(93)E1474-U

teresting to test the validity of general theoretical models, but also, and probably even more, to understand their specific properties. Transition metal clusters indeed are very promising species on account of their important possible applications in chemistry and in material science. Let us mention, as examples, two research fields: magnetic properties in clusters of ferromagnetic elements in the scope of magnetism [10,11] and chemical reactivity in connection with catalytic processes [12,13]. The important instrumental stride which made these experiments on transition metal clusters possible, even for the most refractory ones, is the invention of the laser vaporization technique [14,15].

The determination of the cluster geometry is the first unavoidable stage for understanding other more specific properties. Several methods involving free clusters can provide informations about this question: measurements of intensity anomalies in the mass distribution of the produced clusters (depending on the process of the cluster growth) [16,17], chemical reactivity experiments [13,18] and near-threshold photoionization experiments [8,19].

Photoionization experiments performed on nickel, cobalt and iron clusters are reported in this Letter. The metallic clusters are produced by the laser vaporization technique, laser photoionized with a photon energy close to the threshold and then analyzed by standard time-of-flight mass spectrometry. For the small clusters ($N \lesssim 100$) of these three metals, experimental values of their ionization potentials have already been published [20–22]. Our results, which are quantitative for iron only, are in very good agreement with the former.

For larger sizes ($100 \lesssim N \lesssim 800$) the results we obtained for nickel and cobalt clusters look very similar. In both cases, a regular structure, periodic on a $N^{1/3}$ scale, is observed. It is found to be consistent with the filling of successive shells of atoms assuming an icosahedral cluster geometry. The details of this structure agree with the so-called umbrella model proposed by Martin et al. [16,23] to explain the filling sequence.

On the contrary, there is no evidence for a clear and single geometric shell structure in the case of iron clusters. By changing the source conditions, it is possible to modify the features observed in the mass spectra, probably revealing a competition between several different structures.

2. Experimental setup

A detailed description of our experimental setup can be found in an earlier publication [8]. Only the main points will be briefly recalled. Our cluster source is designed according to the one described by Milani and de Heer [24]. A frequency-doubled Nd:YAG pulsed laser ($\lambda = 532$ nm) is focused onto a rod of the metal to be studied (Fe, Ni or CO), where it creates a hot metallic plasma. In synchronism with the laser shot, a fast pulsed valve delivers a sudden and intense peak flow of helium. This carrier gas recombines the laser-produced plasma, cools it, and induces the cluster growth. Several different nozzles were successively tried as exit aperture of the source chamber; best results and heaviest clusters were obtained with a conical nozzle.

A few centimeters downstream from the nozzle, the cluster beam passes through a skimmer and forms a free supersonic beam. Neutral clusters are then photoionized and the mass distribution of the ionized species is analyzed by standard time-of-flight mass spectrometry. Near threshold photoionization is performed with a frequency-doubled tunable dye laser pumped by an XeCl excimer laser. Individual mass spectra are recorded and added in a fast digital oscilloscope and the averaged spectrum is then transferred into a microcomputer for further analysis.

3. Results for small clusters ($N \lesssim 70$)

The resolution of our mass spectrometer is sufficient to clearly separate the successive cluster peaks in this size range. So, it is possible to study a given physical property for each individual cluster size separately. We determine the ionization potentials (IP) of iron clusters Fe_N for $9 \leqslant N \leqslant 68$ using a standard procedure [8,21]. Mass spectra are recorded for a series of different ionization photon energies. The laser fluence, recorded at the same time, is kept low enough to avoid multiphoton processes. After normalizing the peak height to the laser fluence for each cluster and each photon energy, we obtain pho-

toionization efficiency curves. The IP values are determined from these curves by a linear extrapolation in the threshold region.

Our results for iron clusters are displayed in fig. 1. For comparison purpose the earlier measurements performed by Yang and Knickelbein [22] for the same clusters are also presented in fig. 1. The two curves look very similar: we notice a rapid and irregular decrease of the IP with cluster size below $N=25$, followed by a smooth and nearly flat behaviour above $N=25$. However, several slight discrepancies may be noted. First, as a general rule, our values are a little bit lower than those measured by Yang and co-workers. This is not surprising since our measurements are performed with a cluster source at room temperature (300 K) while these authors worked with a liquid nitrogen cooled source (77 K). A higher cluster temperature certainly explains this systematic difference. Secondly, the ionizing photons are obtained in our experiment by frequency doubling in a BBO crystal. So, their is energy is limited below $h\nu=5.63$ eV. For the smallest clusters ($N\leqslant 17$), the IPs are close to this upper limit and only a short frequency range is available to construct the photoionization efficiency curve above threshold. For this reason our experimental IPs are certainly less accurate and probably underestimated. This explains the larger discrepancy between the two curves below $N=17$. Finally, two slight differences remain unexplained: the abrupt increases of the IP for $N=21$–22 and $N=40$–41 observed by Yang and co-workers are clearly missing on our curve. Nevertheless, our results largely confirm their measurements and we do not observe any feature revealing a regular shell structure. This is quite different from what happens in alkali or trivalent metal clusters [2,5,6]. Moreover, the evolution of the IP with cluster size is not well described by the $1/R$ law in the case of iron clusters.

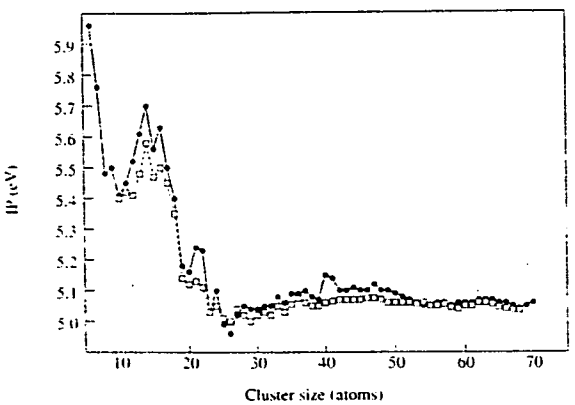

Fig. 1. Iron cluster IPs versus cluster size. Our results (□) are compared with those obtained by Yang et al. (●, ref. [22]). For $N>25$, there is no evidence for shell structure.

Concerning the cobalt and nickel clusters, IP values were measured and published three years ago up to $N=92$ and $N=90$, respectively [22,21]. For nickel clusters, they are beyond 5.6 eV and beyond or near 5.5 eV for cobalt. As mentioned above, our UV laser is not well suited for such high IPs. Since these quantities had already been measured we estimated it needless to perform the same experiments again. However, we recorded a few near-threshold photoionization spectra which look consistent with the published results. In such a spectrum, indeed, peak-to-peak abrupt intensity changes reveal the anomalies in the ionization threshold and, then, the shell effects. It is therefore possible to get from these mass spectra as many physical informations as from the final IP curve provided one is only interested in the abrupt changes of the IP (shell effects) and not in its absolute value nor in its slow evolution with cluster size. Moreover, extracting a complete IP curve requires much more time and several normalization procedures with respect to the laser fluence and the cluster beam intensity. This is a source of additional uncertainty which rubs out the weakly pronounced effects. In other words, weak shell effects will be visible on the primary mass spectra but will be blurred within the extrapolation method used for IP assignments (Watanabe, linear extrapolation) and the error bars on the final IP curve. For instance, our mass spectra of iron clusters in the mass range $N=25$–75 exhibit clearly irregular peak intensities while the IP curve we have obtained is nearly flat. The emergence of these structured features encouraged us to pursue and to look at photoionization mass spectra of heavier clusters.

4. Results for larger clusters ($50\lesssim N\lesssim 800$)

Mass spectra obtained with a photon energy near

the photoionization threshold have been recorded. They present reproducible irregularities in relative mass intensities.

Spectra of cobalt and nickel in a large mass range are shown in fig. 2. They both exhibit strong effects at the reported sizes (55, 147, 309, 561). These features are consistent with closing of successive atomic shells in a cubo-octahedral or an icosahedral structure. Several smaller effects are noticeable for intermediates sizes. To make these oscillations more apparent, we use a simple and usual method: a sufficiently smoothed bell-shape envelope is subtracted from the untreated spectrum. We can eventually also smooth the resulting difference. Such a processed spectrum is displayed in the lower part of fig. 2. Only nickel cluster spectrum is shown but the same structures are available for cobalt.

The hypothesis of successive atomic shell filling is supported by the sequence reproductibility in the spectral features. It is shown in fig. 3 for nickel (left part) and cobalt (right part) on a $N^{1/3}$ scale. These spectra correspond, from top to bottom, to the filling of atomic shells from $N=55$ (second closed shell) to

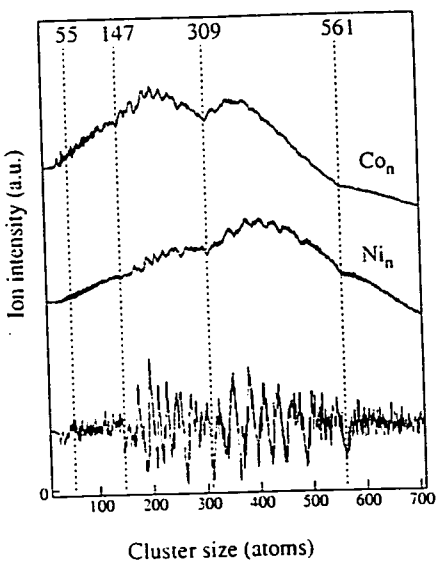

Fig. 2. Mass spectra of cobalt and nickel clusters. Characteristic sizes corresponding to the major shell effects are reported. The lower spectrum is the same as the nickel cluster one with suitable mathematic treatment to make structures more apparent (see text). These structures are consistent with icosahedral atomic shell filling.

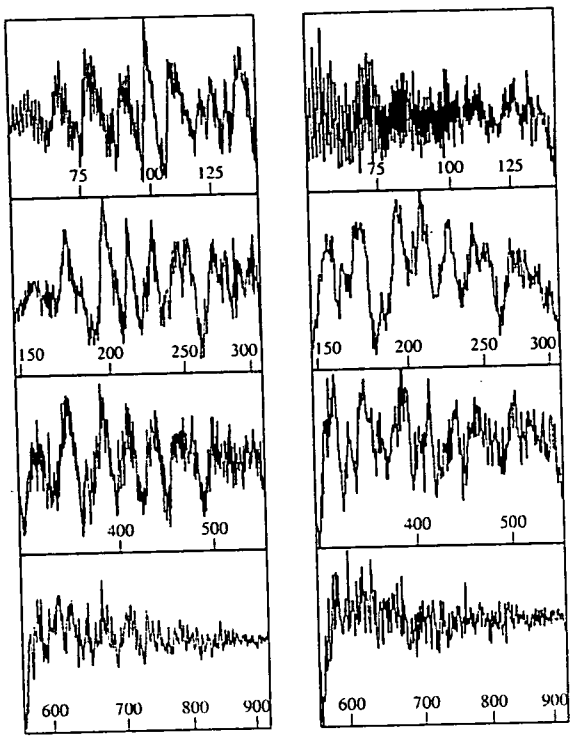

Fig. 3. Nickel (left part) and cobalt (right part) mass spectra on a $N^{1/3}$ scale. The sequence of shell filling is reproducible from one shell to another one. From the top to the bottom, spectra show the filling of the shells 55–147 atoms, 147–309 atoms, 309–561 atoms, 561–923 atoms. Few sizes (in atoms) are indicated, Ion signal is given in arbitrary units.

$N=925$ (sixth closed shell). Their likeness shows that the same structure is available all over the studied mass range. The main difficulty is to identify undoubtedly the exact one. For this, we assume that features of spectra at intermediate sizes correspond to subshell closings.

The difference between these two atomic shell geometries (cubo-octahedron and icosahedron) appears when looking at the subshell filling. In the case of the cubo-octahedron, the filling sequence is not expected to be regular because there are 14 non-equivalent faces: eight close-packed triangular ones and six not close-packed square ones. This model, not described in the literature, is expected to lead to numerous different ways of shell filling, depending on whether added atoms settle down preferentially

on triangular faces (close-packed) or square ones (maximizing the number of nearest-neighbouring atoms). For icosahedron, there are 20 equivalent triangular faces. Subshell closings, corresponding to the filling of successive faces, are almost regularly spaced. Because of the regularity of the observed structure, we leave the cubo-octahedral model and take an interest in the icosahedral one. The problem remains to know the exact subshell filling sequence. Let us recall the two different ways to fill icosahedral atomic shells described in the literature.

The first model, applied for rare gas clusters, was given by Northby [25,26]. The atom–atom interaction is described by a Lennard-Jones potential. Atoms are added one by one on a rigid core (Mackay icosahedra). The most stable cluster structure is obtained by minimizing its total energy. When the atomic shell is half-filled, there is a particular rearrangement of atoms: they take place at this size on icosahedral sites, when they are totally free on cluster surface, just after opening the shell. This model was used successfully to describe features in mass spectra of rare gas clusters. Later, Martin et al. proposed another model for icosahedral shell filling in calcium and magnesium clusters [16,23]. This one is known as the "umbrella" model. In this case, atoms, added one by one on the rigid core, are forced to take place on icosahedral sites (atoms are not so free like in the preceding model). Enhanced stability is achieved each time a face is covered, and especially when a corner and its five surrounding faces are covered (umbrella shape).

In the case of nickel and cobalt, the agreement between experimental results and the umbrella model predictions is very good (see table 1). The correlation is shown in fig. 4. For large clusters (above 200 atoms), the major effects are observed for the completion of a new umbrella. However, this correlation is not so clear for light clusters ($\lesssim$200 atoms), because the completions of successive subshells and umbrellas are close to each other. Thus our experimental results are consistent with the predictions of both models. We are not able to determine very accurately the exact structure in this size range, but the major effects remain consistent with icosahedral atomic shell sequence.

These results provide an experimental proof of the icosahedral structure of cobalt and nickel clusters. They agree with theoretical predictions. In the case of nickel, the icosahedral structure is predicted up to 2000 atoms [27]. The exact one is determined more precisely: our results are in agreement with the filling sequence according to the umbrella model. We were not able to determine the cluster structure above 800 atoms, because in the present stage of the experi-

Table 1
Comparison between experimental results and theoretical predictions of icosahedral atomic shell model described in the literature. The subshell index indicates for experimental results the minima index since the last atomic shell closing feature. It corresponds to the number of covered triangular faces. The corresponding sizes predicted by the two models are reported

Subshell index	4th shell				5th shell			
	our results		umbrella model [23]	rare gas clusters model [25]	our results		umbrella model	rare gas clusters model
	Ni_n	Co_n			Ni_n	Co_n		
0	147	147	147	147	309	309	309	309
5	180	180	178	178	362	360	360	360
8	201	199	200	197	395	395	395	391
10	218	216	216	210	421	420	420	412
12	233	233	232		447	445	445	
14	249	247	248		470	471	470	
15	259	259	258		482	486	485	
17	276	276	274		508	511	510	
18	286	284	284		522	526	525	
19	294	295	294		541	544	540	
20	309	309	309		561	561	561	

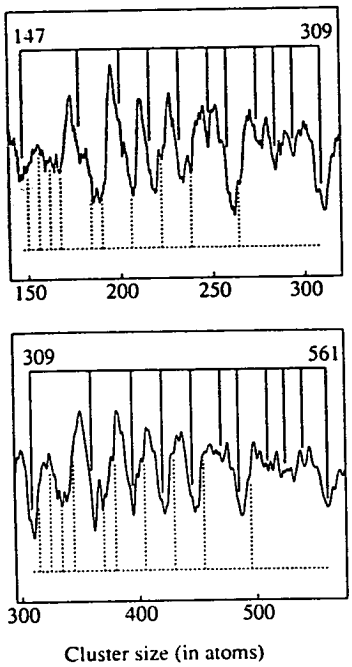

Fig. 4. Shell filling sequence for nickel clusters (on a N scale). The carried effects correspond to icosahedral subshell closings "as umbrellas" (——) and "as not umbrellas" (- - -). Ion signal is given in arbitrary units.

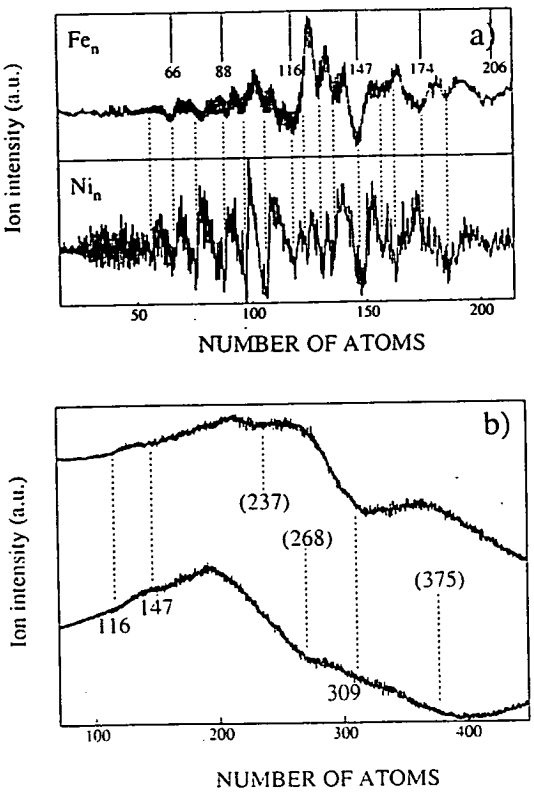

Fig. 5. (a) Comparison between processed mass spectra of iron and nickel clusters. In this case, icosahedral structure is put into evidence. Sizes corresponding to jellium-like structure are also reported at the top of the figure. Under certain circumstances these jellium-like structures are dominant in the spectrum (see text). (b) Unprocessed mass spectra of iron clusters obtained with different source operating conditions. The different major features in these spectra lead us to assume a competition between different cluster structures.

ment we do not produce efficiently heavier clusters in our source.

In the size range 50–150, our results agree with those obtained by Riley and co-workers [18,28] through chemical investigations. By counting the average number of ammonia (or water) molecules adsorbed on bare clusters, they deduced high stability for characteristic cluster sizes. In the case of cobalt and nickel, they found icosahedral structure. Our experiments, which involve an alternative method of investigation, extend their conclusion to a much larger size domain. However in our case, the mass spectrum of small cobalt clusters is not very much structured (see the upper right spectrum in fig. 3). This result must be compared to the magnetic studies of cobalt clusters by Bucher et al. [11]. These authors show that a structural transition occurs and that isomerism exists in the size range 50–70 for cobalt. This can explain our results.

The behavior of iron clusters is quite different. For small sizes ($50 \leqslant N \leqslant 200$), the results are similar to those obtained for nickel and cobalt clusters and are in favor of icosahedral structure (fig. 5a). However, even in this size domain, the relative intensities of the observed features are strongly dependent on the source conditions. Under circumstances corresponding to higher cluster temperatures, some intense structures emerge in the mass spectra. These structures are regularly spaced on a $N^{1/3}$ scale. The observed numbers ($N=66$, 87, 113, 147, 171, 206) are very close to those predicted in the spherical jellium shell model with three valence electrons per atom ($N_e=3N$). In the shell model, the major shell closings are expected for $N=66$, 85, 112, 146, 182, 225. In these last conditions, all the subshells of the ico-

sahedral structure remain present in the mass spectra, as superimposed to the main features. It is difficult to go further in the interpretation, but there is clearly a competition between an icosahedral structure and a "jellium-like structure" which could correspond to "liquid" iron clusters.

For larger sizes (fig. 5b), the mass spectra remain structured, and the observed structures are strongly dependent on the source conditions. In the present stage of the experiment we are not able to identify any regular structure, but it is clear that we have a strong competition between different isomers.

In the small size range, our results on iron clusters are in good agreement with other authors who have used other investigation methods. Riley and coworkers [29] have performed chemical probe of the iron clusters ($2 < N < 165$) and found numerous different structures. During their IP measurements, Yang et al. [22] have also evoked the existence of isomers to explain the ionization cross section close to the threshold. More recently, Armentrout and coworkers [30] have measured the bond energies of iron clusters in the size range $2 \leqslant N \leqslant 19$. They found isomers which are weakly bound for $6 \leqslant N \leqslant 19$ and the isomer percentage reaches 30% for $N = 19$. This competition between isomers is not surprising in iron cluster since in the bulk there is also competition between different cristalline structures.

5. Conclusion

In conclusion, we have shown in this Letter that cluster photoionization near the threshold followed by time-of-flight mass spectrometry is an efficient way to determine the geometric structure of transition metal clusters.

We have identified icosahedral atomic shell structure of nickel and cobalt clusters up to 800 atoms. Our results are well correlated with the umbrella model proposed by Martin et al. for magnesium an calcium clusters. However, the situation is less clear for light clusters. For smaller ones ($N < 70$), the exact structure is not well identified by this method because subshell closings are close together in the different growth sequences. Moreover, icosahedral features are less evident and isomer species can exist in this size domain.

For iron, the situation is more complex. The observed features depend strongly on source operating conditions. There may be icosahedral structure for light clusters, but this is probably in competition with other ones that are not clearly identified. The predominance of one of them by changing source conditions is not easy to obtain.

References

[1] S. Bjørnholm, Contemp. Phys. 31 (1990) 309.
[2] W.D. Knight, K. Clemenger, W.A. de Heer, W.A. Saunders, M.Y. Chou and M.L. Cohen, Phys. Rev. Letters 52 (1984) 2141;
J. Pedersen, S. Bjørnholm, J. Borgreen, K. Hansen, T.P. Martin and H.D. Rasmussen, Nature 353 (1991) 733;
C. Bréchignac, Ph. Cahuzac, F. Carlier, M. de Frutos and J.Ph. Roux, Phys. Rev. B 47 (1993) 2271.
[3] W. Eckhardt, Phys. Rev. B 29 (1984) 1558;
H. Nishioka, K. Hansen and B.R. Mottelson, Phys. Rev. B 42 (1990) 9377.
[4] T.P. Martin, T. Bergmann, H. Göhlich and T. Lange, Chem. Phys. Letters 172 (1990) 209.
[5] J.L. Persson, R.L. Whetten, H.P. Cheng and R.S. Berry, Chem. Phys. Letters 186 (1991) 215;
B. Baguenard, M. Pellarin, C. Bordas, J. Lermé, J.L. Vialle and M. Broyer, Chem. Phys. Letters, 205 (1993) 13.
[6] M. Pellarin, B. Baguenard, C. Bordas, M. Broyer, J. Lermé and J.L. Vialle, Phys. Rev. Letters, submitted for publication.
[7] T.P. Martin, U. Näher and H. Schaber, Chem. Phys. Letters 199 (1992) 470.
[8] M. Pellarin, B. Baguenard, M. Broyer, J. Lermé, J.L. Vialle and A. Perez, J. Chem. Phys. 98 (1993) 944.
[9] P. Stampfli and K.H. Bennemann, Phys. Rev. Letters 69 (1992) 3471.
[10] W.A. de Heer, P. Milani and A. Chatelain, Phys. Rev. Letters 65 (1990) 488.
[11] J.P. Bucher, D.C. Douglass and L.A. Bloomfield, Phys. Rev. Letters 66 (1991) 3052.
[12] S.C. Richtsmeier, E.K. Parks, K. Liu, L.G. Pobo and S.J. Riley, J. Chem. Phys. 82 (1985) 3659.
[13] P. Fayet, M.J. McGlinchey and L. Wöste, J. Am. Chem. Soc. 109 (1987) 1733.
[14] T.G. Dietz, M.A. Duncan, D.E. Powers and R.E. Smalley, J. Chem. Phys. 74 (1981) 6511.
[15] J.B. Hopkins, P.R.R. Landgridge-Smith, M.D. Morse and R.E. Smalley, J. Chem. Phys. 78 (1983) 1627.
[16] T.P. Martin, U. Näher, T. Bergmann, H. Göhlich and T. Lange, Chem. Phys. Letters 183 (1991) 119.
[17] O. Echt, K. Sattler and E. Recknagel, Phys. Rev. Letters 47 (1981) 1121.
[18] T.D. Klots, B.J. Winter, E.K. Parks and S.J. Riley, J. Chem. Phys. 95 (1991) 8919;
E.K. Parks, B.J. Winter, T.D. Klots and S.J. Riley, J. Chem. Phys. 94 (1991) 1882.

[19] H. Göhlich, T. Lange, T. Bergmann, U. Näher and T.P. Martin, Chem. Phys. Letters 187 (1991) 67.
[20] E.A. Rohlfing, D.M. Cox, A. Kaldor and K.H. Johnson, J. Chem. Phys. 81 (1984) 3846.
[21] M.B. Knickelbein, S. Yang and S.J. Riley, J. Chem. Phys. 93 (1990) 94.
[22] S. Yang and M.B. Knickelbein, J. Chem. Phys. 93 (1990) 1533.
[23] T.P. Martin, T. Bergmann, H. Göhlich and T. Lange, Chem. Phys. Letters 176 (1991) 343; J. Phys. Chem. 95 (1991) 6421.
[24] P. Milani and W.A. de Heer, Rev. Sci. Instrum. 61 (1990) 1835.
[25] J.A. Northby, J. Chem. Phys. 87 (1987) 6166;
I.A. Harris, R.S. Kidwell and J.A. Northby, Phys. Rev. Letters 53 (1984) 2390;
W. Miehle, O. Kandler, T. Leiswer and O. Echt, J. Chem. Phys. 91 (1989) 5940.
[26] J. Farges, M.F. de Feraudy, B. Raoult and G. Torchet, J Chem. Phys. 84 (1986) 3491.
[27] C.L. Cleveland and U. Landman, J. Chem. Phys. 94 (1991 7376.
[28] B.J. Winter, T.D. Klots, E.K. Parks and S.J. Riley, Z. Physi D 19 (1991) 375;
T.D. Klots, B.J. Winter, E.K. Parks and S.J. Riley, J. Chem. Phys. 92 (1990) 2110.
[29] E.K. Parks, B.H. Weiller, P.S. Bechthold, W.F. Hoffman G.C. Neiman, L.G. Pobo and S.J. Riley, J. Chem. Phys. 8 (1988) 1622;
E.K. Parks, G.C. Nieman, L.G. Pobo and S.J. Riley, J. Chem Phys. 88 (1988) 6260.
[30] L. Lien, C.X. Su and P.B. Armentrout, J. Chem. Phys. 9 (1992) 4072.